ONE, TWO, MANY NANOCRYSTALS

CHARACTERIZING LEAD HALIDE NANOSTRUCTURES FROM SINGLE PARTICLE TO BULK

A Dissertation

Submitted to the Graduate School

of the University of Notre Dame

in Partial Fulfillment of the Requirements

for the Degree of

Doctor of Philosophy

by

Stefano Toso

_____

Liberato Manna, Co-Director

_____

Masaru Kuno, Co-Director

_____

Luca Gavioli, Co-Director

Graduate Program in Chemistry and Biochemistry
Notre Dame, Indiana
April 2023

ONE, TWO, MANY NANOCRYSTALS

CHARACTERIZING LEAD HALIDE NANOSTRUCTURES FROM SINGLE PARTICLE TO BULK

A Dissertation for the Degree of

Doctor of Philosophy

by

Stefano Toso

_____

Liberato Manna, Co-Director

_____

Masaru Kuno, Co-Director

_____

Luca Gavioli, Co-Director

International Doctoral Program in Science
Università Cattolica del Sacro Cuore, Italy
Cycle XXXIV, Academic Year 2022-23

ONE, TWO, MANY NANOCRYSTALS

CHARACTERIZING LEAD HALIDE NANOSTRUCTURES FROM SINGLE PARTICLE TO BULK

Abstract

by

Stefano Toso

Over the past few decades colloidal chemistry has provided access to a growing variety of inorganic nanostructures with diverse and customizable properties, which can be tailored to many different applications. However, such diversity presents challenges when it comes to characterizing the structure of functional nanomaterials, where the small size and the increased complexity impose technical limitations.

This Thesis aims to address these challenges by developing novel approaches to characterize and describe the structure of nanomaterials, which are here demonstrated on lead halide semiconductor nanostructures. These materials are widely investigated for their appealing properties and the structural diversity they express at the nanoscale, and pose therefore a variety of compelling scientific questions. Here are discussed four case studies, each characterized by increasing nanoscale complexity.

I) Colloidal nanocrystals of previously unknown lead chalcohalide phases are used to demonstrate strategies for solving the structure of novel inorganic materials by means

of combined electron and X-ray diffraction techniques. Guidelines are proposed for each step of the structure solution process, from the stoichiometry determination to the cell indexation and the final structure refinement.

II) Epitaxial dimers formed by cesium lead halide compounds are rationalized as reaction intermediates in the chemical transformation of colloidal nanocrystals, and the structural relationships enabling their formation are explored. Following this lead, perovskite/chalcohalide heterostructures are demonstrated as effective templates for the phase-selective synthesis of colloidal nanocrystals.

III) Superlattices of lead halide perovskite nanocrystals are used to develop a novel approach for characterizing the nanoscale structure of self-assembled nanocrystal solids. This method is based on diffraction techniques developed for multilayer thin films grown by physical methods, and relies on the analysis of collective interference phenomena in the wide-angle X-ray diffraction pattern of samples.

IV) Microcrystalline samples of hybrid layered Ruddlesden-Popper perovskites, composed by nanoscale stacks of organic and inorganic layers, are investigated through a geometric analysis of their unit cell parameters to determine the inhomogeneous distribution of different halides alloyed within their structure.

To my family, past, present, and future

CONTENTS

FIGURES

x

LIST OF ABBREVIATIONS

3D-ED	**3**-**D**imensional **E**lectron **D**iffraction
3D-FT	**3**-**D**imensional **F**ourier **T**ransform
Ap	**AP**ical
AZO	**A**luminum-doped **Z**inc **O**xide
BA	**B**utyl**A**mmonium
BzBr	**B**enzoyl **B**romide
BzCl	**B**enzoyl **C**hloride
BzI	**B**enzoyl **I**odide
Ct	**C**en**T**ral
DDT	1-**D**o**D**ecane**T**hiol
DFT	**D**ensity **F**unctional **T**heory
DMF	**D**i**M**ethyl**F**ormamide
DOS	**D**ensity **O**f States
DSE	**D**ebye **S**cattering **E**quation
DZVP	**D**ouble **Z**eta **V**alence plus **P**olarization
Eq	**EQ**uatorial
FA	**F**orm**A**midinium
FFT	**F**ast **F**ourier **T**ransform
FTIR	**F**ourier-**T**ransform **I**nfra**R**ed
GISAXS	**G**razing-**I**ncidence **S**mall-**A**ngle **X**-ray **S**cattering
GIWAXS	**G**razing-**I**ncidence **W**ide-**A**ngle **X**-ray **S**cattering
HAADF	**H**igh-**A**ngle **A**nnular **D**ark **F**ield
HR	**H**igh-**R**esolution
ICP	**I**nductively **C**oupled **P**lasma
IPR	**I**nverse **P**articipation **R**atio
LED	**L**ight-**E**mitting **D**evice
LPA	**L**orentz-**P**olarization-**A**bsorption

MA	**M**ethyl**A**mmonium
MS	**M**ass **S**pectrometry
NPDR	**N**ormalized **P**hotocurrent to **D**ark current **R**atio
OA	**O**leic **A**cid
ODE	1-**O**cta**DE**cene
OES	**O**ptical **E**mission **S**pectroscopy
OLA	**OL**eyl**A**mine
PA	**P**ropan**A**mmonium
PBE	**P**erdew-**B**urke-**E**rnzerhof
PCE	**P**ower **C**onversion **E**fficiency
PDA	**P**ropan**D**i**A**mmonium
PDF	**P**air **D**istribution **F**unction
PL	**P**hoto**L**uminescence
PLQY	**P**hoto**L**uminescence **Q**uantum **Y**ield
SAXS	**S**mall-**A**ngle **X**-ray **S**cattering
SCXRD	**S**ingle-**C**rystal **X**-**R**ay **D**iffraction
SEM	**S**canning **E**lectron **M**icroscope (or **M**icroscopy)
SOC	**S**pin-**O**rbit **C**oupling
STEM	**S**canning **T**ransmission **E**lectron **M**icroscope
TEM	**T**ransmission **E**lectron **M**icroscope (or **M**icroscopy)
TGA	**T**hermo**G**ravimetric **A**nalysis
XPS	**X**-ray **P**hotoelectron **S**pectroscopy
XRD	**X**-**R**ay **D**iffraction
XRF	**X**-**R**ay **F**luorescence
XRPD	**X**-**R**ay **P**olycristalline (or **P**owder) **D**iffraction

PREFACE

This Thesis is the result of a collaboration between the Nanochemistry group at the Istituto Italiano di Tecnologia, the department of Chemistry and Biochemistry at the University of Notre Dame, and the department of Mathematics and Physics at the Università Cattolica del Sacro Cuore within the framework of the International Doctoral Program in Science. The scientific results obtained are summarized in eight chapters.

Chapter 1 briefly discusses the historical importance of nanochemistry in the development of functional materials with physical properties modulated by the nanometric structure of matter, and sets the development of methods for the structural characterization of such nanomaterials as the goal of this Thesis.

Chapter 2 introduces the reader to lead halide semiconductors, that are the class of materials which provided the case studies for this Thesis. This chapter discusses the crystal structures of the most relevant phases within the family, and outlines the many advantages that make these materials ideal for developing novel approaches to the structural characterization of nanomaterials.

Chapter 3 outlines the principles of diffraction techniques for the structural characterization of crystalline materials, with a specific focus on the challenges posed by the finite size of nanomaterials and the characterization techniques applied in this Thesis.

Chapter 4 discusses the challenges associated with the discovery and structure determination of unknown crystalline materials at the nanoscale. Successful approaches are demonstrated on nanocrystals of $Pb_4S_3Br_2$, $Pb_3S_2Cl_2$ and of a novel polymorph of $BiSCl$, three materials first reported in the scientific works supporting this Thesis.

Chapter 5 introduces the concept of colloidal epitaxial heterostructures, discusses their role as reaction intermediates in the chemical transformation of lead halide nanocrystals, and proposes their use as phase-specific templates for the synthesis of colloidal nanomaterials. This synthetic approach is demonstrated on lead sulfochloride nanocrystals by exploiting the newly reported $CsPbCl_3$/$Pb_4S_3Cl_2$ heterostructures.

Chapter 6 proposes a novel method for the characterization of highly ordered nanocrystal superlattices, based on the coherent interference of X-rays diffracted by each individual nanocrystal at wide angles. This novel approach, here validated on self-assembled lead halide nanocrystal solids, probes both the atomic and the nanoscale structure of superlattices with one single experiment, and provides a wealth of structural information hardly accessible otherwise.

Chapter 7 investigates the structure of mixed-halide Ruddlesden-Popper perovskites, a class of promising light-harvesting materials composed of nanoscale organic and inorganic layers alternated, and demonstrates an intrinsic tendency of these materials to segregate halides in different crystallographic sites within their structure.

Chapter 8 summarizes the findings of this Thesis, highlighting how, despite the apparent similarities between materials, the characterization approach adopted had to be highly different depending on the sample and the length scale that was probed.

ACKNOWLEDGMENTS

After four years, two continents and many projects, my PhD has finally come to an end. During this journey I had the pleasure and the privilege of meeting the best friends, colleagues, and mentors one can dream of. All of them contributed to making these four years exciting, productive, and overall one of the best times of my life. For that, I would like to express my deepest gratitude.

First and foremost, I want to thank **Liberato Manna**, my main supervisor at IIT. During all these years he has supported me in every possible way, granting me the freedom to pursue my own projects and investing in my personal and scientific development. If there is one single person who made all this possible, that's him.

I also want to thank my co-supervisors **Masaru (Ken) Kuno** and **Luca Gavioli** for their guidance and for contributing to the creation of the International Doctoral Program, which allowed me to spend one year of my PhD at the University of Notre Dame. I am especially grateful to Ken for welcoming me in his group, and for pushing me beyond my limits when I felt lost or stuck.

I also want to thank **Cinzia Giannini**, whom I met at the start of my PhD and has never left my side since. She taught me everything I know about diffraction and, considered that it is about 90% of my thesis, I wouldn't call it a small thing! But there is

much more than that: even if we met in person only for a short month, she has cared about me as much as a family member since.

My most special thank-you goes to **Dmitry Baranov**, who has been to me a mentor, a colleague, and a dear friend all at the same time. He helped me through hard moments in science and life, and has been the most generous and passionate teacher one could wish for. I hope one day I will make good use of your example. Best of luck with your new adventure in Lund, you deserve it all!

Four years, two home institutions, and so many people met along the road! It would take another dissertation to thank everyone personally, but let me at least mention all those who made my PhD so special. First, a big hug to all my old and new friends in Genova: **Aleksandra Predeina**, **Alex Schleusener**, **Andrea Doricchi**, **Andrea Griesi**, **Aniruddha Ray**, **Anna Cabona**, **Beatriz Martín-García**, **Cansunur Demirci**, **Christian Rossi**, **Clara Otero Martínez**, **Emma Sartori**, **Federica Costantino**, **Federico Locardi**, **Francesco Foggetti**, **Fulvio Bellato**, **Giulia Biffi**, **Gabriele Saleh**, **Irene Martin**, **Juliette Zito**, **Laura Graf**, **Lea Pasquale**, **Luca Rebecchi**, **Manuela De Franco**, **Marco Piccinni**, **Marco Ricci**, **Marta Campolucci**, **Martina Foschi,** **Martina Rizzo**, **Matilde Cirignano**, **Michele Ghini**, **Nikolaos Livakas**, **Pascal Rush**, **Salvatore Buonocore**, **Sergio Fiorito**, **Umberto Filippi**, and **Wid Mekseriwattana.** Among them, Giulia and Emma deserve a special place for helping me during hard moments of my life: thank you so much, and look forward to better times!

I also want to thank all the colleagues and collaborators who made my work in IIT possible, fruitful, and very enjoyable as well: **Ahmed Abdelhady**, **Doriana Debellis**, **Federico Catalano**, **Filippo Drago**, **Francesco Di Stasio**, **Francesco De Donato**, **Gabriele La**

cold month far from home, **Jakob Dahl** for getting me started with the art of coding, and all my colleagues and dear friends from Puglia **Anna Moliterni**, **Carlo Giansante**, **Davide Altamura**, **Francesco Scattarella**, and **Rocco Caliandro** for the many projects and time spent together. I also take this chance to thank all the countless colleagues and collaborators who co-authored my research and ultimately made it possible.

My last and dearest thought goes to all the members of my family, beginning with my parents **Giandomenico** and **Sandra**, who have supported (and endured) me throughout these years. They have always believed in my chances of completing such a challenging journey, and were a safe harbor in the roughest of seas. Thank you so much! A big hug also to my cousins and friends **Giorgio**, **Pietro** and **Marta**, and fond memories of my uncles **Fiorenzo** and **Angela**, who hold a special place in my heart.

So here it is, the last lines left to write in my PhD thesis! These are for you who are reading. Be my guest among these pages: I hope you will enjoy them as much as I loved working on the science they tell!

CHAPTER 1:

INTRODUCTION

Nanochemistry, or the science of producing nanostructured materials by chemical means, has been developed for centuries, either by chance or by intention.[1–3] Even excluding natural nanostructures, such as opals (Figure 1.1a-b) and asbestos, the first occurrences of functional nanomaterials can be traced back to the pigments used to confer brilliant colors to glass and pottery. The most renown example is arguably the Lycurgus cup, a roman manufact dating back to the 4th century that owns its mutable color to plasmonic nanoparticles embedded in glass (Figure 1.1c-d). In the following eras, countless other examples can be found: from the 9th century middle-eastern pottery to the stained-glass windows of 13th century cathedrals, nanomaterials have known an empirical and somehow tentative development. However, it was only in 1857 that Michael Faraday published the first proper scientific study addressing the properties of nanoparticles, under the title "*Experimental Relations of Gold (and other Metals) to Light*".[4] Since then, decades of advancements in materials chemistry and characterization techniques provided the fertile background that allowed to kickstart, in the middle of the last century, the steady and thriving progress that nanochemistry still experiences today.

The driving force of this process is the observation that reshaping well-known materials into nanoscale structures can disclose novel and appealing properties. Some examples are the already mentioned plasmonic behavior in metallic nanomaterials,[5,6] the superparamagnetic response in magnetic nanoparticles,[7–9] the optical interference effects in photonic crystals,[10–12] and so on. Nanostructured semiconductors (Figure 1.1e-f), the topic of this thesis, are instead dominated by the correlation between size and electronic properties that goes under the name of quantum confinement.[18–22]
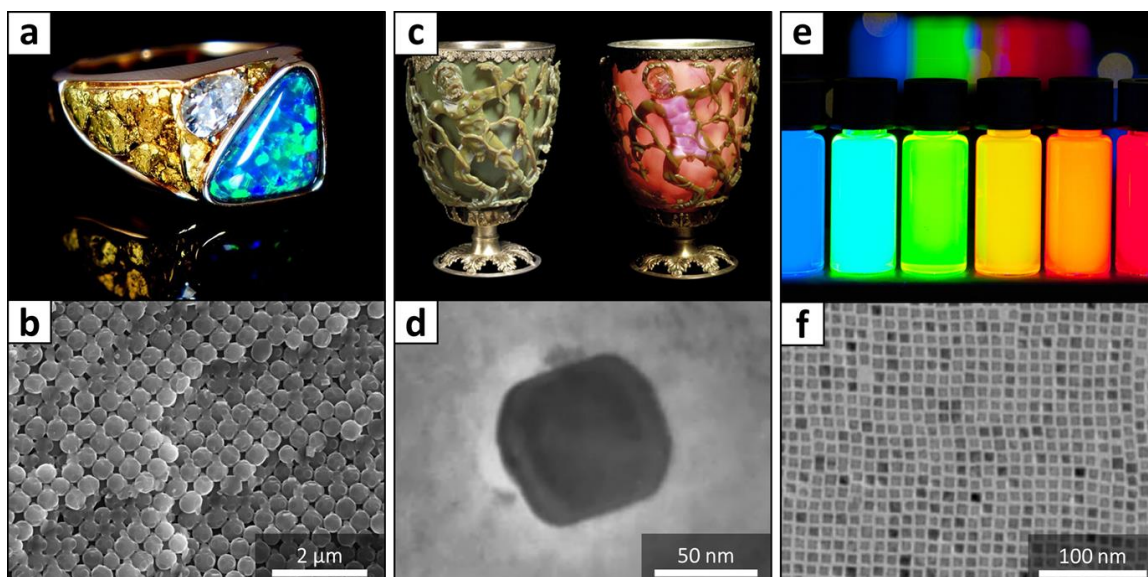
Figure 1.1. Natural, ancient, and modern nanocrystals. a) Opals are natural nanocrystal solids composed of silica nanobeads (b, scanning electron microscopy image). Their bright colors come from light interference effects. c) The Lycurgus cup owes its peculiar dichroism to nanocrystals of an Ag/Au alloy embedded in the glass (d, transmission electron microscopy image). e) Modern quantum dots synthesized by colloidal chemistry methods. f) Transmission electron microscopy image of monodisperse CdSe cubic nanocrystals. Adapted from Refs. 1,13-17.

Nanochemistry became so attractive because it gives new life to old materials. For example, one of the semiconductors that are most studied at the nanoscale, cadmium sulfide (CdS), naturally occurs as a mineral under the name of Greenockite, was first obtained artificially in 1817,[23] and is responsible for the brilliant yellow of Vincent van Gogh's worldwide renown Sunflowers.[24] It is by no means a new material. Yet, researchers all over the world still investigate its properties in the form of nanocrystals nowadays.[25,26] Another example are the cesium lead halide perovskites, a group of materials especially relevant for this thesis, that were obtained back in 1893 by H. L. Wells.[27] In his report, he first wrote that "*Diese Farben sind sehr auffallend*" (these colors are remarkable), referring to their brilliant yellow, orange, and red hues. Little he knew that, more than 120 years after,[28] scientists would become fascinated again by the intense blue, green and red fluorescence that the exact same materials display when reshaped into nanocrystals. However, as the field advanced so did the complexity of nanomaterials. For example, the number of elements included in semiconductor nanocrystals is quickly rising from one or two (Si, CdSe, InP, …),[26,29,30] to three ($CsPbBr_3$, $CuInS_2$, BiSBr, …),[31–33] four ($Cu_2Ga_xIn_{4-x}S7$, $CsAgInCl_6$, …),[34,35] or more.[36–38] Likewise, our control over the synthesis of nanomaterials now gives access to a variety of shapes, spanning from spheres to cubes, from wires to platelets, and even producing more exotic outcomes like octapods,[39] nano-bones[40] and nano-flowers.[41] We discovered how to combine multiple nanoscopic domains into heterostructures,[42] and even how to assemble billions of nanoparticles into nanocrystal solids.[10]

While these advancements offer countless possibilities, the growing complexity of nanomaterials challenges our ability to study them. The aim of this thesis is to take up the challenge. In my research, I focused on a specific class of nanomaterials, the lead-halide semiconductors, and undertook the investigation of their structure at four different scales: individual nanocrystals, heterostructure dimers, colloidal superlattices and layered bulk crystals. Each of them poses different questions, comes with different challenges, and requires a different strategic approach. As we are about to discuss, the materials I selected hold great promises for the future of solution-processed optoelectronics, and achieving a deep understanding of their structure is a crucial step in this direction. However, I took this challenge with the mindset of developing methods not limited to these sole materials, but applicable to those to come.

1.1 Copyright

Some elements of this chapter were adapted from external sources:

1.2 Bibliography

1. Montanarella, F. & Kovalenko, M. V. Three Millennia of Nanocrystals. *ACS Nano* **16**, 5085–5102 (2022).

2. Heiligtag, F. J. & Niederberger, M. The fascinating world of nanoparticle research. *Mater. Today* **16**, 262–271 (2013).

3. Colomban, P. The use of metal nanoparticles to produce yellow, red and iridescent colour, from bronze age to present times in lustre pottery and glass: Solid state chemistry, spectroscopy and nanostructure. *J. Nano Res.* **8**, 109–132 (2009).

4. Faraday, M. The Bakerian Lecture: Experimental Relations of Gold (and Other Metals) to Light. *Philos. Trans. R. Soc. London* **147**, 145–181 (1857).

5.   Zheng, J. *et al.* Gold Nanorods: The Most Versatile Plasmonic Nanoparticles. *Chem. Rev.* **121**, 13342–13453 (2021).

6.   Creighton, J. A. & Eadon, D. G. Ultraviolet–visible absorption spectra of the colloidal metallic elements. *J. Chem. Soc. Faraday Trans.* **87**, 3881–3891 (1991).

7.   Mahmoudi, M., Sant, S., Wang, B., Laurent, S. & Sen, T. Superparamagnetic iron oxide nanoparticles (SPIONs): Development, surface modification and applications in chemotherapy. *Adv. Drug Deliv. Rev.* **63**, 24–46 (2011).

8.   Jeong, U., Teng, X., Wang, Y., Yang, H. & Xia, Y. Superparamagnetic colloids: Controlled synthesis and niche applications. *Adv. Mater.* **19**, 33–60 (2007).

9.   Neuberger, T., Schöpf, B., Hofmann, H., Hofmann, M. & Von Rechenberg, B. Superparamagnetic nanoparticles for biomedical applications: Possibilities and limitations of a new drug delivery system. *J. Magn. Magn. Mater.* **293**, 483–496 (2005).

10.   Boles, M. A., Engel, M. & Talapin, D. V. Self-assembly of colloidal nanocrystals: From intricate structures to functional materials. *Chem. Rev.* **116**, 11220–11289 (2016).

11.   Kim, S. H., Lee, S. Y., Yang, S. M. & Yi, G. R. Self-assembled colloidal structures for photonics. *NPG Asia Mater.* **3**, 25–33 (2011).

12.   Hynninen, A. P., Thijssen, J. H. J., Vermolen, E. C. M., Dijkstra, M. & Van Blaaderen, A. Self-assembly route for photonic crystals with a bandgap in the visible region. *Nat. Mater. 2007 63* **6**, 202–205 (2007).

13.   Barber, D. J. & Freestone, I. C. An Investigation of the Origin of the Colour of the Lycurgus Cup by Analytical Transmission Electron Microscopy. *Archaeometry* **32**, 33–45 (1990).

14.   Lv, L., Li, J., Wang, Y., Shu, Y. & Peng, X. Monodisperse CdSe Quantum Dots Encased in Six (100) Facets via Ligand-Controlled Nucleation and Growth. *J. Am. Chem. Soc.* **142**, 19926–19935 (2020).

15.   Black Opal Ring with Diamond. https://commons.wikimedia.org/wiki/File:Black_Opal_Ring_with_Diamond.jpg.

16.   Minerals Colored by Physical Processes. http://minerals.gps.caltech.edu/COLOR_Causes/Physical_Process/.

17.   Quantum Dots with emission maxima in a 10-nm step are being produced at PlasmaChem in a kg scale. https://commons.wikimedia.org/w/index.php?curid=26950552.

18.   Kuno, M. *Introductory Nanoscience: Physical and Chemical Concepts*. *Garland Science* (2011).

19.   Kuno, M., Gushchina, I., Toso, S. & Trepalin, V. No One Size Fits All: Semiconductor Nanocrystal Sizing Curves. *J. Phys. Chem. C* **126**, 11867–11874 (2022).

20.   Baskoutas, S. & Terzis, A. F. Size-dependent band gap of colloidal quantum dots. *J. Appl. Phys.* **99**, 013708 (2006).

21.   Efros, A. L. & Rosen, M. Electronic structure of semiconductor nanocrystals. *Annu. Rev. Mater. Sci.* **30**, 475–521 (2000).

22.   Kamal, J. S. *et al.* Size-dependent optical properties of zinc blende cadmium telluride quantum dots. *J. Phys. Chem. C* **116**, 5049–5054 (2012).

23.   Cadmium: An Illusive Presence | Dartmouth Toxic Metals. https://sites.dartmouth.edu/toxmetal/more-metals/cadmium-an-illusive-presence/.

24.   Van Der Snickt, G. *et al.* Combined use of Synchrotron Radiation Based Micro-X-ray Fluorescence, Micro-X-ray Diffraction, Micro-X-ray Absorption Near-Edge, and Micro-Fourier Transform Infrared Spectroscopies for Revealing an Alternative Degradation Pathway of the Pigment Cadmium Ye. *Anal. Chem.* **84**, 10221–10228 (2012).

25.   Houtepen, A. J., Hens, Z., Owen, J. S. & Infante, I. On the Origin of Surface Traps in Colloidal II-VI Semiconductor Nanocrystals. *Chem. Mater.* **29**, 752–761 (2017).

26.   Murray, C. B., Norris, D. J. & Bawendi, M. G. Synthesis and Characterization of Nearly Monodisperse CdE (E = S, Se, Te) Semiconductor Nanocrystallites. *J. Am. Chem. Soc.* **115**, 8706–8715 (1993).

27.   Wells, H. L. Über die Cäsium- und Kalium-Bleihalogenide. *Zeitschrift für Anorg. Chemie* **3**, 195–210 (1893).

28.   Schmidt, L. C. *et al.* Nontemplate synthesis of $CH_3NH_3PbBr_3$ perovskite nanoparticles. *J. Am. Chem. Soc.* **136**, 850–853 (2014).

29. Wilson, W. L., Szajowski, P. F. & Brus, L. E. Quantum confinement in size-selected, surface-oxidized silicon nanocrystals. *Science (80-.).* **262**, 1242–1244 (1993).

30. Ramasamy, P., Kim, N., Kang, Y. S., Ramirez, O. & Lee, J. S. Tunable, Bright, and Narrow-Band Luminescence from Colloidal Indium Phosphide Quantum Dots. *Chem. Mater.* **29**, 6893–6899 (2017).

31. Protesescu, L. *et al.* Nanocrystals of Cesium Lead Halide Perovskites ($CsPbX_3$, X = Cl, Br, and I): Novel Optoelectronic Materials Showing Bright Emission with Wide Color Gamut. *Nano Lett.* **15**, 3692–3696 (2015).

32. Berends, A. C., Mangnus, M. J. J., Xia, C., Rabouw, F. T. & De Mello Donega, C. Optoelectronic Properties of Ternary I-III-VI 2 Semiconductor Nanocrystals: Bright Prospects with Elusive Origins. *J. Phys. Chem. Lett.* **10**, 1600–1616 (2019).

33. Quarta, D. *et al.* Colloidal Bismuth Chalcohalide Nanocrystals. *Angew. Chemie* **61**, e202201747 (2022).

34. Pan, D. *et al.* Synthesis of quaternary semiconductor nanocrystals with tunable band gaps. *Chem. Mater.* **21**, 2489–2493 (2009).

35. Locardi, F. *et al.* Colloidal Synthesis of Double Perovskite $Cs_2AgInCl_6$ and Mn-Doped $Cs_2AgInCl_6$ Nanocrystals. *J. Am. Chem. Soc.* **140**, 12989–12995 (2018).

36. Chang, S. H. *et al.* Facile colloidal synthesis of quinary $CuIn_{1-x}Ga_x(SySe_{1-y})_2$ (CIGSSe) nanocrystal inks with tunable band gaps for use in low-cost photovoltaics. *Energy Environ. Sci.* **4**, 4929–4932 (2011).

37. Xu, Y. *et al.* Preparation of quinary $CuNi_xZn_{2-x}InS_4$ nanocrystals with wurtzite structure and tunable band gap. *J. Alloys Compd.* **820**, 153436 (2020).

38. Braun, M. B., Korala, L., Kephart, J. M. & Prieto, A. L. Synthetic Control of Quinary Nanocrystals of a Photovoltaic Material: The Clear Role of Chalcogen Ratio on Light Absorption and Charge Transport for $Cu_{2-x}Zn_{1+x}Sn(S_{1-y}Se_y)_4$. *ACS Appl. Energy Mater.* **1**, 1053–1059 (2018).

39. Arciniegas, M. P. *et al.* Self-assembly of octapod-shaped colloidal nanocrystals into a hexagonal ballerina network embedded in a thin polymer film. *Nano Lett.* **14**, 1056–1063 (2014).

40. Zhu, J. *et al.* Synthesis of colloidal gold nanobones with tunable negative curvatures at end surface and their application in SERS. *J. Nanoparticle Res.* **19**, (2017).

41.   Vaughn, D. D., Hentz, O. D., Chen, S., Wang, D. & Schaak, R. E. Formation of SnS nanoflowers for lithium ion batteries. *Chem. Commun.* **48**, 5608–5610 (2012).

42.   Bera, S. & Pradhan, N. Perovskite Nanocrystal Heterostructures: Synthesis, Optical Properties, and Applications. *ACS Energy Lett.* **5**, 2858–2872 (2020).

CHAPTER 2:

LEAD HALIDE SEMICONDUCTORS

2.1 Why Lead Halides?

As stated in the Preface, the goal of this thesis is to provide solutions to the many

challenges posed by the structural characterization of nanoscale materials. For this

purpose, any material is in principle appealing. Here, I chose to focus on lead halide

semiconductors, as their rich landscape of structures, morphologies and properties offers

plenty of stimulating case studies.

Indeed, *"lead halide semiconductor"* is an extremely broad label, as there are

plenty of semiconducting compounds that contain both lead and at least one halide. In

general, these materials are attracting a broad interest due to three key characteristics:

appealing properties, cheap elements, and easy processing. To date, lead halide

compounds are actively studied for their ability to photo-generate carriers, that can be

exploited in-situ (photocatalysis),[1–6] converted into a bias (photodetectors and solar

cells),[7–12] or re-emitted with high efficiency (LEDs, scintillators).[13–17] On top of that,

research is fueled by the variety of compounds and structures that stem by combining

lead and halides with something else, be it other elements or some molecules, and by

their intrinsic tendency to transform under stimuli, which creates stability challenges as

well as processing opportunities. In what follows, I provide an overview of the compositional and structural diversity within the vast boundaries of lead halide semiconductors, and comment on additional aspects that make them ideal materials for testing different approaches to structural characterization.

2.2 Structural Diversity in Lead Halides

The properties of lead halide semiconductors are largely dictated by the Pb-X network, that confers them their semiconducting nature and determines their optoelectronic properties. This, in turn, is affected by the composition and crystal structure of the compound, based on which the three distinct subgroups of materials discussed in this thesis can be identified.

2.2.1 A-Pb-X compounds

First come the ternary A-Pb-X compounds, where A is a monovalent cation (Cs^+, methylammonium, formamidinium, …), and X is a halide anion (Cl^-, Br^-, I^-, while F^- is seldom considered) or a mixture of them. These are by far the most studied, as the group includes a variety of compounds with remarkably different properties. Among them, the $APbX_3$ perovskites are in the spotlight.

Indeed, the interest in lead halide semiconductors was largely initiated by the excellent photovoltaic performances of hybrid organic-inorganic iodine-based perovskites such as $MAPbI_3$ (MA = methylammonium), that quickly raised from an initial efficiency of 14.1% in 2013 to the current record of 25.7% in 2021.[20] Their quick

development led to optimization needs, which eventually branched off into many different research directions that are well active nowadays. Topics like the behavior of mixed-halide perovskites, the quest for organic molecules that can be integrated in a lead-halide structure, and the investigation into the chemical transformations of lead halides can be traced back to needs such as tuning the band gap and increasing the stability of perovskites for photovoltaic devices. An important step forward was made in 2014,[21] with the development of the first lead halide perovskite nanocrystals. These quickly captured the attention of the quantum dots community, as they are much easier and faster to process than the traditional II-IV semiconductors (CdS, CdSe), and can achieve remarkably high photoluminescence quantum yields without the need of complex surface treatments and core-shell architectures.[22–24] Differently from the thin films for photovoltaics, lead-halide nanocrystals are often based on Cs^+ as an A^+ cation, due to the better stability and processability of cesium compounds in colloidal syntheses (Figure 2.1).[18,25–27] In this thesis, the $CsPbX_3$ nanocrystals will be protagonists of Chapters 5 and 6, where their structure and morphology will cover a central role.

All $APbX_3$ compounds share a similar structure, consisting of a 3D-connected network of corner-sharing $[PbX_6]^{4-}$ octahedra which hosts the A^+ monovalent cation in a cuboidal cage (Figure 2.1a). Here, the A^+ cation covers a structure stabilization role, as it neutralizes the overall negatively charged lead-halide network while acting as a spacer between the $[PbX_6]^{4-}$ octahedra. Hence, the interplay between A^+ cations and octahedra has a major impact on the structure of $APbX_3$ compounds, as too small or too large cations will be less effective in stabilizing a perovskite structure. This behavior is captured by the

Goldschmidt's tolerance factor t (Equation 2.1), a geometric indicator originally proposed for oxide perovskites[28] and later adapted to halide perovskites[29] that estimates if a ABX$_3$ compound will crystallize in a perovskite structure base on the radii (r) of involved ions.

$$t = \frac{r_A + r_X}{\sqrt{2}(r_B + r_X)}$$

Eq. 2.1

In general, t in the range 0.85-1.10 indicates that an ABX$_3$ compound is likely to adopt a perovskite structure, which in the low-t part of the interval tends to distort from the ideal cubic symmetry through a tilting of the BX$_6$ octahedra. Conversely, t values outside this range suggest that the perovskite phases would be unstable, and different crystal structures will be adopted instead.[29] Due to the rather large radii of halide anions (Cl$^-$ = 1.85 pm, I$^-$ = 2.20 pm), lead halide perovskites tend to adopt distorted structures: Cs$^+$ is too small to ensure an ideal fit, and the intrinsic anisotropy of organic cations, albeit larger, makes them less effective in filling their cavity.[29,30] This results in most of the APbX$_3$ compounds being distorted to some degree, as the [PbX$_6$]$^{4-}$ octahedra adopt different tilting motifs to compensate for the insufficient effective size of A$^+$. Due to the larger ionic radius, iodine-based compounds are the farthest from an ideal perovskite structure, which makes them intrinsically unstable. Indeed, most APbI$_3$ perovskites have a natural tendency to rearrange into the so-called δ-APbX$_3$, a wide-gap non-perovskite phase that has no technological application (Figure 2.1b). This instability is still one of the biggest limitations to the diffusion of perovskite-based photovoltaic solutions.[31–33]

Despite its structural relevance, the A^+ cation has a very limited impact on the electronic properties of the material itself. To give an example, MAPbBr$_3$, FAPbBr$_3$ (FA = formamidinium), and CsPbBr$_3$ feature nearly identical band gap energies of 2.34 eV, 2.30 eV, and 2.34 eV respectively.[34] This is due to the highly ionic nature of the interaction between A^+ and the negatively charged Pb-X network, which results in the A^+ cations contributing to states far in energy from the material band edge. Conversely, the choice of the halide strongly impacts the electronic properties of APbX$_3$. For example, replacing iodine for chlorine in bulk CsPbX$_3$ perovskites changes the band gap energy as much as 1.22 eV (1.76 $\rightarrow$ 2.98 eV).[35] Such band gap dependency on the halide composition is often exploited to tune the photoluminescence of perovskite nanocrystals within the visible spectral range (Figure 2.1c).

Albeit the APbX$_3$ perovskites are undisputedly the most studied lead halides, the family of ternary A-Pb-X compounds includes at least other three stoichiometries: A$_4$PbX$_6$, APbX$_5$, and A$_2$PbX$_4$, the latter known only in the form of Cs$_2$PbI$_2$Cl$_2$ (Figure 2.1a).[36–38] Of these, A$_4$PbX$_6$ deserves some extra attention, especially in the form of the all-inorganic Cs$_4$PbBr$_6$. On paper this is a rather uninteresting compounds, as its structure, consisting of disconnected [PbBr$_6$]$^{4-}$ octahedra kept apart by Cs$^+$ cations, results in a band gap well outside the visible range.[19,39] However, depending on the synthetic conditions, this material can feature a bright green photoluminescence whose origin has been long debated, as it is believed to be originated by either nanoscopic CsPbBr$_3$ inclusions[40–43] or by optically active defects states.[44–46] Moreover, nanocrystals of this compounds are known to convert into CsPbBr$_3$ and vice-versa under mild chemical stimuli, all while

retaining excellent size dispersion and colloidal stability (Figure 2.1d).[19,47–49] This and

similar transformations have been deeply studied in the last few years, and inspired the

research discussed in Chapter 5.
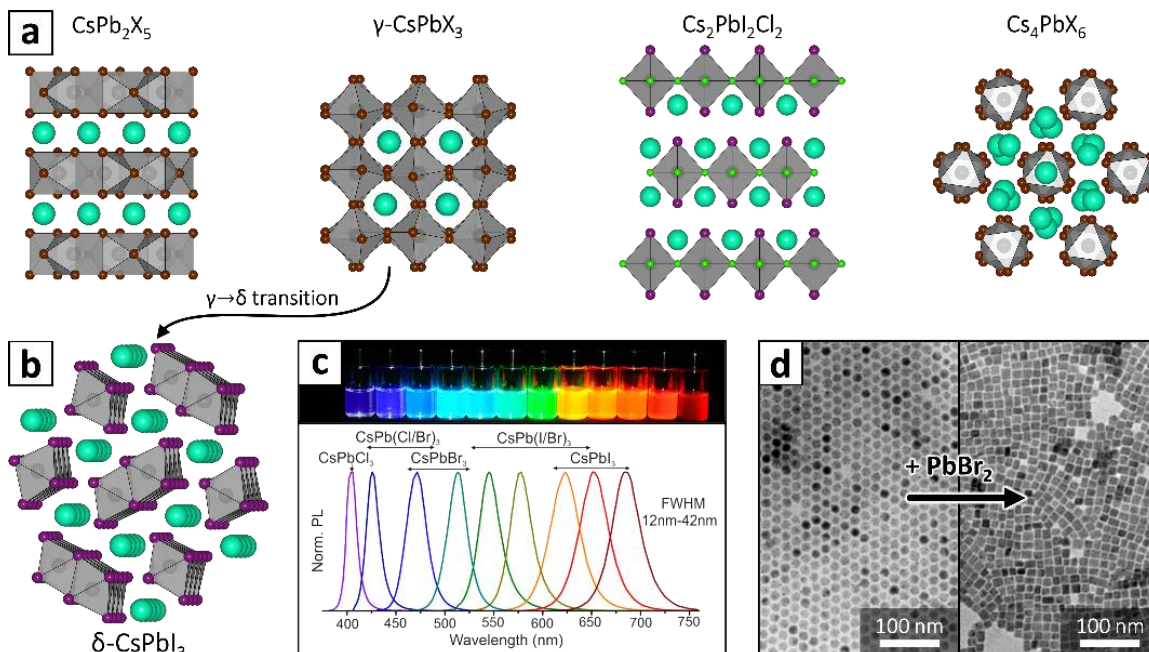
Figure 2.1. Ternary Cs-Pb-X compounds. a) Cs-Pb-X phases shown in order of increasing Cs/Pb ratio. b) Non-perovskite δ-CsPbX$_3$ polymorph, that is the thermodynamically stable structure for CsPbI$_3$. c) Influence of the halide composition on the band gap of γ-CsPbX$_3$ nanocrystals demonstrated by the tuning of photoluminescence. d) Cs$_4$PbX$_6$ nanocrystals can transform into CsPbX$_3$ nanocrystals upon reaction with PbBr$_2$. Atoms color code: cyan = Cs, black = Pb, green = Cl, purple = I, brown = any halide. Adapted from Refs. 18,19.

2.2.2 Layered hybrid lead halides

The layered hybrid lead halides are a class of semiconductors directly derived from the $APbX_3$ perovskites by intercalating long chain organic cations in their structure. These compounds represent a contact point between nano- and bulk-materials, as their crystal structure, which can be grown to the size of centimeters, is composed of neatly stacked lead-halide layers that are few nanometers thick or less. Their general formula is $L_2A_{n-1}Pb_nX_{3n+1}$, where n indicates the number of octahedra in each inorganic layer, A are the small isotropic cations we already encountered for the A-Pb-X ternary compounds, and L are the long-chain ammonium cations. These come in two main groups, that categorize the resulting structures (Figure 2.2a): single-ammonium cations (butylammonium, hexylammonium, phenyl ethyl ammonium, …), which result in the so-called Ruddlesden-Popper perovskites, and diammonium cations (propandiammonium, 3-(aminomethyl)piperidinium), …), which form the so-called Dion-Jacobson perovskites instead.[50–54]

The layered structure confers peculiar properties to these materials, as the long-chain cations insulate the semiconducting layers from each other, turning them into quantum wells.[55] As n increases, the layers become thicker and less confined, eventually yielding conventional 3D perovskites when $n\to\infty$ (Figures 2.2b-d).[51] The many possible combinations of cations, anions and layer thicknesses makes the lead-halide RP perovskites intrinsically tunable, as they all contribute in determining the electronic properties.[51,56,57] Moreover, the increased degrees of freedom conferred by the long-chain cations allows more structural flexibility, removing some of the constraints suffered

by the $APbX_3$ perovskites. For example, layered lead iodides are interesting candidates for photovoltaic applications because they are significantly more stable than their 3D $APbI_3$ counterparts.[9,58–60] In this thesis, the layered hybrid lead halides will be the main topic of Chapter 7, but their neatly stacked structure will be an important reference for the results discussed in Chapter 6 as well.
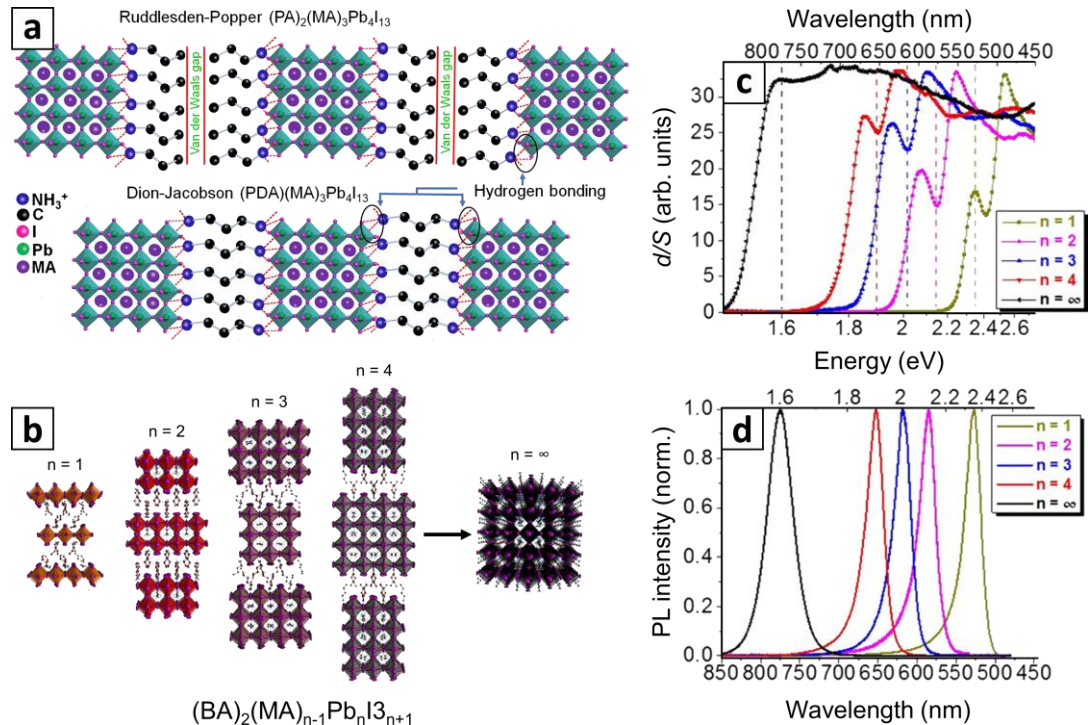
Figure 2.2. Layered hybrid lead halides. a) Structures of Ruddlesden-Popper $(PA)_2(MA)_3Pb_4I_{13}$ and Dion-Jacobson $(PA)_2(MA)_3Pb_4I_{13}$ hybrid layered halides compared. b) Structures of $(BA)_2(MA)_{n-1}Pb_nI_{3n+1}$ hybrid layered halides of different thicknesses, indicated by the increasing n-values. When $n\rightarrow\infty$, the compound becomes the 3D-perovskite $MAPbI_3$. c-d) Absorption (c) and photoluminescence (d) spectra of bulk crystals of the same compounds represented in panel (b), highlighting the effect of quantum confinement on the optoelectronic properties of layered hybrid lead halides. Organic cations abbreviations: MA = methylammonium, BA = butylammonium, PA = propanammonium, PDA = propandiammonium. Adapted from Refs. 50,51.

2.2.3 Lead chalcohalides

The lead chalcohalides, with general formula $Pb_aE_bX_c$ (E = S^{2-}, Se^{2-}, Te^{2-}), are a little-known class of materials that included only 6 compounds when the work behind this thesis started.[61–64] Most of them were reported during the last century, with the recent addition of few metastable phases that could only be obtained at high pressure. The research on these materials is still very exploratory, as not much has been investigated behind their crystal structure and their basic electronic properties. However, the lead chalcohalides might be gaining attention in the next future in the context of a broader rediscovery of nanostructured metal-chalcohalides as next-generation materials for photovoltaics.[65] To lead chalcohalides are dedicated the Chapters 4 and 5 of this thesis. As their relevance is mostly bond to their novelty within the frame of the metal chalcohalide family, we will discuss them separately there.

2.3 Lead Halides as Playground Materials

The appealing optoelectronic properties of lead halides provide a solid motivation to their investigation. However, these materials are well-suited for the purposes of this thesis for many other, more technical reasons.

2.3.1 Advanced synthetic control

As the goal of this project is to tackle the characterization of nanostructured semiconductors ad different length scales, selecting a set of materials that offers a suitable morphological variety is crucial. Lead halides are ideal in this sense, as reliable

synthetic protocols have been developed for many different phases, shapes, and sizes. For example, $CsPbBr_3$ can be shaped into nanoclusters, nanocubes, nanoplatelets, nanowires, thin-films, and single-crystals with little effort.[18,66–70] Crucially, synthesis protocols for lead halide nanocrystals are now advanced enough to provide highly monodisperse samples. This enables the accessible preparation of nanocrystal solids, that requires extremely homogeneous batches of nanoparticles to start with. The importance of this last point will be apparent in Chapter 6 of this thesis.

Moreover, the deep knowledge accumulated by the community on the colloidal chemistry of lead halide compounds,[26,27] and of lead-based semiconductors at large,[71,72] provides a solid foundation for exploring new directions. This is at the core of Chapter 4, where synthetic conditions well-established for the synthesis of lead halide and lead chalcogenide nanocrystals were combined to obtain novel lead chalcohalide compounds.

2.3.2 Ionicity and crystallinity

Compared to other semiconductors often studied at the nanoscale, such as cadmium chalcogenides and indium pnictides, the nature of bonds in lead halides is remarkably more ionic.[73,74] This is not particularly true for the Pb-X network, whose partially covalent nature is responsible for the relatively narrow band gap of compounds like $CsPbI_3$.[35] It is the case, however, for the almost purely ionic interactions between the anionic Pb-X network and the cations that are responsible for neutralizing the overall charge, namely Cs^+ and the variety of ammonium ions discussed above.

Indeed, the ionicity (*i.e.*, the difference in Pauling electronegativity) of Pb-X bonds falls in the range ~0.3-0.8 for the halides of interest, which is comparable to that of many technologically relevant chalcogenides (~0.9-0.4 for CdS / CdSe / CdTe; ~0.2 for PbS / PbSe / PbTe) and pnictogenides (~0.4 for InP / InAs).[75] Conversely, the ionicity of a Cs-X pair is in the range ~2.9-2.3, and that of NH_3R-X is likely similar, as the Mulliken electronegativity of the $\cdot NH_4$ radical is estimated to be ~0.89, similar to that of cesium (Cs = 0.79).[76] Hence, while the bonds within the Pb-X network are somehow comparable to those of other semiconductors, the structure of most lead halide compounds in its complex is highly ionic, as it is heavily dominated by electrostatic interactions.[77] The main consequence is that ions, and especially halides, are remarkably mobile in these compounds. This causes a severe problem affecting solar cells based on lead halides, that is the tendency of bromine and iodine to segregate in the structure of $APbX_3$ perovskites and related compounds under illumination.[33,81] This phenomenon, known as *halide segregation*, causes significant instability and performance drops in photovoltaic devices, and is the main motivation behind the project presented in Chapter 7. In other contexts, however, such high ion mobility can be an advantage. For example, it allows for some interesting post-synthesis treatments on lead halide nanocrystals, such as ion exchange and ion trade reactions,[19,82–85] that can alter the composition and even the stoichiometry of particles by diffusing ions within their structure. This topic will be discussed extensively in Chapter 5.

Moreover, the high ionic mobility in Cs-Pb-X compounds allows these materials to dynamically reconstruct their lattice and keep the concentration of defects low. This,

combined with an intrinsic defect tolerance, is likely why $CsPbX_3$ nanocrystals can achieve high quantum yields even in absence of surface treatments and protective shells.[86–89] It also ensures that lead halide nanoparticles are highly crystalline, and that they are single-crystalline in nature. Even when sub-domains are observed, they are formed through twinning or the creation of planar defects (Figure 2.3).[78–80]
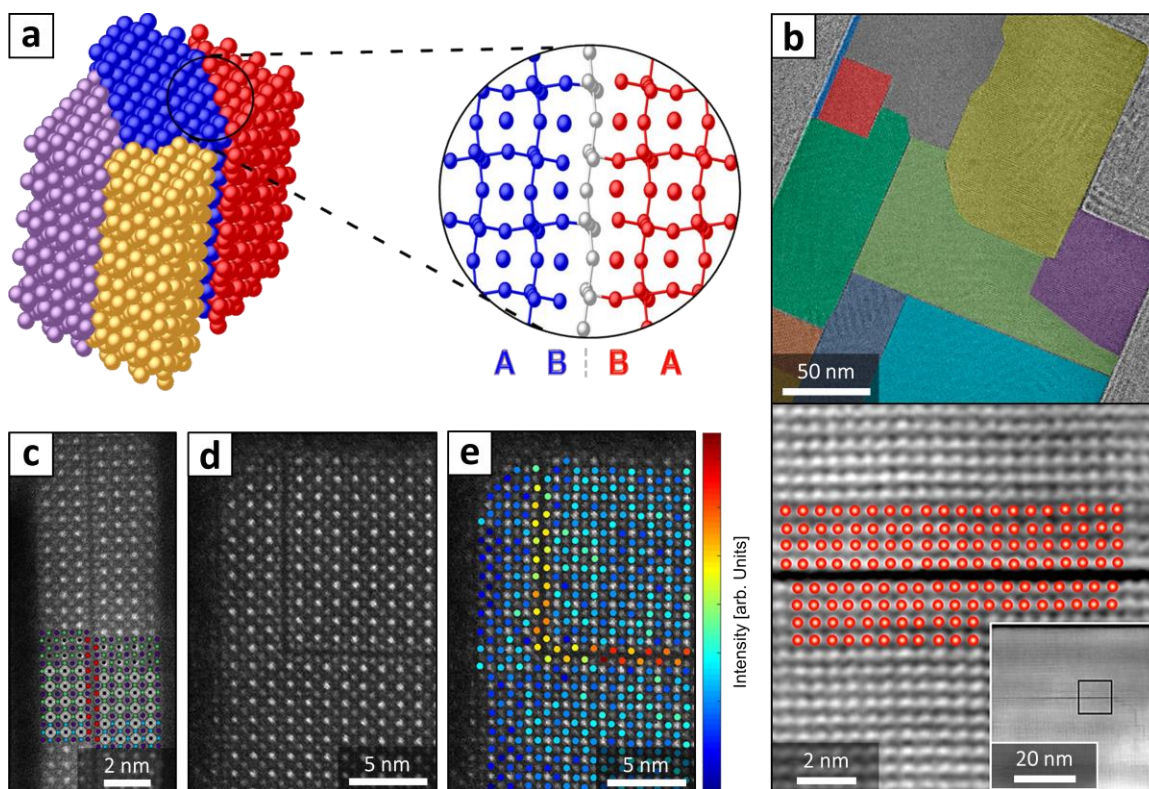
Figure 2.3. Coherent defectivity in cesium lead halides. a) Representation of coherent nano-twinning in $CsPbBr_3$ nanocrystals, with the structure of a twin boundary highlighted. b) Mosaicity in $CsPbBr_3$ nanosheets, due to the formation of Ruddlesden-Popper-like stacking faults. c-e) Similar fault can be induced in thicker $CsPbX_3$ nanocrystals by alloying in their structure Cl, Br, and I at the same time. This causes iodine to segregate in specific planes, creating the stacking faults. Note that none of these defects results in a decoherence in the relative orientation of crystalline domains. Adapted from Refs. 78–80.

Hence, they preserve the same crystallographic orientation within the entire nanoparticle, that behave as defected single-crystals rather than polycrystalline systems. This shall not be taken as granted:[90] to cite few examples, SiO_2 nanoparticles are often amorphous,[91–94] and Ag or Au nanoparticles can be composed of many crystalline domains oriented in different directions.[95–97] Dealing with monocrystalline particles greatly simplifies the description of nanocrystal diffraction profiles, that is a crucial step for the analyses presented in Chapter 6 of this thesis.

2.3.3 Heavy elements

Finally, lead halides offer plenty of electron density, as lead ($Z_{Pb} = 82$) is among the heaviest non-radioactive elements, and many of the other elements involved in lead halide semiconductors also come with a high number of electrons ($Z_{Br} = 35$; $Z_I = 53$; $Z_{Cs} = 55$). This is especially convenient for structural studies, as the signal collected in scattering or microscopy experiments based on X-rays or electrons comes from the interaction of the probe beam with the electron density of the material. Therefore, lead halides provide strong signals compared to other, lighter materials, allowing to minimize the sample exposure while enhancing the signal/background ratio, therefore minimizing challenges related to sample instability and poor quality of data.

2.4 Source Publications and Contributions

This chapter is based on the following publications:

I. **Toso, S.**, Baranov, D. & Manna, L. *Hidden in Plain Sight: The Overlooked Influence of the Cs⁺ Substructure on Transformations in Cesium Lead Halide Nanocrystals*. ACS Energy Lett. 5, 3409–3414 (2020). [Ref. 84]

II. **Toso, S.**, Baranov, D. & Manna, L. *Metamorphoses of Cesium Lead Halide Nanocrystals*. Acc. Chem. Res. 54, 498–508 (2021). [Ref. 85]

Publications (I-II) provide an overview of the compounds within the Cs-Pb-X ternary system and of their transformations at the nanoscale, and served as a base to organize this chapter. Both publications stemmed from a series of stimulating discussions with Dmitry Baranov and Liberato Manna, whom I thank for their critical perspective, guidance, and help in preparing these manuscripts.

2.5 Copyright

Some elements of this chapter were adapted from external sources:

2.6 Bibliography

1. Zhu, X. *et al.* Lead halide perovskites for photocatalytic organic synthesis. *Nat. Commun.* **10**, 1–10 (2019).

2. Zhu, X., Lin, Y., Sun, Y., Beard, M. C. & Yan, Y. Lead-Halide Perovskites for Photocatalytic α-Alkylation of Aldehydes. *J. Am. Chem. Soc.* **141**, 733–738 (2019).

3. Pradhan, S. *et al.* Stable lead-halide perovskite quantum dots as efficient visible light photocatalysts for organic transformations. *Nanoscale Adv.* **3**, 1464–1472 (2021).

4. Dubose, J. T. & Kamat, P. V. Probing Perovskite Photocatalysis. Interfacial Electron Transfer between CsPbBr$_3$ and Ferrocene Redox Couple. *J. Phys. Chem. Lett.* **10**, 6074–6080 (2019).

5. Kobosko, S. M., Dubose, J. T. & Kamat, P. V. Perovskite Photocatalysis. Methyl Viologen Induces Unusually Long-Lived Charge Carrier Separation in CsPbBr$_3$ Nanocrystals. *ACS Energy Lett.* **5**, 221–223 (2020).

6. DuBose, J. T. & Kamat, P. V. Efficacy of Perovskite Photocatalysis: Challenges to Overcome. *ACS Energy Lett.* **7**, 1994–2011 (2022).

7. Kojima, A., Teshima, K., Shirai, Y. & Miyasaka, T. Organometal halide perovskites as visible-light sensitizers for photovoltaic cells. *J. Am. Chem. Soc.* **131**, 6050–6051 (2009).

8. Lee, M. M., Teuscher, J., Miyasaka, T., Murakami, T. N. & Snaith, H. J. Efficient hybrid solar cells based on meso-superstructured organometal halide perovskites. *Science (80-.).* **338**, 643–647 (2012).

9. Tsai, H. *et al.* High-Efficiency Two-Dimensional Ruddlesden-Popper Perovskite Solar Cells. *Nature* **536**, 312–317 (2016).

10. Wang, Z. *et al.* Efficient ambient-air-stable solar cells with 2D-3D heterostructured butylammonium-caesium-formamidinium lead halide perovskites. *Nat. Energy* **2**, 1–10 (2017).

11. Dou, L. *et al.* Solution-processed hybrid perovskite photodetectors with high detectivity. *Nat. Commun.* **5**, 1–6 (2014).

12. Zhao, Y. & Zhu, K. Organic–inorganic hybrid lead halide perovskites for optoelectronic and electronic applications. *Chem. Soc. Rev.* **45**, 655–689 (2016).

13. Song, J. *et al.* Quantum Dot Light-Emitting Diodes Based on Inorganic Perovskite Cesium Lead Halides ($CsPbX_3$). *Adv. Mater.* **27**, 7162–7167 (2015).

14. Stranks, S. D. & Snaith, H. J. Metal-halide perovskites for photovoltaic and light-emitting devices. *Nat. Nanotechnol.* **10**, 391–402 (2015).

15. Tan, Z. K. *et al.* Bright light-emitting diodes based on organometal halide perovskite. *Nat. Nanotechnol.* **9**, 687–692 (2014).

16. Wei, H. *et al.* Dopant compensation in alloyed $CH_3NH_3PbBr_{3-x}Cl_x$ perovskite single crystals for gamma-ray spectroscopy. *Nat. Mater.* **16**, 826–833 (2017).

17. Chen, Q. *et al.* All-inorganic perovskite nanocrystal scintillators. *Nature* **561**, 88–93 (2018).

18. Protesescu, L. *et al.* Nanocrystals of Cesium Lead Halide Perovskites ($CsPbX_3$, X = Cl, Br, and I): Novel Optoelectronic Materials Showing Bright Emission with Wide Color Gamut. *Nano Lett.* **15**, 3692–3696 (2015).

19. Akkerman, Q. A. *et al.* Nearly Monodisperse Insulator Cs_4PbX_6 (X = Cl, Br, I) Nanocrystals, Their Mixed Halide Compositions, and Their Transformation into CsPbX3Nanocrystals. *Nano Lett.* **17**, 1924–1930 (2017).

20.   Best Research-Cell Efficiency Chart | Photovoltaic Research | NREL. *Journal of the American Chemical Society* vol. 5 1–8 https://www.nrel.gov/pv/cell-efficiency.html (2020).

21.   Schmidt, L. C. *et al.* Nontemplate synthesis of $CH_3NH_3PbBr_3$ perovskite nanoparticles. *J. Am. Chem. Soc.* **136**, 850–853 (2014).

22.   Dutta, A., Behera, R. K., Pal, P., Baitalik, S. & Pradhan, N. Near-Unity Photoluminescence Quantum Efficiency for All $CsPbX_3$ (X=Cl, Br, and I) Perovskite Nanocrystals: A Generic Synthesis Approach. *Angew. Chemie - Int. Ed.* **58**, 5552–5556 (2019).

23.   Di Stasio, F., Christodoulou, S., Huo, N. & Konstantatos, G. Near-Unity Photoluminescence Quantum Yield in $CsPbBr_3$ Nanocrystal Solid-State Films via Postsynthesis Treatment with Lead Bromide. *Chem. Mater.* **29**, 7663–7667 (2017).

24.   Quarta, D. *et al.* Stable Ligand Coordination at the Surface of Colloidal $CsPbBr_3$ Nanocrystals. *J. Phys. Chem. Lett.* **10**, 3715–3726 (2019).

25.   Haque, A. *et al.* Internal Heterostructure of Anion-Exchanged Cesium Lead Halide Nanocubes. *J. Phys. Chem. C* **122**, 13399–13406 (2018).

26.   Akkerman, Q. A., Rainò, G., Kovalenko, M. V. & Manna, L. Genesis, challenges and opportunities for colloidal lead halide perovskite nanocrystals. *Nat. Mater.* **17**, 394–405 (2018).

27.   Dey, A. *et al.* State of the Art and Prospects for Halide Perovskite Nanocrystals. *ACS Nano* **15**, 10775–10981 (2021).

28.   Goldschmidt, V. M. Die Gesetze der Krystallochemie. *Naturwissenschaften* **14**, 477–485 (1926).

29.   Travis, W., Glover, E. N. K., Bronstein, H., Scanlon, D. O. & Palgrave, R. G. On the application of the tolerance factor to inorganic and hybrid halide perovskites: A revised system. *Chem. Sci.* **7**, 4548–4556 (2016).

30.   Kieslich, G., Sun, S. & Cheetham, A. K. An extended Tolerance Factor approach for organic–inorganic perovskites. *Chem. Sci.* **6**, 3430 (2015).

31.   Sutton, R. J. *et al.* Cubic or Orthorhombic? Revealing the Crystal Structure of Metastable Black-Phase $CsPbI_3$ by Theory and Experiment. *ACS Energy Lett.* **3**, 1787–1794 (2018).

32. Masi, S., Gualdrón-Reyes, A. F. & Mora-Seró, I. Stabilization of Black Perovskite Phase in $FAPbI_3$ and $CsPbI_3$. *ACS Energy Lett.* **5**, 1974–1985 (2020).

33. Steele, J. A. *et al.* Thermal unequilibrium of strained black $CsPbI_3$ thin films. *Science (80-.).* **365**, 679–684 (2019).

34. Mannino, G. *et al.* Temperature-Dependent Optical Band Gap in $CsPbBr_3$, $MAPbBr_3$, and $FAPbBr_3$ Single Crystals. *J. Phys. Chem. Lett.* **11**, 2490–2496 (2020).

35. Paul, T. *et al.* Tunable cathodoluminescence over the entire visible window from all-inorganic perovskite $CsPbX_3$ 1D architecture. *J. Mater. Chem. C* **6**, 3322–3333 (2018).

36. Li, J. *et al.* $Cs_2PbI_2Cl_2$, All-Inorganic Two-Dimensional Ruddlesden-Popper Mixed Halide Perovskite with Optoelectronic Response. *J. Am. Chem. Soc.* **140**, 11085–11090 (2018).

37. Trihalide S B, P., Christian, Y. & Mølle, K. N. On the Structure of Caesium Hexalogeno-Plumbates(II). *Mat. Fys. Medd. Dan. Vid. Selsk* **32**, (1959).

38. Nazarenko, O. *et al.* Luminescent and Photoconductive Layered Lead Halide Perovskite Compounds Comprising Mixtures of Cesium and Guanidinium Cations. *Inorg. Chem.* **56**, 11552–11564 (2017).

39. Zhang, Z. *et al.* Aqueous Solution Growth of Millimeter-Sized Nongreen-Luminescent Wide Bandgap Cs_4PbBr_6 Bulk Crystal. *Cryst. Growth Des.* **18**, 6393–6398 (2018).

40. Quan, L. N. *et al.* Highly Emissive Green Perovskite Nanocrystals in a Solid State Crystalline Matrix. *Adv. Mater.* **29**, (2017).

41. Riesen, N., Lockrey, M., Badek, K. & Riesen, H. On the origins of the green luminescence in the 'zero-dimensional perovskite' Cs_4PbBr_6: Conclusive results from cathodoluminescence imaging. *Nanoscale* **11**, 4001–4007 (2019).

42. Chen, X. *et al.* Centimeter-Sized Cs_4PbBr_6 Crystals with Embedded $CsPbBr_3$ Nanocrystals Showing Superior Photoluminescence: Nonstoichiometry Induced Transformation and Light-Emitting Applications. *Adv. Funct. Mater.* **28**, (2018).

43. Akkerman, Q. A., Abdelhady, A. L. & Manna, L. Zero-Dimensional Cesium Lead Halides: History, Properties, and Challenges. *J. Phys. Chem. Lett.* **9**, 2326–2337 (2018).

44. Yin, J. *et al.* Point Defects and Green Emission in Zero-Dimensional Perovskites. *J. Phys. Chem. Lett.* **9**, 5490–5495 (2018).

45. Yin, J. *et al.* Intrinsic Lead Ion Emissions in Zero-Dimensional Cs_4PbBr_6 Nanocrystals. *ACS Energy Lett.* **2**, 2805–2811 (2017).

46. Wang, L., Liu, H., Zhang, Y. & Mohammed, O. F. Photoluminescence Origin of Zero-Dimensional Cs4PbBr6 Perovskite. *ACS Energy Lett.* **5**, 87–99 (2020).

47. Li, Y., Huang, H., Xiong, Y., Kershaw, S. V. & Rogach, A. L. Reversible transformation between $CsPbBr_3$ and Cs_4PbBr_6 nanocrystals. *CrystEngComm* **20**, 4900–4904 (2018).

48. Wu, L. *et al.* From Nonluminescent Cs_4PbX_6 (X = Cl, Br, I) Nanocrystals to Highly Luminescent $CsPbX_3$ Nanocrystals: Water-Triggered Transformation through a CsX-Stripping Mechanism. *Nano Lett.* **17**, 5799–5804 (2017).

49. Palazon, F. *et al.* Postsynthesis Transformation of Insulating Cs_4PbBr_6 Nanocrystals into Bright Perovskite $CsPbBr_3$ through Physical and Chemical Extraction of CsBr. *ACS Energy Lett.* **2**, 2445–2448 (2017).

50. Ahmad, S. *et al.* Dion-Jacobson Phase 2D Layered Perovskites for Solar Cells with Ultrahigh Stability. *Joule* **3**, 794–806 (2019).

51. Stoumpos, C. C. *et al.* Ruddlesden-Popper Hybrid Lead Iodide Perovskite 2D Homologous Semiconductors. *Chem. Mater.* **28**, 2852–2867 (2016).

52. Li, X., Hoffman, J. M. & Kanatzidis, M. G. The 2D Halide Perovskite Rulebook: How the Spacer Influences Everything from the Structure to Optoelectronic Device Efficiency. *Chem. Rev.* **121**, 2230–2291 (2021).

53. Li, X. *et al.* Two-Dimensional Dion-Jacobson Hybrid Lead Iodide Perovskites with Aromatic Diammonium Cations. *J. Am. Chem. Soc.* **141**, 12880–12890 (2019).

54. Mao, L. *et al.* Hybrid Dion-Jacobson 2D Lead Iodide Perovskites. *J. Am. Chem. Soc.* **140**, 3775–3783 (2018).

55. Wang, Q. *et al.* Quantum confinement effect and exciton binding energy of layered perovskite nanoplatelets. *AIP Adv.* **8**, 25108 (2018).

56. Pan, D. *et al.* Deterministic Fabrication of Arbitrary Vertical Heterostructures of Two-Dimensional Ruddlesden–Popper Halide Perovskites. *Nat. Nanotechnol.* **16**, 159–165 (2021).

57. Dhanabalan, B. *et al.* Engineering the Optical Emission and Robustness of Metal-Halide Layered Perovskites through Ligand Accommodation. *Adv. Mater.* **33**, 2008004 (2021).

58. Smith, I. C., Hoke, E. T., Solis-Ibarra, D., McGehee, M. D. & Karunadasa, H. I. A Layered Hybrid Perovskite Solar-Cell Absorber with Enhanced Moisture Stability. *Angew. Chemie - Int. Ed.* **53**, 11232–11235 (2014).

59. Grancini, G. *et al.* One-Year Stable Perovskite Solar Cells by 2D/3D Interface Engineering. *Nat. Commun.* **8**, 1–8 (2017).

60. Liu, Y. *et al.* Surface-Tension-Controlled Crystallization for High-Quality 2D Perovskite Single Crystals for Ultrahigh Photodetection. *Matter* **1**, 465–480 (2019).

61. Ider, A., Laval, J. P., Frit, B., Carré, J. & Bastide, J. P. Crystal Structure of $PbTeF_6$. *J. Fluor. Chem.* **78**, 15–20 (1996).

62. Krebs, B. Die Kristallstrukturen von Pb_4SeBr_6, $Pb_5S_2J_6$ und $Pb_7S_2Br_{10}$. *ZAAC - J. Inorg. Gen. Chem.* **396**, 137–151 (1973).

63. Ni, D., Guo, S., Yang, Z. S., Powderly, K. M. & Cava, R. J. $Pb_4S_3I_2$ –A high-pressure phase in the PbS-PbI_2 system. *Solid State Sci.* **91**, 49–53 (2019).

64. Ni, D., Guo, S., Powderly, K. M., Zhong, R. & Cava, R. J. A high-pressure phase with a non-centrosymmetric crystal structure in the $PbSe$–$PbBr_2$ system. *J. Solid State Chem.* **280**, 106–111 (2019).

65. Palazon, F. Metal Chalcohalides: Next Generation Photovoltaic Materials? *Sol. RRL* **6**, 2100829 (2022).

66. Zhang, B. *et al.* Stable $CsPbBr_3$ Nanoclusters Feature a Disk-like Shape and a Distorted Orthorhombic Structure. *J. Am. Chem. Soc.* **144**, 5059–5066 (2022).

67. Akkerman, Q. A. *et al.* Solution Synthesis Approach to Colloidal Cesium Lead Halide Perovskite Nanoplatelets with Monolayer-Level Thickness Control. *J. Am. Chem. Soc.* **138**, 1010–1016 (2016).

68. Zhang, D. *et al.* Synthesis of Composition Tunable and Highly Luminescent Cesium Lead Halide Nanowires through Anion-Exchange Reactions. *J. Am. Chem. Soc.* **138**, 7236–7239 (2016).

69. Zhong, Y. *et al.* Large-scale thin $CsPbBr_3$ single-crystal film grown on sapphire via chemical vapor deposition: Toward laser array application. *ACS Nano* **14**, 15605–15615 (2020).

70. Dirin, D. N., Cherniukh, I., Yakunin, S., Shynkarenko, Y. & Kovalenko, M. V. Solution-Grown CsPbBr 3 Perovskite Single Crystals for Photon Detection. *Chem. Mater.* **28**, 8470–8474 (2016).

71.   Lu, H., Carroll, G. M., Neale, N. R. & Beard, M. C. Infrared quantum dots: Progress, challenges, and opportunities. *ACS Nano* **13**, 939–953 (2019).

72.   Mcdonald, S. A. *et al.* Solution-processed PbS quantum dot infrared photodetectors and photovoltaics. *Nat. Mater.* **4**, 138–142 (2005).

73.   Mizusaki, J., Arai, K. & Fueki, K. Ionic conduction of the perovskite-type halides. *Solid State Ionics* **11**, 203–211 (1983).

74.   Eames, C. *et al.* Ionic transport in hybrid lead iodide perovskite solar cells. *Nat. Commun.* **6**, 1–8 (2015).

75.   Wikipedia - Electronegativities of the elements. https://en.wikipedia.org/wiki/Electronegativities_of_the_elements_(data_page).

76.   Whiteside, A., Xantheas, S. S. & Gutowski, M. Is electronegativity a useful descriptor for the Pseudo-Alkali metal NH_4? *Chem. - A Eur. J.* **17**, 13197–13205 (2011).

77.   Walsh, A. Principles of chemical bonding and band gap engineering in hybrid organic-inorganic halide perovskites. *J. Phys. Chem. C* **119**, 5755–5760 (2015).

78.   Akkerman, Q. A. *et al.* Fully Inorganic Ruddlesden-Popper Double Cl-I and Triple Cl-Br-I Lead Halide Perovskite Nanocrystals. *Chem. Mater.* **31**, 2182–2190 (2019).

79.   Dang, Z. *et al.* Temperature-Driven Transformation of $CsPbBr_3$ Nanoplatelets into Mosaic Nanotiles in Solution through Self-Assembly. *Nano Lett.* **20**, 1808–1818 (2020).

80.   Bertolotti, F. *et al.* Coherent Nanotwins and Dynamic Disorder in Cesium Lead Halide Perovskite Nanocrystals. *ACS Nano* **11**, 3819–3831 (2017).

81.   Slotcavage, D. J., Karunadasa, H. I. & McGehee, M. D. Light-Induced Phase Segregation in Halide-Perovskite Absorbers. *ACS Energy Lett.* **1**, 1199–1205 (2016).

82.   Nedelcu, G. *et al.* Fast Anion-Exchange in Highly Luminescent Nanocrystals of Cesium Lead Halide Perovskites ($CsPbX_3$, X = Cl, Br, I). *Nano Lett.* **15**, 5635–5640 (2015).

83.   Akkerman, Q. A. *et al.* Tuning the optical properties of cesium lead halide perovskite nanocrystals by anion exchange reactions. *J. Am. Chem. Soc.* **137**, 10276–10281 (2015).

84. Toso, S., Baranov, D. & Manna, L. Hidden in Plain Sight: The Overlooked Influence of the Cs$^+$ Substructure on Transformations in Cesium Lead Halide Nanocrystals. *ACS Energy Lett.* **5**, 3409–3414 (2020).

85. Toso, S., Baranov, D. & Manna, L. Metamorphoses of Cesium Lead Halide Nanocrystals. *Acc. Chem. Res.* **54**, 498–508 (2021).

86. Kang, J. & Wang, L. W. High Defect Tolerance in Lead Halide Perovskite CsPbBr$_3$. *J. Phys. Chem. Lett.* **8**, 489–493 (2017).

87. Kovalenko, M. V., Protesescu, L. & Bodnarchuk, M. I. Properties and potential optoelectronic applications of lead halide perovskite nanocrystals. *Science (80-.).* **358**, 745–750 (2017).

88. Huang, H., Bodnarchuk, M. I., Kershaw, S. V., Kovalenko, M. V. & Rogach, A. L. Lead Halide Perovskite Nanocrystals in the Research Spotlight: Stability and Defect Tolerance. *ACS Energy Lett.* **2**, 2071–2083 (2017).

89. Ten Brinck, S., Zaccaria, F. & Infante, I. Defects in lead halide perovskite nanocrystals: Analogies and (many) differences with the bulk. *ACS Energy Lett.* **4**, 2739–2747 (2019).

90. Moreau, L. M. *et al.* Defining Crystalline/Amorphous Phases of Nanoparticles through X-ray Absorption Spectroscopy and X-ray Diffraction: The Case of Nickel Phosphide. *Chem. Mater.* **25**, 2394–2403 (2013).

91. Croissant, J. G., Butler, K. S., Zink, J. I. & Brinker, C. J. Synthetic amorphous silica nanoparticles: toxicity, biomedical and environmental implications. *Nat. Rev. Mater. 2020 512* **5**, 886–909 (2020).

92. Guo, Q. *et al.* Synthesis of disperse amorphous SiO$_2$ nanoparticles via sol–gel process. *Ceram. Int.* **43**, 192–196 (2017).

93. Leroy, P., Devau, N., Revil, A. & Bizi, M. Influence of surface conductivity on the apparent zeta potential of amorphous silica nanoparticles. *J. Colloid Interface Sci.* **410**, 81–93 (2013).

94. Zhang, H. *et al.* Processing pathway dependence of amorphous silica nanoparticle toxicity: Colloidal vs pyrolytic. *J. Am. Chem. Soc.* **134**, 15790–15804 (2012).

95. Peng, S. *et al.* A Facile Synthesis of Monodisperse Au Nanoparticles and their Catalysis of CO Oxidation. *Nano Res.* **1**, 229–234 (2008).

96.	Xia, Y., Xiong, Y., Lim, B. & Skrabalak, S. E. Shape-Controlled Synthesis of Metal Nanocrystals: Simple Chemistry Meets Complex Physics? *Angew. Chemie - Int. Ed.* **48**, 60–103 (2009).

97.	Zhou, C., Yu, J., Qin, Y. & Zheng, J. Grain size effects in polycrystalline gold nanoparticles. *Nanoscale* **4**, 4228–4233 (2012).

CHAPTER 3:

NANOSCALE CRYSTALLOGRAPHY

3.1 Principles of Diffraction

Now that we have familiarized with the materials, it is time to discuss what makes them challenging to investigate. As the focus of this thesis is the structural characterization, this means understanding why nanoscale materials are sometimes hard to investigate by structure-oriented techniques, and especially through diffraction-based experiments. As mentioned in Chapter 2, all the lead halides contain at least two electron-dense elements (lead and one halide), and tend to be highly crystalline. These two factors make them ideal for diffraction experiments: indeed, in this work lead halide samples very rarely posed challenges at the data acquisition step. The challenge, however, lies in the data analysis.

Before discussing each technique in detail, the reader should familiarize with the principles of diffraction. The key concept is that the signal measured during a diffraction experiment comes from the constructive interference of a probe beam (X-rays, electrons or neutrons), that is scattered by the atoms in the sample. Of this interference pattern we measure the intensity, that is proportional to the square modulus of the probe wavefunction amplitude. These principles are true for any diffraction experiments and

any material, regardless of its morphology and crystallinity. The task of crystallography is, in short, to retrace this path in reverse and reconstruct the structure of the sample from its diffraction pattern.

3.1.1 The scattering vector

The scattering vector $\vec{q}$ holds a central role in diffraction, to the point that diffraction techniques are often classified based on the range of $|\vec{q}|$ (from now on simply indicated as q) they cover. The scattering vector $\vec{q}$ describes the deflection of the radiation probe following an interaction with the sample. As such, it is defined as the difference between radiation wave vectors before ($\vec{k}$) and after ($\vec{k'}$) a scattering event (Figure 3.1, Equation 3.1).[1,2]

$$\vec{q} = \vec{k'} - \vec{k}$$
Eq 3.1
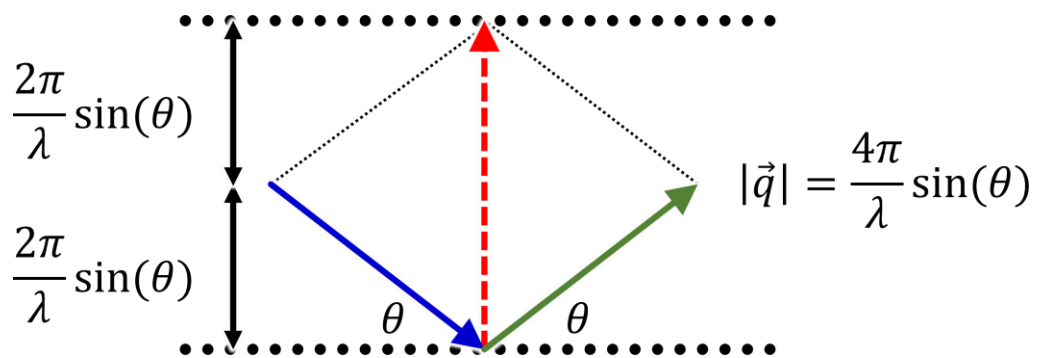
Figure 3.1. Geometric construction of the scattering vector. The difference between the diffracted (green) and the incident (blue) wave vectors is the scattering vector (red).

Since the scattering event results in a wave deflection, q is experimentally measured as the deflection angle between $\vec{k}$ and $\vec{k'}$ (Figure 3.1). This angle is often called 2θ (the reader might know it as the *x*-axis in powder diffraction data plots), and is related to *q* by Equation 3.2.[1,2]

$$q = 4\pi \frac{\sin{(\theta)}}{\lambda_{probe}}$$ Eq 3.2

As Equation 3.2 suggests, the *q*-range that can be probed is limited to $0 \leq q \leq 4\pi/\lambda$, as $sin(\theta) \leq 1$. Hence, shorter wavelengths allow to probe a wider *q*-range, which is why electron diffraction (λ ≈ 0.1 − 0.02 Å, tunable) and synchrotron light sources (λ ≈ 2.5 − 0.1 Å, tunable) are sometimes preferred to the X-ray cathodes used in laboratories ($\lambda_{Cu-k\alpha}$ = 1.542 Å). It is also important to know that *q* is related to the probed direct space periodicities *d* as follows:[1]

$$q = \frac{2\pi}{d}$$ Eq 3.3

Note that combining Equations 3.2-3 gives the Bragg's law (Equation 3.4):[1,3]

$$\lambda = 2d \sin{(\theta)}$$ Eq 3.4

Equation 3.3 suggests that if it was possible to collect diffraction data over a sufficiently wide *q*-range and at a sufficient resolution, one single diffraction experiment could probe all the length scales and hence fully characterize the sample in one go.

However, Equation 3.2 limits the experimental range accessible to a certain radiation. Plus, technical aspects impose additional limitations on the q-range probed by one experiment, as this must be traded for angular resolution. This forces the user to choose the right q-range for answering their scientific question.

For this reason, diffraction techniques are often labelled as "wide-angle" ($q > 0.5$ Å^{-1}) or "small angle" ($q < 0.5$ Å^{-1}). The first provide information on small length scales ($d < 10$ Å), and are used to characterize the atomic structure of matter. The second instead provide large scale information ($d > 10$ Å), and when applied to colloidal nanoparticles they are used to probe their size and shape, long-range interactions, or self-assembly into ordered superstructures.

3.1.2 A generic scattering equation

To elucidate the atomic structure of a sample from its diffraction pattern, we must find a relation between the position of scatterers within the sample itself and the wavefunction of the diffracted radiation. The most generic expression for such wavefunction is Equation 3.5.[4]

$$\Psi(\vec{q}) = \sum_{i=1}^{N} f_j(q) \cdot e^{-i\vec{q}\cdot\vec{P}} \qquad \text{Eq 3.5}$$

Where j is any of the N atoms in the sample, f_j is the atomic scattering factor, $\vec{q}$ is the scattering vector, and $\vec{P}$ is the spatial position of the scatterer. For X-rays and electrons f_j is proportional to the electron density, thus making heavier elements easier

to detect. Note that this equation relies on some approximations, such as the negligible incidence of multiple scattering phenomena (kinematic approximation) and the assumption that the amplitude of the incident radiation is constant through the sample volume (Born approximation).[5]

Unfortunately, Equation 3.5 is of little use by itself, as it requires to know the position of every single atom in the sample to describe the diffraction experiment. However, depending on the nature of the sample (gaseous, liquid, amorphous or crystalline), this equation is the starting point to derive other expressions that trade off atomistic detail for versatility. Here, we focus on crystalline solids, starting from the simplest case: the infinite perfect crystal.

3.2 Infinite Perfect Crystals

The key idea for describing an infinite and perfect crystal is that its structure is periodic in space.[1] This periodicity is captured by the direct lattice {R}, an infinite set of vectors that is constructed starting from the three lattice base vectors $\vec{a}, \vec{b}, \vec{c}$, and includes all their integer sums (Equation 3.6):

$$\{\vec{R}\} = \{(n_1\vec{a} + n_2\vec{b} + n_3\vec{c}) \quad \forall \quad n_1, n_2, n_3 \in \mathbb{Z}\} \qquad \text{Eq 3.6}$$

Each vector of the direct lattice identifies the origin of a unit cell, a delimited volume of the crystal that always contains the same atoms in the same positions, and repeats with the periodicity of the direct lattice {R}. The position $\vec{r}$ of each atom j inside

the unit cell is expressed as the sum of the three lattice base vectors $\vec{a}, \vec{b}, \vec{c}$ multiplied by the fractional coordinates x,y,z, whose value is in the range $0 \le x, y, z < 1$ (Equation 3.7). Hence, the position $\vec{P}$ of any atom j in the crystal can be written as the sum of one direct lattice vector $\vec{R}$ and one atom position vector $\vec{r}$ within the unit cell (Equation 3.8):

$$\vec{r}_j = x_j\vec{a} + y_j\vec{b} + z_j\vec{c} \qquad \text{Eq 3.7}$$

$$\vec{P}_j = \left(n_{1j} + x_j\right)\vec{a} + \left(n_{2j} + y_j\right)\vec{b} + \left(n_{3j} + z_j\right)\vec{c} = \vec{R}_j + \vec{r}_j \qquad \text{Eq 3.8}$$

Starting from the definition of direct lattice $\{R\}$, we shall also define a reciprocal lattice $\{G\}$, that is composed by all the vectors satisfying the following requirement (Equation 3.9):

$$\left\{\vec{G}\right\} = \left\{e^{i\vec{G}\cdot\vec{R}} = 1 \quad \forall \ \vec{R} \in \{R\}\right\} \qquad \text{Eq 3.9}$$

Like $\{R\}$, also $\{G\}$ has three base vectors $\vec{a}^{*}, \vec{b}^{*}, \vec{c}^{*}$, whose integer sums identify all the possible $\vec{G}$ vectors (Equations 3.10-11) The integer numbers h,k,l that identify each $\vec{G}$ vector are better known as the Miller indices.

$$\left\{\vec{G}\right\} = \{(h\vec{a}^{*} + k\vec{b}^{*} + l\vec{c}^{*}) \ \forall \ h, k, l \in \mathbb{Z}\} \qquad \text{Eq 3.10}$$

$$\begin{cases} a \cdot \vec{a}^{*} = 2\pi \ ; \ \ a \cdot \vec{b}^{*} = a \cdot \vec{c}^{*} = 0 \\ b \cdot \vec{b}^{*} = 2\pi \ ; \ \ b \cdot \vec{a}^{*} = b \cdot \vec{c}^{*} = 0 \\ c \cdot \vec{c}^{*} = 2\pi \ ; \ \ c \cdot \vec{b}^{*} = a \cdot \vec{a}^{*} = 0 \end{cases} \qquad \text{Eq 3.11}$$

The reciprocal lattice $\{G\}$ has a central importance in the theory of diffraction. Indeed, it can be demonstrated (see Ref. 1 for the full discussion) that a perfect and infinite crystal produces constructive interference only when the scattering vector q is one of the reciprocal lattice vectors (Equation 3.12).

$$\text{Diffraction condition: } \vec{q} \in \{G\} \qquad\qquad \text{Eq 3.12}$$

Taking advantage of these considerations, and especially of Equations 3.9-12, we can now rewrite Equation 3.5 by breaking it down into two contributions, the first related to the unit cells within the crystal, and the second to the atoms within one unit cell (Equation 3.13):

$$\Psi(\vec{G}_{h,k,l}) = \sum_{n}^{N_{cells}} e^{-i\vec{G}\cdot\vec{R}_n} \sum_{j}^{J_{at.\ in\ cell}} f_j(\vec{G})\cdot e^{-i\vec{G}\cdot\vec{r}_j} = N_{Cells} \sum_{j}^{J_{at.\ in\ cell}} f_j(\vec{G})\cdot e^{-i\vec{G}\cdot\vec{r}_j} \qquad \text{Eq 3.13}$$

Finally, we can exploit the properties of $\{G\}$ and $\{R\}$ (Equations 3.9-10) to rewrite the last summation in a form that is independent of both $\vec{a}, \vec{b}, \vec{c}$ and $\vec{a}^*, \vec{b}^*, \vec{c}^*$ (Equation 3.14). Here, $S_{h,k,l}$ is known as the *structure factor*, and describes the scattering of a single unit cell when $\vec{q} = \vec{G}_{hkl}$.

$$\Psi(\vec{G}_{h,k,l}) = N_{Cells} \sum_{m}^{M_{Atoms}} f_m(\vec{G})\cdot e^{-i\,2\pi(hx+ky+lz)} = N_{Cells}\cdot S_{h,k,l} \qquad \text{Eq 3.14}$$

Equation 3.14 finally describes the radiation scattered by an infinite and perfect crystal. Compared to Equation 3.5, its great advantages are that only selected scattering vectors should be monitored (Equation 3.12), and that the summation is now limited to the handful of atoms inside one unit cell, instead of being extended to all the atoms in the crystal. This also means that the diffraction features are expected to be infinitely sharp, hence described by Dirac δ distributions, since constructive interference occurs only when $\vec{q} \in \{G\}$. This greatly simplifies the analysis of samples where the number of unit cells per crystal is large enough to be considered infinite and size-related effects become negligible. On this approximation are based the structure solution from single-crystal diffraction experiments, and any powder diffraction method applied to specimens with crystallites larger than $\sim 10^2$ nm.

3.3 The Nanoscale Problem

When considering nanomaterials, the assumption of having an infinite crystal is immediately lost. In fact, for simple inorganic materials the unit cell parameters are on the order of 5-20 Å, meaning that a ~ 100 nm thick nanoparticle is composed of only 50-200 unit cell layers, a number that is far from infinite. Such number becomes even lower for nanocrystals typically obtained by colloidal synthesis (5-30 nm), and particles like nanoplatelets or nanowires can be as thin as one unit cell or less.

The main consequence is that the diffraction condition stated in Equation 3.9 holds no more. While it is still true that the maximum of diffracted intensity is found when $\vec{q} \in \{G\}$, for finite-size crystals a significant fraction of the diffracted intensity is

found outside the condition stated by Bragg's law (of which $\vec{q} \in \{G\}$ is an alternative formulation). This non-Bragg contribution goes under the name of diffuse scattering, and appears for any crystal that is not infinite and/or not perfect, like in the presence of strain or of defects.

The finite-size effects can be described by considering the interference of a finite number N of crystal planes, equally spaced with the periodicity of the lattice d_{hkl} along the considered [hkl] direction (Equation 3.15):[4]

$$\Psi(q) = \sum_{n=0}^{N-1} S_{hkl}(q) \cdot e^{-iqnd_{hkl}} = S(q) \cdot \frac{1 - e^{-iqNd_{hkl}}}{1 - e^{-iqd_{hkl}}} \qquad \text{Eq 3.15}$$

Note that the first half of Equation 3.15 closely resembles Equation 3.5, that described the scattering of a generic ensemble of atoms. However, in this case the scatterers are not atoms, but unit cell planes characterized by a structure factor S_{hkl}, and the position of each atomic plane is now an integer multiple of d_{hkl}, hence capturing the periodicity of the crystal. Finally, we are not considering q as a vector anymore, because its direction is now set perpendicular to the (hkl) crystal planes and only its modulus matters. The diffracted intensity is given by the square modulus of the scattering factor:[4]

$$I(q) = |S(q)|^2 \cdot \left(\frac{1 - e^{-iqNd_{hkl}}}{1 - e^{-iqd_{hkl}}} \right) \cdot \left(\frac{1 - e^{iqNd_{hkl}}}{1 - e^{iqd_{hkl}}} \right) = |S(q)|^2 \cdot \left(\frac{sin^2\left(\frac{qdN}{2}\right)}{sin^2\left(\frac{qd}{2}\right)} \right) \qquad \text{Eq 3.16}$$

Equation 3.16 describes the diffraction profile of a finite crystal, that is composed of several peaks periodic in the q space surrounded by fading ripples. Only one of such

peaks is shown in Figure 3.2, as the next would be found at q = 2 Å^{-1}. For thick crystals,

the diffraction profile approaches the limit of a sequence of Dirac's deltas, that is the

result predicted by the theory for an infinite and perfect crystal (see Equation 3.12).

Conversely, as the number of planes in the crystal gets smaller, the peaks broaden

progressively until the diffraction profile becomes a modulated curve (see the case of

N = 2). A real-word example of finite-size broadening is provided in Figure 3.2b, where

the diffraction patterns of microcrystalline and nanocrystalline powders of CsPbBr$_3$,

collected with the same instrumental configuration, are compared.
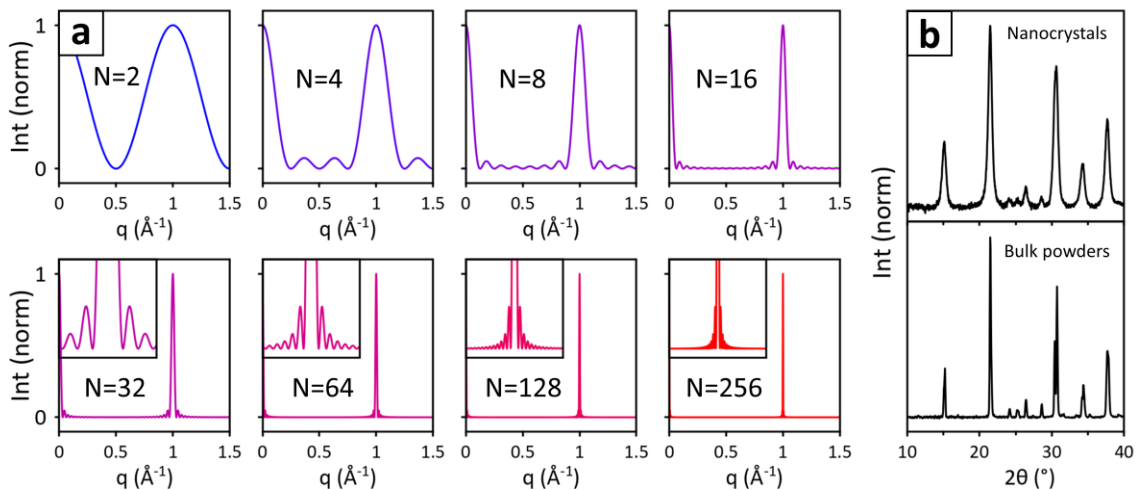
Figure 3.2. Effect of a crystal size on its diffraction pattern. a) Simulated diffraction profiles for crystals formed by an increasing number of planes *N*. Insets are enlarged views of the base of the peak. b) Experimental diffraction pattern of CsPbBr$_3$ nanocrystals and bulk powders compared. Both patterns were acquired with the same instrument, therefore differences are only attributed to the nature of samples. Data are from this thesis, see Ref. 6.

As demonstrated by Equation 3.16, the finite-size broadening of diffraction features is intrinsically part of how a diffraction experiment perceives a sample, and as such is unavoidable. However, its impact differs from technique to technique, and strategies have been developed to take it into account, minimizing its negative influence or even taking advantage of it to extract valuable information. In the next paragraphs, the reader will find an overview of the diffraction techniques used in this thesis, with a specific focus on how each of them copes with nanoscale materials.

3.4 Single-Crystal Diffraction Techniques

Diffraction techniques for crystalline materials are mainly divided in single-crystal and polycrystalline techniques. As we are about to discuss, this distinction implies much more than simply a different sample morphology, and makes these two groups of techniques best suited for different, highly complementary tasks.

The primary goal of single-crystal diffraction techniques is to solve the structure of an unknown material, which means determining the lattice base vectors and the coordinates of each atom inside the unit cell. Hence, the need of probing interatomic distances makes them purely wide-angle techniques (see Paragraph 3.1.1). In a single-crystal diffraction experiment, the data is collected from an individual crystal, whose orientation with respect to the incident beam is known exactly at any time. This allows to relate the position of signals on the detector with the crystal orientation.

For example, each diffraction spot in Figure 3.3a corresponds to one of the possible scattering vectors satisfying the diffraction conditions (Equation 3.12). The

43

position of reflections encodes information about the lattice periodicity, for which an adequate unit cell can be chosen through a process called indexation. Moreover, from the study of systematic absences, that are families of diffraction spots whose intensity is systematically null, it is possible to infer the symmetry operations within the crystal and hence identify its space group. Finally, from the quantitative analysis of reflection intensities it is possible to reconstruct the nature and position of each atom within the unit cell. This process relies on the theory outlined in Paragraph 3.1, and is known in its complex as *structure solution*.
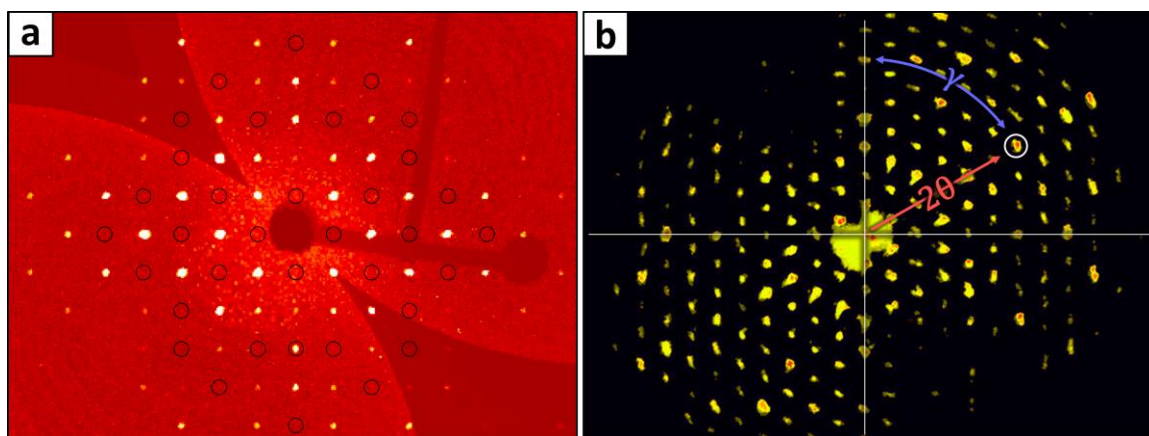
Figure 3.3. Single-Crystal X-ray and electron diffraction data. a) SCXRD (hk0) frame collected on a crystal of $(MA)(BA)_2Pb(Br_{0.5}I_{0.5})_7$ (data from this Thesis, see Chapter 7). The black circles indicate some of the systematic extinctions, which can be used to infer the presence of symmetry operations in the crystal, and therefore identify its space group. b) 3D-ED (hk0) frame collected on a nanocrystal of franzinite.[7] Compared to SCXRD, 3D-ED produces broader and less resolved diffraction spots due to finite-size effects and inherent instrumental limitations. However, being spread in the reciprocal space, the spots are still well resolved, and can be indexed and integrated to produce a reliable structure solution. Overlaid to the frame, 2θ and γ angles are shown for a selected reflection, circled in white. Panel (b) is adapted from Ref. 7.

The most widespread single-crystal technique is by far the Single Crystal X-ray Diffraction (SCXRD), that uses X-rays as a probe radiation. This can be performed in a laboratory, where Mo or Cu X-ray cathodes are mostly used as radiation sources, or at a synchrotron facility. In both cases, this technique requires single-crystal specimens of relatively large sizes (100 μm for lab-sources, 20-30 μm for synchrotrons), with a theoretical lower limit of ~1 μm.[8] This means that SCXRD is unaffected by finite-size effects, but on the other hand it cannot be applied to nanoscale materials. In this thesis, SCXRD was used in Chapter 7 to investigate bulk crystals of layered lead halides.

Differently from X-ray based setups, electron microscopes allow to visualize and target much smaller crystals, and their electron beam can be used to perform diffraction experiments. If the microscope is equipped with a suitable tilting stage the specimen can be rotated at will, and it becomes possible to perform an experiment alike SCXRD on individual nanocrystals as small as 30-50 nm.[7] This technique is called 3D-Electron Diffraction (3D-ED), and since it probes small crystallites is not exempt from finite-size diffraction effects (Figure 3.3b). However, their impact is relatively small, as the diffraction data come in the form of spots that are separated not only in 2θ, but also in γ. This allows to resolve them despite the finite-size broadening, and causes at most some limited issue during the intensity integration process. Hence, 3D-ED is ideal for solving the structure of unknown nanocrystals, and was extensively used for this purpose in Chapter 4 of this thesis. However, collecting good-quality electron diffraction data on small particles is far from trivial, and the technique suffers some limitations due to the non-

negligible chance of multiple diffraction phenomena, that challenge the applicability of the kinematic approximation.[5]

3.5 Polycrystalline Wide-Angle Techniques

Like single-crystals, also polycrystalline samples can be probed by X-rays (Polycrystalline X-ray Diffraction, PXRD), or by a large electron diffraction beam illuminating an area (Selected Area Electron Diffraction, SAED). The principle remains unchanged, and results are ideally comparable. However, PXRD generally produces data with better resolution, and it is often preferred for data that must undergo detailed analyses. Note that here we are exclusively referring to wide-angle techniques, as polycrystalline small-angle techniques will be discussed in a dedicated paragraph.

When a polycrystalline sample is measured, all the information on the orientation of crystals with respect to the incident beam, that is encoded in the γ angle, is lost (Figure 3.4). Indeed, each individual crystallite still diffracts at specific γ angles, but since the sample is composed by many of them oriented in random directions, all the countless spots characterized by the same 2θ angle but falling at different γ angles now merge together to form diffraction rings. These are then radially integrated to produce a 2θ/intensity profile, that is the usual outcome of a polycrystalline diffraction experiment (Figure 3.4). This is a major limitation, as not only valuable information is lost, but the remaining signals are in strong overlap with each other. Indeed, all the reflections falling at the same 2θ value now contribute to the same diffraction ring and become indistinguishable: the number of equivalent reflections participating to a ring is called

multiplicity. This results in a major information loss: for example, in Figure 3.3b the 6-fold symmetry of the material is made apparent by the multiplicity and γ position of peaks with the same 2θ. Conversely, there is no immediate way to understand whether a ring in Figure 3.4a stems from a hexagonal, a cubic or a tetragonal material.
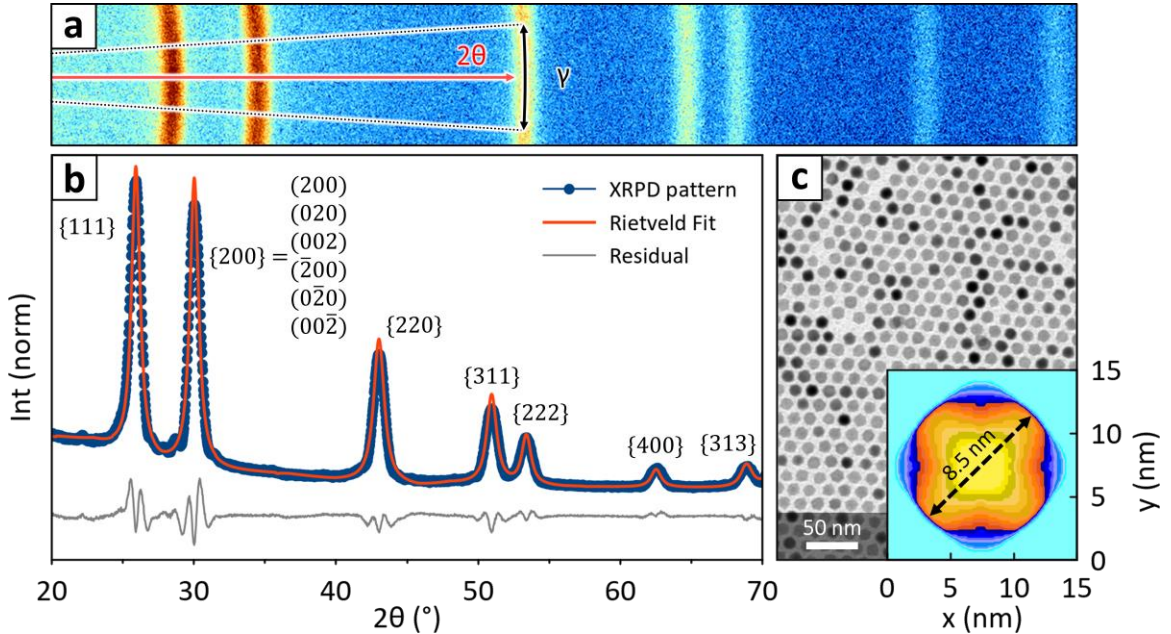
Figure 3.4. X-ray diffraction data from a polycrystalline sample. a) Diffraction rings from a PbS nanocrystals powder sample. b) XRPD pattern obtained by radial integration of panel (a, blue). The {hkl} indexes denote families of individual (hkl) planes equivalent by symmetry, which therefore share the same 2θ angle. Overlaid is the simulated pattern obtained by Rietveld fit (red). c) Transmission electron microscopy (TEM) of the sample. The inset shows the average nanocrystal morphology derived from the Rietveld fit, that correctly captures the spheroidal shape but slightly underestimates the nanocrystal size (11.5 nm TEM vs 8.5 nm XRPD), possibly due to a lower crystallinity of the particle surface. Data from this thesis, see Ref. 9.

Moreover, reflections that fall at different, but close 2θ values are easily distinguished by γ in a single-crystal experiment, while for a polycrystalline sample they are at risk of overlap. This is especially true if the diffraction features are broadened by finite-size effects, or if the number of reflections grows very large, as it is the case for complex structures with large unit cells and low symmetry. This considered, polycrystalline diffraction techniques might appear inferior to their single-crystal counterparts. The reality is, however, that they are extremely powerful: simply, they are better suited for different tasks. First, obtaining polycrystalline samples is much simpler than growing single crystals, and polycrystalline diffraction experiments are generally easier and faster to perform. Moreover, these techniques can be applied to nanomaterials of any size and shape, a condition that does not apply to single crystal-techniques. Polycrystalline diffraction also bears strong statistical significance, as billions of crystallites are probed at the same time.

However, the main strength of polycrystalline diffraction is its ability to deal with non-ideal samples. SCXRD experiments require specimens that are carefully grown for the specific purpose of a structure solution, and are selected to be as close to ideality as possible. Moreover, single-crystal diffraction relies on the theory developed for an infinite and perfect crystal (Paragraph 3.1), and at the average-user level the ability of dealing with non-ideal effects is limited to the deconvolution of twinned crystals and the correction of absorption effects to account for the crystal shape. Conversely, polycrystalline diffraction excels in dealing with real-world samples. As such, models for describing finite-size effects, preferred crystallite orientation, strain, and defects are

implemented in most software packages. Moreover, compared with single-crystal diffraction, polycrystalline techniques allow for a much more visual and immediate interpretation of the diffraction data, that is convenient for routine analyses.

3.5.1 Visual interpretation of PXRD data

The PXRD data can be analyzed at increasing levels of complexity, and its inspection provides a level of detail that can be very shallow or very deep depending on the analysis approach. At its shallower level, PXRD is used to identify the presence of know crystalline phases in a sample. This is done by matching the position of reflections in the 2θ scale with a database, and it is arguably the most widespread use of the technique. Based on the relative intensity of reflections it is also possible to estimate the relative concentration of different crystalline phases within the sample, even in absence of a more elaborate analysis of data.

Through PXRD it is also possible to estimate the size of nanocrystals by taking advantage of the finite-size effects. For this, it is commonly applied the Scherrer equation,[10–12] that relates the broadening of a (hkl) reflection with the thickness of nanocrystals along the [hkl] direction (Equation 3.17):

$$L_{hkl} = \frac{K_{hkl}\lambda}{\beta_{hkl}\cos\theta_{hkl}} \qquad \text{Eq 3.17}$$

Where L is the crystallite size, λ is the radiation wavelength, b is the width of the chosen reflection (after deconvolution of instrumental broadening), and θ_{hkl} is its Bragg

angle. Although Equation 3.17 is nominally straightforward to use, it is limited by the possible overlap of unresolved peaks, by the need of deconvoluting the instrumental profile, and by the appropriate choice of the dimensionless Scherrer constant, *K*. This choice depends on the definition of *b* (most often full width at half maximum), on the Miller indices (*hkl*) of the chosen reflection, and on the assumed particle morphology.

3.5.2 Rietveld and Le Bail pattern analyses

The Rietveld profile fit is arguably the most widespread approach to a deeper analysis of PXRD patterns (Figure 3.4b-c).[13] In short, it consists of fitting the diffraction profile based on a multiparametric model. If performed properly, the Rietveld analysis allows to refine information like the unit cell parameters, the position of atoms inside the unit cell, the content of mixed-occupancy atomic sites, the average size and shape of crystallites, their preferred orientation within the sample, and the presence of strain.

To compute a simulated XRPD pattern, the method first calculates the angular positions of Bragg reflections based on the lattice of the material (see Equation 3.12). Then, the integrated area of each reflection is calculated as the combination of several contributions (Equation 3. 18):

$$I_{hkl} = K \cdot p_{hkl} \cdot LPA(\theta) \cdot T_{hkl} \cdot |S_{hkl}|^2 \qquad \text{Eq 3.18}$$

Where *K* is a scaling factor, p_{hkl} is the multiplicity factor that describes how many equivalent reflections participate to one experimental peak, *LPA* is the θ-dependent

Lorentz-Absorption-Polarization correction that accounts for geometric contributions to the experimental intensity of peaks, T_{hkl} is the preferred orientation factor describing the statistic orientation of crystallites with respect to the instrument reference frame, and $|S_{hkl}|^2$ is the square modulus of the Bragg reflection structure factor S (see Equation 3.14). Finally, the peak intensity calculated according to Equation 3.18 are fed into a peak profile function, that computes the actual shape of Bragg reflections by taking into account the instrumental broadening, the source wavelength dispersion, and the contributions of the sample microstructure (that is, size and shape of crystallites and microstrain) to the peak profile.

All these steps depend on a large number of variables, such as unit cell parameters, atomic coordinates, preferred orientation coefficients and so on, that can be therefore extracted from the experimental profile by performing a least squares optimization of the calculated XRPD pattern to match the experimental one. Note that this is an optimization approach aimed to refine a starting guess, hence the name Rietveld *refinement* that is sometimes used, and the technique cannot provide the structure of an unknown material. In this sense, it is an approach complementary to SCXRD. In most cases not all parameters can be refined at the same time, and the user might need to make a choice depending on their scientific question. For example, both the position of atoms in the unit cell and the preferred orientation of crystallites in the sample can be inferred by the intensity of reflections. If there is a suspect that the sample might be textured, then it is better to keep the position of atoms fixed to that determined by SCXRD and refine

only the preferred orientation of crystallites, as co-refining both might lead to overfit and unreliable results.

Even if the Rietveld model includes correction capable of handling scenarios like the presence of anisotropic and oriented crystallites, specimens very far from ideality can still pose challenges in their refinement. In those cases, if the priority is refining parameters that depend solely on the position and shape of the diffraction peaks, but not on their intensity (*i.e.*, unit cell parameters, crystallite size, and lattice strain) it might be convenient to adopt a less elaborate form of full-profile analysis known as Le Bail fit.[14] Like in the Rietveld approach, a Le Bail fit first predicts the position of Bragg reflections based on the material unit cell, and then convolutes each reflection with a peak profile to capture the experimental XRPD profile. However, while in a Rietveld fit the intensity of reflections is calculated based on a variety of structural, instrumental, and geometric factors (see Equation 3.18), the Le Bail fit adjusts the peak intensity arbitrarily to ensure the best possible match with the experimental profile, trading information for usability.

In this thesis, both Rietveld and Le Bail approaches have been used extensively for a variety of tasks, especially in Chapters 4 and 7. It is worth noting, however, that both methods rely on the diffraction theory for infinite and perfect crystals (Paragraph 3.1). Indeed, the very first step of both Rietveld and Le Bail procedures relies on Equation 3.12 to predict the position of Bragg reflections, with the underlying assumption that crystallites in the sample are reasonably close to the ideal scenario of an infinite crystal, and that the impact of finite size and imperfections is limited to the peak profiles.

3.5.3 Structure solution from polycrystalline data

Although challenging, solving an unknown structure from PXRD data is not impossible. The solution proceeds through the same workflow as SCXRD: indexation, intensity extraction, symmetry determination, and structure solution. For polycrystalline samples, the first three steps of the process effectively rely on a Le Bail fit, as a tentative unit cell is first proposed, and then a full-profile fit routine tries to adapt it to the experimental peaks, with the aim of extracting the integrated intensities for each of them.

Compared to SCXRD however, the indexation step is heavily hindered by the loss of information associated with the γ angle in PXRD, as the only way left to determine the unit cell is comparing the position of all peaks in the diffractogram and finding a set of six parameters ($a, b, c, \alpha, \beta, \gamma$) that matches them all. This becomes especially challenging for low symmetry phases and/or for nanomaterials, where the high number of peaks and their overlap due to finite size effects makes it challenging to deconvolute their position.

If a unit cell is reliably identified, the Le Bail fit allows to associate to each reflection an intensity and, if no intensity is detected, it means that a systematic extinction has been identified. Together, all extinctions allow to infer information on the crystal structure symmetry. Here the loss of information associated with the γ angle is again a huge limitation, as the overlap of peaks falling at similar 2θ values might hide some of the extinctions, leaving with a list of possible space groups rather than with one or few options. Finally, once the unit cell and space group are known the multiplicity of each peak becomes know as well, and it is possible to associate to each reflection an

intensity. From now on, the dataset becomes equivalent to that of a SCXRD experiment, and the structure solution proceeds unchanged.

All the limitations discussed above make it clear that SCXRD should always be preferred to solve an unknown structure, when applicable. However, being able to solve a structure by PXRD data is a powerful asset for materials that cannot be obtained as large single crystals. This is the case, for example, of large biomolecules difficult to crystallize, but also of nanomaterials of unknown structure and composition, where SCXRD is not an option and 3D-ED might not be accessible. Indeed, in this thesis, PXRD was extensively used in Chapter 4 to help solving the structures of unknown nanomaterials.

3.5.4 Total scattering techniques

The main strength and limitation of all methods discussed so far is that they rely on the diffraction theory for perfect and infinite crystals. This makes them simple to implement and extremely versatile in most cases, but it is a clear shortcoming for poorly crystalline samples, such as highly defective, partially amorphous, or nanocrystalline materials. In all these cases, the ideal scattering condition $\vec{q} \in \{G\}$ relaxes, and significant portions of the diffracted intensity are found in between the Bragg peaks. This additional signal is called *diffuse scattering*, and encodes information about the non-ideality of the material.

To take advantage of the diffuse scattering one must move past the perfect crystal theory, and rely on total scattering methods instead. As the name suggests, this family of techniques can account for the totality of the intensity scattered by a sample, provided

that a suitable structural model is given. The foundation of total scattering methods is the Debye scattering equation, first published in 1915,[15,16] that describes the intensity scattered by an isotropic sample without making any assumption on its periodicity or atomic structure. For a monoatomic system, the Debye Scattering equation can be written in the form of Equation 3.18.[16,17]

$$I(q) = Nf^2 + f^2 \sum_i^N \sum_{j \neq i}^N \frac{\sin qr_{ij}}{qr_{ij}} \qquad \text{Eq 3.18}$$

Where f is the scattering atom of the element considered, i and j are different atoms belonging to an ensemble of N atoms, and r_{ij} is the distance between the two. In 1927, Zernike and Prin generalized this equation by considering electrons as scatterers instead of atoms, and were able to correlate the diffracted intensity to the electron density of the sample (Equation 3.19):[17,18]

$$I(q) = Nf^2 \left\{ 1 + \int 4\pi r^2 [\rho(r) - \rho_a] \frac{\sin qr}{qr} dr \right\} \qquad \text{Eq 3.19}$$

Where $\rho(r)$ is the electron density at a given position r, and ρ_a is the average electron density in the sample. It can be demonstrated that, if $\rho(r)$ - $\rho_a \neq 0$ over a reasonably short range, Equation 3.19 is equivalent to Equation 3.20:

$$I(q) = Nf^2 \left(1 + \sum_i Y_i \frac{\sin qr_i}{qr_i} \right) \qquad \text{Eq 3.20a}$$

$$Y_i = \int_{r_i - \delta/2}^{r_i + \delta/2} 4\pi r^2 [\rho(r) - \rho_a] dr \qquad \text{Eq 3.20b}$$

Where Y_i represents the electron density deviation from the sample average in a shell of thickness δ around any given atom i. Equation 3.20 is central to total scattering methods, because it relates the Intensity scattered by the sample to the electron density within the sample through a Fourier series. This is the foundation of perhaps the most popular total scattering method, that is the Pair Distribution Function (PDF) analysis. In short, PDF is a function defined within the real space that expresses the distribution of distances between pairs of scatterers. It is obtained by performing the Fourier transform of a diffraction pattern, thar must be collected over an extended q-range to minimize truncation artifacts. For this reason, PDF analyses must be conducted on laboratory instruments equipped with Mo or Ag sources, that provide a shorter wavelength compared to Cu, or at a synchrotron facility.

In principle, a PDF profile contains the exact same information as the diffractogram that was used to calculate it, and as such a PDF analysis and a Debye Scattering Equation (DSE)-based refinement are equivalent in terms of results. However, reciprocal space data (Figure 3.5a-b) facilitate an interpretation of data oriented to symmetry and lattice periodicities, while direct space data (Figure 3.5c) are better suited for interpreting the atomistic structure at a local level. Indeed, peaks in a PDF profile, and especially those falling in the short-range part of it, can be directly attribute to interatomic distances within the sample and are often studied to solve questions related to local distortions or coordination environments. In Chapter 4 of this thesis, PDF analysis was paired with Rietveld fits to gain additional insight into the local structure of materials by retrieving the information encoded by the diffuse scattering, which is not considered by

the Rietveld method. On a practical standpoint, diffraction profiles can be analyzed either in the reciprocal q-space or in the direct r-space, and in both cases an atomistic model of the sample is refined by optimizing the match between the experimental and the simulated profile, be it in q (DSE) or in r (PFD). However, it might be convenient to optimize the instrumental setup for the specific analysis, as PDF benefits from a more extended q-range that minimizes truncation artifacts upon performing the Fourier transform operation, while a DSE-based analysis would benefit from a higher resolution in ranges where the most prominent Bragg peaks fall, even if limited to a shorter q-range.
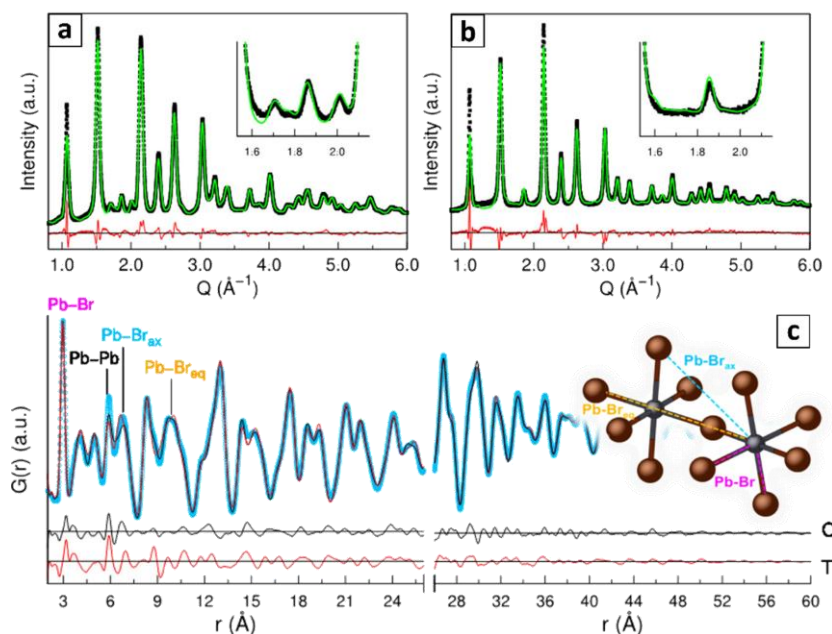
Figure 3.5. Total scattering techniques. a-b) Total scattering refinements of CsPbBr$_3$ nanocrystals diffractograms collected at room temperature (a) and at 410 K (b). The differences highlighted in the insets can be attributed to the orthorhombic γ-CsPbBr$_3$ to cubic α-CsPbBr$_3$, that in bulk is stable above 403 K.[19] Even if DSE fits may resemble a Rietveld fit (Figure 3.4c), the underlying calculations are deeply different. c) PDF profile collected on the same sample at room temperature. Adapted from Ref. 20.

3.6 Small-Angle Diffraction Techniques

Until now we have been focusing on wide-angle techniques, that probe q-ranges comparable with interatomic distances and are therefore used to study the atomic-scale structure of materials. Instead, diffraction experiments performed at lower angles are informative of nanometric distances, and can be especially useful for the study of nanomaterials (Figure 3.6). Here we shall focus on two techniques: Small Angle X-ray Scattering (SAXS) and Grazing Incidence Small Angle X-ray Scattering (GISAXS).

The main difference between SAXS and GISAXS is the experimental geometry. In SAXS, an X-ray beam shines through a sample, prepared in form of a thin slice if solid or placed in a capillary if liquid or powdery, and the signal is collected by a wide-area detector placed behind it (Figure 3.6a). GISAXS instead requires a sample deposited or grown on a flat substrate, and works by shining a grazing X-ray beam on its surface and collecting the scattered radiation downstream of the sample (Figure 3.6c). The applications of small-angle incidence techniques are vast, as there is plenty of nanostructured materials, many of them not even crystalline and therefore of little interest for wide-angle techniques, that can take advantage of such methods.[23] For brevity, here we will focus only on nanoparticle-related ones.

A first application of small-angle techniques to nanoparticles is the determination of their average shape and of their size distribution, that is most often obtained by performing a SAXS experiment on a liquid dispersion of particles. Such experiment produces data in the form of concentric rings (Figure 3.6a) that, similar to what is done for PXRD, are radially integrated to produce a 2θ/intensity diffraction profile (Figure 3.6b).

This profile is then analyzed by matching it with simulations performed by assuming an average shape and a distribution of size parameters for the nanoparticles population, that can be refined by optimizing the fit.[12,21,24–27] In addition to this, SAXS is often used to detect the formation of ordered aggregates in a colloidal suspension of nanocrystals, as the nanoscale periodicities associated to the aggregate structure would result in the formation of sharp diffraction features within the SAXS profile. These diffraction signals are equivalent to the Bragg peaks measured at wide-angle during a PXRD experiment, with the sole difference that the scatterers are nanocrystals instead of atoms. Indeed, they can be indexed according to a nanometric-scale unit cell, which enables determining the packing geometry of nanocrystal assemblies.[22,28–30]

However, just like in wide-angle techniques, the study of ordered nanocrystal aggregates would benefit from the information encoded in the γ angle, that is lost for SAXS experiments performed on liquid suspensions. Therefore, GIWAXS is often preferred to SAXS for ordered nanocrystal solids, also known as superlattices, where particles pack in geometries periodically repeated over long distances like atoms in a traditional crystal. The advantage of GISAXS over a SAXS experiment is that superlattices grown on a substrate or at a flat liquid-air interface often retain a precise orientation with respect to their support (Figure 3.6c). Similar to the SCXRD vs PXRD case in wide-angle techniques, this means that the orientation of the sample with respect to the incident X-ray beam is also fixed, and that the data will come in the form of resolved spots rather than rings (Figure 3.6d). This eases the data analysis, as information like the packing geometry and the assembly disorder become more accessible through the indexation of diffraction

spots or the analysis of their shape. In this thesis, GISAXS was used in Chapter 6 to

characterize CsPbBr₃ nanocrystal superlattices.
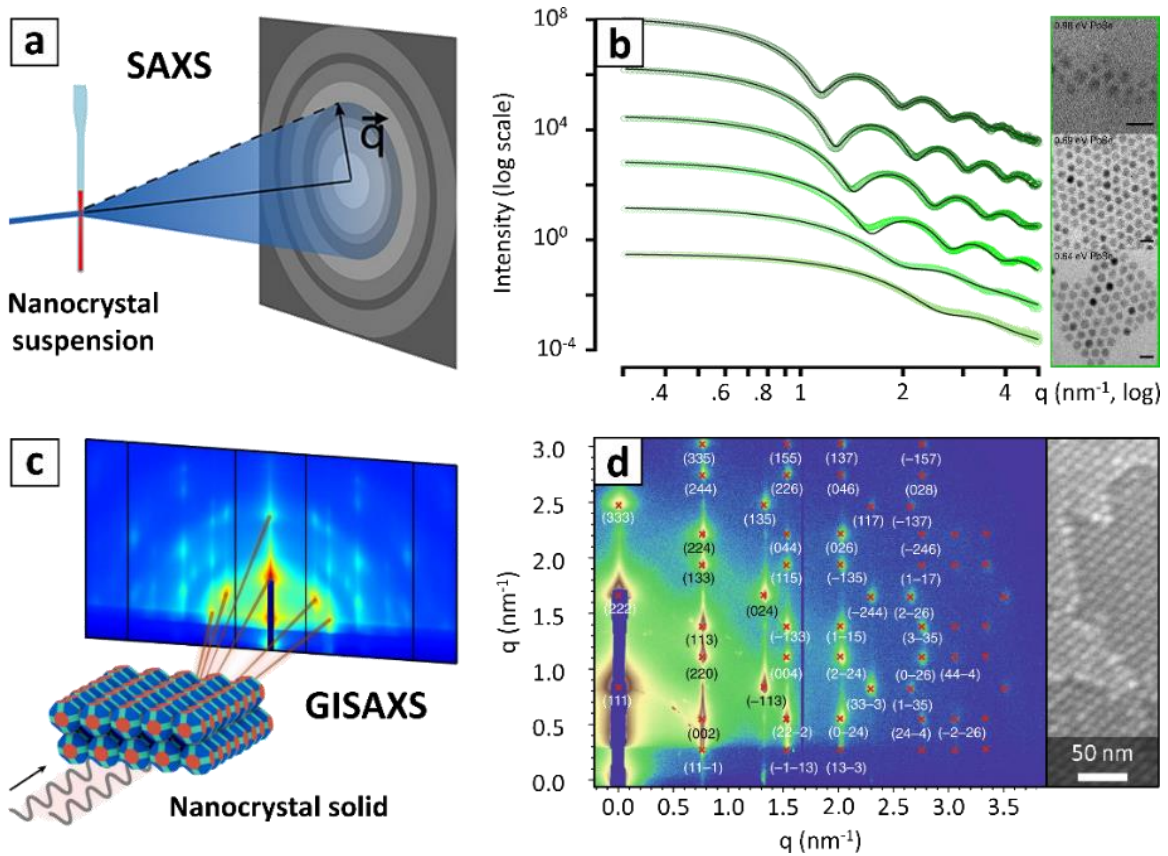
Figure 3.6. Small-Angle scattering techniques. a) Scheme of a SAXS measurement. b) SAXS data collected on PbSe nanocrystals of different sizes. Inset: TEM images of some of the PbSe samples measured by SAXS. c) Scheme of a GISAXS measurement performed on a superlattice of colloidal nanocrystals. d) GISAXS pattern collected on a superlattice of Ag nanocrystals packed in an FCC geometry. The diffraction spots are indexed according to the FCC supercell. Inset: SEM image of the same sample. Adapted from Refs. 21,22.

As a final note, it is worth mentioning that both SAXS and the GISAXS do have a

corresponding wide-angle technique that is performed in the same geometry. For SAXS

this is simply a PXRD experiment performed in transmission, and falls within what discussed in Paragraph 3.5. The wide-angle technique performed in a grazing-incidence geometry is instead called GIWAXS (Grazing-Incidence Wide-Angle X-ray Scattering). If performed on disordered samples, this technique is again analogue to PXRD, as it simply produces diffraction rings corresponding to the Bragg peaks of the sample atomic structure. However, when performed on samples where nanocrystals are strongly oriented, like in superlattices, GIWAXS produces data remindful of SCXRD, with localized spots due to the partially constrained orientation of the crystallites with respect to the incident beam.[31,32] This analysis can be very insightful when studying how the atomic lattice of nanoparticles is aligned within a superstructure, and is especially sensitive to the tilting disorder. For this reason, GIWAXS was applied in Chapter 6 of this thesis to complement GIWAXS in the investigation of $CsPbBr_3$ nanocrystal superlattices.

3.7 Structural Characterization by Imaging

Diffraction techniques are not the only option when it comes to investigate the structure of materials. This is especially true for what concerns the morphological aspects, as electron microscopy techniques allow to visualize objects down to the sub-nanometer scale. Indeed, Scanning Electron Microscopy (SEM)[33] and Transmission Electron Microscopy (TEM)[34] are routinely used in the field of colloidal nanomaterials to characterize the morphology of samples, as they are a visual and immediate way to access the nanoparticles size, shape, and size distribution (Figure 3.7a). In this they are complementary to SAXS, and they are often used together when these parameters matter

the most, like in the construction of band gap vs size curves for colloidal semiconductor nanocrystals.[12] Electron microscopy techniques, however, are also valid tools for studying the atomic structure of nanomaterials.[34] For example, high-resolution scanning TEM (HR-STEM) instruments can image single atomic columns,[35] and are especially versatile in situations that would be challenging for diffraction techniques, like materials whose structure is unknown, as the lack of a starting model complicates refinement-based approaches, or situations where fine details are inspected, such as the position of dopants,[36–38] and the presence of defects or small lattice distortions (Figures 3.7b-e, more examples are found in Figure 2.3).[39–44] In this thesis, low-resolution TEM was used to characterize the morphology of nanocrystals, while HR-STEM was employed in Chapters 4 and 5 to investigate novel nanomaterials and their epitaxial heterostructures.

Finally, electron microscopies provide information on the composition and electronic structure of samples by techniques like SEM/TEM Energy-Dispersive X-ray Spectroscopy (EDXS), and Electron Energy Loss Spectroscopy (EELS).[34,35] EDXS exploits the X-rays generated by the interaction between the electron beam and the sample to characterize the elemental composition of the sample itself, be it over a large area or at a very local scale. This is especially useful to determine the stoichiometry of an unknown material, or to map the distribution of elements within the sample in case of inhomogeneities.[46,47] EELS instead measures the energy variations of an initially monochromated electron beam upon interaction with a material sample, and can probe the elemental composition of a specimen, the nature of chemical bonds within it, the valence state of elements it is composed of, and details of its electronic structure like the

band gap for semiconducting materials.[36,48,49] In this thesis, SEM-EDXS and TEM-EDXS were diffusely used to characterize the composition of samples.
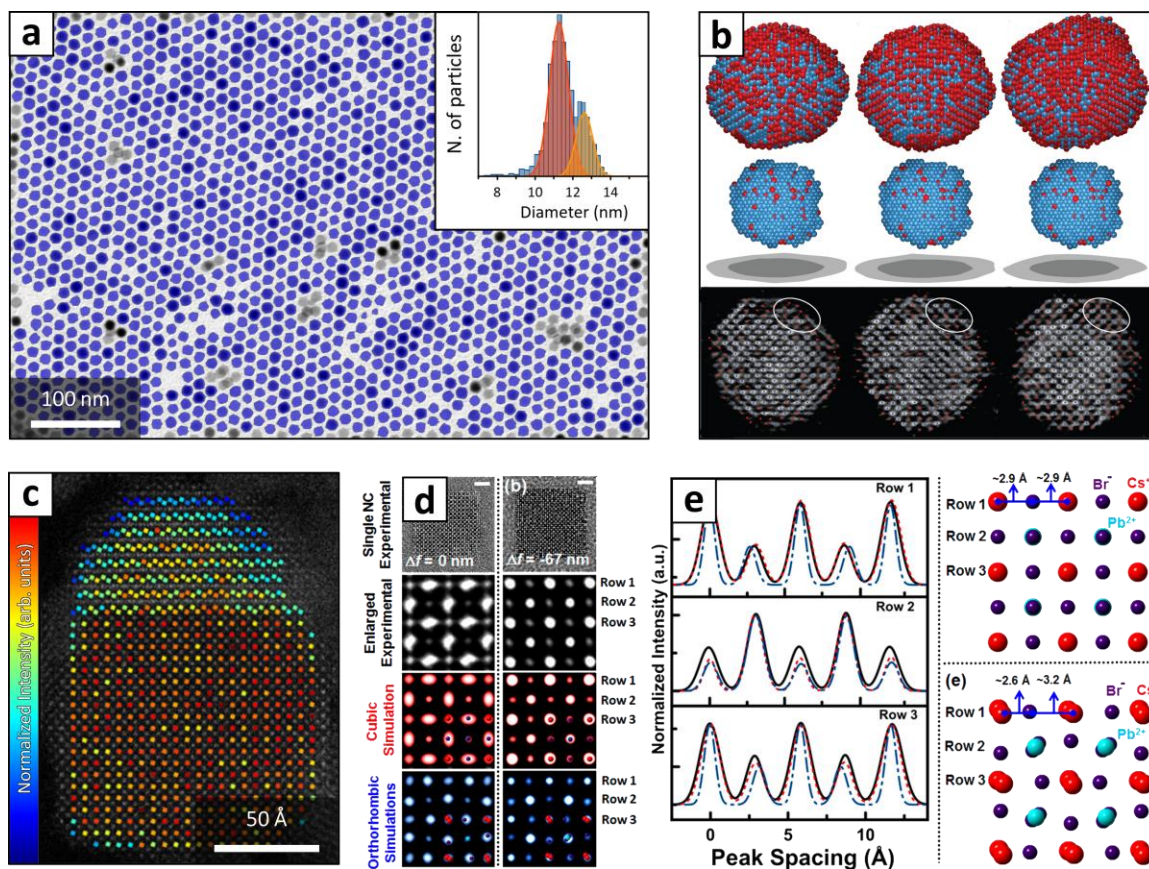
Figure 3.7. Examples of TEM analyses. a) PbS nanocrystals showing a bimodal size distribution, as highlighted in the inset. Only the particles highlighted by the blue mask were measured, discarding aggregates (data from this thesis, see Ref. 9). b) 3D atomic models of Pt nanocrystals (blue) doped with iron atoms (red), reconstructed by electron tomography during a thermal annealing experiment. c) Quantitative intensity analysis in a HR-STEM image used to identify Pb-containing columns in a $Pb_4S_3Cl_2$-$CsPbCl_3$ heterostructure (data from this thesis, see Ref. 45). d) HR-TEM images of a $CsPbBr_3$ nanocrystal captured at different focal planes. e) The quantitative analysis of each focal plane was then used to model the structure of the material. Adapted from Refs. 9,37,40,45.

3.8 Source Publications and Contributions

This chapter is based on the following publications:

I. Kuno, M., Gushchina, I., **Toso, S.** & Trepalin, V. *No One Size Fits All: Semiconductor Nanocrystal Sizing Curves*. J. Phys. Chem. C 126, 11867–11874 (2022). [Ref. 12]

II. **Toso, S.***; Baranov, D.*; Altamura, D.; Scattarella, F.; Dahl, J.; Wang, X.; Marras, S.; Alivisatos, A. P.; Singer, A.; Giannini, C.; Manna, L. *Multilayer Diffraction Reveals That Colloidal Superlattices Approach the Structural Perfection of Single Crystals*. ACS Nano 2021, 15, 6243–6256. [Ref. 9]

III. **Toso, S.**; Baranov, D.; Giannini, C.; Marras, S.; Manna, L. *Wide-Angle X-Ray Diffraction Evidence of Structural Coherence in CsPbBr$_3$ Nanocrystal Superlattices*. ACS Mater. Lett. 2019, 1, 272–276. [Ref. 6]

IV. **Toso, S.***; Imran, M.*; Mugnaioli, E.; Moliterni, A.; Caliandro, R.; Schrenker, N. J.; Pianetti, A.; Zito, J.; Zaccaria, F.; Wu, Y.; Gemmi, M.; Giannini, C.; Brovelli, S.; Infante, I.; Bals, S.; Manna, L. *Halide Perovskites as Disposable Epitaxial Templates for the Phase-Selective Synthesis of Lead Sulfochloride Nanocrystals*. Nat. Commun. 2022 131 2022, 13, 1–10. [Ref. 45]

These authors contributed equally

Publication (I) discusses the use of SAXS experiments and of the Debye-Scherrer equation to determine the average size of nanocrystals. **Publication (II)** discusses the influence of size on the diffraction profile of nanocrystals. **Publications (II-IV)** are the sources of data shown in Figures 3.2,4,7.

3.9 Copyright

Some elements of this chapter were adapted from external sources:

3.10 Bibliography

1. Ashcroft, N. & Mermin, N. *Solid State Physics*. (Holt, Rinehart and Winston, 1976).

2. Birkholz, M. *Thin Film Analysis by X-Ray Scattering*. (Wiley, 2005). doi:10.1002/3527607595.

3. Bragg, W. H. & Bragg, W. L. The reflection of X-rays by crystals. *Proc. R. Soc. London. Ser. A, Contain. Pap. a Math. Phys. Character* **88**, 428–438 (1913).

4. Warren, B. E. *X-ray Diffraction*. (Courier Corporation, 1990).

5. Als-Nielsen, J. & McMorrow, D. *Elements of Modern X-ray Physics: Second Edition*. (John Wiley and Sons, 2011).

6. Toso, S., Baranov, D., Giannini, C., Marras, S. & Manna, L. Wide-Angle X-ray Diffraction Evidence of Structural Coherence in $CsPbBr_3$ Nanocrystal Superlattices. *ACS Mater. Lett.* **1**, 272–276 (2019).

7. Gemmi, M. *et al.* 3D Electron Diffraction: The Nanocrystallography Revolution. *ACS Cent. Sci.* **5**, 1315–1329 (2019).

8. Holton, J. M. & Frankel, K. A. The minimum crystal size needed for a complete diffraction data set. *Acta Crystallogr. Sect. D Biol. Crystallogr.* **66**, 393–408 (2010).

9. Toso, S. *et al.* Multilayer Diffraction Reveals That Colloidal Superlattices Approach the Structural Perfection of Single Crystals. *ACS Nano* **15**, 6243–6256 (2021).

10. Scherrer, P. Bestimmung der inneren Struktur und der Größe von Kolloidteilchen mittels Röntgenstrahlen. in *Kolloidchemie Ein Lehrbuch* vol. 1918 387–409 (1912).

11. Langford, J. I. & Wilson, A. J. C. Scherrer after sixty years: A survey and some new results in the determination of crystallite size. *J. Appl. Crystallogr.* **11**, 102–113 (1978).

12.   Kuno, M., Gushchina, I., Toso, S. & Trepalin, V. No One Size Fits All: Semiconductor Nanocrystal Sizing Curves. *J. Phys. Chem. C* **126**, 11867–11874 (2022).

13.   Rietveld, H. M. A profile refinement method for nuclear and magnetic structures. *J. Appl. Crystallogr.* **2**, 65–71 (1969).

14.   Le Bail, A., Duroy, H. & Fourquet, J. L. Ab-initio structure determination of $LiSbWO_6$ by X-ray powder diffraction. *Mater. Res. Bull.* **23**, 447–452 (1988).

15.   Debye, P. Zerstreuung von Röntgenstrahlen. *Ann. Phys.* **351**, 809–823 (1915).

16.   Gelisio, L. & Scardi, P. 100 years of Debye's scattering equation. *Acta Crystallogr. Sect. A Found. Adv.* **72**, 608–620 (2016).

17.   Scardi, P., Billinge, S. J. L., Neder, R. & Cervellino, A. Celebrating 100 years of the Debye scattering equation. *Acta Crystallogr. Sect. A Found. Adv.* **72**, 589–590 (2016).

18.   Zernike, F. & Prins, J. A. Die Beugung von Röntgenstrahlen in Flüssigkeiten als Effekt der Molekülanordnung. *Zeitschrift für Phys.* **41**, 184–194 (1927).

19.   Cottingham, P. & Brutchey, R. L. Depressed Phase Transitions and Thermally Persistent Local Distortions in $CsPbBr_3$ Quantum Dots. *Chem. Mater.* **30**, 6711–6716 (2018).

20.   Bertolotti, F. *et al.* Coherent Nanotwins and Dynamic Disorder in Cesium Lead Halide Perovskite Nanocrystals. *ACS Nano* **11**, 3819–3831 (2017).

21.   Maes, J. *et al.* Size and concentration determination of colloidal nanocrystals by small-angle x-ray scattering. *Chem. Mater.* **30**, 3952–3962 (2018).

22.   Yu, Y., Yu, D., Sadigh, B. & Orme, C. A. Space- and time-resolved small angle X-ray scattering to probe assembly of silver nanocrystal superlattices. *Nat. Commun.* **9**, 1–9 (2018).

23.   Giannini, C., Holy, V., De Caro, L., Mino, L. & Lamberti, C. Watching nanomaterials with X-ray eyes: Probing different length scales by combining scattering with spectroscopy. *Prog. Mater. Sci.* **112**, 100667 (2020).

24.   Li, T., Senesi, A. J. & Lee, B. Small Angle X-ray Scattering for Nanoparticle Research. *Chem. Rev.* **116**, 11128–11180 (2016).

25.   Glatter, O. & Krakty, O. *Small angle x-ray scattering*. (John Wiley & Sons, Ltd, 1982).

26. Beaucage, G., Kammler, H. K. & Pratsinis, S. E. Particle size distributions from small-angle scattering using global scattering functions. *J. Appl. Crystallogr.* **37**, 523–535 (2004).

27. Mattoussi, H., Cumming, A. W., Murray, C. B., Bawendi, M. G. & Ober, R. Characterization of CdSe nanocrystallite dispersions by small angle x-ray scattering. *J. Chem. Phys.* **105**, 9890–9896 (1996).

28. Choi, J. J. *et al.* Controlling nanocrystal superlattice symmetry and shape-anisotropic interactions through variable ligand surface coverage. *J. Am. Chem. Soc.* **133**, 3131–3138 (2011).

29. Choi, J. J., Bian, K., Baumgardner, W. J., Smilgies, D. M. & Hanrath, T. Interface-induced nucleation, orientational alignment and symmetry transformations in nanocube superlattices. *Nano Lett.* **12**, 4791–4798 (2012).

30. Hanrath, T., Choi, J. J. & Smilgies, D. M. Structure/processing relationships of highly ordered lead salt nanocrystal superlattices. *ACS Nano* **3**, 2975–2988 (2009).

31. Smilgies, D. M. & Hanrath, T. Superlattice self-assembly: Watching nanocrystals in action. *EPL* **119**, 28003 (2017).

32. Mahmood, A. & Wang, J. L. A Review of Grazing Incidence Small- and Wide-Angle X-Ray Scattering Techniques for Exploring the Film Morphology of Organic Solar Cells. *Sol. RRL* **4**, 2000337 (2020).

33. Goldstein, J. I. *et al. Scanning electron microscopy and x-ray microanalysis*. (Springer New York, 2017).

34. Williams, D. B. & Carter, C. B. *Transmission electron microscopy: A textbook for materials science*. (Springer US, 2009).

35. Nellist, P. D. *Scanning transmission electron microscopy*. *Springer Handbooks* (Springer New York, 2019).

36. Servanton, G., Pantel, R., Juhel, M. & Bertin, F. Two-dimensional quantitative mapping of arsenic in nanometer-scale silicon devices using STEM EELS-EDX spectroscopy. *Micron* **40**, 543–551 (2009).

37. Zhou, J. *et al.* Observing crystal nucleation in four dimensions using atomic electron tomography. *Nature* **570**, 500–503 (2019).

38. Castell, M. R., Muller, D. A. & Voyles, P. M. Dopant mapping for the nanotechnology age. *Nat. Mater.* **2**, 129–144 (2003).

39. Cooper, D., Denneulin, T., Bernier, N., Béché, A. & Rouvière, J. L. Strain mapping of semiconductor specimens with nm-scale resolution in a transmission electron microscope. *Micron* **80**, 145–165 (2016).

40. Brennan, M. C., Kuno, M. & Rouvimov, S. Crystal Structure of Individual $CsPbBr_3$ Perovskite Nanocubes. *Inorg. Chem.* **58**, 1555–1560 (2019).

41. Béché, A., Rouvière, J. L., Barnes, J. P. & Cooper, D. Strain measurement at the nanoscale: Comparison between convergent beam electron diffraction, nano-beam electron diffraction, high resolution imaging and dark field electron holography. *Ultramicroscopy* **131**, 10–23 (2013).

42. Shamsi, J. *et al.* Colloidal CsX (X = Cl, Br, I) Nanocrystals and Their Transformation to $CsPbX_3$ Nanocrystals by Cation Exchange. *Chem. Mater.* **30**, 79–83 (2018).

43. Akkerman, Q. A. *et al.* Fully Inorganic Ruddlesden-Popper Double Cl-I and Triple Cl-Br-I Lead Halide Perovskite Nanocrystals. *Chem. Mater.* **31**, 2182–2190 (2019).

44. Dang, Z. *et al.* Temperature-Driven Transformation of $CsPbBr_3$ Nanoplatelets into Mosaic Nanotiles in Solution through Self-Assembly. *Nano Lett.* **20**, 1808–1818 (2020).

45. Toso, S. *et al.* Halide perovskites as disposable epitaxial templates for the phase-selective synthesis of lead sulfochloride nanocrystals. *Nat. Commun. 2022 131* **13**, 1–10 (2022).

46. D'Alfonso, A. J., Freitag, B., Klenov, D. & Allen, L. J. Atomic-resolution chemical mapping using energy-dispersive x-ray spectroscopy. *Phys. Rev. B - Condens. Matter Mater. Phys.* **81**, 100101 (2010).

47. Cacovich, S. *et al.* Unveiling the Chemical Composition of Halide Perovskite Films Using Multivariate Statistical Analyses. *ACS Appl. Energy Mater.* **1**, 7174–7181 (2018).

48. Egerton, R. F. & Malac, M. EELS in the TEM. *J. Electron Spectros. Relat. Phenomena* **143**, 43–50 (2005).

49. Brescia, R. *et al.* Bandgap determination from individual orthorhombic thin cesium lead bromide nanosheets by electron energy-loss spectroscopy. *Nanoscale Horizons* **5**, 1610–1617 (2020).

CHAPTER 4:

UNKNOWN NANOMATERIALS

4.1 A Quest for New Materials

Colloidal chemistry targets primarily known compounds, as knowing in advance the properties of a material is a huge advantage for designing functional nanomaterials: direct gap semiconductors are ideal for quantum dots, conductive materials for plasmonics, and so on. Moreover, nanoscopic samples are not ideal to identify and characterize novel compounds, since the small size and the presence of impurities, solvents, surfactants and unreacted precursors pose additional challenges to all characterization steps. As a result, little effort has been devoted in exploiting nanochemistry for the discovery of novel compounds. However, the peculiar reaction conditions typical of colloidal chemistry, that are remarkably different from those of solid-state processes, offer great opportunities in this direction.

Indeed, there are several reports of previously unknown phases that were accidentally discovered at the nanoscale. Most of them are polymorphs of already known structures, whose formation is induced by the influence of surface ligands or the relaxation of highly anisotropic nanostructures.[1] One remarkable example is ε-Co, a metastable allotrope of cobalt that was discovered in nanocrystals in 1999 and has not been obtained in bulk to date,[2] demonstrating that even the structure of chemically

70

simple materials can be heavily influenced by nanoscale effects. More recent examples are the monoclinic Ag_2Se,[3] the orthorhombic PbS,[4] the wurtzite-Cu_2SnSe_3,[5] that are all nanoscale-exclusive metastable polymorphs of compounds already known in bulk. Reports of completely unknown stoichiometries first obtained at the nanoscale are instead less common, mostly due to our already extensive knowledge of binary and ternary phase diagrams. One notable example are the rock-salt $Pb_mSb_{2n}Se_{m+3n}$ and $Pb_mSb_{2n}Te_{m+3n}$ compounds, whose formation in bulk is prevented by the immiscibility of their terminal binary compounds $PbSe/Sb_2Se_3$ and $PbTe/Sb_2Te_3$.[6,7] While these findings are relatively rare, their incidence is expected to increase due to the evolution of colloidal synthesis techniques, the growing number of studies, and above all the increasing complexity of investigated materials. Indeed, as the number of elements per colloidal synthesis grows from one or two to many, the chances of encountering novel structures increases dramatically.

However, characterizing the structure of a novel nanoscale material comes with additional challenges. When a new compound is identified in bulk, its crystal structure is determined by Single-Crystal X-ray Diffraction (SCXRD). This technique allows to routinely solve the structure of inorganic compounds and small molecules, provided that a crystal large enough can be obtained. Unfortunately, even the most advanced micro-focused X-ray sources require crystals at least 20-30 µm in size,[8,9] making this technique inadequate for nanocrystalline materials. Hence, different routes must be found. In this Chapter, the discoveries of previously unknown lead (and bismuth) chalcohalides in the form of colloidal nanocrystals will serve as case studies to demonstrate how to overcome this

challenge. The entire workflow will be discussed, from the stoichiometry determination to the lattice indexation and finally the structure solution, with a specific focus on how different techniques can cooperate.

4.1.1 Why chalcohalides?

Metal chalcohalides are a vast family of compounds with general formula $M_aE_bX_c$, where M^{n+} is a metal cation, E^{2-} is a chalcogenide anion (S^{2-}, Se^{2-}, Te^{2-}), and X^- is a halide anion (F^-, Cl^-, Br^-, I^-). Considering all the ~95 metals in the periodic table this results in ~1140 ternary combinations, a number that does not account for the many possible stoichiometries and polymorphs, nor for quaternary chalcohalides (*e.g.*, $AgBiSX_2$).[10] Within this large group, the most appealing for optoelectronic applications are the transition- and post-transition-metal chalcohalides,[11] many of which are semiconductors with band gap in the visible or near-infrared regions. The availability of involved elements contributes to make chalcohalides strong candidates for future applications. So far, they have been explored mainly in bulk form, with research efforts focusing on germanium chalcohalide glasses[12] and silver chalcohalide antiperovskites[11,13] for their high ionic conductivity, and pnictogen chalcohalides for ferroelectric and photoelectric applications.[11,14–18]

As is often the case in materials for electronics, one main challenge is their rather limited processability, which involves high-temperatures and complex post-synthetic treatments. This is further complicated by the often anisotropic shape of grains due to the strongly directional crystal structures of many technologically-relevant

chalcohalides.[19–24] One possible answer to the processability challenge is the development of nanocrystals, that require lower temperatures, can be prepared in the form of solutions and inks, and are easily processed into films by spin coating or ink-printing techniques. Nevertheless, the landscape of metal chalcohalide nanomaterials is still narrow, and focused strongly on antimony[25–29] and bismuth[25,29–33] chalcohalide nanowires. This opens many opportunities for impactful advancements, and make metal chalcohalide nanocrystals quite appealing.

4.2 Nanocrystals of Lead Chalcohalides

The interest in lead-based chalcohalide nanocrystals stems from the extensive knowledge built on lead chalcogenide and cesium lead halide nanocrystals in the past decades. Indeed, PbE nanocrystals have been widely investigated for near-infrared optoelectronics,[34,35] while the $CsPbX_3$ perovskites and related compounds revolutionized the field of nanocrystals for applications in the visible range.[36,37] This created a solid synthetic background, establishing procedures and vast libraries of precursors and ligands. Another key aspect is that PbE and $CsPbX_3$ nanocrystals are obtained under similar conditions: many synthetic procedures for both classes of materials rely on 1-octadecene as a solvent, exploit long chain amines and/or carboxylic acids as surfactants, and take place in a temperature range of 100-200 °C.[36,38–41] With these premises, it is simple to identify synthetic conditions where suitable precursors of lead, a chalcogenide, and a halide can be combined, producing favorable circumstances for the synthesis of lead chalcohalides. Despite this, lead chalcohalides are among the least known

compounds of this vast class of ternary materials. Prior to our studies, only four stable ternary compositions were known in bulk ($PbTeF_6$, $Pb_7S_2Br_{10}$, $Pb_5S_2I_6$, Pb_4SeBr_6),[42,43] together with two recently reported high-pressure metastable phases ($Pb_4S_3I_2$, $Pb_3Se_2Br_2$).[44,45] In addition, lead is known to form quaternary chalcohalides with other heavy elements like Bi, As, Hg, or Sb.[46–49] The majority of these compounds was never studied in depth, and none of them had been obtained at the nanoscale when this project started. This made the quest for lead chalcohalide nanocrystals especially appealing, since, being related to both PbE and lead halides, they could display promising optoelectronic properties and a high degree of chemical compatibility with these widely studied semiconductors.

4.2.1 Synthesis of Pb-S-Br nanocrystals

The credit for starting the exploration of lead chalcohalide nanocrystals goes to my colleague Dr. Quinten Akkerman at the Italian Institute of Technology, who performed the first successful synthesis of Pb-S-Br nanocrystals, that I later optimized and investigated. Here, the choice to work with sulfur was dictated by the easier colloidal processability and the wider availability of precursors than selenium and tellurium. Bromine instead was selected because of its ionic radius, intermediate between those of chlorine and iodine, and by the deep knowledge of the $PbBr_2$ reactivity in nonpolar solvents coming from prior research on $CsPbBr_3$ nanocrystals.[36,52,53]

The first synthetic approach was derived from a procedure published for PbS nanosheets,[4] which relied on the thermal degradation of lead thiocyanate to release

sulfide ions in the reaction environment. In short, Pb-S-Br nanocrystals were prepared by dissolving $Pb(SCN)_2$ and $PbBr_2$ in a mixture of 1-octadecene, oleic acid and oleylamine at 120°C in air. Once limpid, the solution was quickly heated above 150 °C at a rate of ~20°C/min, causing the decomposition of $[SCN]^-$ ions and triggering the nucleation of Pb-S-Br nanocrystals. The reaction progress was tracked by taking aliquots of a batch at different temperatures and measuring the size of nanoparticles by Transmission Electron Microscopy (TEM, see Figure 4.6 in the Supplementary Material). Once the target temperature was reached, the reaction was quenched and the particles were recovered by centrifugation. By quenching the reaction in the 160-190 °C temperature range, the synthesis could be tuned to yield spherical nanocrystals with 7-16 nm average diameter (Figure 4.1a, see also Figure 4.6). Above 190°C the unreacted $PbBr_2$ precipitated, contaminating the product. However, larger particles could be obtained by a seeded-growth approach, where smaller Pb-S-Br nanocrystals kept at a constant temperature of 170°C reacted with a solution of $PbBr_2$ and $Pb(SCN)_2$ added at a rate of 5 mL/h.

This procedure yielded particles up to ~30 nm in diameter (Figure 4.1b), and as a side-product led to the formation of nanoplatelets of the same material, most of which could be separated by decanting the reaction product (Figure 4.7). X-ray Powder Diffraction (XRPD) demonstrated that the particles were crystalline, as also confirmed by High-Resolution High-Angle Annular Dark Field Scanning TEM (HAADF-STEM, Figure 4.1c). However, the pattern did not match with that of $Pb_7S_2Br_{10}$, that was the only lead sulfobromide known at the time, indicating that we had obtained a novel compound.

4.2.2 Structure solution of Pb-S-Br nanocrystals

The workflow for solving an unknown structure proceeds through three main steps: stoichiometry identification, unit cell determination, and structure solution. The first task is not trivial for nanomaterials, as surface termination effects in small particles can cause deviations from the ideal stoichiometry. Moreover, this specific case was complicated by the overlap of the Pb-M (2.34 eV) and the S-K spectral lines (2.31 eV), often used for elemental analysis by Scanning Electron Microscopy – Energy Dispersive X-ray Spectroscopy (SEM-EDXS). Eventually, the stoichiometry was determined by X-ray Photoelectron Spectroscopy (XPS), which yielded an elemental ratio of Pb:S:Br = 43:32:25. A combination of thermogravimetry and XRPD analyses further supported this result, yielding an elemental ratio of Pb:S:Br = 45:34:22 and demonstrating that the material decomposes to $Pb_7S_2Br_{10}$ and PbS when heated above ~250°C (Figure 4.8). Such elemental ratio is compatible within experimental error with a charge balanced $Pb_4S_3Br_2$ stoichiometry, which proved to be correct.

The unit cell determination was more challenging. In bulk, this step is accomplished by collecting and indexing few frames of a SCXRD experiment, a highly automated process that can be completed in few minutes by any commercial instrument. If a single crystal is not available, the cell can still be determined by indexing a XRPD pattern with algorithms such as N-TREOR.[54,55] However, this approach requires a limited peak overlap, since the algorithm must deconvolute each peak to index them separately. This complicates the indexation of low-symmetry phases, that possess a high number of peaks, and of nanomaterials, where peaks are broadened by finite-size effects.

76

Indeed, this approach was unsuccessful on our samples. Instead, we relied on single crystal 3D-Electron Diffraction (3D-ED), that can solve the structure of nanocrystals as small as ~30-50 nm.[56] 3D-ED data (Figure 4.1d) were collected on samples accreted by seeded-growth, that were the largest available, leading to the identification of an orthorhombic unit cell with parameters a = 8.2(2) Å, b = 14.6(3) Å, c = 8.1(2) Å, and systematic extinctions compatible with the space group Pnma. The cell parameters were independently confirmed by acquiring an atomic-resolution 3D tomography of a $Pb_4S_3Br_2$ nanocrystal (Figure 4.9), from which parameters a = 8.3 Å, b = 15.1 Å, c = 8.2 Å were extracted through a 3D-Fourier transform operation (3D-FT). Despite the successful unit cell determination, $Pb_4S_3Br_2$ nanocrystals were barely matching the size limit of ~30-50 nm required to collect reliable 3D-ED data. Luckily, some of the side-product nanoplatelets left in the sample were large enough to collect high-quality data (Figure 4.10), from which we obtained a first structure model (Figure 4.11).

To check its reliability, we exploited the information extracted by 3D-ED to repeat the structure solution starting from XRPD data.[55] This method could not be applied from the start due to the failure of the indexation procedure. However, the unit cell and space group determined by 3D-ED could be fed directly into the software EXPO2014,[55] thus bypassing the problematic indexation step and allowing a reliable extraction of the peak intensities. The models obtained by 3D-ED and XRPD were remarkably similar, and upon Density Functional Theory (DFT) relaxation they converged to the same structure (Figure 4.11). Later, we also collected high-quality XRPD and Pair Distribution Function (PDF) profiles at the Brookhaven National Laboratory synchrotron facility, which allowed us to

refine the structure model both in the direct and in the reciprocal spaces (Figure 4.1e).

The structure model resulting from the combined refinement is shown in Figure 4.1f.
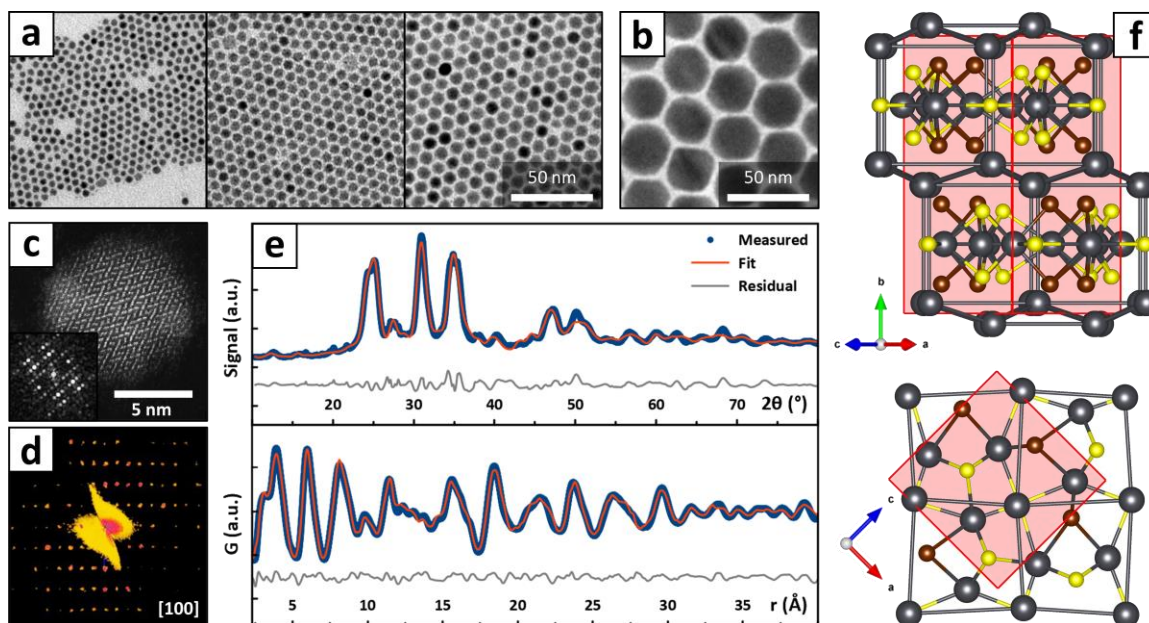
Figure 4.1. $Pb_4S_3Br_2$ nanocrystals and their structure solution.
a) TEM images of $Pb_4S_3Br_2$ nanocrystals obtained by tuning the reaction quenching temperature. From left to right: 160-170-180 °C. b) Larger $Pb_4S_3Br_2$ nanocrystals obtained by a seeded-growth approach. c) HAADF-STEM image of a $Pb_4S_3Br_2$ nanocrystal and its Fast Fourier Transform (FFT). d) (100) 3D-ED frame collected on a $Pb_4S_3Br_2$ nanocrystal. e) XRPD (top) and PDF (bottom) experimental and refined $Pb_4S_3Br_2$ profiles. f) Two views of the refined $Pb_4S_3Br_2$ structure. The unit cell projection is shown in red. Adapted from Refs. 50,51.

Ultimately, we found that $Pb_4S_3Br_2$ is isostructural to $Pb_4S_3I_2$, a high-pressure metastable phase that was reported less than one year before our experiments took place,[44] although a first empirical observation of these compounds might date back to 1901.[57] Crucially, the unit cell of $Pb_4S_3Br_2$ is significantly shorter along the *b* axis if

compared with that of $Pb_4S_3I_2$ (14.7 vs 15.6 Å). This, combined with the broadening of diffraction peaks, prevented us from immediately recognizing the structural similarities from the XRPD pattern (Figure 4.12).

4.2.3 Synthesis and structure solution of Pb-S-Cl nanocrystals

These results on $Pb_4S_3Br_2$ motivated further investigations into lead sulfohalides, with the aim of expanding the pool of materials: since $Pb_4S_3I_2$ had been reported in the literature before, it was an obvious candidate. Indeed, by replacing $PbBr_2$ with PbI_2 in the synthesis we obtained $Pb_4S_3I_2$ nanocrystals with the shape of elongated wires, whose structure was easily confirmed by XRPD (Figure 4.12).

The case of chlorine-based materials was more interesting, as at the time no ternary Pb-S-Cl compound was known, and there was no guarantee that lead sulfochloride nanocrystals would have formed. Nevertheless, replacing $PbBr_2$ with $PbCl_2$ in the synthesis again yielded a nanocrystalline product. Unfortunately, the reaction product was heavily contaminated by PbS, that often forms when $PbCl_2$ is reacted with a source of sulfur in a nonpolar medium (Figure 4.13).[39,58–60] A size-selective precipitation procedure allowed to retrieve small but phase-pure nanocrystals of this novel lead sulfochloride, which we initially assigned to a $Pb_3S_2Cl_2$ cubic phase based on similarities of the XRPD pattern with that of the recently discovered $Pb_3Se_2Br_2$.[45]

To solve the issue of contamination, we developed a different synthetic method for $Pb_3S_2Cl_2$, which consisted in the injection of elemental sulfur dissolved in 1-octadecene into a solution of $PbCl_2$, oleylamine and oleic acid in the same solvent at 170°C. The

procedure again yielded remarkably homogeneous nanocrystals with an average diameter of ~8 nm, but this time free of contaminations (Figure 4.2a).

Despite the similarities with $Pb_3Se_2Br_2$, the analysis of the $Pb_3S_2Cl_2$ nanocrystals XRPD pattern revealed that such structural prototype was inadequate to fit the data (Figure 4.12). Specifically, a cubic phase could not describe accurately the position of diffraction peaks, suggesting that some structural distortion was at play. However, finite size broadening effects, combined with a most likely mild distortion, caused a severe overlap of reflections that made the distorted unit cell impossible to determine.

Again, 3D-ED was best suited to overcome the issue of reflection overlap. To obtain nanocrystals of suitable size we applied the same seeded-growth approach developed for $Pb_4S_3Br_2$. During the process PbS again nucleated as a side product, forming large nanocrystals that could be completely removed by decanting and filtering the reaction product (Figure 4.14), yielding phase-pure $Pb_3S_2Cl_2$ nanocrystals with a diameter of about ~30 nm (Figure 4.2b). From them, 3D-ED (Figure 4.2c) extracted a primitive triclinic unit cell with parameters $a \approx b$ = 7.8(2) Å; c = 7.7(2) Å and α = 109.7(5)°, β = 109.1(5)°, γ = 109.4(5)°. This cell is compatible within experimental error with several higher-symmetry unit cell choices: I-centered cubic (a = 9.0 Å), primitive hexagonal (a = 12.8 Å; c = 7.7 Å), trigonal (a = 7.8 Å; α = 109.4°), or C-centered monoclinic ($a \approx b$ = 12.7 Å, c = 7.7 Å, β = 144.3°). Two structure solution attempts, performed in the cubic I-43d and in the monoclinic Cc space groups, both produced models with a connectivity comparable with that of the reported $Pb_3Se_2Br_2$ structure (Figure 4.15). Notably, Cc is one of the subgroups of I-43d (Figure 4.16), meaning that the two are related by a loss of

symmetry operations, and *Cc* is still capable of describing any structure belonging to *I*-43d. This strongly supported the hypothesis of a minor distortion of the cubic prototype.
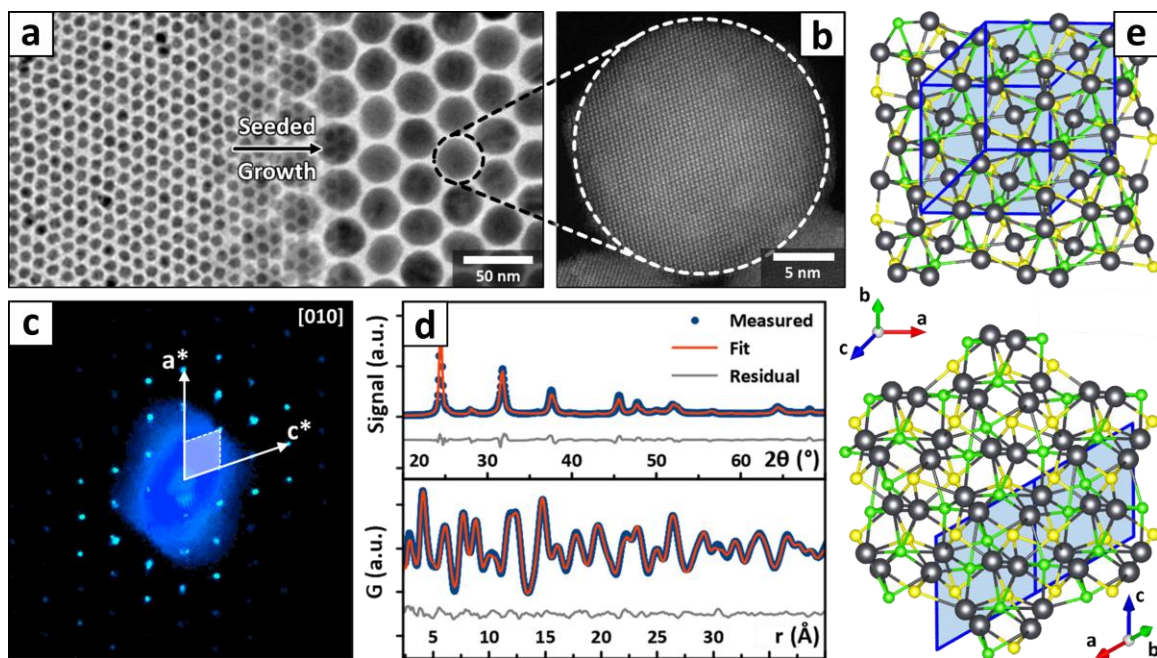
Figure 4.2. Pb₃S₂Cl₂ nanocrystals and their structure solution.
a) $Pb_3S_2Cl_2$ nanocrystals as synthesized (left) and after the accretion process (right). b) HAADF-STEM image of a $Pb_3S_2Cl_2$ nanocrystal. c) [010] 3D-ED frame collected on a $Pb_3S_2Cl_2$ nanocrystal. d) XRPD (top) and PDF (bottom) fits obtained by refining the $Pb_3S_2Cl_2$ structure in the *Cc* space group. e) Two views of the *Cc* monoclinic $Pb_3S_2Cl_2$ structure shown along the high symmetry directions of the corresponding pseudocubic cell ([100] top, [111] bottom). A projection of the monoclinic cell is overlaid in blue, and the corresponding lattice vectors directions are indicated by labelled arrows. Adapted from Ref. 51.

However, the quality of data collected by 3D-ED was insufficient to identify the correct cell choice. For that, we again relied on XRPD and PDF data collected at the Brookhaven National Laboratory synchrotron facility (Figure 4.2d). First, we repeated the solution process from XRPD by assuming the lowest symmetry *Cc* space group, that was

selected based on the best agreement between the calculated and the experimental positions of reflections, and we obtained a structure fully compatible with that produced by 3D-ED. Then, the model was refined by alternating the analysis of XRPD and PDF data (Figure 4.2d). It is important to note that the two datasets were independent from each other, as the position of the detector was optimized for the two experiments. By alternating refinements in the reciprocal and direct spaces we could make the best use of complementary information, as PDF analysis is ideal for refining the local coordination of atoms, while the Rietveld analysis is better suited to refine accurately the unit cell parameters. Moreover, by introducing the PDF dataset we minimized the risk of biases due to the recycling, for the Rietveld refinement, of the same XRPD dataset that was used for the structure solution. The refinement resulted in the model shown in Figure 4.2e.

4.2.4 Pb-S-X structures compared.

Before focusing on the properties of lead sulfohalides, it is worth familiarizing with their structures (Figure 4.3). As mentioned above, $Pb_4S_3I_2$ and $Pb_4S_3Br_2$ share the same stoichiometry, connectivity, and symmetry. Conversely, under comparable reaction conditions chlorine forms the pseudocubic $Pb_3S_2Cl_2$. One relevant difference between these two structures is that, if cut along the (010) plane, $Pb_4S_3X_2$ features a square network of Pb^{2+} cations connected by S^{2-} and X^-. Such connectivity resembles that of a $CsPbX_3$ perovskite, and is not found in the $Pb_3S_2Cl_2$ structure instead. This difference will have a central importance in Chapter 5 of this thesis.
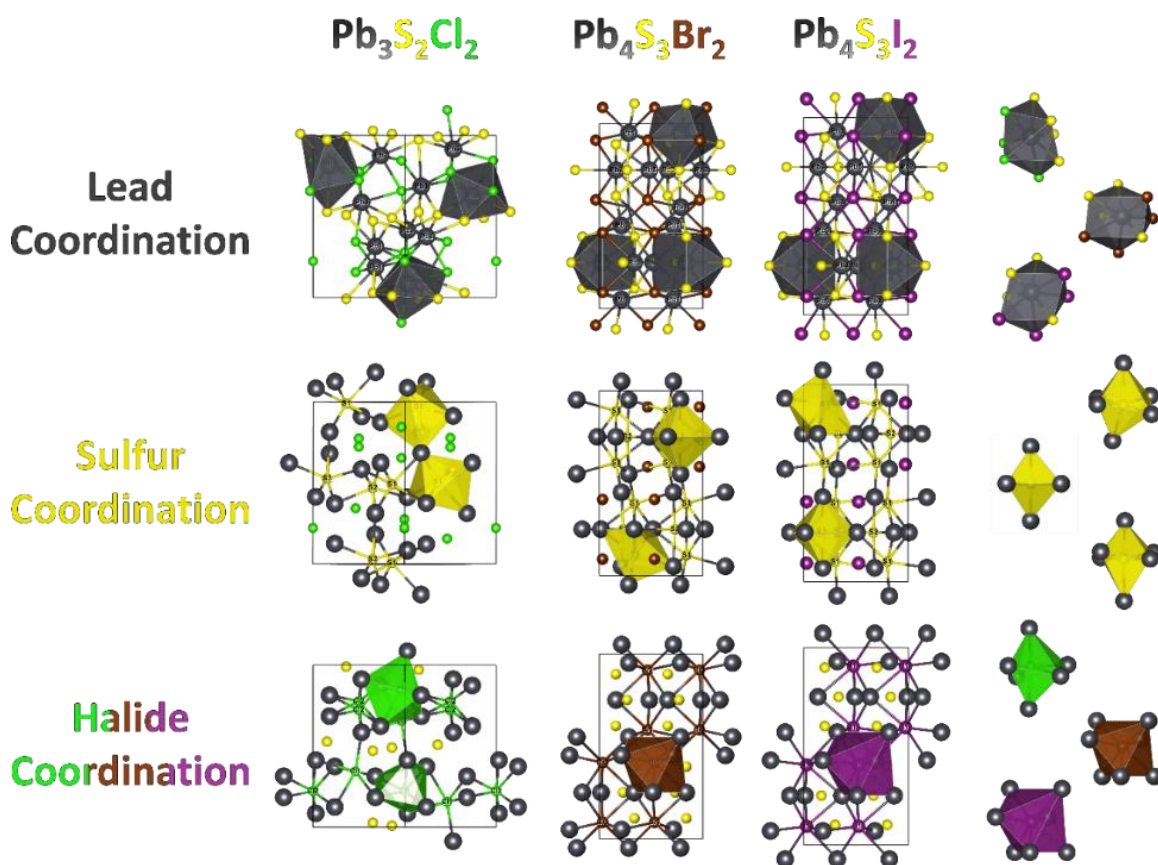
Figure 4.3. Refined structures of Pb₃S₂Cl₂, Pb₄S₃Br₂, and Pb₄S₃I₂. Structures of the three lead sulfohalides studied in this chapter compared. On the right, coordination polyhedra of lead (top), sulfur (middle) and halides (bottom) in the three compounds. Atoms color code: grey = Pb; yellow = S; green = Cl; brown = Br; purple = I. Adapted from Ref. 51.

The ratio between the ionic radii of the E^{2-} chalcogenide and of the X^- halide is likely determinant in selecting which one of the two structure forms, a hypothesis supported by the existence of the $Pb_3Se_2Br_2$ phase.[45] Indeed, $Pb_4E_3X_2$ appears to be favored if $r_{E^{2-}}/r_{X^-} \approx 1$ ($Se^{2-}/Br^- = 1.01$; $S^{2-}/Cl^- = 1.02$),[45] while $r_{E^{2-}}/r_{X^-} < 1$ favors $Pb_3E_3X_2$ ($S^{2-}/Br^- = 0.94$; $S^{2-}/I^- = 0.84$).[44,61] Notably, in both structures Pb^{2+} is surrounded by 8 anions and S^{2-} features a distorted octahedral coordination.

Conversely, the coordination of halides changes: in $Pb_3S_2Cl_2$ the smaller Cl^- ions share the same octahedral coordination as S^{2-}, while the larger Br^- and I^- ions in $Pb_4S_3X_2$ are surrounded by 7 Pb^{2+} ions in a pentagonal bipyramidal configuration. The reason is likely that bulkier anions can accommodate an enlarged coordination environment. Interestingly, $Pb_3S_2Cl_2$ is the first reported chalcohalide where Cl^- is coordinated by an octahedron of Pb^{2+} ions. Such coordination has been recently proposed on the surface of PbS nanocrystals synthesized in excess of $PbCl_2$ to account for the formation of a Cl-rich shell that improves the optical properties,[39,58–60] suggesting that these nanocrystals might be passivated by a layer of some lead sulfochloride compound.

4.2.5 Demonstrative applications of $Pb_4S_3Br_2$ nanocrystals.

The optoelectronic properties of lead chalcohalide nanocrystals will be discussed in depth in Chapter 5 of this thesis, in conjunction with those of other related materials. Nevertheless, here are summarized some preliminary results that motivated testing $Pb_4S_3Br_2$ nanocrystals as the photoactive material in demonstrative devices. All three synthesized sulfohalides absorb visible light: the onset of their absorption spectrum falls between the wide gap energies of PbX_2 (> 2.41 eV)[62,63] and the small gap energy of PbS (0.41 eV),[64,65] that are the terminal binary compounds of the ternary Pb-S-X system (Figure 4.4a). The absorption of samples fades towards lower energies and becomes negligible after ~650 nm (1.9 eV), causing these materials to appear red. The featureless absorption profile of lead sulfohalides points to their nature of indirect gap semiconductors, that was later confirmed by Tauc plot analysis (see Chapter 5).

Consistently, no significant photoluminescence was detected at room temperature in the range 500 – 1700 nm.

Now focusing on $Pb_4S_3Br_2$, calculations performed at the DFT/PBE level of theory and including spin-orbit coupling (SOC) confirmed its nature of indirect semiconductor, and estimated an energy gap of ~1.5 eV, smaller than the absorption spectrum would suggest (Figure 4.4b). However, the PBE functional is known to underestimate the bandgap for extended systems, due to a strongly localized hole.[66] In this case, the spin-free bandgap value is a better approximation to the experimental bandgap as a consequence of error cancellation.[67] Indeed, the band gap computed without SOC lied at 1.98 eV, closer to the absorption spectrum onset located at 1.9 eV. The calculated Density of States (DOS) highlights that the main contribution to the band-edge states comes from Pb and S, while the Br-related states are mainly located deeper below the valence band edge (Figure 4.4b). Interestingly, the absorption spectrum of $Pb_4S_3Br_2$ nanocrystals appears to be unaffected by their size within our tunability range (7-16 nm), suggesting that quantum confinement effects are negligible for this material (Figure 4.17).

The energy gap values of lead sulfohalides encouraged testing them in photosensitive devices. Given the comparable optical properties, we decided to focus only on $Pb_4S_3Br_2$ nanocrystals as a test material, on which we performed basic stability tests. The nanocrystals were stored at room temperature in the dark, both as a diluted colloidal suspension in toluene and as dry powders. No difference was found in the absorption spectra and XRPD patterns after two months (Figure 4.18). We then evaluated the surface passivation of $Pb_4S_3Br_2$ nanocrystals. Fourier Transform Infrared (FTIR, Figure

4.19) spectroscopy demonstrated that as-prepared samples were passivated by a variety of moieties: oleic acid and oleylamine (C-H stretching and bending, C=O stretching, C-N stretching), and thiocyanate (SCN$^-$ stretching).[4,68,69] The presence of long-chain ligands is unfavorable for fabricating working devices, as they reduce the nanocrystal film conductivity. Therefore, we attempted two ligand exchange procedures by using alternatively NH_4SCN or 1-ethyl-3-methylimidazolium iodide. FTIR performed on treated films demonstrated that the exchanges were successful, as the long-chain ligands were replaced by shorter ones. We applied these procedures to fabricate a photoconductor device based on $Pb_4S_3Br_2$ nanocrystals, that demonstrated a very low dark current ($I_{dark} <$ 1 pA at 20 V) and a photocurrent of $I_{photo} \approx$ 10 nA under white light illumination (400-750 nm, 100 mW/cm^2, Figure 4.5c), for a Normalized Photocurrent to Dark current Ratio of NPDR = R/I_{dark} = (8.5 ± 2.8)·10^5 mW^{-1}.[70] The device responsivity was $R = I_{photo}/P_{opt}$ = 4 ± 1 mA/W (P_{opt} = optical power on the device).[71]

After the photoconductor, we tested a solar cell by depositing on a ITO/glass substrate some aluminum-doped zinc oxide (AZO) as the electron transport layer, $Pb_4S_3Br_2$ nanocrystals as a photoactive layer, MoO_x as buffer layer, and Au as top contact (Figure 4.5d,e). With this configuration, the solar cells showed a power conversion efficiency of PCE = 0.21 ± 0.02%, a short-circuit current density of J_{sc} = 1.09 ± 0.07 mA/cm^2, and an open-circuit voltage of V_{oc} = 0.58 ± 0.03 V under a standard AM1.5G illumination (Figure 4.5f). The solar cells also demonstrated a good stability under environmental conditions atmosphere, retaining 60% of their PCE after two months of storage.
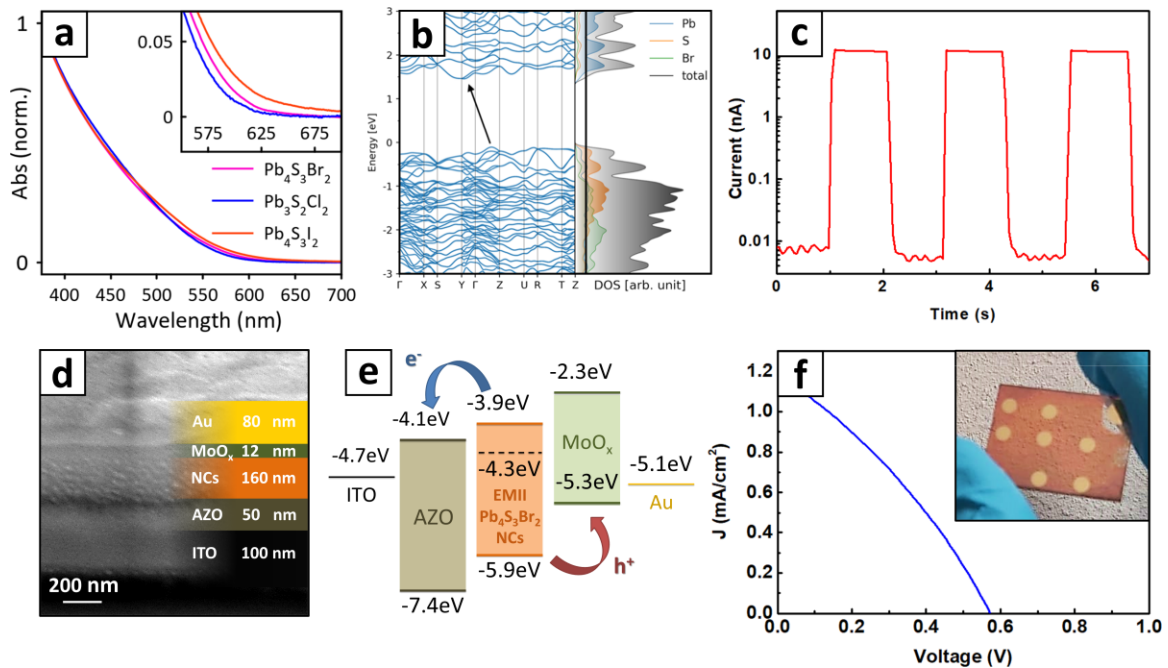
Figure 4.4. Demonstrative applications of Pb₄S₃Br₂ nanocrystals.
a) Absorption spectra of Pb₃S₂Cl₂, Pb₄S₃Br₂, and Pb₄S₃I₂ nanocrystals compared. b) Band structure and element-labelled DOS computed for Pb₄S₃Br₂ at the DFT/PBE level of theory, including SOC. c) Current response during light on/light off cycles of a photodetector device based on Pb₄S₃Br₂ nanocrystals. d) SEM cross-section of a solar cell stack based on Pb₄S₃Br₂ nanocrystals. e) Energy level alignment in the stack. (f) Solar cell current–voltage curve under AM1.5G illumination. Inset: photograph of a Pb₄S₃Br₂-based solar cell. Adapted from Ref. 50.

Compared with state-of-the-art nanocrystal-based devices, neither the photoconductor not the solar cell excelled in performances. For example, responsivity in lead-halide perovskites photoconductors exceeds 10^6 A/W, and even early results with CdE (E = S, Se, Te) reached 200 mA/W.[72–74] Nevertheless, the obtained NPDR was comparable to that of metal/semiconductor/metal devices and nanomembrane-enhanced Ge-detectors,[75] and was better than devices based on semiconductor/CNT,[76] semiconductor/graphene,[77] and nanostructured silicon,[78] typically featuring values of

~10^4 mW^{-1}. This result was due to the very low dark current, suggesting that $Pb_4S_3Br_2$-based devices might be useful when a very low power consumption is needed. As for the solar cell, the PCE is far from the results achieved with $CsPbI_3$ (13.4%),[79] or CdTe nanocrystals (11.6%).[80] This considered, $Pb_4S_3Br_2$ might be better suited in the role of charge transport layer providing some additional photogeneration[62,63] rather than as the main active layer of a photovoltaic device. In fact, $Pb_4S_3Br_2$ films reached a responsivity comparable to polymers (0.2-0.7 mA/W),[54] which are commonly used as charge transport layers. Nevertheless, these preliminary results are enough to justify further investigations in these and similar nanocrystals as potential upcoming optoelectronic materials.

4.3 Polymorphism in Bismuth Chalcohalides

A diversion toward bismuth chalcohalides might appear out of place in a thesis devoted to lead-based semiconductors. However, this side-project shows of how the structure of unknown nanocrystals, that was challenging to obtain for lead chalcohalides, can be solved using only XRPD if suitable conditions are met. Moreover, it provides an example of nanoscale-exclusive polymorphism, that as we discussed in the introduction to this chapter is the most common source for novel structures at the nanoscale.

In contrast with the still little explored lead chalcohalides, bismuth ones are rather well known. More than 10 different stoichiometries have been reported within the Bi-E-X ternary system, the most investigated being BiEX and $Bi_{13}E_{18}X_2$. Those materials have also been reported at the nanoscale, mostly in form of iodine-based nanowires or nanorods.[25,29–33,81] My interest in bismuth chalcohalides dates back to 2020, when Dr.

Carlo Giansante and Dr. Danila Quarta from CNR-Nanotech developed a flexible colloidal synthesis for BiSX nanocrystals (X = Cl, Br, I), and I was invited to collaborate on the structural characterization of the products. For this purpose, with the help of colleagues at the IC-CNR we collected and analyzed XRPD and PDF data at the NSLS-II synchrotron. Bromine- and iodine-based nanocrystal samples were quickly identified as BiSBr and BiSI, and their structure was fully compatible with that reported in bulk (Figure 4.20, data not shown for BiSI).

The case of bismuth sulfochloride proved more challenging. The synthesis yielded a yellow colloidal suspension, that was composed of nanoribbons largely variable in length (~200-1500 nm) but with a rather defined width (~25 nm, Figure 4.5a). Interestingly, their XRPD pattern (Figure 4.5b) did not match with any reported Bi-S-Cl structure (BiSCl, $Bi_4S_5Cl_2$, $Bi_{6+x}S_{6+3x}Cl_{6-3x}$).[82–84] Moreover, the SEM-EDXS analyses indicated an elemental ratio of Bi:S:Cl = 1:1.2:1.4, that could be compatible with Cl/S-terminated BiSCl nanocrystals, but was far enough from the ideal 1:1:1 stoichiometry to raise suspects. These circumstances pointed either to a case of BiSCl polymorphism or to the discovery of a completely new compound, and called for a structure solution.

Unlike lead chalcohalides however, the relatively large size of Bi-S-Cl nanoribbons limited the finite size diffraction broadening. Moreover, the XRPD profile (Figure 4.5b) featured relatively few and well-resolved Bragg peaks. This is not necessarily a signature of a high-symmetry phase: think of the monoclinic $Pb_3S_2Cl_2$, where the PXRD pattern apparently contained only few peaks due to a very mild deviation from the cubic symmetry (see Figure 4.2d). Nevertheless, it is an optimal condition to attempt the

pattern indexation. This process was performed with the software EXPO2014, and differently from the case of Pb-chalcohalides, it successfully identified a list of unit cell candidates. The best matching option was an orthorhombic cell with parameters a = 7.91 Å; b= 9.14 Å; c = 4.10 Å, whose volume was very close to that of the unit cell of bulk BiSCl (296 Å^3 vs 309 Å^3). This is a good hint of a case of polymorphism, as the density of two polymorphs cannot be too different.

The systematic absences were compatible with the space group Pnma, that is curiously the same as bulk BiSCl. Assuming this space group as correct, we proceeded with the extraction of integrated intensities and the subsequent structure solution, which eventually led to one plausible candidate with stoichiometry 1:1:1 and a connectivity remarkably similar to bulk BiSCl. This solution seemed plausible, but had to be evaluated with care. In fact, the intensity of diffraction peaks can be severely altered if crystallites are anisotropic or adopt a preferred orientation within the sample. These were realistic pitfalls, as our nanocrystals were strongly elongated. We therefore proceeded to a combined Rietveld (Figure 4.5b) and PDF refinement, where the good match with experimental data proved the solution correct. The refined structure model is shown in Figure 4.5c, compared with that reported for bulk BiSCl.

Like in the bulk structure, BiSCl nanocrystals were formed by neutral $[(BiSCl)_2]_\infty$ ribbons held together by electrostatic interactions. The two polymorphs are differentiated by their arrangement, as shown in Figure 4.5c. DFT calculations confirmed the stability of the novel polymorph, indicating an energy difference of only 10.5 meV atom^{-1} between the two structures. It is unclear however why the colloidal

synthesis led to its formation in first place. Possible explanations are kinetic factors in the growth of nanocrystals (*e.g.*, the ribbons nucleate individually in solution and then assemble), stabilization effects due to the influence of surface termination, or an anisotropic relaxation of the structure made possible by the limited crystal size.
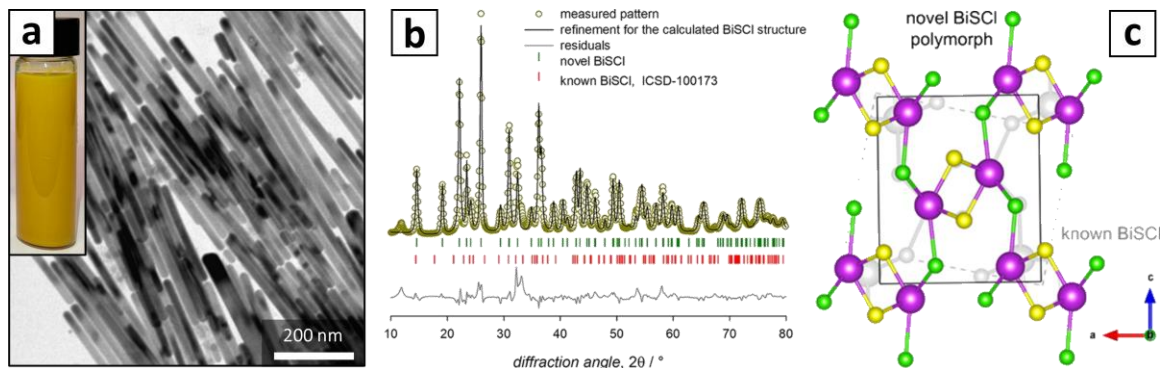
Figure 4.5. Polymorphism in bismuth chalcohalide nanocrystals. a) TEM image of BiSCl nanocrystals. Inset: suspension of BiSCl nanocrystals. b) Rietveld fit of the XRPD data based on the structure solution model, and comparison with the reflection list of the bulk BiSCl structure. c) Superimposed structures of both the bulk (grey) and the disclosed (colored) BiSCl polymorphs. Atoms color code: Bi = purple; S = yellow; Cl = green. Adapted from Ref. 19.

4.4 Conclusions

This chapter provided three case-studies where the structure of an unknown nanomaterial was solved: $Pb_4S_3Cl_2$, $Pb_3S_2Cl_2$ and BiSCl. While the task was the same, differences in experimental conditions, in the prior knowledge about the materials, and in their intrinsic structure required different solution strategies, and provided a broad overview of possible pitfalls and solutions. Here I summarized some key observations, divided by the solution step they refer to.

4.4.1 Sample preparation and data collection

Nanocrystal samples used for a structure solution procedure should be phase pure and well purified. The main reason is ensuring that the composition determined experimentally is as close as possible to the material stoichiometry, and that all diffraction features seen in XRPD belong to the material of interest. It is not trivial to understand whether a sample satisfies these conditions, since no reference stoichiometry or diffraction pattern are available for an unknown material. However, impurities might be spotted by looking for particles with obviously different morphology in TEM, as different materials might produce different shapes and sizes. Also, if a known compound forms as an impurity, it might be still identified by matching the XRPD diffractogram with a database. Ideally, synthesis conditions should be optimized to obtain nanocrystals as large as possible. Larger nanocrystals facilitate 3D-ED experiments and mitigate finite-size broadening effects, facilitating the structure solution from XRPD data. Moreover, larger nanocrystals have a lower surface/volume ratio, that decreases the influence of surface termination on their composition.

Finally, it is crucial that diffraction data are collected properly. For 3D-ED, this means identifying an isolated nanoparticle that is single-crystalline in nature and is large enough to provide reliable data upon intensity integration. A safe threshold is ~50 nm, but smaller nanocrystals might still provide usable data. For XRPD and PDF, samples must be prepared so to minimize preferred orientation effects, as they would alter the experimental intensity of peaks in the diffractogram. Ideally, this is achieved by measuring in transmission a sample placed inside a rotating capillary. If such geometry is not

available, samples should be prepared in the form of dry powders, grinded in a mortar and compressed in a flat pellet. Drop cast of solutions must be avoided, as the slow evaporation of solvents promotes the orientation of nanocrystals and even the formation of superlattices. Finally, if data are collected with variable width slits or variable counting times, proper corrections must be applied.

4.4.2 Determining the stoichiometry

The stoichiometry of a material decides the content of its unit cell: its determination is a fundamental step in the structure solution process, especially when based on XRPD only. Here, a combination of different techniques (SEM/TEM-EDXS, XPS, XRF, ICP-OES/MS, TGA+XRPD) can be beneficial to avoid misinterpretation or interferences. Another important, yet no trivial step is interpreting the experimental result. Candidate stoichiometries must be chemically reasonable: for example, in ionic or partially ionic compounds the stoichiometry must ensure the charge balance. However, this might not be enough: for example, the composition we measured by XPS for $Pb_4S_3Br_2$ nanocrystals (Pb:S:Br = 43:32:25) was compatible within a reasonable error with $Pb_3S_2Br_2$, $Pb_7S_5Br_4$ and $Pb_{10}S_7Br_6$ as well, that are all valid stoichiometries. There is no real solution to this problem, and all options should be considered possible until the next steps disproof all but one.

4.4.3 Cell indexation, symmetry determination, and structure solution

The cell indexation is arguably the most critical step of the structure solution process, as it is at the same time the most challenging and the most informative. The best

option is performing a 3D-ED experiment, that by reconstructing the full reciprocal lattice is ideal to identify a suitable unit cell. However, 3D-ED is not a widely available technique, and requires relatively large nanocrystals. If these can be obtained but 3D-ED is not available, electron diffraction data or HRTEM images collected on nanocrystals that spontaneously orient along a specific zone axis might provide useful information on the nanocrystal symmetry. Alternatively, a cell might be extracted by indexing XRPD data. This procedure however might be challenging or even impossible for small nanocrystals and/or low-symmetry phases. Here is where additional information from electron diffraction or HRTEM could come in handy, as even identifying some of the symmetry operations and measuring few unit cell parameters greatly narrows the parameters space for indexation.

The space group is again best identified by 3D-ED through the analysis of systematic extinctions. If not available, XRPD can be used as well. However, in case of low symmetry structures or small nanocrystals the overlap of reflections might prevent from uniquely identify the space group, leaving with a list of candidates. This, combined with multiple unit cell choices deriving from a possibly uncertain indexation can result in quite a long list of options. Such list can be limited by ranking the candidates by consistency between the experimental and predicted peak positions and extinctions, a step that is done automatically by most XRPD-based structure solution programs. After that, the only option is attempting a structure solution for each top candidate, and evaluate the plausibility of the resulting structure models. However, if unit cell and space group are reliably determined, the chances of a successful structure increase dramatically.

First, the combination of unit cell volume and space group narrow down the possible stoichiometries. For example, for $Pb_4S_3Br_2$ we found a unit cell with volume 975 $Å^3$ and Z = 4 (number of asymmetric units, depends on the space group). For it to be correct, the unit cell must be large enough to contain 4×(4+3+2) = 36 atoms that, considering the ~30 $Å^3$/atom typical of inorganic solids, equals 1080 $Å^3$. This is a reasonable value, as opposed for example to the 1920 $Å^3$ for a hypothetical $Pb_7S_5Br_4$ stoichiometry, that can be discarded. Second, once the unit cell is known the position of diffraction peaks can be predicted, and the extraction of intensities from XRPD is likely to succeed even in case of peak overlap. Once the reflection intensities have been extracted, be it by 3D-ED or by XRPD, they are fed to the structure solution algorithms. Those are largely automated, and for small cells containing heavy elements, like many inorganic compounds, they are likely to converge on a solution if the extracted intensities are reliable.

4.4.4 Structure refinement

The previous structure solution step relies on the determination of reflection intensities, that both in the case of 3D-ED and XRPD might be altered by other factors than the position of atoms within the structure. For example, 3D-ED can be affected by secondary scattering phenomena or by data of suboptimal quality. On the other hand, integrated peak intensities in XRPD can be affected by the anisotropic shape of crystallites and/or by preferred orientation effects. For these reasons, after the structure solution it is advisable to perform a refinement step that keeps into account microstructural effects.

We also found beneficial alternating Rietveld refinements with PDF refinements, as the short-range section of the PDF profile is less affected by anisotropic morphologies, and optimizing the structure on dataset different the one used for the XRPD-based solution might prevent the refinement from converging to a false local minimum. Finally, applying total scattering techniques like PDF at the refinement stage allows to take advantage of the diffuse scattering that is neglected by the ab-initio structure solution and Rietveld refinement procedures, potentially leading to more accurate results.

Finally, the solution procedure might produce a candidate structure that performs poorly at the refinement stage, like the cubic *I-4*3d model produced by 3D-ED for $Pb_3S_2Cl_2$. In this case, it might be worth lowering the structure symmetry to a subgroup of the starting space group, and check if that improves the match. Indeed, this gives a chance to capture mild distortions that might have gone undetected in first place.

4.5 Methods

This section summarizes the methods adopted for the experiments and analyses discussed in this chapter. For brevity, only the most relevant information is reported. For additional details, please refer to the original open-access publications [Refs. 19,50,51].

4.5.1 Synthesis methods

<u>Thiocyanate heat-up synthesis of $Pb_4S_3X_2$ nanocrystals.</u> 0.2 mmol of PbX_2 and 0.2 mmol of $Pb(SCN)_2$ where dissolved in a mixture of 10 mL 1-octadecene (ODE), 250 μL of oleylamine (OLA) and 250 μL of oleic acid (OA) at 120°C in a 25 mL three-necked flask. The solution was quickly heated (~20°C/min) and started turning from light-yellow to dark red above 150°C while the nanocrystals nucleated and grew. The reaction was quenched by cooling the flask in a water bath; size control was achieved by varying the maximum temperature reached before quenching. Nanocrystals were recovered by centrifugation or by ethyl acetate-assisted precipitation followed by centrifugation (6000 rpm for 5 min in both cases) depending on their size. All the syntheses were performed in air, without pre-drying chemicals or solvents.

<u>S-ODE injection synthesis of $Pb_3S_2Cl_2$ nanocrystals.</u> A S-ODE stock solution was prepared by mixing 0.064 g (2 mmol) of S powder with 10 mL of ODE (pre-degassed at 120 °C under vacuum for an hour) in a 20 mL glass vial inside a glove box filled with N_2. The resulting mixture was sonicated until the complete dissolution of the sulfur powder. For the synthesis of $Pb_3S_2Cl_2$ nanocrystals, 0.21 g of $PbCl_2$ (0.8 mmol) were solubilized at 120 °C in a mixture of 2 mL of OLA, 2 mL of OA, and 20 mL of ODE in a 100 mL flask. The solution

was then heated up to 170 °C, and 2 mL of the S-ODE stock solution, pre-heated at 150 °C, were swiftly injected. The nanocrystals formed ~10-30 s after the injection, as revealed by the color change of the solution from pale yellow to red. After 1 min, the reaction was quenched by cooling the flask with a room-temperature water bath. The nanocrystals were recovered by adding 40 mL of ethyl acetate, followed by a centrifugation at 6000 rpm for 5 min.

<u>Seeded growth of $Pb_4S_3Br_2$ and $Pb_3S_2Cl_2$ nanocrystals.</u> A stock solution of reagents was prepared by dissolving PbX_2 ($Pb_4S_3Br_2$ = 0.6 mmol, $Pb_3S_2Cl_2$ = 0.8 mmol) and $Pb(SCN)_2$ ($Pb_4S_3Br_2$ = 0.6 mmol, $Pb_3S_2Cl_2$ = 1.6 mmol) in a mixture of 30 mL of ODE, 750 μL OLA and 750 μL OA in a 100 mL flask at 120°C. Once the two solids dissolved, the stock solution was cooled to room temperature, filtered with a 0.2 μm PTFE syringe filter, and loaded on a syringe pump. Then, 11 mL ($Pb_4S_3Br_2$) / 12 mL ($Pb_3S_2Cl_2$) of a crude nanocrystal reaction mixture (thiocyanate route for $Pb_4S_3Br_2$, S-ODE route for $Pb_3S_2Cl_2$) were heated to 170 °C, and the stock solution of PbX_2 and $Pb(SCN)_2$ was added dropwise at a controlled rate of 5 mL/h ($Pb_4S_3Br_2$) / 10 mL/h ($Pb_3S_2Cl_2$). Finally, the reaction mixture was centrifuged, and the product washed with ethyl acetate and resuspended in toluene or hexane. For $Pb_4S_3Br_2$, a subsequent decantation step was performed to remove the nanoplatelets that were formed, which remained in the supernatant. For $Pb_3S_2Cl_2$, an additional filtration with a 0.2 μm PTFE syringe filter was performed to remove the large PbS impurities.

<u>BiSX nanocrystal synthesis.</u> In a typical synthesis of BiSBr nanocrystals, 0.3 mmol of Bi(Ac)3 and 3 mmol of OA were mixed in 3 g of ODE. The mixture was degassed through repeated

vacuum and nitrogen cycles at about 80 °C, and then heated to 110°C to dissolve Bi(Ac)$_3$ until the solution became colorless and optically transparent. After that, the solution was cooled to 80 °C and again subjected to vacuum to remove the acetic acid released by the formation of bismuth(III)-oleate complexes. The solution was then heated again to 180°C under nitrogen, and half equivalent of (Me$_3$Si)$_2$S (0.15 mmol = 32 µL) and one equivalent of benzoyl bromide (BzBr, 0.3 mmol = 35 µL) in 2 mL of ODE were swiftly co-injected. The reaction proceeded for 15 minutes, then the heating mantle was removed, and the reaction was quenched by immersing the flask in an ice bath. The product was recovered by centrifugation and redispersed in toluene. BiSCl, and BiSI nanocrystals were obtained by replacing the halogen precursor with benzoyl chloride (BzCl) or benzoyl iodide (BzI). BiSCl nanocrystals were synthesized by co-injecting (Me$_3$Si)$_2$S and BzCl; we note that the lower reactivity of BzCl compared to BzBr required the use of 0.5 mmol of BzCl to obtain BiSCl. BiSI nanocrystals were synthesized by co-injecting (Me$_3$Si)$_2$S and BzI; we note that the higher reactivity of BzI compared to BzBr required the use of 0.15 mmol of BzI to obtain BiSI. BzI was obtained by reacting BzCl with an excess (1.5 equivalents) of NaI at 80 °C for five hours.

4.5.2 Electron microscopy characterization methods

3D-ED and nanocrystal structure solution. 3D-ED data from Pb$_4$S$_3$Br$_2$ and Pb$_3$S$_2$Cl$_2$ nanocrystals were collected on a Zeiss Libra TEM operating at 120 kV and equipped with a LaB$_6$ source. Data were acquired in STEM mode after defocusing the beam to achieve a parallel illumination. A beam size of about 150 nm in diameter was obtained by inserting

a 5 μm C2 condenser aperture. A mild illumination was adopted to avoid any alteration or amorphization of the sample, and to slow down the accumulation of organic contaminants. 3D-ED data were recorded with an ASI Timepix detector, which is sensitive to single electrons and delivers a pattern that is virtually background-free.[85] The camera length was 180 mm, with a theoretical resolution limit of 0.75 Å. 3D-ED data from $Pb_4S_3Br_2$ nanoplatelets were collected with a precessing beam obtained by a Nanomegas DIGISTAR P1000 device, while the sample was tilted in fixed steps of 1° for a total range up to 70°.[86,87] 3D-ED data were analyzed using ADT3D[88] and PETS[89] for cell and space group determination. The intensity integration for the structure determination was performed with PETS, using the standard integration and interpolation options. The *ab initio* structure solution was obtained using direct methods implemented in the software SIR2014.[90] Data were treated within the kinematic approximation: $I_{hkl} \propto F^2_{hkl}$.

HAADF-STEM imaging and atomic resolution electron tomography. HAADF-STEM analyses were performed with a probe-corrected Thermo Fisher Titan microscope operating at 300 kV, with a semi-convergence angle of 20 mrad. For the 3D tomography of $Pb_4S_3Br_2$ nanocrystals, a tilt series of atomically resolved projection images was acquired on a single nanocrystal from -70° to +70°, with a tilt increment of 2°. To minimize the drift and compensate for scanning distortions during the acquisition, a series of images with a short dwell time was acquired at each tilt angle. Data restoration and registration were necessary before the tilt series could be aligned with respect to a common tilt axis. The first step was restoring the individual images of the time series by using a convolutional neural network.[91] Next, these images were used as an input for a rigid and nonrigid

average registration procedure.[91] After an iterative alignment based on the phase correlation method, the tilt series was reconstructed using the simultaneous iterative reconstruction technique algorithm.[92] The so-obtained reconstruction yielded atomic resolution data which were converted into a 3D representation of the reciprocal space by calculating a Fourier Transform. From this 3D-FT, a 3D mask matching with the 3D-ED diffraction pattern corresponding to the nanocrystals was built, from which the unit cell parameters were extracted.

4.5.3 XRPD and PDF characterization methods

<u>Lab-grade XRPD data collection.</u> Lab-grade XRPD analyses were performed in θ:2θ scan mode on a Panalytical Empyrean diffractometer, equipped with a 1.8 kW Cu-K$_\alpha$ ceramic anode working at 45 kV-40 mA and a PIXcel[3D] detector. XRPD data were acquired on samples in the form of dry powders or drop-casted solutions; the measurements were carried out in air at room temperature using a zero-diffraction silicon substrate.

<u>Synchrotron XRPD and PDF data collection.</u> Synchrotron diffraction data were collected at the 28ID-2 beamline of the National Synchrotron Light Source (NSLS-II) of the Brookhaven National Laboratory with an X-ray energy of 67-68 keV (variable from session to session, exact values were noted for each measurement) and a 0.5 mm × 0.5 mm beam size. A Perkin Elmer XRD 1621 digital imaging detector (2048 × 2048 pixels and 200 × 200 μm pixel size) was mounted orthogonal to the beam path in two positions: ~230 mm and ~1370 mm downstream of the sample (variable from session to session, exact values were noted for each measurement). All samples were mounted inside 1 mm spinning

capillaries and measured in both setups, optimized for PDF and XRPD measurements respectively. Nickel or lanthanum hexaboride (LaB$_6$) standards were measured to calibrate the wavelength and the detector geometry, including the sample-to-detector distance. An empty capillary was measured for background estimation. Diffraction images were azimuthally integrated and converted into intensity profiles vs 2θ and vs momentum transfer $q = 4\pi \sin \vartheta / \lambda_{X-ray}$ by using the FIT2D program.[93] PDF profiles were calculated up to interatomic distances *r* of 50 Å from the *Q* profiles with the program PDFGetX3.[94] The parameters for PDF calculation (background subtraction scale factor, minimum and maximum values of *Q*, degree of data-correction polynomial) were optimized on individual PDF profiles, to avoid large termination effects and preserve the signal to noise ratio. The Q_{max} values were 23.7 Å^{-1} for Pb$_3$S$_2$Cl$_2$, 22.0 Å^{-1} for Pb$_4$S$_3$Br$_2$ and Pb$_4$S$_3$I$_2$, 23.2 Å^{-1} for BiSBr and 28.8 Å^{-1} for BiSCl, respectively.

XRPD-based structure solution. The *ab initio* structure solution from XRPD data was carried out using EXPO2014.[55] The full pattern decomposition process relies on a Le Bail fit where unit cell parameters belong to the set of refined variables. The resulting integrated intensities were automatically supplied to Direct Methods[95] to carry out the structure solution step, implemented in the form of an automatic procedure that provides a set of twenty candidate structure models. Among them, the most plausible one, that are those satisfying the main crystallochemical rules, was recognized by visual inspection of the structure *via* graphical interface. This procedure was applied to Pb$_4$S$_3$Br$_2$, Pb$_3$S$_2$Cl$_2$, and BiSCl nanocrystals with minor differences. Only, the pattern indexation for BiSCl was performed *ab initio* prior to the Le Bail fit using the software *N*-TREOR09,[54] which is

implemented in EXPO2014, while for $Pb_4S_3Br_2$ and $Pb_3S_2Cl_2$ the starting unit cell parameters were provided by 3D-ED, and subsequently optimized during the Le Bail fit procedure.

Combined Rietveld + PDF refinement. Both XRPD and DFT data were exploited to refine the structures of $Pb_3S_2Cl_2$, $Pb_4S_3Br_2$, $Pb_4S_3I_2$, BiSBr, and BiSCl nanocrystals by alternating the refinement in the direct (PDF) and reciprocal (XRPD) spaces. To analyze the PDF profiles, the PDFGUI[96–98] and DiffPy-CMI[16] software packages were used. At this stage, Rietveld fits were performed using the automated refinement procedure implemented in EXPO2014. Refined parameters were, in this order: zero-shift; background parameters; scale factor; peak profile parameters; crystal structure parameters; anisotropic spherical harmonics parameters for the crystallite shape. In the last step of the refinement, all parameters were simultaneously refined. In most cases, a last manual Rietveld refinement step was performed with the FULLPROF suite,[99] that provides a better control over the microstructural parameters of the sample. Refined parameters were (according to the need of each fit): scale factor, multiple points linear interpolation background, unit cell parameters, isotropic or anisotropic crystallite size (spherical harmonics), atomic coordinates, and thermal factors (isotropic normally, anisotropic if needed). The instrumental resolution function for the diffractometer was obtained by fitting the XRPD pattern of a LaB_6 standard.[100]

PDF refinements were executed for interatomic distances above 1.5 Å, to avoid finite-size artifacts in the low r range, and up to 45 Å, with a step of 0.01 Å. As a first step, the scale factor, lattice parameters, peak shape parameters Q_{broad} (peak broadening from

increased intensity noise at high Q) and δ_1 (coefficient for the 1/r contribution to the peak

sharpening) parameters were refined separately. As a second step, anisotropic atomic

displacement parameters were included in the refinement, then the atomic position

parameters were refined in a last step. More elaborated refinements were carried out by

using scripts developed within the DiffPy-CMI framework,[16] which implements

procedures able to refine the shape of nanocrystals.

4.6 Source Publications and Contributions

This chapter is based on the following publications:

I. **Toso, S.***; Akkerman, Q. A.*; Martín-García, B.*; Prato, M.; Zito, J.; Infante, I.; Dang, Z.; Moliterni, A.; Giannini, C.; Bladt, E.; Lobato, I.; Ramade, J.; Bals, S.; Buha, J.; Spirito, D.; Mugnaioli, E.; Gemmi, M.; Manna, L. _Nanocrystals of Lead Chalcohalides: A Series of Kinetically Trapped Metastable Nanostructures_. J. Am. Chem. Soc. 2020, 142, 10198–10211. [Ref. 50]

II. **Toso, S.***; Imran, M.*; Mugnaioli, E.; Moliterni, A.; Caliandro, R.; Schrenker, N. J.; Pianetti, A.; Zito, J.; Zaccaria, F.; Wu, Y.; Gemmi, M.; Giannini, C.; Brovelli, S.; Infante, I.; Bals, S.; Manna, L. _Halide Perovskites as Disposable Epitaxial Templates for the Phase-Selective Synthesis of Lead Sulfochloride Nanocrystals_. Nat. Commun. 2022 131 2022, 13, 1–10. [Ref. 51]

III. Quarta, D.*; **Toso, S.***; Giannuzzi, R.; Caliandro, R.; Moliterni, A.; Saleh, G.; Capodilupo, A.-L.; Debellis, D.; Prato, M.; Nobile, C.; Maiorano, V.; Infante, I.; Gigli, G.; Giannini, C.; Manna, L.; Giansante, C. _Colloidal Bismuth Chalcohalide Nanocrystals_. Angew. Chemie 2022, e202201747. [Ref. 19]

*_These authors contributed equally_

Publication (I) reports the synthesis of $Pb_3S_2Cl_2$, $Pb_4S_3Br_2$ and $Pb_4S_3I_2$ nanocrystals via the thiocyanate heat-up route, describes the structure solution process for $Pb_4S_3Br_2$, contains the preliminary optoelectronic characterizations and DFT calculations on all the three materials, and reports the fabrication and performances of the test devices based on $Pb_4S_3Br_2$ nanocrystals. **Publication (II)** reports the synthesis of $Pb_3S_2Cl_2$, _via_ S-ODE injection route, describes the structure solution process for $Pb_3S_2Cl_2$ and the synchrotron-based structure refinement for all the three materials, and discusses in more detail their structural differences. **Publication (III)** reports the synthesis of colloidal bismuth chalcohalide nanocrystals and describes the identification and structure solution of the BiSCl polymorph. The synthetic protocol reported in this publication is subject of a patent

application entitled "*Process for the Production of Nanocrystals of Metal Chalcohalides*", IT 102022000001577, inventors Carlo Giansante, Danila Quarta, Stefano Toso, Roberto Giannuzzi, Rocco Caliandro, Anna Moliterni, Cinzia Giannini, Liberato Manna, Giuseppe Gigli.

4.7 Copyright

Some elements of this chapter were adapted from external sources:

4.8 Bibliography

1. Tappan, B. A. & Brutchey, R. L. Polymorphic Metastability in Colloidal Semiconductor Nanocrystals. *ChemNanoMat* **6**, 1567–1588 (2020).

2. Dinega, D. P. & Bawendi, M. G. A solution-phase chemical approach to a new crystal structure of cobalt. *Angew. Chemie - Int. Ed.* **38**, 1788–1791 (1999).

3. Tappan, B. A. *et al.* Crystal Structure of Colloidally Prepared Metastable Ag_2Se Nanocrystals. *Nano Lett.* **21**, 5881–5887 (2021).

4. Akkerman, Q. A. *et al.* Ultrathin Orthorhombic PbS nanosheets. *Chem. Mater.* **31**, 8145–8153 (2019).

5. Norako, M. E., Greaney, M. J. & Brutchey, R. L. Synthesis and characterization of wurtzite-phase copper tin selenide nanocrystals. *J. Am. Chem. Soc.* **134**, 23–26 (2012).

6. Soriano, R. B., Arachchige, I. U., Malliakas, C. D., Wu, J. & Kanatzidis, M. G. Nanoscale stabilization of new phases in the $PbTe-Sb_2Te_3$ System: $Pb_mSb_{2n}Te_{m+3n}$ nanocrystals. *J. Am. Chem. Soc.* **135**, 768–774 (2013).

7.   Soriano, R. B., Wu, J. & Kanatzidis, M. G. Size as a Parameter to Stabilize New Phases: Rock Salt Phases of $Pb_mSb_{2n}Se_{m+3n}$. *J. Am. Chem. Soc.* **137**, 9937–9942 (2015).

8.   Holton, J. M. & Frankel, K. A. The minimum crystal size needed for a complete diffraction data set. *Acta Crystallogr. Sect. D Biol. Crystallogr.* **66**, 393–408 (2010).

9.   Shapiro, D. A. *et al.* X-Ray Powder Diffraction from Sub-Micron Crystals of Photosystem-1 Membrane Protein. (2008).

10.   Ruck, M., Poudeu, P. F. P. & Söhnel, T. Synthese, Kristallstruktur und elektronische Bandstruktur der isotypen Sulfidchloride $CuBiSCl_2$ und $AgBiSCl_2$. *Zeitschrift fur Anorg. und Allg. Chemie* **630**, 63–67 (2004).

11.   Palazon, F. Metal Chalcohalides: Next Generation Photovoltaic Materials? *Sol. RRL* **6**, 2100829 (2022).

12.   Ren, J. *et al.* Conductivity study on GeS_2-Ga_2S_3-AgI-Ag chalcohalide glasses. *J. Appl. Phys.* **114**, 023701 (2013).

13.   Reuter, B. & Hardel, K. Silbersulfidbromid und Silbersulfidjodid. *Angew. Chemie* **72**, 138–139 (1960).

14.   Nitsche, R. & Merz, W. J. Photoconduction in ternary V-VI-VII compounds. *J. Phys. Chem. Solids* **13**, 154–155 (1960).

15.   Fatuzzo, E. *et al.* Ferroelectricity in SbSI. *Phys. Rev.* **127**, 2036–2037 (1962).

16.   Butler, K. T. *et al.* Quasi-particle electronic band structure and alignment of the V-VI-VII semiconductors SbSI, SbSBr, and SbSeI for solar cells. *Appl. Phys. Lett.* **108**, 112103 (2016).

17.   Butler, K. T., Frost, J. M. & Walsh, A. Ferroelectric materials for solar energy conversion: Photoferroics revisited. *Energy Environ. Sci.* **8**, 838–848 (2015).

18.   Ganose, A. M., Savory, C. N. & Scanlon, D. O. Beyond methylammonium lead iodide: prospects for the emergent field of ns^2 containing solar absorbers. *Chem. Commun.* **53**, 20–44 (2017).

19.   Quarta, D. *et al.* Colloidal Bismuth Chalcohalide Nanocrystals. *Angew. Chemie* **61**, e202201747 (2022).

20. Wlaźlak, E. *et al.* Heavy pnictogen chalcohalides: The synthesis, structure and properties of these rediscovered semiconductors. *Chem. Commun.* **54**, 12133–12162 (2018).

21. Moroz, M. V. & Prokhorenko, M. V. Phase equilibria and thermodynamic properties of saturated solid solutions based on the compounds BiSeI, $Bi_{19}Se_{27}I_3$, and BiI3 in the Ag–Bi–Se–I system. *Inorg. Mater.* **52**, 765–769 (2016).

22. Ganesha, R., Arivuoli, D. & Ramasamy, P. Growth of some group V-VI-VII compounds from the vapour. *J. Cryst. Growth* **128**, 1081–1085 (1993).

23. Li, S. *et al.* Bismuth chalcogenide iodides $Bi_{13}S_{18}I_2$ and BiSI: Solvothermal synthesis, photoelectric behavior, and photovoltaic performance. *J. Mater. Chem. C* **8**, 3821–3829 (2020).

24. Farooq, S. *et al.* High Gain Solution-Processed Carbon-Free BiSI Chalcohalide Thin Film Photodetectors. *Adv. Funct. Mater.* **31**, (2021).

25. Mombrú Frutos, M. *et al.* Understanding the Crystal Growth of Bismuth Chalcohalide Nanorods through a Self-Sacrificing Template Process: A Comprehensive Study. *Inorg. Chem.* **61**, 9231–9241 (2022).

26. Mistewicz, K. *et al.* A simple route for manufacture of photovoltaic devices based on chalcohalide nanowires. *Appl. Surf. Sci.* **517**, 146138 (2020).

27. Nowak, M., Kauch, B. & Szperlich, P. Determination of energy band gap of nanocrystalline SbSI using diffuse reflectance spectroscopy. *Rev. Sci. Instrum.* **80**, 046107 (2009).

28. Balakrishnan, S. K., Parambil, P. C. & Edri, E. Mechanistic Insight into the Topotactic Transformation of Trichalcogenides to Chalcohalides. *Chem. Mater.* **34**, 3468–3478 (2022).

29. Nowak, M., Jesionek, M. & Mistewicz, K. Fabrication techniques of group 15 ternary chalcohalide nanomaterials. in *Nanomaterials Synthesis* 337–384 (Elsevier, 2019).

30. Liu, J., Wu, J., Wang, N., Tian, F. & Li, J. Surface reconstruction of BiSI nanorods for superb photocatalytic Cr(VI) reduction under near-infrared light irradiation. *Chem. Eng. J.* **435**, 135152 (2022).

31. Fa, W. J. *et al.* The competitive growth of BiOI and BiSI in the solvothermal process. *Adv. Mater. Res.* **236**–**238**, 1919–1922 (2011).

32. Lee, J., Min, B. K., Cho, I. & Sohn, Y. Synthesis and characterization of 1-D BiSI and 2-D BiOI nanostructures. *Bull. Korean Chem. Soc.* **34**, 773–776 (2013).

33. Choi, Y. C. & Jung, K. W. Recent Progress in Fabrication of Antimony/Bismuth Chalcohalides for Lead-Free Solar Cell Applications. *Nanomater. 2020, Vol. 10, Page 2284* **10**, 2284 (2020).

34. Lu, H., Carroll, G. M., Neale, N. R. & Beard, M. C. Infrared quantum dots: Progress, challenges, and opportunities. *ACS Nano* **13**, 939–953 (2019).

35. Mcdonald, S. A. *et al.* Solution-processed PbS quantum dot infrared photodetectors and photovoltaics. *Nat. Mater.* **4**, 138–142 (2005).

36. Dey, A. *et al.* State of the Art and Prospects for Halide Perovskite Nanocrystals. *ACS Nano* **15**, 10775–10981 (2021).

37. Akkerman, Q. A., Rainò, G., Kovalenko, M. V. & Manna, L. Genesis, challenges and opportunities for colloidal lead halide perovskite nanocrystals. *Nat. Mater.* **17**, 394–405 (2018).

38. Protesescu, L. *et al.* Nanocrystals of Cesium Lead Halide Perovskites (CsPbX$_3$, X = Cl, Br, and I): Novel Optoelectronic Materials Showing Bright Emission with Wide Color Gamut. *Nano Lett.* **15**, 3692–3696 (2015).

39. Green, P. B. *et al.* PbS Nanocrystals Made Using Excess Lead Chloride Have a Halide-Perovskite-Like Surface. *Chem. Mater.* **10**, 27 (2021).

40. Liu, J. *et al.* Size-tunable near-infrared PbS nanoparticles synthesized from lead carboxylate and sulfur with oleylamine as stabilizer. *Nanotechnology* **19**, 345602 (2008).

41. Wang, Y. *et al.* Shape-controlled synthesis of PbS nanocrystals via a simple one-step process. *Langmuir* **28**, 16436–16443 (2012).

42. Ider, A., Laval, J. P., Frit, B., Carré, J. & Bastide, J. P. Crystal Structure of PbTeF$_6$. *J. Fluor. Chem.* **78**, 15–20 (1996).

43. Krebs, B. Die Kristallstrukturen von Pb$_4$SeBr$_6$, Pb$_5$S$_2$J$_6$ und Pb$_7$S$_2$Br$_{10}$. *ZAAC - J. Inorg. Gen. Chem.* **396**, 137–151 (1973).

44. Ni, D., Guo, S., Yang, Z. S., Powderly, K. M. & Cava, R. J. Pb$_4$S$_3$I$_2$ –A high-pressure phase in the PbS-PbI$_2$ system. *Solid State Sci.* **91**, 49–53 (2019).

45. Ni, D., Guo, S., Powderly, K. M., Zhong, R. & Cava, R. J. A high-pressure phase with a non-centrosymmetric crystal structure in the PbSe–PbBr$_2$ system. *J. Solid State Chem.* **280**, 106–111 (2019).

46. Islam, S. M. *et al.* Direct Gap Semiconductors Pb$_2$BiS$_2$I$_3$, Sn$_2$BiS$_2$I$_3$, and Sn$_2$BiSI$_5$. *Chem. Mater.* **28**, 7332–7343 (2016).

47. Doussier, C., Moëlo, Y., Léone, P., Meerschaut, A. & Evain, M. Crystal structure of Pb$_2$SbS$_2$I$_3$, and re-examination of the crystal chemistry within the group of (Pb/Sn/Sb) chalcogeno-iodides. *Solid State Sci.* **9**, 792–803 (2007).

48. Blachnik, R., Buchmeier, W. & Dreisbach, H. A. Structure of lead(II) dimercury(II) diiodide disulfide. *Acta Crystallogr. Sect. C Cryst. Struct. Commun.* **42**, 515–517 (1986).

49. Biagioni, C. *et al.* Determination of the crystal structure and redefinition of tsugaruite, Pb$_{28}$As$_{15}$S$_{50}$Cl, the first lead-arsenic chloro-sulfosalt. *Can. Mineral.* **59**, 125–137 (2021).

50. Toso, S. *et al.* Nanocrystals of Lead Chalcohalides: A Series of Kinetically Trapped Metastable Nanostructures. *J. Am. Chem. Soc.* **142**, 10198–10211 (2020).

51. Toso, S. *et al.* Halide perovskites as disposable epitaxial templates for the phase-selective synthesis of lead sulfochloride nanocrystals. *Nat. Commun. 2022 131* **13**, 1–10 (2022).

52. Lu, C. *et al.* Cesium Oleate Precursor Preparation for Lead Halide Perovskite Nanocrystal Synthesis: The Influence of Excess Oleic Acid on Achieving Solubility, Conversion, and Reproducibility. *Chem. Mater.* **31**, 62–67 (2019).

53. Almeida, G. *et al.* Role of Acid-Base Equilibria in the Size, Shape, and Phase Control of Cesium Lead Bromide Nanocrystals. *ACS Nano* **12**, 1704–1711 (2018).

54. Altomare, A. *et al.* Advances in powder diffraction pattern indexing: N-TREOR09. *J. Appl. Crystallogr.* **42**, 768–775 (2009).

55. Altomare, A. *et al.* EXPO2013: A kit of tools for phasing crystal structures from powder data. *J. Appl. Crystallogr.* **46**, 1231–1235 (2013).

56. Gemmi, M. *et al.* 3D Electron Diffraction: The Nanocrystallography Revolution. *ACS Cent. Sci.* **5**, 1315–1329 (2019).

57. Tenher, V. The sulphohalides of lead. *J. Am. Chem. Soc.* **23**, 680–682 (1901).

58.   Winslow, S. W., Liu, Y., Swan, J. W. & Tisdale, W. A. Quantification of a PbCl$_x$ Shell on the Surface of PbS Nanocrystals. *ACS Mater. Lett.* **1**, 209–216 (2019).

59.   Green, P. B., Li, Z. & Wilson, M. W. B. PbS Nanocrystals Made with Excess PbCl$_2$ Have an Intrinsic Shell that Reduces Their Stokes Shift. *J. Phys. Chem. Lett.* **10**, 5897–5901 (2019).

60.   Brittman, S. *et al.* Effects of a Lead Chloride Shell on Lead Sulfide Quantum Dots. *J. Phys. Chem. Lett.* **10**, 1914–1918 (2019).

61.   Shannon, R. D. Revised Effective Ionic Radii and Systematic Studies of Interatomic Distances in Halides and Chalcogenides. *Acta Crystallogr. Sect. A* **32**, 751–767 (1976).

62.   Plekhanov, V. G. Investigation of the reflectance spectra of PbCl$_2$ and PbBr$_2$ single crystals with orthorhombic structure. *Phys. status solidi* **68**, K35–K38 (1975).

63.   Zhong, M. *et al.* Large-scale 2D PbI$_2$ monolayers: Experimental realization and their indirect band-gap related properties. *Nanoscale* **9**, 3736–3741 (2017).

64.   Saran, R. & Curry, R. J. Lead sulphide nanocrystal photodetector technologies. *Nat. Photonics* **10**, 81–92 (2016).

65.   Moreels, I. *et al.* Size-tunable, bright, and stable PbS quantum dots: A surface chemistry study. *ACS Nano* **5**, 2004–2012 (2011).

66.   Baerends, E. J. Density functional approximations for orbital energies and total energies of molecules and solids. *J. Chem. Phys.* **149**, 054105 (2018).

67.   Giansante, C. *et al.* 'darker-than-black' PbS quantum dots: Enhancing optical absorption of colloidal semiconductor nanocrystals via short conjugated ligands. *J. Am. Chem. Soc.* **137**, 1875–1886 (2015).

68.   Koh, W. K., Saudari, S. R., Fafarman, A. T., Kagan, C. R. & Murray, C. B. Thiocyanate-capped PbS nanocubes: Ambipolar transport enables quantum dot based circuits on a flexible substrate. *Nano Lett.* **11**, 4764–4767 (2011).

69.   Bala, T., Prasad, B. L. V., Sastry, M., Kahaly, M. U. & Waghmare, U. V. Interaction of different metal ions with carboxylic acid group: A quantitative study. *J. Phys. Chem. A* **111**, 6183–6190 (2007).

70.   Chui, C. O., Okyay, A. K. & Saraswat, K. C. Effective dark current suppression with asymmetric MSM photodetectors in group IV semiconductors. *IEEE Photonics Technol. Lett.* **15**, 1585–1587 (2003).

71.   Rosina, I. *et al.* Metastable CdTe@HgTe Core@Shell Nanostructures Obtained by Partial Cation Exchange Evolve into Sintered CdTe Films Upon Annealing. *Chem. Mater.* **32**, 2978–2985 (2020).

72.   Wang, H. & Kim, D. H. Perovskite-based photodetectors: Materials and devices. *Chem. Soc. Rev.* **46**, 5204–5236 (2017).

73.   García De Arquer, F. P., Armin, A., Meredith, P. & Sargent, E. H. Solution-processed semiconductors for next-generation photodetectors. *Nat. Rev. Mater.* **2**, (2017).

74.   Wang, Y., Song, L., Chen, Y. & Huang, W. Emerging New-Generation Photodetectors Based on Low-Dimensional Halide Perovskites. *ACS Photonics* **7**, 10–28 (2020).

75.   Xia, Z. *et al.* Single-crystalline germanium nanomembrane photodetectors on foreign nanocavities. *Sci. Adv.* **3**, (2017).

76.   Behnam, A. *et al.* Experimental characterization of single-walled carbon nanotube film-Si Schottky contacts using metal-semiconductor-metal structures. *Appl. Phys. Lett.* **92**, (2008).

77.   An, Y., Behnam, A., Pop, E. & Ural, A. Metal-semiconductor-metal photodetectors based on graphene/p-type silicon Schottky junctions. *Appl. Phys. Lett.* **102**, (2013).

78.   Das, M., Sarmah, S. & Sarkar, D. UV-Visible optical photo-detection from porous silicon (PS) MSM device. *Superlattices Microstruct.* **101**, 228–235 (2017).

79.   Sanehira, E. M. *et al.* Enhanced mobility $CsPbI_3$ quantum dot arrays for record-efficiency, high-voltage photovoltaic cells. *Sci. Adv.* **3**, eaao4204 (2017).

80.   Zhang, H., Kurley, J. M., Russell, J. C., Jang, J. & Talapin, D. V. Solution-Processed, Ultrathin Solar Cells from $CdCl_3^-$-Capped CdTe Nanocrystals: The Multiple Roles of $CdCl_3^-$ Ligands. *J. Am. Chem. Soc.* **138**, 7464–7467 (2016).

81.   Xu, B. *et al.* Manipulating Band Structure through Reconstruction of Binary Metal Sulfide for High-Performance Thermoelectrics in Solution-Synthesized Nanostructured $Bi_{13}S_{18}I_2$. *Angew. Chemie* **130**, 2437–2442 (2018).

82.   Voutsas, G. P. & Rentzeperis, P. J. The crystal structure of the paraelectric bismuth thiochloride, BiSCl. *Zeitschrift für Krist. - Cryst. Mater.* **152**, 109–118 (1980).

83. Krämer, V. Structure of the bismuth chloride sulphide $Bi_4Cl_2S_5$. *Acta Crystallogr. Sect. B Struct. Crystallogr. Cryst. Chem.* **35**, 139–140 (1979).

84. Poudeu, P. F. P. & Ruck, M. The intergrowth structure of $Ag_{1.2}Bi_{17.6}S_{23}Cl_8$ and its relation to the tubular structure of $Bi6+\delta S6+3\delta Cl6-3\delta$ and the pavonite homologue $Ag_{3x}Bi_{5-3x}S_{8-6x}Cl_{6x-1}$. *J. Solid State Chem.* **179**, 3636–3644 (2006).

85. Gemmi, M. & Lanza, A. E. 3D electron diffraction techniques. *Acta Crystallogr. Sect. B Struct. Sci. Cryst. Eng. Mater.* **75**, 495–504 (2019).

86. Vincent, R. & Midgley, P. A. Double conical beam-rocking system for measurement of integrated electron diffraction intensities. *Ultramicroscopy* **53**, 271–282 (1994).

87. Mugnaioli, E., Gorelik, T. & Kolb, U. 'Ab initio' structure solution from electron diffraction data obtained by a combination of automated diffraction tomography and precession technique. *Ultramicroscopy* **109**, 758–765 (2009).

88. Kolb, U., Krysiak, Y. & Plana-Ruiz, S. Automated electron diffraction tomography - Development and applications. *Acta Crystallogr. Sect. B Struct. Sci. Cryst. Eng. Mater.* **75**, 463–474 (2019).

89. Palatinus, L. *et al.* Specifics of the data processing of precession electron diffraction tomography data and their implementation in the program PETS2.0. *Acta Crystallogr. Sect. B Struct. Sci. Cryst. Eng. Mater.* **75**, 512–522 (2019).

90. Burla, M. C. *et al.* Crystal structure determination and refinement via SIR2014. *J. Appl. Crystallogr.* **48**, 306–309 (2015).

91. Altantzis, T. *et al.* Three-Dimensional Quantification of the Facet Evolution of Pt Nanoparticles in a Variable Gaseous Environment. *Nano Lett.* **19**, 477–481 (2019).

92. Gilbert, P. Iterative methods for the three-dimensional reconstruction of an object from projections. *J. Theor. Biol.* **36**, 105–117 (1972).

93. Hammersley, A. P., Svensson, S. O., Hanfland, M., Fitch, A. N. & Häusermann, D. Two-Dimensional Detector Software: From Real Detector to Idealised Image or Two-Theta Scan. *High Press. Res.* **14**, 235–248 (1996).

94. Juhás, P., Davis, T., Farrow, C. L. & Billinge, S. J. L. PDFgetX3: a Rapid and Highly Automatable Program for Processing Powder Diffraction Data Into Total Scattering Pair Distribution Functions. *J. Appl. Crystallogr.* **46**, 560–566 (2013).

95. Giacovazzo, C. *Phasing in Crystallography: A Modern Perspective*. *Oxford University Press* (Oxford University Press, 2014).

96. Farrow, C. L. *et al.* PDFfit2 and PDFgui: Computer Programs for Studying Nanostructure in Crystals. *J. Phys. Condens. Matter* **19**, 335219 (2007).

97. Caliandro, R. & Belviso, D. B. RootProf: Software for Multivariate Analysis of Unidimensional Profiles. *J. Appl. Crystallogr.* **47**, 1087–1096 (2014).

98. Juhás, P., Farrow, C. L., Yang, X., Knox, K. R. & Billinge, S. J. L. Complex Modeling: a Strategy and Software Program for Combining Multiple Information Sources to Solve Ill posed Structure and Nanostructure Inverse Problems. *Acta Crystallogr. Sect. A Found. Adv.* **71**, 562–568 (2015).

99. Rodriguez-Carvajal J. A Program for rietveld refinement and pattern matching analysis. in *Abstracts of the satellite meeting on powder diffraction of the XV congress of the IUCr* 127–8 (1990).

100. Giannini, C. *et al.* X-ray Diffraction: A powerful technique for the multiple-length-scale structural analysis of nanomaterials. *Crystals* vol. 6 87 (2016).

101. Aroyo, M. I. *et al.* Crystallography online: Bilbao crystallographic server. *Bulg. Chem. Commun.* **43**, 183–197 (2011).

102. Aroyo, M. I. *et al.* Bilbao Crystallographic Server: I. Databases and crystallographic computing programs. *Zeitschrift fur Krist.* **221**, 15–27 (2006).

103. Aroyo, M. I., Kirov, A., Capillas, C., Perez-Mato, J. M. & Wondratschek, H. Bilbao Crystallographic Server. II. Representations of crystallographic point groups and space groups. *Acta Crystallogr. Sect. A Found. Crystallogr.* **62**, 115–128 (2006).
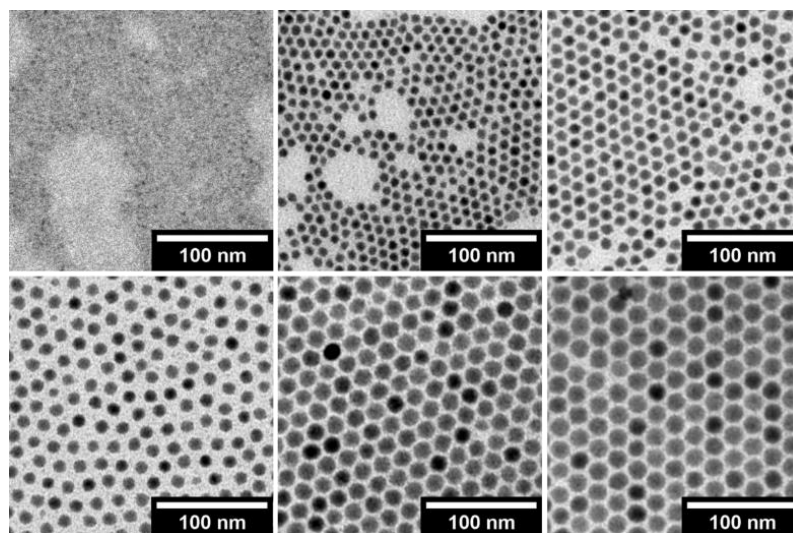
Figure 4.6. Size evolution of Pb₄S₃Br₂ nanocrystals during their synthesis. Pb4S3Br2 nanocrystals quenched at different temperatures. From left to right and from top to bottom: 150 – 160 – 165 – 170 – 180 – 190°C. [Ref. 50]
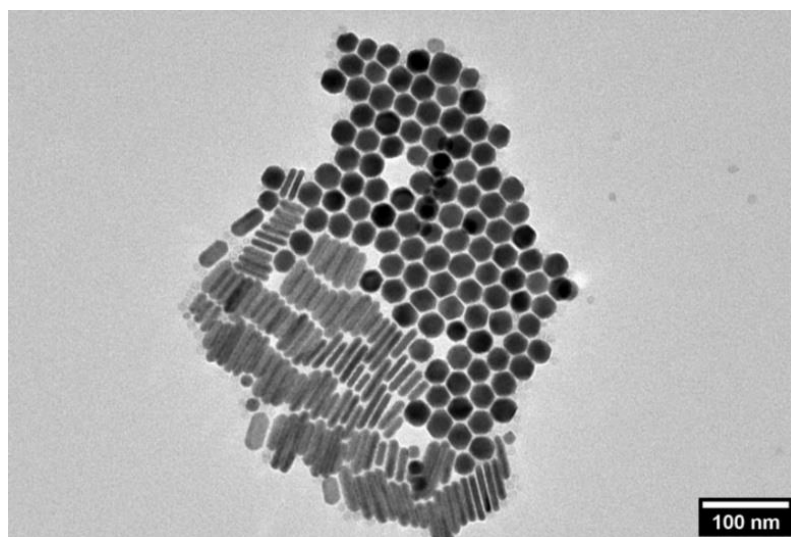
Figure 4.7. Accreted Pb₄S₃Br₂ nanocrystals and side-product nanoplatelets. Pb₄S₃Br₂ nanocrystals and nanoplatelets obtained by seeded growth. Most platelets were removed by decanting the sample, but few remained. [Ref. 50]

116
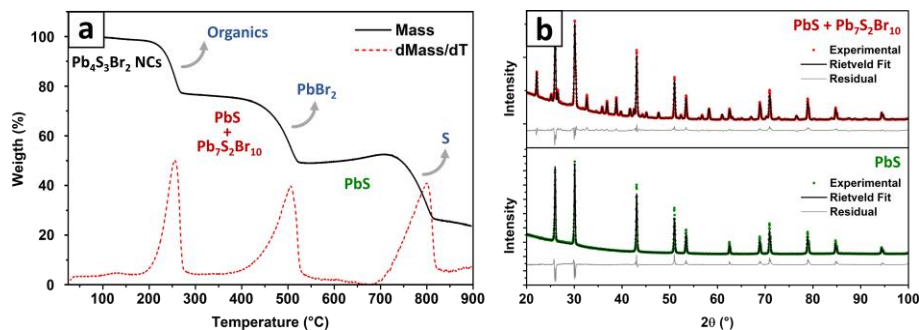
Figure 4.8. TGA + XRPD analysis of Pb₄S₃Br₂ nanocrystals. a) TGA curve of $Pb_4S_3Br_2$ nanocrystals, showing three distinct weight losses upon heating. b) XRPD patterns collected after the first two mass losses, demonstrating that the decomposition products are PbS and $Pb_7S_2Br_{10}$ at the first step, and PbS at the second step. By comparing the mass fractions of the remaining PbS and the lost $PbBr_2$ it is possible to infer the stoichiometry of the compound. [Ref. 50].
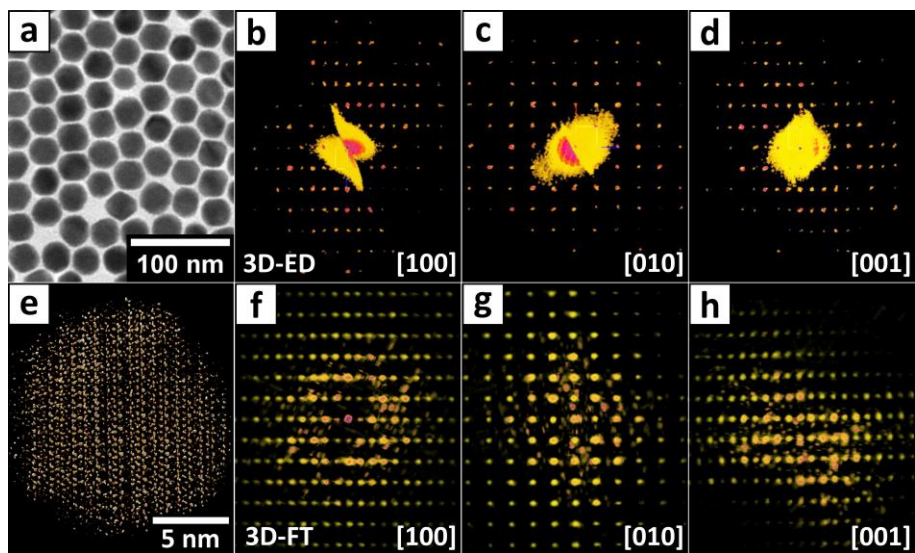
Figure 4.9. 3D-ED and 3D-FT of Pb₄S₃Br₂ nanocrystals. a) TEM image of the $Pb_4S_3Br_2$ nanocrystals characterized by 3D-ED. b-d) 3D-ED frames collected along different zone axes. e) 3D electron tomography reconstruction of a spherical $Pb_4S_3Br_2$ nanocrystal. f-h) Projections of the corresponding 3D-FT map along different zone axes. [Ref. 50].
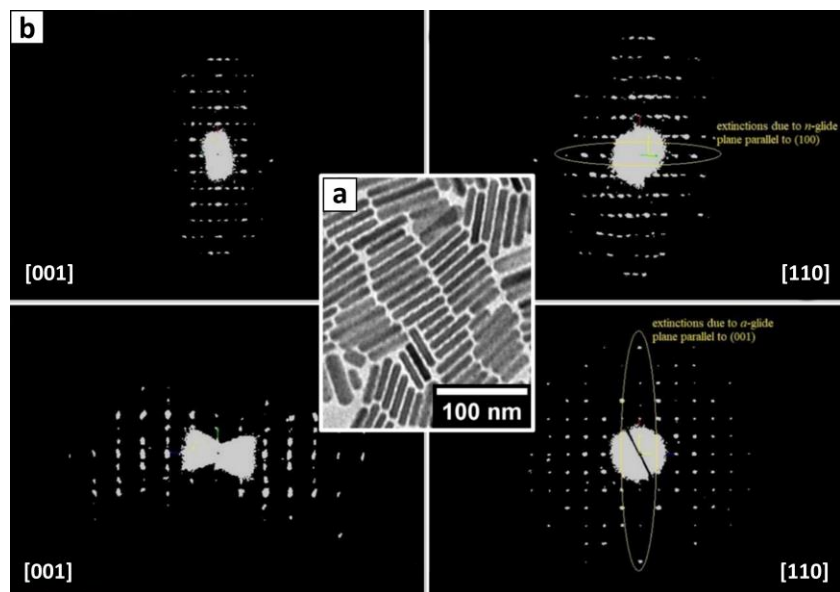
Figure 4.10. 3D-ED on Pb₄S₃Br₂ nanoplatelets. a) TEM image of the Pb₄S₃Br₂ nanoplatelets investigated via 3D-ED. b) Reconstruction of the nanoplatelet reciprocal lattice viewed along four main directions, showing the systematic extinctions exploited for the space group determination. [Ref. 50].
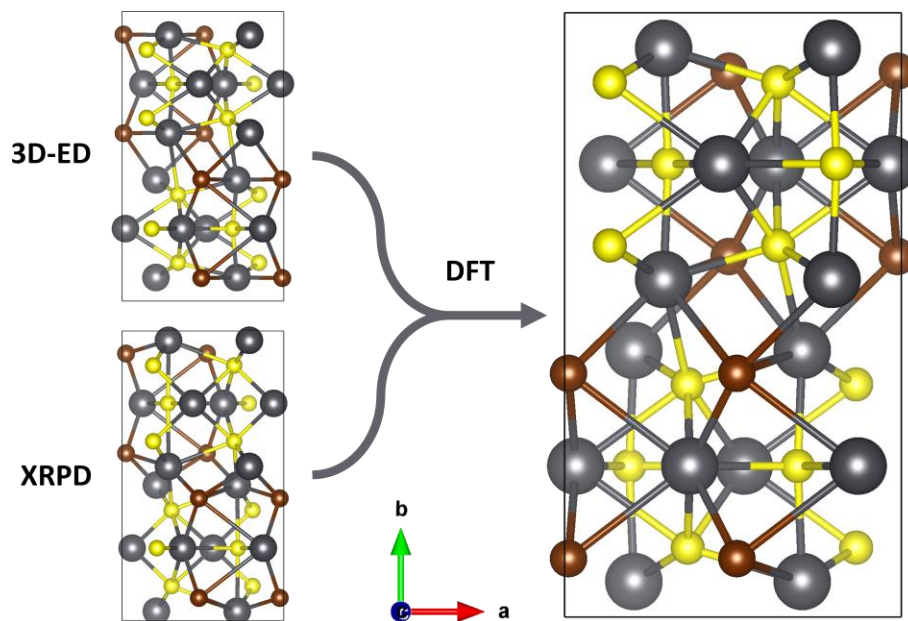
Figure 4.11. Pb₄S₃Br₂ structure solution by 3D-ED and XRPD. The structure models produced by 3D-ED and XRPD converged to the same structure upon DFT relaxation. [Ref. 50].

118
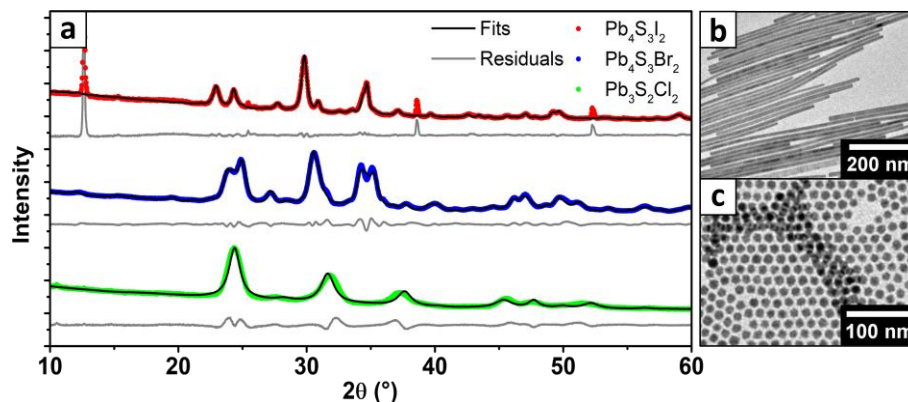
Figure 4.12. $Pb_4S_3I_2$ and $Pb_3S_2Cl_2$ nanocrystals. a) XRPD patterns of $Pb_4S_3I_2$, $Pb_4S_3Br_2$, and $Pb_3S_2Cl_2$ nanocrystals compared. The relative Rietveld fits are overlaid; the residual peaks in the pattern of $Pb_4S_3I_2$ come from an impurity, most likely PbI_2 nanosheets or flakes. Here, $Pb_3S_2Cl_2$ was fitted according to a cubic $Pb_3Se_2Br_2$ prototype, that however failed to capture the position of diffraction peaks accurately. The mismatch could not be compensated by simply resizing a cubic unit cell, suggesting that the sample adopted a lower symmetry structure. b,c) TEM images of $Pb_4S_3I_2$ (b) and $Pb_3S_2Cl_2$ nanocrystals (c). [Ref. 50].
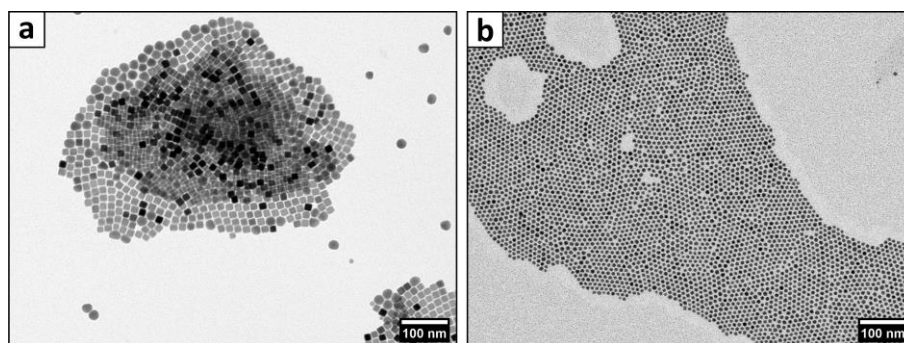
Figure 4.13. $Pb_3S_2Cl_2$ nanocrystals obtained by thiocyanate heat-up. a) The rounded $Pb_3S_2Cl_2$ nanocrystals recovered in the precipitate were heavily contaminated by cubic PbS nanocrystals (both are visible in the image). b) Smaller but phase-pure $Pb_3S_2Cl_2$ nanocrystals could be obtained by quenching the reaction at 170°C and recovering the supernatant via ethyl-acetate assisted precipitation. [Ref. 50].
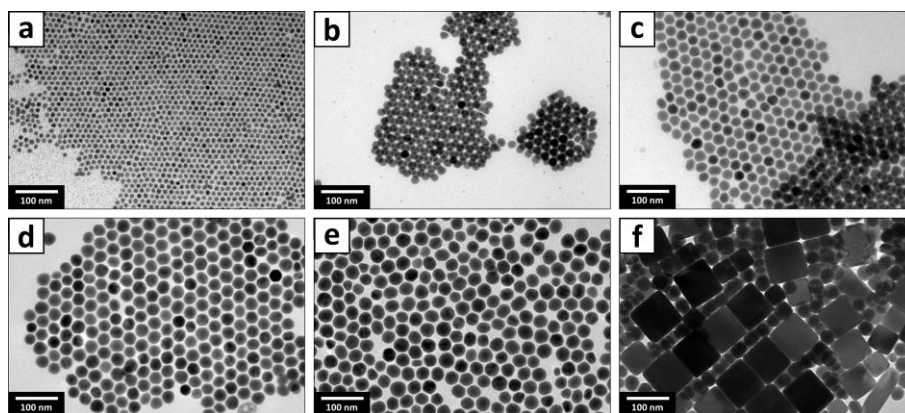
Figure 4.14. Seeded-growth of Pb₃S₂Cl₂. Aliquots of the $Pb_3S_2Cl_2$ accretion reaction mixture taken a) at the start of the process, and after b) 1h, c) 2h, d) 4h, e) 5h:15min. f) Large PbS impurities formed during the process, as found in the 5h:15min sample (e). [Ref. 51].
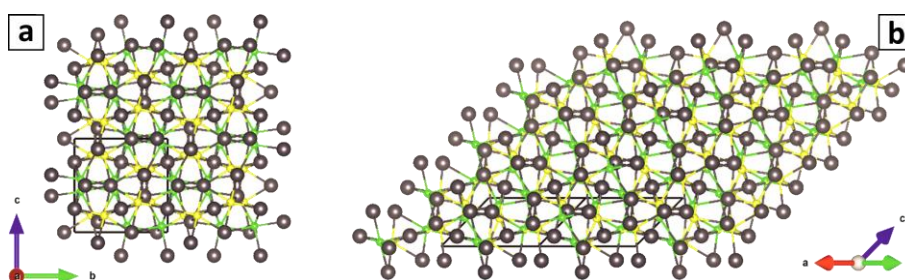
Figure 4.15. Pb₃S₂Cl₂ structure solutions obtained from 3D-ED data. Models obtained a) in the space group *I*-43d (but with S and Cl positions assigned, resulting in a symmetry drop to $I2_13$) and b) in the space group *Cc*. The sulfur and chlorine species are assigned tentatively, due to the insufficient difference in the scattering factors. The unit cell choice in panel (b) is shown prior to the standardization later performed on the refined $Pb_3S_2Cl_2$ model (black lines). Atoms color code: Pb = grey; S = yellow; Cl = green. [Ref. 51].
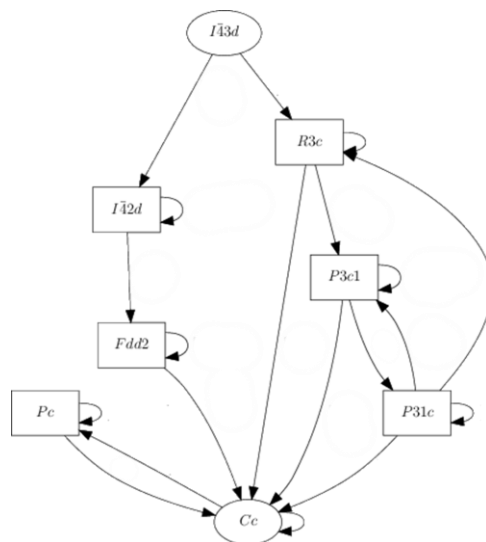
Figure 4.16. Group-subgroup relations connecting *I-43d* to *Cc*. The *I*-43d and the *C*c spage groups are related to each other by a progressive reduction of symmetry operations. Therefore, any structure that is described by *I*-43d can be described by *C*c as well, using a larger asymmetric unit. Graph generated using the tools provided by the Bilbao Crystallographic Server.[101–103]
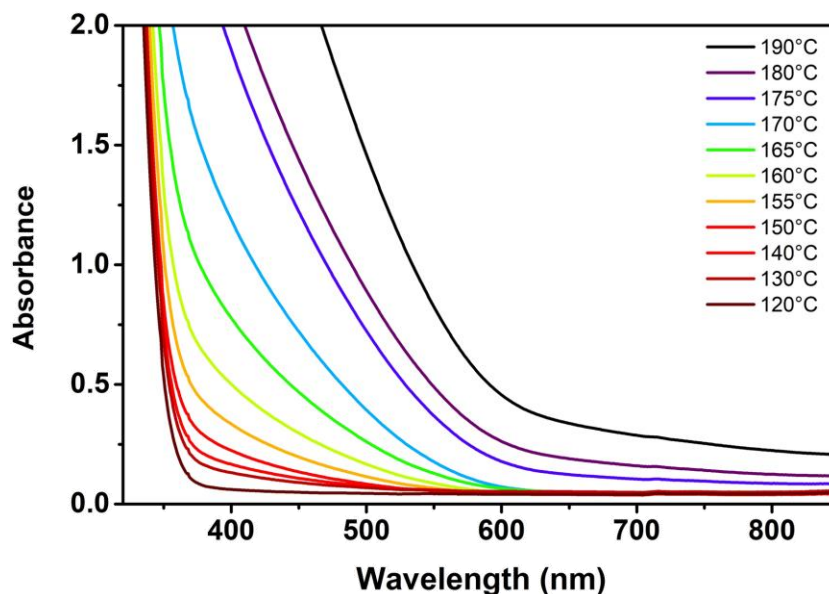
Figure 4.17. Absorbance of Pb$_4$S$_3$Br$_2$ nanocrystals of different sizes. The size was changed by quenching the reaction at different temperatures. Spectra shown as collected, without rescaling. [Ref. 50].
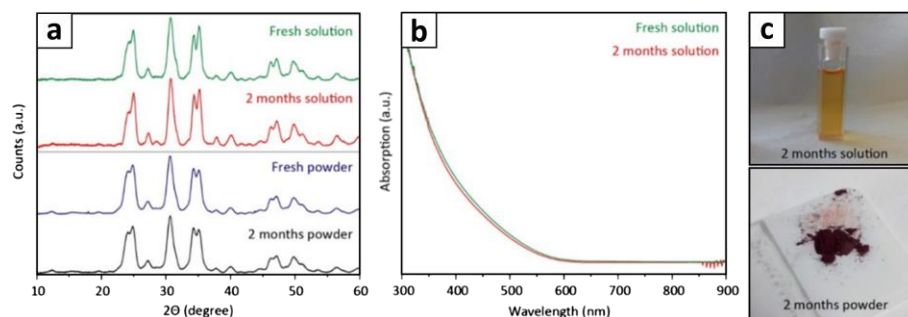
Figure 4.18. Temporal stability of Pb₄S₃Br₂ Nanocrystals. a) XRPD patterns of Pb₄S₃Br₂ nanocrystals colloidal suspension and dry powder as prepared and after 2 months of aging in a dry and dark environment. b) Absorption spectra of the solution before and after aging. c) Photographs of the two samples after 2 months of aging. [Ref. 50].
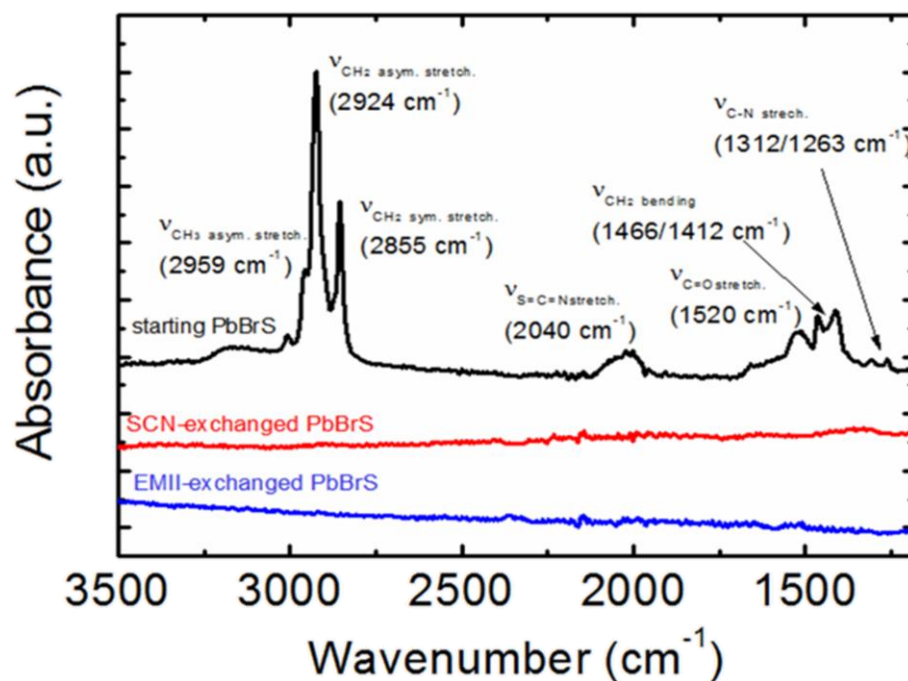
Figure 4.19. FTIR characterization of films of Pb₄S₃Br₂ nanocrystals before and after ligand exchange. FTIR spectra of the as-synthesized Pb₄S₃Br₂ Nanocrystals, showing the characteristic signal of organic ligands (*black*) compared with that of Nanocrystals after being exchanged with SCN and EMII (*red, blue*). After the treatments, the original ligands have been quantitatively removed. [Ref. 50].
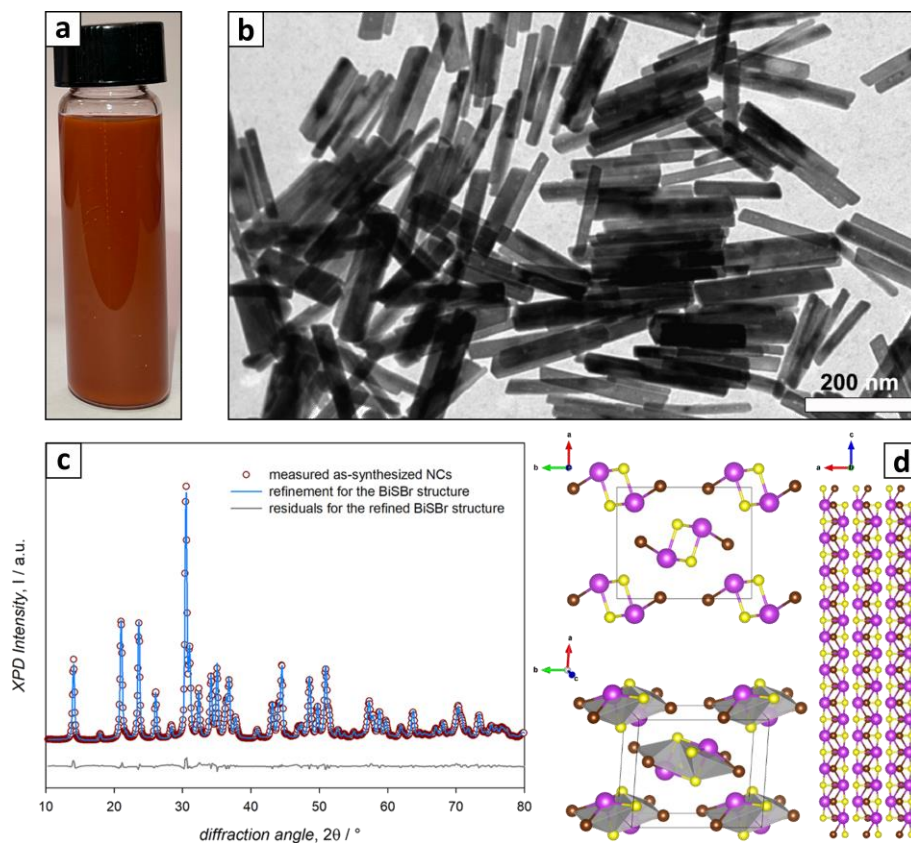
Figure 4.20. BiSBr nanocrystals. a) Daylight picture of a toluene colloidal dispersion of the BiSBr nanocrystals. b) TEM image of BiSBr nanocrystals. c) Rietveld fitting of the synchrotron XRPD pattern of BiSBr nanocrystals (to facilitate the comparison with data collected on lab-grade setups, the 2θ values of the XPD horizontal axis were converted to emulate the Cu-K$_{\alpha 1}$ radiation). d) Crystal structure of BiSBr, highlighting the 1-D ribbons along the c-axis and the square pyramidal coordination of Bi. [Ref. 19]

CHAPTER 5:

NANOCRYSTAL DIMERS

5.1 Coupling Materials at the Nanoscale

In the previous chapter we discussed the challenges posed by the structure solution of unknown compounds at the nanoscale. For that, we needed pure samples containing a single material. However, one of the most appealing features of nanochemistry is the ability of working with more than one material at the same time, and intimately combine them within a single nanostructure. Hybrid nanoparticles formed by multiple materials are often called heterostructures. These are basically always obtained from known compounds, since one must master their individual syntheses to combine them into one procedure. Hence, the challenge posed by heterostructures is not identifying new compounds, but rather understanding the nature of their interaction, and the impact it has on their formation and properties.

That of heterostructures is a rather broad definition, as it does not impose constraints on their morphology nor on the structural relations between domains. The most studied heterostructures based on semiconductors are arguably the epitaxial core-shell systems, where nanocrystals of one material, the cores, are fully surrounded by a shell of an isostructural material, the shell.[1–3] Common examples are CdSe/CdS[4,5] and ZnSe/ZnS[6,7] quantum dots, where the higher gap sulfide shell passivates the selenide core,

boosting the photoluminescence quantum yield while at the same time preserving the quantum confinement of the core itself. Under appropriate synthetic conditions, the same systems that form core-shell architectures can give rise to directional heterostructures, where one material grows in branches around the other, forming structures like tetrapods and octapods.[8,9] In all these cases, the fact that the two materials are isostructural ensures an ideal match at the interface, that is straightforward to describe. However, heterostructures are also systems like $CsPbBr_3/PbS$ or $CsPbBr_3/SiO_2$, where crystalline[10] or amorphous[11,12] domains grow attached to the surface of the nanocrystal core, but the interface is not bound by structural constraints, and the surface of the core particle might be only partially covered.[13,14]

In this chapter we will focus on an intermediate case, that of epitaxial heterostructures between materials with different crystal structures. Here, the atomic lattices of the two domains might still match along some, but not all, directions, and factors like the strain induced by lattice mismatch, or the compatibility of coordination environments at the interface must be taken into careful consideration.[15] Nevertheless, these interfaces can be still rationalized based on the structure of interacting materials, as opposed to amorphous or disordered interfaces. This kind of heterostructures is appealing for prospective applications, as pairing deeply different materials might lead to unexpected properties that would not be expressed by isolated domains. At the same time, having a fully crystalline interface might minimize defect states and ensure an optimal electronic coupling between the two domains.

Apart from properties and applications of the finished object however, the formation of epitaxial heterostructures can deeply impact the chemical reactivity at the nanoscale as well. In this chapter, we will discuss how solid-state reactions occurring in nanocrystals sometimes proceed through intermediate heterostructures, and vice versa, how heterostructures can be exploited as artificial intermediates to force one reaction to happen. Both cases are driven by structure-related principles that, once rationalized, become useful tools to explain, predict, or design similar transformations.

5.2 Cs$^+$ Subnetwork in Cs-Pb-X Nanocrystals

We will start by rationalizing reactivity in cesium lead halide nanocrystals. As anticipated in Chapter 2, the Cs-Pb-X ternary system includes a variety of phases and structures (CsX, Cs$_4$PbX$_6$, CsPb$_2$X$_4$, γ- and δ-CsPbX$_3$, CsPb$_2$X$_5$, PbX$_2$), that have all been shaped into nanostructures.[16–22] These are well-known for easily undergoing halide exchange reactions,[17,23–26] and even transforming from one phase to another upon addition or sequestration of CsX or PbX$_2$ neutral units. Indeed, literature provides many examples of CsX → CsPbX$_3$,[16] CsPbX$_3$ ⇄ Cs$_4$PbX$_6$,[27–31] and CsPbX$_3$ → CsPb$_2$X$_5$[32,33] transformations. All these processes can be labelled as "ion trade reactions", as ions are exchanged, acquired or released (in short, traded) during the process.[34] These are driven by unbalances in the partition equilibrium of ions or neutral species between nanocrystals and their environment, and can be triggered by simply increasing the concentration of a reactant in the surrounding medium, or providing a sequestration mechanism that extracts ions from the nanocrystal structure.[34] In this, Cs-Pb-X compounds are favored by

their high ionicity, that lowers the activation energy for the ion migration within the structure and leads to a high reactivity.[35,36]

The concept of ion trade reactions provides a unified, yet macroscopic picture of the reactivity in Cs-Pb-X nanocrystals.[34] However, it does not explain how reactions take place at the atomic scale. Interestingly, these processes often preserve the colloidal stability and size distribution of starting samples despite the apparently harsh transformations undergone by nanocrystals, that see their stoichiometry and crystal structure change.[34] Many of these reactions can be reverted, and some even cycled multiple times,[16,27] suggesting that some mechanism must be at play in converting one phase into another without disrupting the nanocrystal frame. As we are about to discover, this is where heterostructures play a central role.

5.2.1 Cs^+ subnetwork as a structural motif

Before diving deeper into the role of heterostructures however, we must find a common thread among Cs-Pb-X phases. Usually, $[PbX_6]^{4-}$ octahedra are considered their main structural motif. Such octahedra are disconnected in Cs_4PbX_6, they share corners in the perovskite γ-$CsPbX_3$, and edges in the δ-$CsPbX_3$ non-perovskite structure. This approach is useful when discussing electronic properties, as they mostly depend on the Pb-X-Pb connectivity.[38] However, thinking in terms of $[PbX_6]^{4-}$ octahedra excludes many Cs-Pb-X materials that can either generate or be generated by reacting one of the three above. For example, CsX nanocrystals can be transformed into $CsPbX_3$,[16] and $CsPb_2X_5$ can be obtained from the thermal decomposition of $CsPbX_3$.[39] However, neither CsX nor

$CsPb_2X_5$ possess $[PbX_6]^{4-}$ octahedra: CsBr contains no lead, while $CsPb_2X_5$ contains $[PbX_8]^{6-}$ biaugmented triangular prisms.[40]

A better choice is focusing on the arrangement of Cs^+ cations instead (Figure 5.1). From such perspective, the parent structure of the group is CsX, where the Cs^+ ions form a subnetwork of cubic cages, each enclosing a single X^- anion. Such subnetwork is found in all the other Cs-Pb-X compounds (except δ-$CsPbX_3$), albeit expanded and sometimes distorted. Starting from CsX, we can replace X^- with composite $[Pb_nX_{2n+1}]^-$ polyanions, which equals adding n neutral units of PbX_2 to each unit of CsX. Depending on the amount of PbX_2 added, the anionic network adapts its connectivity, the cation subnetwork expands and distorts to host it, and the whole series of structures can be obtained.
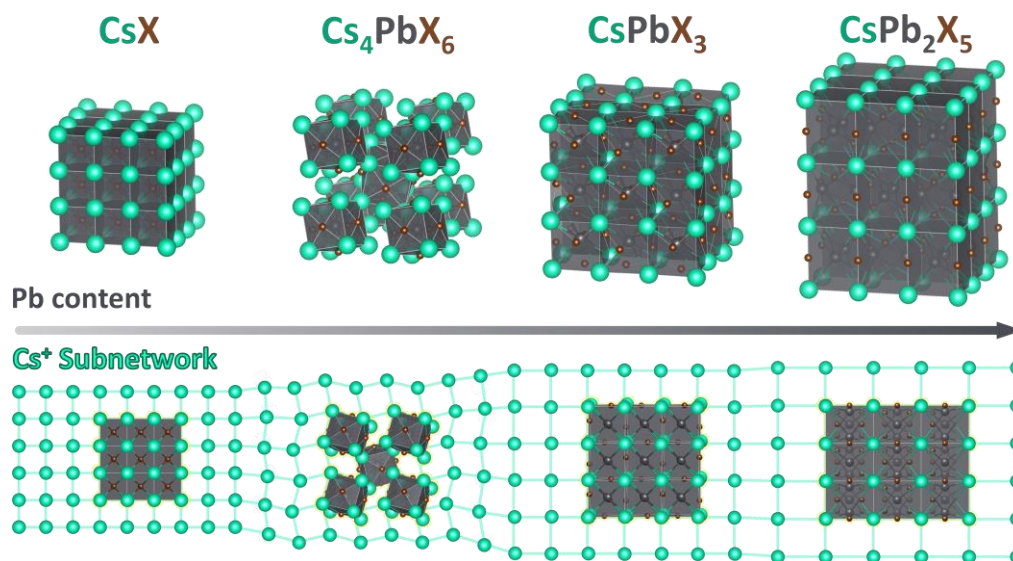
Figure 5.1. Cs^+ subnetwork in the Cs-Pb-X ternary system. The structures of CsX, Cs_4PbX_6, γ-$CsPbX_3$, and $CsPb_2X_5$ are shown in order of increasing lead content (top). All these structures are interconnected by a common structural motif: a cuboidal subnetwork of Cs^+ cations that expands and distorts along with the series (bottom). Adapted from Ref. 37.

We begin with Cs_4PbX_6, where only 1/4 of the Cs^+ cages incorporate lead in the form of disconnected $[PbX_6]^{4-}$ ions, resulting in an average $[Pb_{0.25}X_{1.5}]^-$ polyanion per cage. Note that the filled cages retain a cubic shape, while the empty ones distort to become rhombohedral (empty cages are shaded in red in Figure 5.2). That distortion is driven by the electrostatic interaction between the Cs^+ cations in the corner of one cube and X^- anions on the faces of the surrounding ones, and results in the crystal structure changing symmetry from cubic to hexagonal. Note that both symmetries possess a three-fold axis, that is preserved by the transformation.

In γ-$CsPbX_3$, all the cages become filled with $[PbX_3]^-$. The center of each cage is taken by Pb^{2+} ions, while X^- ions are on the faces, shared between neighboring cages. This is equivalent to the more familiar description of the perovskite structure through corner-sharing $[PbX_6]^{4-}$ octahedra. Moving along the series, in $CsPb_2X_5$ each cage encloses a $[Pb_2X_5]^-$ polyanion. Here, the two Pb^{2+} cations and four of the five X^- anions are fully enclosed by the cage, while the remaining X^- anion is found at one edge and is therefore shared with the neighboring cages. This configuration leads to a connected network of $[PbX_8]^{6-}$ biaugmented triangular prisms.

Finally, PbX_2 has no Cs^+ subnetwork, therefore it might not be considered part of the list. However, given that to build the structure series we had to add an increasing number of neutral PbX_2 units per each CsX, we can imagine PbX_2 as an infinitely large $[Pb_nX_{2n+1}]^-$ network (with $n \to \infty$) enclosed in a single Cs^+ cage where the Cs-Cs distance has expanded to infinity.

5.2.2 Heterostructures as reaction intermediates

The persistence of the Cs^+ subnetwork across the Cs-Pb-X system is more than an interesting coincidence: it is the key to explain how these compounds can interconvert so easily. In essence, a reaction converting a Cs-Pb-X compound into another can proceed while preserving the subnetwork all throughout the transformation, thus ensuring that the process does not tear the crystal apart. Crucially, as the reaction proceeds and the nanocrystals progressively change composition and structure, epitaxial heterostructures must be formed between the reagent and the product domains. This is a direct consequence of the Cs^+ subnetwork preservation, as the need of transforming one phase into another without excessively displacing the Cs^+ ions impose strict constraints on the orientation and interface match between the parent and product structures. To provide an overview of these transformations, we will focus mainly on the Cs-Pb-Br system, since the many reports on these materials provide a variety of experimental examples. We shall start from the simplest structure of the series, that is CsBr.

Shamsi *et al.* achieved the transformation of CsBr nanocrystals to γ-CsPbBr$_3$ perovskite nanocrystals by reaction with Pb(oleate)$_2$.[16] The transformation preserved the starting size distribution, pointing against a dissolution-recrystallization mechanism where CsBr would be dissolved and CsPbBr$_3$ would nucleate from free ions in solution. Instead, the reaction proceeded by the progressive insertion of PbBr$_2$ into the CsBr structure, with Pb^{2+} coming from Pb(oleate)$_2$ and Br^- from a partial etching of the nanocrystal surface, and crucially resulted in the formation of CsBr/CsPbBr$_3$ core-shell epitaxial heterostructures as intermediates (Figure 5.2a). Heterostructures became

130

smaller as the transformation proceeded, consistent with the expected etching and release of excess Cs^+ in the environment. At the same time, the epitaxial connection ensured that the Cs^+ subnetwork was shared between the two domains. As expected, the lattice constants difference (CsBr ≈ 4.3 Å; $CsPbBr_3$ ≈ 5.8 Å) produced some strain at the interface, that was measured by HRTEM.[16]

The next set of transformations concerns the conversion of $CsPbBr_3$ to Cs_4PbBr_6 and back. This equilibrium was reported to be reversible and easily triggerable by a variety of stimuli: addition and subtraction of $PbBr_2$ or CsBr, and changes in the concentration of ligands in the environment. One interesting example was reported by Li *et al.*, who cycled the transformation back and forth while retaining the nanocrystal size distribution.[27] Specifically, the $CsPbBr_3 \rightarrow Cs_4PbBr_6$ reaction was triggered by adding a mixture of ligands (oleic acid and oleylamine), which increased the $PbBr_2$ solubility in the environment, while the inverse $Cs_4PbBr_6 \rightarrow CsPbBr_3$ reaction was driven by the direct addition of $PbBr_2$. Remarkably, they observed that the nanocrystal size at each cycle of the transformation was compatible with a constant number of Cs^+ atoms. All these observations are consistent with a subnetwork-preserving reaction mechanism: $PbBr_2$ is readily incorporated in (or released by) each Cs^+ cage, as the process only requires a mild distortion of the Cs^+ subnetwork.

Baranov *et al.* provided a strong proof for this mechanism: while studying the $Cs_4PbBr_6 \rightarrow CsPbBr_3$ transformation, they succeeded in isolating intermediate $CsPbBr_3/Cs_4PbBr_6$ epitaxial heterostructures where the Cs^+ subnetwork was continuous across the whole nanocrystals, with little distortion at the interface (Figure 5.2b).[41]

Interestingly, the transformation proceeded from one single nucleation point on the nanocrystal surface, from where it extended to the remaining regions. The lack of multiple nucleation points of can be explained based on the proposed Cs^+ subnetwork-assisted mechanism: once the transformation is started, the strain induced by the epitaxial connection locally straightens the distorted Cs^+ subnetwork of Cs_4PbBr_6 to match that of $CsPbBr_3$. This local expansion might facilitate the further diffusion of $PbBr_2$ at the interface, resulting in a sort of self-catalyzed reaction.

Another interesting example is the $Cs_4PbBr_6 \rightarrow CsPbBr_3$ transformation driven by CsBr extraction. This was reported upon reaction of nanocrystals with solid Prussian Blue $(Fe^{III}_4[Fe^{II}(CN)_6]_3)$,[28] a compound that selectively intercalates Cs^+, or after their exposure to a hexane-water interface.[29] In both cases, no intermediate heterostructures were isolated. However, the size distribution of nanocrystals was preserved, a piece of evidence that again played against a dissolution-recrystallization mechanism. Also, the nanocrystals contracted in size after the reaction, as expected for a partial etching. This is a key point: indeed, Cs_4PbBr_6 nanocrystals should undergo etching when CsBr is extracted from their surface. However, for each four CsBr units etched away, one unit of $PbBr_2$ is also freed. No $PbBr_2$ was detected at the end of the process by XRD, that can be explained by $PbBr_2$ being incorporated in the remaining portion of Cs_4PbBr_6 nanocrystals, driving their transformation to $CsPbBr_3$. The extraction of Cs^+ ions stopped when nanocrystals had been entirely converted to $CsPbBr_3$: any further extraction of CsBr would have been accompanied by the release of $PbBr_2$, which, as already said, was not detected in the final product.

Furthermore, in the case of the water-driven process, authors compared the size of particles before and after the transformation, finding it compatible with a constant number of Pb atoms (Cs_4PbBr_6 diameter = 17.8 nm, $CsPbBr_3$ expected / measured edge length = 10.8 / 12.2 nm).[29] We repeated the analysis for the Prussian Blue-driven transformation, finding an excellent match (Cs_4PbBr_6 diameter = 9.8 nm, $CsPbBr_3$ expected / measured edge length = 5.9 / 6.3 nm). This further supports our mechanistic hypothesis. It is worth mentioning however that a dissolution-recrystallization mechanism is still possible for these reactions, given the right conditions. For example, Palazon *et al.* and Udayabhaskararao *et al.* both triggered the $CsPbX_3 \rightarrow Cs_4PbX_6$ transformation by adding amines, which can sequestrate lead by forming a complex.[30,31] However, ammonium ions are known to compete with Cs^+ in the structure of lead-halide perovskites, thus causing the Cs^+ subnetwork degradation and the consequent recrystallization.[43,44]

To conclude the series, fewer reports exist on the $CsPbBr_3 \rightarrow CsPb_2Br_5$ transformation, mainly because of the less appealing optical and electronic properties of $CsPb_2Br_5$. In general, this transformation is slower than the previous ones or requires harsher conditions such as continuous illumination or heating.[32,33] For example, Huang et *al*. reacted $CsPbBr_3$ nanosheets with an excess of $PbBr_2$ at 60°C for three days, obtaining epitaxial heterostructures.[45] Since there is little interest in pure $CsPb_2Br_5$, the transformation was halted at that stage. The preservation of the Cs^+ subnetwork helps rationalizing these observations as well. To occur, the $CsPbBr_3 \rightarrow CsPb_2Br_5$ transformation must stretch the Cs^+ cages in one direction, lowering their symmetry from cubic to

tetragonal. Consequently, the lattice parameter in the elongated direction becomes way too large (~9.7 Å) to match with that of $CsPbBr_3$ (~5.8 Å), leaving only the (001) plane of $CsPb_2Br_5$ as a possible interface with $CsPbBr_3$. The high-quality HRTEM images captured by Zheng *et al*. on a co-synthesized heterostructure help visualizing this connection (Figure 5.2c).[42] The main consequence of this structural constraint is that the transformation cannot proceed cell-by-cell as for all the previous examples: it must take place layer by layer, slowing down the reaction.
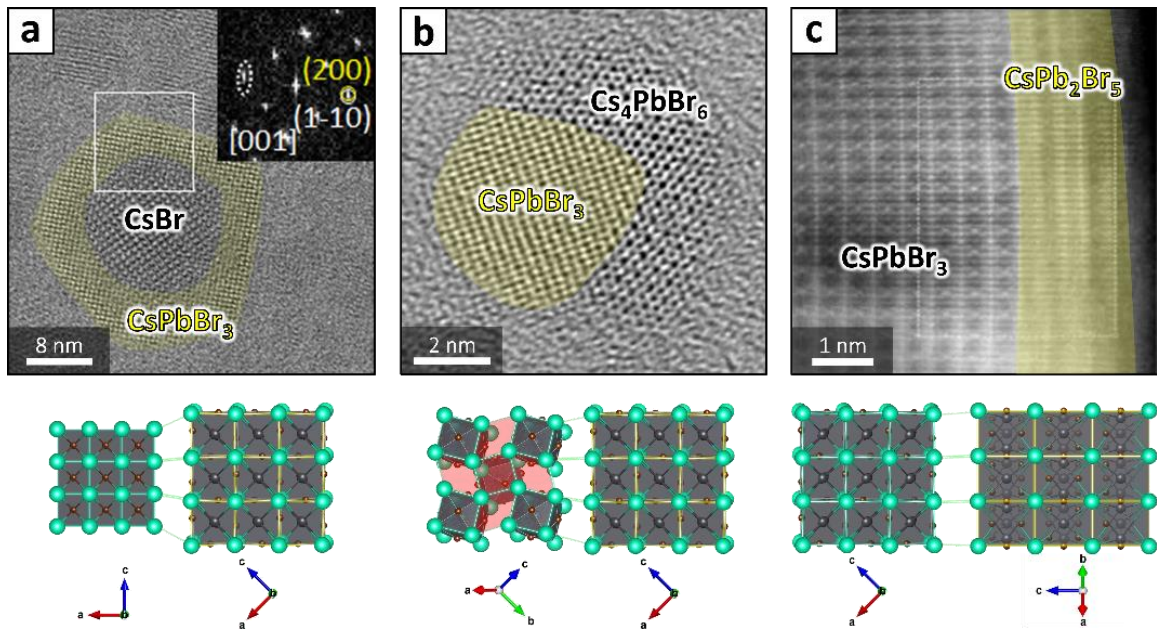
Figure 5.2. Epitaxial heterostructures between Cs-Pb-Br compounds. HRTEM images of a) $CsBr$-$CsPbBr_3$, b) Cs_4PbBr_6-$CsPbBr_3$, and c) $CsPbBr_3$-$CsPb_2Br_5$ heterostructures.[16,41,42] Below are simplified models of the epitaxial connections, highlighting the expansion and distortion of the Cs^+ subnetwork when moving from lead poor (cyan-shaded) to lead rich compounds (yellow-shaded). Empty cages in the Cs_4PbBr_6 structure are shaded in red. Adapted from Ref. 37, HRTEM images originally from Refs. 16,41,42.

5.2.3 Influence on the Cs^+ subnetworks on reaction products

Overall, reactions within the Cs-Pb-X system appear to proceed through the insertion or extraction of $PbBr_2$ in or from the somehow static Cs^+ subnetwork. This logic can be applied to explain some peculiar reports that would be hard to justify otherwise. For example, the $CsBr \rightarrow CsPbBr_3$ transformation seems to bypass the Cs_4PbBr_6 intermediate.[16] The reason is likely found in the self-catalyzed nature of the $Cs_4PbBr_6 \rightarrow$ $CsPbBr_3$ transformation, that was proposed above: Cs_4PbBr_6 might form in the early stages of the reaction, but the incoming $PbBr_2$ will likely react more favorably with it, completing its transformation to $CsPbBr_3$, rather than reacting with CsBr. Yet, small domains of Cs_4PbBr_6, although not observed to date, might exist at the $CsBr$-$CsPbBr_3$ interface and act as a strain-releasing transient layer (Figure 5.3a). Another counterintuitive observation is that, when reacted with a source of lead, both CsI and Cs_4PbI_6 nanocrystals form the metastable γ-$CsPbI_3$ perovskite phase instead of the thermodynamically favored non-perovskite δ-$CsPbI_3$.[16,17] This happens because the arrangement of Cs^+ ions in δ-$CsPbI_3$ is completely different from that found in CsI and Cs_4PbI_6. Thus, the transformation to δ-$CsPbI_3$ would entail a major structural rearrangement, that requires a high activation energy and proceeds through a recrystallization. Therefore, both compounds prefer to transform to the structurally compatible, yet metastable γ-$CsPbI_3$ perovskite structure. However, the γ-$CsPbI_3 \rightarrow \delta$-$CsPbI_3$ transformation still happens afterwards by recrystallization, as indicated by the formation of much larger crystallites.[46,47]
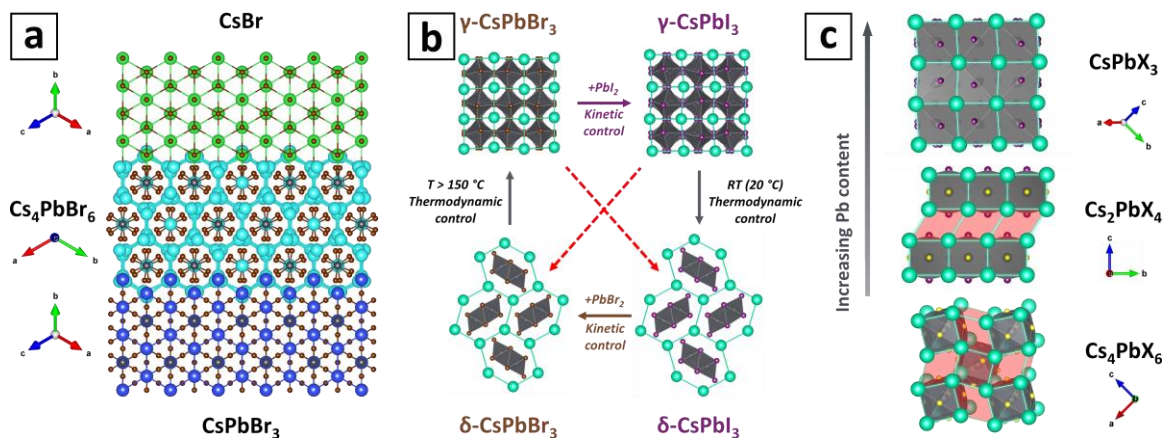
Figure 5.3. Influence of the Cs⁺ subnetwork on the product of reactions. a) Hypothetical ternary $CsBr/Cs_4PbBr_6/CsPbBr_3$ interface, highlighting the continuity of the Cs⁺ subnetwork (Cs⁺ ions green in CsBr, cyan in Cs_4PbBr_6, and blue in $CsPbBr_3$). b) Halide exchange reactions in γ- and δ-$CsPbX_3$ preserve the respective Cs⁺ subnetworks, at the cost of yielding metastable products. These can still convert to the stable ones either spontaneously ($CsPbI_3$) or upon heating ($CsPbBr_3$), but this requires a disruptive recrystallization process. c) The Ruddlesden-Popper perovskite Cs_2PbX_4 (middle) has an intermediate structure between that of lead-rich $CsPbX_3$ (top) and of the lead-poor Cs_4PbX_6 (bottom). Empty Cs⁺ cages are highlighted in red. Adapted from Ref. 37.

These mechanistic considerations can be extended to γ-$CsPbBr_3 \rightarrow \gamma$-$CsPbI_3$ and δ-$CsPbI_3 \rightarrow \delta$-$CsPbBr_3$ halide-exchange reactions (Figure 5.3b, the second observed only in bulk).[23,24,48] Both reactions transform a stable structure (γ-$CsPbBr_3$ and δ-$CsPbI_3$) into a metastable one (γ-$CsPbI_3$ and δ-$CsPbBr_3$) under kinetic control, instead of producing the thermodynamically stable products (δ-$CsPbBr_3$ and γ-$CsPbI_3$). Again, the transformations are driven by the preservation of the Cs⁺ subnetwork, as $\gamma \rightarrow \gamma$ and $\delta \rightarrow \delta$ transformations do not require any major rearrangement, as opposed to $\gamma \rightleftarrows \delta$ transformations. Remarkably, the further conversion of δ-$CsPbBr_3$ to the stable γ-$CsPbBr_3$ phase could be

achieved only by heating above 150°C, demonstrating that a high activation energy is required to disrupt and rearrange the Cs^+ subnetwork.[48]

One last example is the transformation of $Cs_2PbI_2Cl_2$ nanoplatelets into nanocrystals of γ-$CsPbBr_3$ or Cs_4PbCl_6 upon reaction with $PbBr_2$ and $MnCl_2$, respectively.[49] It is surprising that reacting the same compound with two different halides of M^{2+} cations results alternatively in the formation of M^{2+} rich or M^{2+} poor phases. However, this can be again explained by the preservation of the Cs^+ subnetwork based on two key observations. First, we note that the $Cs_2PbCl_2I_2$ structure features cubic Cs^+ cages filled with $[PbI_2Cl_2]^{2-}$ alternated with distorted non-cubic empty cages, for an average $[Pb_{0.5}ICl]^-$ unit per cage, and hence fits into the structural series discussed above (Figure 5.3c). The filled cages are shifted by half-cell to let Cs^+ in one layer interact with I^- in the neighboring one, providing an electrostatic stabilization mechanism like that of Cs_4PbX_6. Second, we must note that $Cs_2PbI_2Cl_2$ is stabilized by the different ionic radii of Cl^- and I^-, while no single-halide Cs_2PbX_4 structure is known.

When $Cs_2PbI_2Cl_2$ is reacted with $MnCl_2$, the excess of chlorine would cause a I → Cl halide exchange to a hypothetical Cs_2PbCl_4 structure, that however is not stable. At the same time, Mn^{2+} is not able to enter the structure of $CsPbCl_3$ in large amounts,[50] leaving the system with a shortage of bivalent cations. The only option left to $Cs_2PbCl_2I_2$ is therefore expelling PbI_2 and converting into Cs_4PbCl_6. From the Cs^+ subnetwork point of view, this requires distorting some of the cages, as half of them become empty. Similarly, the reaction with $PbBr_2$ would cause the replacement of both I^- and Cl^- and the formation of Cs_2PbBr_4, that once again is not stable. In this case however there is an excess of $PbBr_2$

available, that differently from $MnCl_2$ can enter the structure, thus removing any distortions from the Cs^+ subnetwork and delivering stable γ-$CsPbBr_3$.

5.3 Chalcohalide-Perovskite Heterostructures

In Paragraph 5.2 we have learned that the preservation of the Cs^+ subnetwork is a viable principle to rationalize chemical transformations proceeding through the formation of heterostructures between Cs-Pb-X compounds. However, cesium lead halides are a rather peculiar case, as they are all formed by the same elements and share strict structural relations. In the more general scenario of heterostructures formed by materials sharing some or no elements, a common structural denominator might be hard to identify. However, finding a way to rationalize and possibly predict the formation of heterostructures would be a leap forward, as the always growing pool of compounds explored at the nanoscale results in more and more possible heterostructures coming within our reach.

Examples are the fully epitaxial $Pb_4S_3Br_2$/$CsPbBr_3$ heterostructures (Figure 5.4) obtained by Dr. Muhammad Imran, a colleague at the Istituto Italiano di Tecnologia, soon after our report on lead chalcohalides was published (see Chapter 4 of this thesis).[51] The protocol he developed relied on sub-nanometer size $CsPbBr_3$ nanoclusters acting as single sources of Cs, Pb, Br, and surfactants.[52,53] These were mixed with a solution of elemental sulfur in 1-octadecene, and then injected in a vial containing 1-octadecene and dodecanethiol at 200°C (Figure 5.4a). The reaction produced heterostructures formed by a cubic shaped $CsPbBr_3$ domain with an edge length of 20.3 ± 2.2 nm, bounded to a

smaller and hemispherical $Pb_4S_3Br_2$ domain (Figure 5.4b). Samples prepared with different growth times demonstrated that the perovskite domain formed first, swiftly followed by the heterogeneous nucleation of the chalcohalide on one of the facets of the perovskite nanocube. Owing to my previous experience with lead chalcohalides and with the rationalization of Cs-Pb-X/Cs-Pb-X epitaxial interfaces, I had the opportunity of joining the team effort with the task of investigating the $Pb_4S_3X_2$/CsPbX$_3$ dimers on a structural perspective.
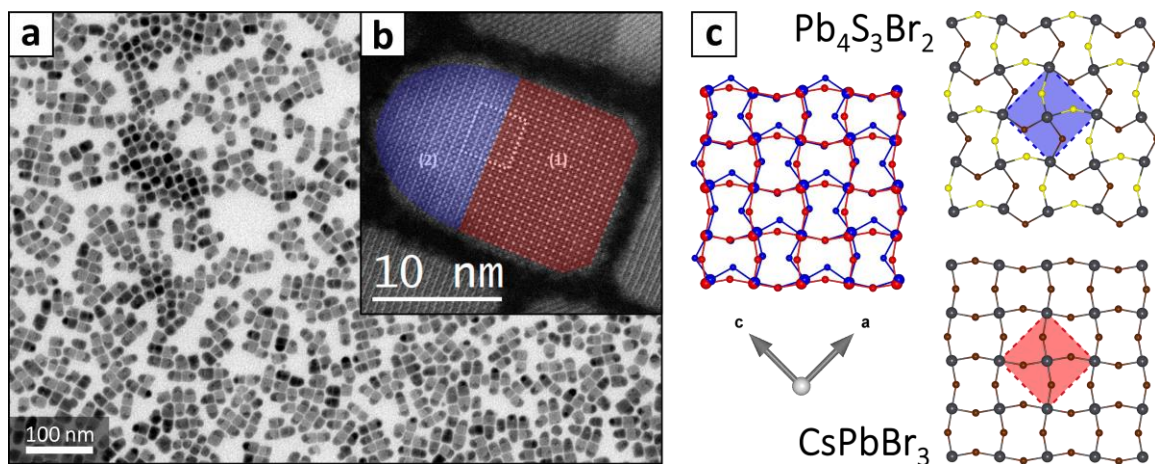
Figure 5.4. $Pb_4S_3Br_2$/CsPbBr$_3$ epitaxial heterostructures. a) TEM image of as-synthesized $Pb_4S_3Br_2$/CsPbBr$_3$ heterostructures. b) HAADF-STEM image of one heterostructure, showing the sharp boundary between the perovskite (red) and the chalcohalide (blue) domains. c) Atomic planes of $Pb_4S_3Br_2$ (top) and CsPbBr$_3$ (bottom) concurring to the formation of the interface. The overlay of the two planes (middle) highlights the excellent match between the atomic frameworks of CsPbBr$_3$ and $Pb_4S_3Br_2$. Adapted from Ref. 51.

5.3.1 On the $Pb_4S_3X_2$/CsPbX$_3$ interface

The epitaxial match between $Pb_4S_3X_2$ and CsPbX$_3$ is made possible by two structural features. First, the chalcohalide and the perovskite share a plane of Pb^{2+} ions

arranged in a square grid and connected by anions (X^- for the perovskites, both S^{2-} and X^- for the chalcohalide), which serves as an interface between the two domains (Figure 5.4c; in red in Figure 5.5a). Crucially, the existence of such plane in both the chalcohalide and the perovskite, despite the different local coordination environments, allows to ascribe the interfacial plane of the heterostructure to both materials at the same time.

Second, $Pb_4S_3X_2$ shares deep similarities with some of the Cs-Pb-X phases, which are easily overlooked at first sight (Figure 5.8). Indeed, the structure of $Pb_4S_3X_2$ is similar to that of $CsPb_2X_5$, as both are formed by polyanions of identical geometry ($[Pb_2X_5]^-$ for $CsPb_2X_5$, $[Pb_2S_3X_2]^{4-}$ for $Pb_4S_3X_2$) enclosed in a cationic subnetwork (Cs^+ for $CsPb_2X_5$, Pb^{2+} for $Pb_4S_3X_2$). The only difference is an extra layer of Pb^{2+} ions in between each polyanion, needed to maintain the charge-balance (Figure 5.5a, left). This makes the subnetwork of $Pb_4S_3X_2$ resemble that of another Cs-Pb-X phase, namely Cs_2PbX_4.

These similarities allow the Pb^{2+} cationic subnetwork of $Pb_4S_3X_2$ to find a natural prosecution in the $CsPbX_3$ perovskite domain (Figure 5.5a, right), ensuring the stability of the interface. This likely plays an important role in ensuring that the ions at the interface perceive electrostatic interactions comparable to those they would experience in both pure compounds, hence sensibly lowering any energetic disadvantage associated with the formation of the interface. Remarkably, the Pb^{2+} subnetwork of the chalcohalide matches at the same time with the Cs^+ and Pb^{2+} subnetworks of the perovskite domain, as the two share the same symmetry (Figure 5.9).

5.3.2 Heterostructures as disposable reaction intermediates

Clearly, the constraints we just outlined are strictly phase-specific, and ensure an epitaxial match only between $CsPbX_3$ and $Pb_4S_3X_2$. In Chapter 4 we learned that the synthesis of bromine- and iodine-based lead chalcohalides yields the isostructural compounds $Pb_4S_3Br_2$ and $Pb_4S_3I_2$, both of which would comply with these constraints. Conversely, in similar synthetic conditions chlorine favored the formation of $Pb_3S_3Cl_2$, whose deeply different structure does not offer any compatibility with the $CsPbX_3$ perovskite. This made us wonder whether the synthesis of a hypothetical lead sulfochloride/perovskite heterostructure would fail, or rather if it would lead to the formation of the yet unknown compound $Pb_4S_3Cl_2$ instead. To test this hypothesis, we adapted the synthesis of heterostructures to use chlorine-based precursors, indeed succeeding in the synthesis of $Pb_4S_3Cl_2/CsPbCl_3$ heterostructures (Figure 5.5).

High-Angle Annular Dark-Field Scanning TEM (HAADF-STEM) confirmed that the heterostructures were composed of two highly crystalline domains jointed along a flat interface spanning across the entire nanoparticle (Figure 5.5a,c). As expected, the fast Fourier transform (FFT) of the cubic-shaped domain matched with the perovskite $CsPbCl_3$, while the other domain was incompatible with the monoclinic $Pb_3S_2Cl_2$. Instead, the unit cell parameters and the overall FFT symmetry match with what expected for a orthorhombic $Pb_4S_3Cl_2$ structure (insets of Figure 5.5c).[51] The connectivity predicted for the $Pb_4S_3Cl_2/CsPbCl_3$ interface, shown in Figure 5.5a, was further confirmed by highlighting the atomic columns belonging to the Pb^{2+} cationic subnetwork through the quantitative analysis of HAADF-STEM images (Figure 5.5d).
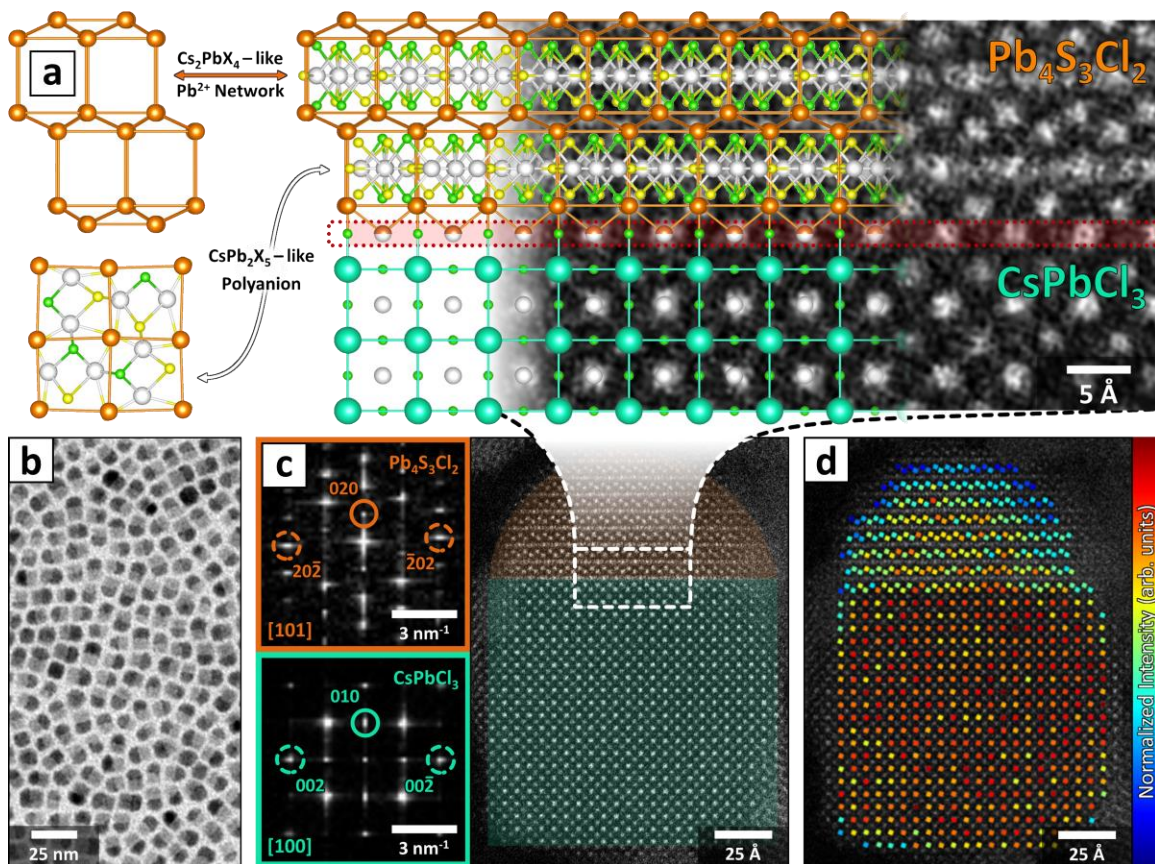
Figure 5.5. Pb$_4$S$_3$Cl$_2$/CsPbCl$_3$ epitaxial heterostructures. a) Left: Cs$_2$PbX$_4$-like Pb^{2+} subnetwork (orange Pb^{2+}) and CsPb$_2$X$_5$-like [Pb$_2$S$_3$Cl$_2$]$^-$ polyanion (white Pb^{2+}, yellow S^{2-}, green Cl$^-$) found in Pb$_4$S$_3$Cl$_2$. Right: model of the Pb$_4$S$_3$Cl$_2$/CsPbCl$_3$ epitaxial interface superimposed to a close-up view of panel (c). Atoms color code: Cs = cyan; Pb = orange/white; S = yellow; Cl = green. b) TEM image of as synthesized Pb$_4$S$_3$Cl$_2$/CsPbCl$_3$ heterostructures. c) HAADF-STEM image of a Pb$_4$S$_3$Cl$_2$/CsPbCl$_3$ heterostructure. Insets: FFTs of Pb$_4$S$_3$Cl$_2$ (top) and CsPbCl$_3$ (bottom) domains. Solid-line spots correspond to planes parallel to the heterostructure interface; dashed-line spots are perpendicular to the interface and share similar periodicities, ensuring that the lattices match. d) Column intensity map of the Pb-containing columns in the perovskite phase and in the Cs$_2$PbX$_4$-like subnetwork of the Pb$_4$S$_3$Cl$_2$ domain. Color correlates with total intensity scattered from the corresponding atomic column (red = higher intensity; blue = lower intensity). Adapted from Ref. 54.

Notably, only a negligible fraction of non-dimeric chalcohalide nanocrystals was observed in the sample, indicating that $Pb_4S_3Cl_2$ nucleated exclusively on the surface of $CsPbCl_3$ domains. This can be explained by a two-step process. First, alike the case of $CsPbBr_3$,[51] the $CsPbCl_3$ nanoclusters turned into nanocrystals during the early reaction stages. Then, the just formed perovskite nanocrystals acted as phase-selective heterogeneous nucleation seeds for $Pb_4S_3Cl_2$, providing a significant advantage over the homogeneous nucleation of $Pb_3S_2Cl_2$, which was indeed suppressed.

Such result is remarkable, as exploiting a predicted epitaxial relation with a known substrate ($CsPbCl_3$) enabled designing the synthesis for a yet unknown compound ($Pb_4S_3Cl_2$). However, this new product was still bound to the perovskite template. To set it free we then took advantage of the solubility of $CsPbCl_3$ in polar solvents by selectively etching the perovskite domains (Figure 5.6). Briefly, the heterostructures dispersed in hexane were first treated with oleylamine to improve the colloidal stability of the etched nanocrystals in nonpolar media, then the perovskite domains were etched upon exposure to dimethylformamide (DMF), that formed an emulsion with hexane. The procedure yielded remarkably uniform $Pb_4S_3Cl_2$ nanocrystals, whose structure was confirmed via high-resolution HAADF-STEM imaging and analysis of the lattice by means of FFTs (Figure 5.6b,c). Interestingly, the nanocrystals appeared to be sphere-shaped, even if the original chalcohalide domains in the heterostructures were hemispherical. We attribute this change of morphology to the need of lowering the surface energy of the extended and non-passivated facet left after the dissolution of the perovskite. It is likely that the excess

ions released by the etching process will recrystallize on the chalcohalide domains, thus reshaping them into a more stable spherical morphology.
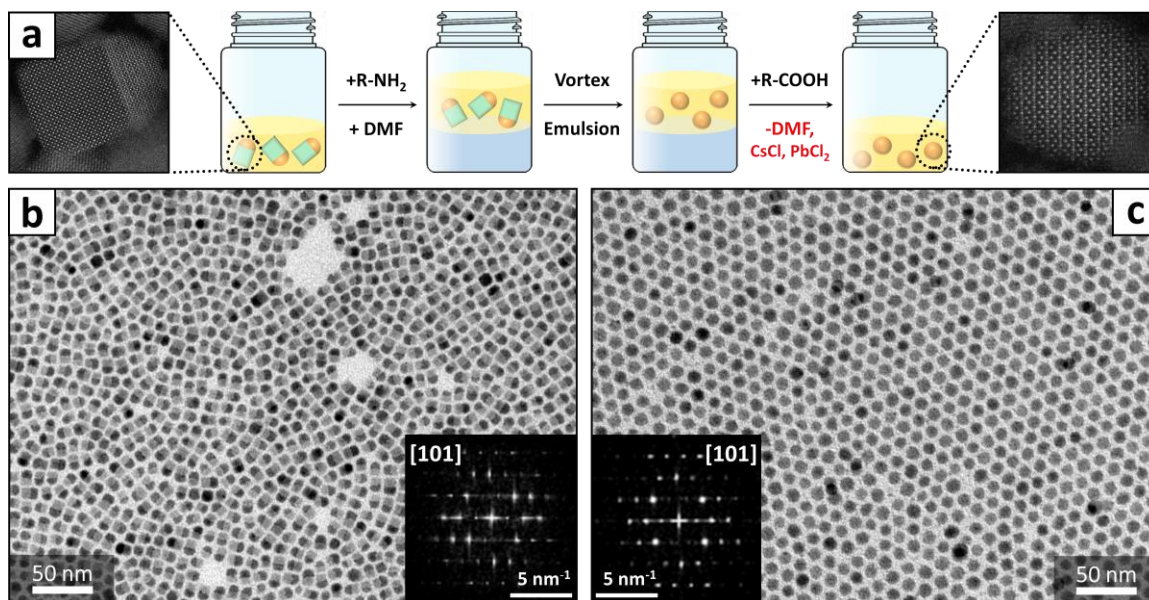
Figure 5.6. Selective etching of Pb$_4$S$_3$Cl$_2$/CsPbCl$_3$ heterostructures. a) Scheme of the DMF-assisted etching procedure that transforms Pb$_4$S$_3$Cl$_2$/CsPbCl$_3$ heterostructures into Pb$_4$S$_3$Cl$_2$ nanocrystals in presence of surfactants (R-NH$_2$ = oleylamine, R-COOH = oleic acid). Lateral panels show HAADF-STEM images of heterostructures (left) and nanocrystals (right). b) TEM images of pristine heterostructures and c) etched nanocrystals. Insets show the FFTs computed on atomic-resolution HAADF-STEM images shown in panel (a). For the heterostructure, the FFT was computed on the chalcohalide domain only. The two FFTs compared demonstrate that the Pb$_4$S$_3$Cl$_2$ domains retain the same crystal structure before and after the etching procedure. Adapted from Ref. 54.

5.3.3 Optoelectronic properties of lead chalcohalides

Combined with the results discussed in Chapter 4 of this thesis, the synthesis of chalcohalide-perovskite heterostructures and the etching of Pb$_4$S$_3$Cl$_2$ nanocrystals produced a rich variety of chalcohalide-based samples. Here we will focus on chlorine-

based materials, that offer the wider variety of stoichiometries ($Pb_3S_2Cl_2$ and $Pb_4S_3Cl_2$) and are available both as heterostructures and as stand-alone nanocrystals. Results obtained on $Pb_4S_3Br_2$-based nanomaterials were similar (see Figures 5.11-12): differences will be pointed out when relevant.

The free-standing $Pb_3S_2Cl_2$ and $Pb_4S_3Cl_2$ nanocrystals exhibited overlapping and featureless absorption spectra (Figure 5.7a, solid blue and orange lines). As anticipated in Chapter 4, a Tauc plot analysis performed on all obtained sulfohalides indicated the character of indirect semiconductors with allowed gap transitions.[55] The extrapolated optical gap values fell in the low-energy part of the visible spectrum, and were remarkably close to each other: $Pb_4S_3I_2$ = 1.823 eV; $Pb_4S_3Br_2$ = 1.822 eV; $Pb_4S_3Cl_2$ = 1.813 eV; $Pb_3S_2Cl_2$ = 1.791 eV (see Figure 5.10 and Figure 5.12, not shown for $Pb_4S_3I_2$). This is in stark contrast with the direct semiconductor nature of lead chalcogenides and lead-halide perovskites, that in the latter case feature gap energies strongly dependent on the halide composition.[19,24,56] The chalcohalide absorption tail is also visible for $Pb_4S_3Cl_2$/$CsPbCl_3$ heterostructures, combined with the blunt absorption edge of the direct-gap $CsPbCl_3$ domain (~3.1 eV = 400 nm,[19,24] Figure 5.7a, solid black plot). Such edge was instead sharp for free-standing $CsPbCl_3$ nanocrystals (Figure 5.7a, solid cyan plot), suggesting an intimate electronic connection between the two domains in the heterostructures. This was further supported by the almost complete suppression of the $CsPbCl_3$ photoluminescence (PL) when the perovskite domain was involved in a heterojunction (Figure 5.7b, inset).
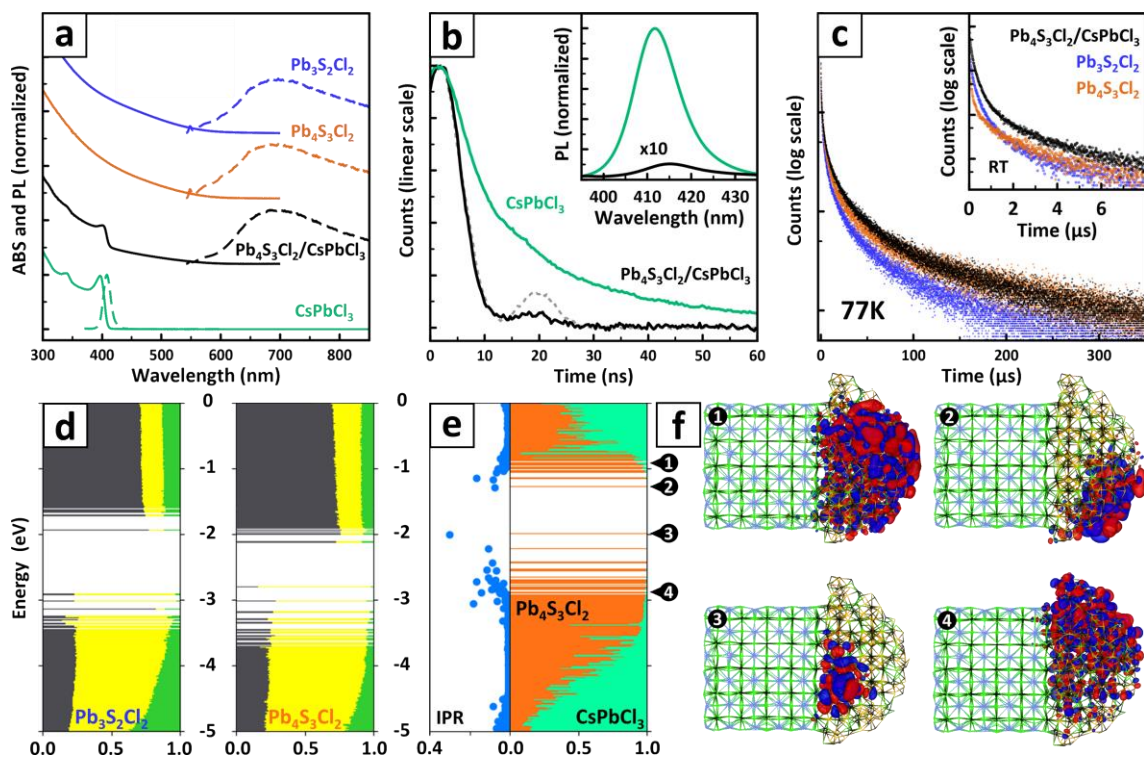
Figure 5.7. Optoelectronic properties of lead sulfochloride nanostructures. a) Absorption and PL spectra (solid and dashed lines) of free-standing $Pb_3S_2Cl_2$, $Pb_4S_3Cl_2$, $CsPbCl_3$ nanocrystals and $Pb_4S_3Cl_2/CsPbCl_3$ heterostructures. b) Decay of the ~410 nm PL from $CsPbCl_3$ in nanocrystals and in heterostructures. Dashed grey line = time response of the setup. Inset: PL spectra of $CsPbCl_3$ in nanocrystals and heterostructures (intensity ×10). The slight PL redshift in heterostructures is likely due to quantum confinement relaxation caused by the partial exciton delocalization in the sulfohalide domain. c) Decay of the ~1.8 eV PL of the three samples at room temperature and at 77 K (inset). Color code for panels (a-c): cyan = $CsPbCl_3$, blue = $Pb_4S_3Cl_2$, orange = $Pb_3S_2Cl_2$, black = $Pb_4S_3Cl_2/ CsPbCl_3$ heterostructures. d) Electronic structure of $Pb_3S_2Cl_2$ (left) and $Pb_4S_3Cl_2$ (right) nanocrystals computed by DFT. Color indicates the elemental contribution to molecular orbitals (Pb = grey; S = yellow; Cl = green). e) Electronic structure of $Pb_4S_3Cl_2/CsPbCl_3$ heterostructures, color coded by domain ($Pb_4S_3Cl_2$= orange; $CsPbCl_3$ = cyan). IPR (left panel) quantifies the degree of localization of a state, and indicates that most of gap edge states are localized trap states. f) Representation of molecular orbitals corresponding to band edge delocalized states (1,4) and to band edge trap states (2,3). In both cases, the band edge states are localized on the $Pb_4S_3Cl_2$ domain. Adapted from Ref. 54.

146

The quenching of the perovskite domain PL is likely due to a separation of photoinduced carriers in the heterostructures, for which DFT predicted a nearly type-I band alignment (Figure 5.7e, see also Figure 5.13). Indeed, the molecular orbitals corresponding to the band edge states of $Pb_4S_3Cl_2/CsPbCl_3$ heterostructures are strongly localized on the sulfochloride domain (Figure 5.7f). The faster decay of the perovskite PL in heterostructures with respect to free-standing perovskite nanocrystals (τ_{avg} ~8 ps vs ~18 ps, Figure 5.7b) further supports the hypothesis of a photoinduced carriers separation induced by band alignment. Interestingly, for bromine-based $Pb_4S_3Br_2/CsPbBr_3$ heterostructures DFT predicted a slightly different, nearly type-II band alignment, with conduction band edge states delocalized on the whole structure and valence band edge states strongly localized on the chalcohalide domain (Figure 5.14). Unfortunately, the presence of bright perovskite-only nanocrystals impurities in the $Pb_4S_3Br_2/CsPbBr_3$ heterostructures samples prevented us from gaining deeper insight from the analysis of PL lifetime (Figure 5.10), as their signal dominated that of heterostructures.

Despite being indirect-gap semiconductors, the relaxation of momentum conservation at the nanoscale allowed lead sulfohalides to display a broad PL peak at ~1.8 eV (~690 nm, see Figure 5.7a) both in nanocrystals and in heterostructures, indicating in all the cases a band edge emission. Such emission was barely detectable at room temperature (PLQY < 1%) due to thermal quenching. However, cooling the materials to 77 K resulted in a ~100-fold intensification of the PL, accompanied in the case of heterostructures by a brightening of the residual, yet still negligible, $CsPbCl_3$ emission.

In all three cases, the PL kinetics of the lead chalcohalides was markedly non-exponential, with a dominant sub-microsecond drop followed by a slower decay (Figure 5.7c). The process was slightly slower in the heterostructures with respect to both free-standing $Pb_3S_2Cl_2$ and $Pb_4S_3Cl_2$ NCs, suggesting that the $CsPbCl_3$ domain might suppress some trapping losses by passivating part of the sulfochloride domain surface. This is also consistent with our observation of a more intense PL. At low temperatures, all the PL decays became substantially slower. Fitting the dataset with an Arrhenius function yielded for all the samples an activation energy of ~15 meV. Remarkably, the spectral shape of all the samples followed a nearly identical trend with the temperature, showing a progressive shift to ~1.5 eV (~827 nm) and a band narrowing, further corroborating the strong similarities between the optoelectronic properties of these three systems (Figure 5.12). The behavior of $Pb_4S_3Br_2$ was found to be similar, both in stand-alone nanocrystals and in the $Pb_4S_3Br_2/CsPbBr_3$ heterostructures (Figure 5.10-4).

In general, the experiments reported here and in Chapter 4 of this thesis indicate that the properties of lead sulfohalides are largely independent from both stoichiometry and structure. We rationalized such behavior as a consequence of two factors. First, in these materials the band edge states feature a prominent participation of Pb^{2+} and S^{2-}, while the halides mostly contribute to states buried deep in the valence band, making the electronic properties almost halide-insensitive. Second, regardless of the structure of the specific chalcohalide, the geometry and connectivity of the coordination polyhedra surrounding both Pb^{2+} and S^{2-} is the same (see Figure 4.3), thus making the electronic properties basically structure-insensitive.

5.4 Conclusions

Heterostructures are often studied with the aim of accessing properties different from those of their constituent materials. This is the case, for example, of the $Pb_4S_3X_2/CsPbX_3$ heterostructures presented in Paragraph 5.3, where the suppression of radiative recombination in the perovskite domain and the separation of carriers at the heterojunction might be beneficial for applications like photovoltaics and photocatalysis.

However, the examples discussed in this chapter suggest that epitaxial heterostructures might be even more appealing for controlling the reactivity of constituent materials. For example, the spontaneous formation of epitaxial intermediates during reactions performed on Cs-Pb-X nanocrystals provided a convenient mechanism for transformations that would otherwise be destructive to the starting particles (Paragraph 5.2). The case of $Pb_4S_3Cl_2/CsPbCl_3$ heterostructures is even more interesting, as the presence of the perovskite domain allowed us to obtain a different lead sulfohalide phase than the $Pb_3S_2Cl_2$ produced by direct synthesis. This ultimately means that we could select the reaction product between two competing phases, a problem of great relevance in the synthesis of colloidal inorganic nanomaterials.

The idea of using perovskite nanocrystals as disposable and product-selective epitaxial templates parallels that of reaction-directing groups in organic chemistry and catalysis,[57] and may be extended to other phases with known or predictable epitaxial relations by taking advantage of the vast library of already reported nanomaterials. Such an approach might open new routes for the colloidal syntheses of nanomaterials which

are now hindered by an excessive activation energy for their homogeneous nucleation, or by the competitive formation of undesired phases.

Further progress in this direction, however, will require better prediction tools for prospective epitaxial matches than the simple comparison of lattice parameters. A starting point might be identifying pairs of structures sharing at least one atomic plane with similar geometry, like that found at the interface between $CsPbX_3$ and $Pb_4S_3X_2$. Another might be looking for phases that share similar coordination environments and sublattices, like the Cs^+ sublattice shared among the Cs-Pb-X compounds. Ultimately, a future goal will be to combine these and other, yet to be defined, criteria to sort pairs of matching structures from a database, which would greatly speed up the research into novel epitaxial heterostructures and heterostructure-templated syntheses.

5.5 Methods

This section summarizes the methods adopted for the experiments and analyses discussed in this chapter. For brevity, only the most relevant information is reported. For additional details, please refer to the original open-access publications [Refs. 51,54].

5.5.1 Synthesis methods

<u>Preparation of Cs-oleate precursors.</u> Cs_2CO_3 (2 mmol), oleic acid (OA, 7.5 mmol for $CsPbBr_3$ nanoclusters, 15 mmol for $CsPbCl_3$ nanoclusters) and 1-octadecene (ODE, 17.5 mL) were loaded into a 50 mL 3-neck flask, dried for 1h at 110 °C and then heated under N_2 to 150 °C until the solution turned clear. The resulting mixtures were transferred into glass vials filled with N_2.

<u>Preparation of PbX_2 stock solutions.</u> 2 mmol of $PbBr_2$ or $PbCl_2$ powder, OA (5 mL), and oleylamine (OLA, 5 mL) were mixed with ODE (30 mL) in a 100 mL flask. The reaction mixture was dried/degassed under vacuum for 30 min at 110 °C. Then, the flask was filled with N_2 and the temperature was raised to 150 °C. After complete dissolution of PbX_2, the solution was cooled down to room temperature and stored under N_2.

<u>Preparation of the $Pb(OA)_2$ stock solution.</u> $Pb(OAc)_2·3H_2O$ powder (2mmol), OA (1.3 mL), were mixed with ODE (18.7 mL) in a 50 ml flask. The reaction mixture was degassed under vacuum for 1h at 110 °C and then heated under N_2 to 150 °C until all $Pb(OAc)_2·3H_2O$ reacted with OA. Thereafter, the solution was cooled to room temperature and stored under N_2.

Preparation of the S-ODE stock solution. 1.5 mmol of S powder were mixed with 15 ml of ODE (pre-degassed at 120 °C for an hour) in a 20 mL glass stored under N_2. The mixture was sonicated until the complete dissolution of S.

Synthesis of $CsPbX_3$ nanoclusters. $CsPbBr_3$ and $CsPbBr_3$ nanoclusters were synthesized by adapting a previously reported method.[52] Briefly, 4 mL of the above-mentioned PbX_2 stock solution were transferred into a 20 ml glass vial filled with N_2. Thereafter, 0.20 mL (for $CsPbBr_3$) or 0.25 ml (for $CsPbCl_3$) of the Cs-oleate stock solution were injected into the PbX_2 stock solution (kept at 25°C for $CsPbBr_3$, kept at 40°C for $CsPbCl_3$) and the resulting mixture was kept under continuous stirring. After about 30 minutes, the resulting mixture was centrifuged at 8000 rpm for 5 min, the supernatant was discarded, and the precipitate was re-dispersed in 0.9 mL of degassed ODE.

Synthesis of $Pb_4S_3Br_2/CsPbBr_3$ and $Pb_4S_3Cl_2/CsPbCl_3$ heterostructures. 4.0 mL of degassed ODE were added to a 20 mL glass vial under N_2. The vial was heated to 200 °C, and 100 μL of the above-mentioned $Pb(OA)_2$ solution and 20 μL of 1-dodecanethiol (DDT, diluted in 200 μL pre-dried ODE) were added into the reaction system. Then, a mixture of S (0.1 mL) and $CsPbBr_3$ or $CsPbCl_3$ nanoclusters (0.9 mL) was rapidly injected into the reaction mixture. The reaction was allowed to proceed for 3-5 minutes and was subsequently quenched by immersing the vial in an ice bath. The crude solution was then centrifuged at 4000 rpm for 5 minutes, if needed by adding methyl acetate with volume ratio of 1 to 1, and the precipitate was redispersed in toluene.

Surface treatment of $Pb_4S_3Cl_2/CsPbCl_3$ heterostructures. A $PbCl_2$ solution, prepared by dissolving 1 mmol of $PbCl_2$ salt in ODE (15 mL), oleic acid (2.5 mL) and oleylamine (2.5 mL),

was added to the toluene dispersion containing the heterostructures, and the mixture was vortexed for 1 minute. Then, the solution was centrifuged by adding methyl acetate, and the precipitate was redispersed in hexane or toluene. The role of this treatment was to reconstruct the surface of the $CsPbCl_3$ perovskite domains after the antisolvent-assisted precipitation, and to ensure the long-term colloidal stability of the sample.

Etching of $Pb_4S_3Cl_2$/$CsPbCl_3$ heterostructures. 60 µL of oleylamine were added to 1 mL of heterostructures dispersed in hexane, corresponding to one entire batch of heterostructures. Then, 1 ml of dimethylformamide (DMF) was added to the heterostructures dispersion and the resulting mixture was vortexed for 30 seconds. After the complete phase separation of solvents (2 to 3 minutes), DMF was removed by using a syringe and pre-dried oleic acid (60 µL) was introduced in the hexane dispersion. The etched nanocrystals were centrifuged by adding methyl acetate (1:1 volume ratio) and redispersed in toluene.

Synthesis of $Pb_4S_3Br_2$ nanocrystals. The synthesis adopted in this chapter for $Pb_4S_3Br_2$ nanocrystals is different from that reported in Chapter 4, to ensure a consistent comparison with the $Pb_4S_3Br_2$ domains in the $Pb_4S_3Br_2$/$CsPbBr_3$ heterostructures. However, no significant differences were observed among the two methods. 4.0 mL of degassed ODE were added to a 20 mL glass vial under the N_2. Then the vial was heated to 150 °C, and 400 µL of the above-mentioned $PbBr_2$ solution and 100 µL of DDT were added into the reaction system, separately. Then 100 µL of the above-mentioned S-ODE solution were swiftly injected and annealed for 5 min at 150 °C. The resulting mixture was centrifuged at 4000 rpm for 5 min. The precipitate was discarded, and the supernatant

was washed with 10 mL of acetone. The suspension was centrifuged again at 8000 rpm for 5 min and the precipitate was collected.

Synthesis of CsPbBr$_3$ and CsPbCl$_3$ nanocrystals. 4.0 mL of ODE were added to a 20 mL glass vial under air and heated to 150°C, then 1.0 mL of the above-mentioned seed cluster solution in ODE (CsPbBr$_3$ or CsPbCl$_3$, without S-ODE) was swiftly injected. The mixture was annealed for 3-5 min and subsequently cooled down by using an ice water bath. The resulting mixture was centrifuged at 8000 rpm for 5 min, the supernatant was discarded, and the precipitate was dispersed in 4 mL of toluene.

5.5.2 Characterization methods

HAADF-STEM characterization. High-resolution HAADF-STEM images were acquired with a probe-corrected cubed Thermo Fisher Scientific Themis Z Microscope operating at 300 kV with a probe semi-convergence angle of 20.5 mrad. For a quantitative analysis of the HAADF-STEM image, the intensities of the individual atomic columns in a single heterostructure were analysed by using the StatSTEM software.[58] The color code in the figures correlates with the total intensity scattered from each atomic column. The intensity is calculated by fitting a Gaussian function to each atomic column: the intensity value of each column equals the volume of its Gaussian peak.

Absolute photoluminescence quantum yield. PLQY was measured using an Edinburgh FLS900 fluorescence spectrometer equipped with a Xenon lamp and a monochromator. The PLQY was measured using a calibrated integrating sphere. All samples were diluted

to an optical density of 0.1 at the corresponding excitation wavelength to minimize self-absorption phenomena.

Photoluminescence and PL dynamics. PL and PL dynamics of chalcohalides, both stand-alone and in heterostructures, were investigated using a TM-C10083CA Hamamatsu spectrometer and a Hamamatsu R943-02 time-correlated single-photon counting unit coupled to an Oriel Instruments Cornerstone 260 monochromator using either an Edinburgh Inst. EPL 405 pulsed diode laser (λ_{exc} = 405 nm, pulse duration 40 ps, variable repetition rate) or a frequency tripled/doubled pulsed Nd:YAG laser (λ_{exc} = 355/532 nm, pulse duration 5 ns, repetition rate 140 Hz) as excitation sources. PL and PL dynamics of perovskites, both stand-alone and in heterostructures, were investigated using a frequency-doubled Ti:sapphire laser (λ_{exc} = 360 nm, pulse duration 150 fs, repetition rate 76 MHz) as excitation source and a Hamamatsu streak camera as detector. To perform optical experiments at cryogenic temperatures, the samples were drop-casted onto glass substrates and placed in a variable-temperature insert of a closed-cycle helium cryostat (T = 3.5 – 300 K) or in a liquid nitrogen-cooled Oxford Instruments cryostat.

DFT computational modelling. DFT calculations were performed at the DFT/PBE/DZVP level of theory with CP2K.[59] To identify any surface localized states that could trap charge carriers, we computed the Inverse Participation Ratio (IPR). The IPR, as also demonstrated for other NCs,[60] quantifies the orbital localization of a given molecular orbital, and is defined by Equation 5.1:

$$\text{IPR}_i = \frac{\sum_\alpha |P_{\alpha,i}|^4}{(\sum_\alpha |P_{\alpha,i}|^2)^2}$$
<div align="right">Eq. 5.1</div>

Here, $P_{\alpha,i}$ represents the weight of molecular orbital i on a given atom α expanded in an atomic orbital basis. For finite systems, the IPR provides an estimate of the number of atoms that contribute to a given electronic state i. It can range from the inverse of the number of atoms in the system (when the wave function is distributed equally over all atoms in the system) to 1 in the case of states localized on single atoms. In other terms, IPR values very close to 0 identify delocalized states.

5.6 Source Publications and Contributions

This chapter is based on the following publications:

I. **Toso, S.**; Baranov, D.; Manna, L. _Hidden in Plain Sight: The Overlooked Influence of the Cs$^+$ Substructure on Transformations in Cesium Lead Halide Nanocrystals_. ACS Energy Lett. 2020, 5, 3409–3414. [Ref. 37]

II. **Toso, S.**; Baranov, D.; Manna, L. _Metamorphoses of Cesium Lead Halide Nanocrystals_. Acc. Chem. Res. 2021, 54, 498–508. [Ref. 34]

III. Imran, M.; Peng, L.; Pianetti, A.; Pinchetti, V.; Ramade, J.; Zito, J.; Di Stasio, F.; Buha, J.; **Toso, S.**; Song, J.; Infante, I.; Bals, S.; Brovelli, S.; Manna, L. _Halide Perovskite-Lead Chalcohalide Nanocrystal Heterostructures_. J. Am. Chem. Soc. 2021, 143, 1435–1446.   [Ref. 51]

IV. **Toso, S.***; Imran, M.*; Mugnaioli, E.; Moliterni, A.; Caliandro, R.; Schrenker, N. J.; Pianetti, A.; Zito, J.; Zaccaria, F.; Wu, Y.; Gemmi, M.; Giannini, C.; Brovelli, S.; Infante, I.; Bals, S.; Manna, L. _Halide Perovskites as Disposable Epitaxial Templates for the Phase-Selective Synthesis of Lead Sulfochloride Nanocrystals_. Nat. Commun. 2022 131 2022, 13, 1–10. [Ref. 54]

*These authors contributed equally

Publications (I-II) provide an overview of the compositional and structural diversity in nanocrystals of cesium lead halides, and introduce key concepts like the classification of

ion trade reactions and the preservation of the cationic subnetwork of Cs-Pb-X nanocrystals upon chemical transformations. **Publication (III)** is the first report of the synthesis of $Pb_4S_3Br_2$/CsPbBr$_3$ epitaxial heterostructures. This publication contains a first characterization of the $Pb_4S_3Br_2$/CsPbBr$_3$ epitaxial interface, and includes DFT and optical spectroscopy studies on $Pb_4S_3Br_2$ nanocrystals and $Pb_4S_3Br_2$/CsPbBr$_3$ heterostructures.

Publication (IV) reports the synthesis of $Pb_4S_3Cl_2$/CsPbCl$_3$ epitaxial heterostructures and a deeper analysis of their interface. It discusses the role of heterostructures as on-demand intermediates for phase-specific syntheses based on selective epitaxial relationships with the substrate, and shows the synthesis of $Pb_4S_3Cl_2$ through the etching of disposable CsPbCl$_3$ epitaxial templates. This publication includes DFT and spectroscopy studies on $Pb_3S_3Cl_2$ and $Pb_4S_3Cl_2$ nanocrystals, as well as on $Pb_4S_3Cl_2$/CsPbCl$_3$ heterostructures.

The work discussed in this chapter was made possible by the collaborative effort of a large team of scientists. Hereby, the major contributions are listed. D. Baranov and L. Manna actively contributed with discussion, suggestions, and guidance in writing Publications (I) and (II). Our discussions eventually led to formalizing the concepts of ion trade reactions and of the Cs$^+$ subnetwork preservation in Cs-Pb-X $\rightarrow$ Cs-Pb-X transformations. In Publications (III-IV), M. Imran developed and optimized the synthesis of all heterostructure samples, and optimized the etching procedures for obtaining $Pb_4S_3Cl_2$ nanocrystals starting from $Pb_4S_3Cl_2$/CsPbCl$_3$ heterostructures. He was assisted by L. Peng. The high-resolution TEM data were collected and analyzed by J. Buha, E. Bladt, N. Schrenker, I. Lobato, J. Ramade, and S. Bals. DFT calculations were performed by J. Zito, F. Zaccaria, and I. Infante. The optical characterization of materials was curated by A.

Pianetti and S. Brovelli. With the help of the electron microscopy team, I rationalized the structural relations between all phases involved in the formation of heterostructures, constructed the atomistic models of interfaces, and on these bases predicted the possibility of templating the synthesis of $Pb_4S_3Cl_2$ nanocrystals through a dimeric intermediate, which was eventually achieved experimentally by M. Imran. L. Manna coordinated and supervised all the research projects. All the coauthors not mentioned here were either involved in aspects of the work not discussed in this chapter, or provided general support to the progress of the project. To all colleagues goes my deep gratitude for their invaluable help.

5.7 Copyright

Some elements of this chapter were adapted from external sources:

5.8 Bibliography

1.   Lauhon, L. J., Gudlksen, M. S., Wang, D. & Lieber, C. M. Epitaxial core-shell and core-multishell nanowire heterostructures. *Nature* **420**, 57–61 (2002).

2.   Reiss, P., Protière, M. & Li, L. Core/shell semiconductor nanocrystals. *Small* **5**, 154–168 (2009).

3.   Dabbousi, B. O. *et al.* (CdSe)ZnS core-shell quantum dots: Synthesis and characterization of a size series of highly luminescent nanocrystallites. *J. Phys. Chem. B* **101**, 9463–9475 (1997).

4.   Peng, X., Schlamp, M. C., Kadavanich, A. V. & Alivisatos, A. P. Epitaxial growth of highly luminescent CdSe/CdS core/shell nanocrystals with photostability and electronic accessibility. *J. Am. Chem. Soc.* **119**, 7019–7029 (1997).

5.   Li, J. J. *et al.* Large-scale synthesis of nearly monodisperse CdSe/CdS core/shell nanocrystals using air-stable reagents via successive ion layer adsorption and reaction. *J. Am. Chem. Soc.* **125**, 12567–12575 (2003).

6.   Ji, B., Koley, S., Slobodkin, I., Remennik, S. & Banin, U. ZnSe/ZnS Core/Shell Quantum Dots with Superior Optical Properties through Thermodynamic Shell Growth. *ACS Appl. Mater. Interfaces* **20**, 2387–2395 (2020).

7.   Shen, H. *et al.* Phosphine-free synthesis of high quality ZnSe, ZnSe/ZnS, and Cu-, Mn-doped ZnSe nanocrystals. *Dalt. Trans.* 10534–10540 (2009).

8.   Manna, L., Milliron, D. J., Meisel, A., Scher, E. C. & Alivisatos, A. P. Controlled growth of tetrapod-branched inorganic nanocrystals. *Nat. Mater. 2003 26* **2**, 382–385 (2003).

9.   Arciniegas, M. P. *et al.* Self-assembly of octapod-shaped colloidal nanocrystals into a hexagonal ballerina network embedded in a thin polymer film. *Nano Lett.* **14**, 1056–1063 (2014).

10.   Zhang, X. *et al.* Heterostructural $CsPbX_3$-PbS (X = Cl, Br, I) Quantum Dots with Tunable Vis-NIR Dual Emission. *J. Am. Chem. Soc.* **142**, 4464–4471 (2020).

11.   Gao, F. *et al.* Highly stable and luminescent silica-coated perovskite quantum dots at nanoscale-particle level via nonpolar solvent synthesis. *Chem. Eng. J.* **407**, 128001 (2021).

12.   Zhong, Q. *et al.* One-pot synthesis of highly stable $CsPbBr_3$@SiO_2 core-shell nanoparticles. *ACS Nano* **12**, 8579–8587 (2018).

13. Dutta, S. K., Bera, S. & Pradhan, N. Why Is Making Epitaxially Grown All Inorganic Perovskite-Chalcogenide Nanocrystal Heterostructures Challenging? Some Facts and Some Strategies. *Chem. Mater.* **33**, 3868–3877 (2021).

14. Bera, S. & Pradhan, N. Perovskite Nanocrystal Heterostructures: Synthesis, Optical Properties, and Applications. *ACS Energy Lett.* **5**, 2858–2872 (2020).

15. Liu, J. & Zhang, J. Nanointerface Chemistry: Lattice-Mismatch-Directed Synthesis and Application of Hybrid Nanocrystals. *Chem. Rev.* **120**, 2123–2170 (2020).

16. Shamsi, J. *et al.* Colloidal CsX (X = Cl, Br, I) Nanocrystals and Their Transformation to $CsPbX_3$ Nanocrystals by Cation Exchange. *Chem. Mater.* **30**, 79–83 (2018).

17. Akkerman, Q. A. *et al.* Nearly Monodisperse Insulator Cs_4PbX_6 (X = Cl, Br, I) Nanocrystals, Their Mixed Halide Compositions, and Their Transformation into CsPbX3Nanocrystals. *Nano Lett.* **17**, 1924–1930 (2017).

18. Akkerman, Q. A. *et al.* Fully Inorganic Ruddlesden-Popper Double Cl-I and Triple Cl-Br-I Lead Halide Perovskite Nanocrystals. *Chem. Mater.* **31**, 2182–2190 (2019).

19. Protesescu, L. *et al.* Nanocrystals of Cesium Lead Halide Perovskites ($CsPbX_3$, X = Cl, Br, and I): Novel Optoelectronic Materials Showing Bright Emission with Wide Color Gamut. *Nano Lett.* **15**, 3692–3696 (2015).

20. Yang, T. *et al.* Superior Photodetectors Based on All-Inorganic Perovskite $CsPbI_3$ Nanorods with Ultrafast Response and High Stability. *ACS Nano* **12**, 1611–1617 (2018).

21. Wang, R. *et al.* All-Inorganic Perovskite $CsPb_2Br_5$ Nanosheets for Photodetector Application Based on Rapid Growth in Aqueous Phase. *ACS Appl. Mater. Interfaces* **12**, 41919–41931 (2020).

22. Klein, E., Lesyuk, R. & Klinke, C. Insights into the Formation Mechanism of Two-Dimensional Lead Halide Nanostructures. *Nanoscale* **10**, 4442–4451 (2018).

23. Nedelcu, G. *et al.* Fast Anion-Exchange in Highly Luminescent Nanocrystals of Cesium Lead Halide Perovskites ($CsPbX_3$, X = Cl, Br, I). *Nano Lett.* **15**, 5635–5640 (2015).

24. Akkerman, Q. A. *et al.* Tuning the optical properties of cesium lead halide perovskite nanocrystals by anion exchange reactions. *J. Am. Chem. Soc.* **137**, 10276–10281 (2015).

25. Akkerman, Q. A., Rainò, G., Kovalenko, M. V. & Manna, L. Genesis, challenges and opportunities for colloidal lead halide perovskite nanocrystals. *Nat. Mater.* **17**, 394–405 (2018).

26. Dey, A. *et al.* State of the Art and Prospects for Halide Perovskite Nanocrystals. *ACS Nano* **15**, 10775–10981 (2021).

27. Li, Y., Huang, H., Xiong, Y., Kershaw, S. V. & Rogach, A. L. Reversible transformation between $CsPbBr_3$ and Cs_4PbBr_6 nanocrystals. *CrystEngComm* **20**, 4900–4904 (2018).

28. Palazon, F. *et al.* Postsynthesis Transformation of Insulating Cs_4PbBr_6 Nanocrystals into Bright Perovskite $CsPbBr_3$ through Physical and Chemical Extraction of CsBr. *ACS Energy Lett.* **2**, 2445–2448 (2017).

29. Wu, L. *et al.* From Nonluminescent Cs_4PbX_6 (X = Cl, Br, I) Nanocrystals to Highly Luminescent $CsPbX_3$ Nanocrystals: Water-Triggered Transformation through a CsX-Stripping Mechanism. *Nano Lett.* **17**, 5799–5804 (2017).

30. Palazon, F. *et al.* Changing the Dimensionality of Cesium Lead Bromide Nanocrystals by Reversible Postsynthesis Transformations with Amines. *Chem. Mater.* **29**, 4167–4171 (2017).

31. Udayabhaskararao, T. *et al.* A Mechanistic Study of Phase Transformation in Perovskite Nanocrystals Driven by Ligand Passivation. *Chem. Mater.* **30**, 84–93 (2018).

32. Shen, W., Ruan, L., Shen, Z. & Deng, Z. Reversible light-mediated compositional and structural transitions between $CsPbBr_3$ and $CsPb_2Br_5$ nanosheets. *Chem. Commun.* **54**, 2804–2807 (2018).

33. Li, J. *et al.* Inter-conversion between different compounds of ternary Cs-Pb-Br system. *Materials (Basel).* **11**, (2018).

34. Toso, S., Baranov, D. & Manna, L. Metamorphoses of Cesium Lead Halide Nanocrystals. *Acc. Chem. Res.* **54**, 498–508 (2021).

35. Mizusaki, J., Arai, K. & Fueki, K. Ionic conduction of the perovskite-type halides. *Solid State Ionics* **11**, 203–211 (1983).

36. Eames, C. *et al.* Ionic transport in hybrid lead iodide perovskite solar cells. *Nat. Commun.* **6**, 1–8 (2015).

37. Toso, S., Baranov, D. & Manna, L. Hidden in Plain Sight: The Overlooked Influence of the Cs^+ Substructure on Transformations in Cesium Lead Halide Nanocrystals. *ACS Energy Lett.* **5**, 3409–3414 (2020).

38. Quarti, C., Katan, C. & Even, J. Physical properties of bulk, defective, 2D and 0D metal halide perovskite semiconductors from a symmetry perspective. *J. Phys. Mater.* **3**, 042001 (2020).

39. Palazon, F. *et al.* From $CsPbBr_3$ Nano-Inks to Sintered $CsPbBr_3$-$CsPb_2Br_5$ Films via Thermal Annealing: Implications on Optoelectronic Properties. *J. Phys. Chem. C* **121**, 11956–11961 (2017).

40. Li, G. *et al.* Shape and phase evolution from $CsPbBr_3$ perovskite nanocubes to tetragonal $CsPb_2Br_5$ nanosheets with an indirect bandgap. *Chem. Commun.* **52**, 11296–11299 (2016).

41. Baranov, D. *et al.* Transforming colloidal Cs_4PbBr_6 nanocrystals with poly(maleic anhydride-alt -1-octadecene) into stable $CsPbBr_3$ perovskite emitters through intermediate heterostructures. *Chem. Sci.* **11**, 3986–3995 (2020).

42. Zheng, Y. *et al.* All-inorganic dual-phase halide perovskite nanorings. *Nano Res.* **13**, 2994–3000 (2020).

43. Almeida, G., Infante, I. & Manna, L. Resurfacing halide perovskite nanocrystals. *Science (80-.).* **364**, 833–834 (2019).

44. Quarta, D. *et al.* Stable Ligand Coordination at the Surface of Colloidal $CsPbBr_3$ Nanocrystals. *J. Phys. Chem. Lett.* **10**, 3715–3726 (2019).

45. Huang, Z. P. *et al.* In Situ Growth of 3D/2D ($CsPbBr_3$/$CsPb_2Br_5$) Perovskite Heterojunctions toward Optoelectronic Devices. *J. Phys. Chem. Lett.* **11**, 6007–6015 (2020).

46. Straus, D. B., Guo, S. & Cava, R. J. Kinetically Stable Single Crystals of Perovskite-Phase CsPbI3. *J. Am. Chem. Soc.* **141**, 11435–11439 (2019).

47. Swarnkar, A. *et al.* Quantum dot-induced phase stabilization of α-CsPbI3 perovskite for high-efficiency photovoltaics. *Science (80-.).* **354**, 92–95 (2016).

48. Aebli, M. *et al.* White $CsPbBr_3$: Characterizing the One-Dimensional Cesium Lead Bromide Polymorph. *Helv. Chim. Acta* **103**, (2020).

49. Acharyya, P., Maji, K., Kundu, K. & Biswas, K. 2D Nanoplates and Scaled-Up Bulk Polycrystals of Ruddlesden-Popper $Cs_2PbI_2Cl_2$ for Optoelectronic Applications. *ACS Appl. Nano Mater.* **3**, 877–886 (2020).

162

50.   Parobek, D., Dong, Y., Qiao, T. & Son, D. H. Direct Hot-Injection Synthesis of Mn-Doped CsPbBr$_3$ Nanocrystals. *Chem. Mater.* **30**, 2939–2944 (2018).

51.   Imran, M. *et al.* Halide Perovskite-Lead Chalcohalide Nanocrystal Heterostructures. *J. Am. Chem. Soc.* **143**, 1435–1446 (2021).

52.   Peng, L., Dutta, A., Xie, R., Yang, W. & Pradhan, N. Dot-Wire-Platelet-Cube: Step Growth and Structural Transformations in CsPbBr$_3$ Perovskite Nanocrystals. *ACS Energy Lett.* **3**, 2014–2020 (2018).

53.   Zhang, B. *et al.* Stable CsPbBr$_3$ Nanoclusters Feature a Disk-like Shape and a Distorted Orthorhombic Structure. *J. Am. Chem. Soc.* **144**, 5059–5066 (2022).

54.   Toso, S. *et al.* Halide perovskites as disposable epitaxial templates for the phase-selective synthesis of lead sulfochloride nanocrystals. *Nat. Commun. 2022 131* **13**, 1–10 (2022).

55.   Zanatta, A. R. Revisiting the optical bandgap of semiconductors and the proposal of a unified methodology to its determination. *Sci. Rep.* **9**, 11225 (2019).

56.   Aminorroaya Yamini, S., Patterson, V. & Santos, R. Band-Gap Nonlinearity in Lead Chalcogenide (PbQ, Q = Te, Se, S) Alloys. *ACS Omega* **2**, 3417–3423 (2017).

57.   Rousseau, G. & Breit, B. Removable directing groups in organic synthesis and catalysis. *Angew. Chemie - Int. Ed.* **50**, 2450–2494 (2011).

58.   De Backer, A., van den Bos, K. H. W., Van den Broek, W., Sijbers, J. & Van Aert, S. StatSTEM: an Efficient Approach for Accurate and Precise Model-Mased Quantification of Atomic Resolution Electron Microscopy Images. *Ultramicroscopy* **171**, 104–116 (2016).

59.   Kühne, T. D. *et al.* CP2K: An electronic structure and molecular dynamics software package - Quickstep: Efficient and accurate electronic structure calculations. *J. Chem. Phys.* **152**, 194103 (2020).

60.   Houtepen, A. J., Hens, Z., Owen, J. S. & Infante, I. On the Origin of Surface Traps in Colloidal II-VI Semiconductor Nanocrystals. *Chem. Mater.* **29**, 752–761 (2017).
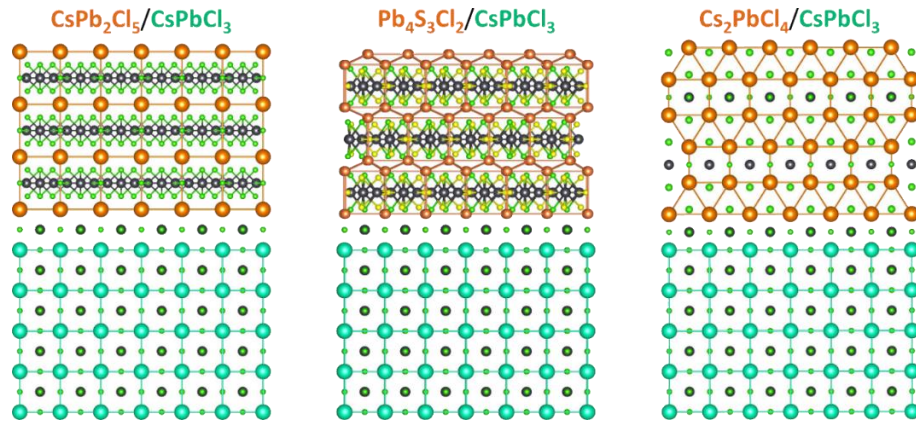
Figure 5.8. Pb₄S₃Cl₂/CsPbCl₃ interface compared with Cs-Pb-X/Cs-Pb-X interfaces. The $Pb_4S_3Cl_2/CsPbCl_3$ interface is shown in the middle, compared with the hypothetical $CsPb_2Cl_5/CsPbCl_3$ and $Cs_2PbCl_4/CsPbCl_3$ interfaces. Atoms color code: Cs = cyan; Pb = grey; S = yellow; Cl = green. The orange atoms are Pb in $Pb_4S_3Cl_2$ and Cs in $CsPb_2Cl_5$ and Cs_2PbCl_4. This color choice highlights the similarities between the two cationic subnetworks. [Ref. 54]
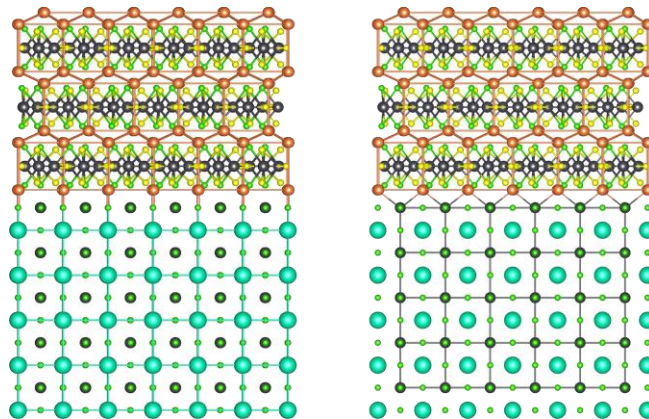
Figure 5.9. Cationic subnetworks at the Pb₄S₃Cl₂/CsPbCl₃ interface. The Pb^{2+} cationic subnetwork of $Pb_4S_3Cl_2$ matches both with the Cs^+ (left) and with the Pb^{2+} (right) subnetworks of $CsPbCl_3$ at the same time. Atoms color code: Cs = cyan; Pb = grey/orange; S = yellow; Cl = green. [Ref. 54]
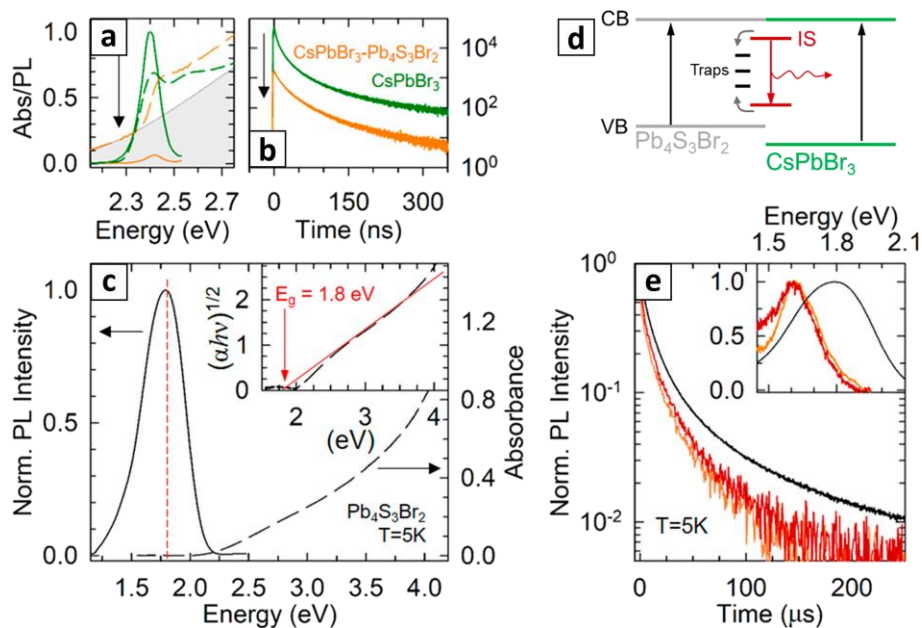
Figure 5.10. Optical properties of Pb$_4$S$_3$Br$_2$ nanocrystals and Pb$_4$S$_3$Br$_2$/CsPbBr$_3$ heterostructures. a) Absorption (dashed lines) and PL (solid lines) spectra of CsPbBr$_3$ nanocrystals and Pb$_4$S$_3$Br$_2$/CsPbBr$_3$ heterostructures. b) PL decay curves of CsPbBr$_3$ nanocrystals and Pb$_4$S$_3$Br$_2$/CsPbBr$_3$ heterostructures normalized to the intensity of bare CsPbBr$_3$ nanocrystals. The black arrow highlights the quenching of the PL intensity in the heterostructure. c) Absorption and PL spectra of Pb$_4$S$_3$Br$_2$ nanocrystals (excitation at 3.5 eV). Tauc plot showing the linear dependence (red line) of $(\alpha h v)^{1/2}$ with the photon energy typical of indirect band gap transitions. The red arrow indicates the optical band gap energy, that is compatible with the PL peak position. d) Schematic depiction of energy levels in Pb$_4$S$_3$Br$_2$/CsPbBr$_3$ heterostructures, highlighting the radiative recombination (red arrow) in interface localized states following the excitation of either the perovskite or sulfobromide domains. e) PL decay curves of the Pb$_4$S$_3$Br$_2$ domain of Pb$_4$S$_3$Br$_2$/CsPbBr$_3$ heterostructures at T = 5 K upon excitation with 2.33 eV and 3.5 eV radiation (orange and red lines, respectively), compared to the PL decay curve of stand-alone Pb$_4$S$_3$Br$_2$ nanocrystals (black line). Inset: PL spectra of Pb$_4$S$_3$Br$_2$/CsPbBr$_3$ heterostructures at T = 5 K at the same excitation energies, compared to the PL spectrum of Pb$_4$S$_3$Br$_2$ nanocrystals at the same temperature. [Ref. 51]
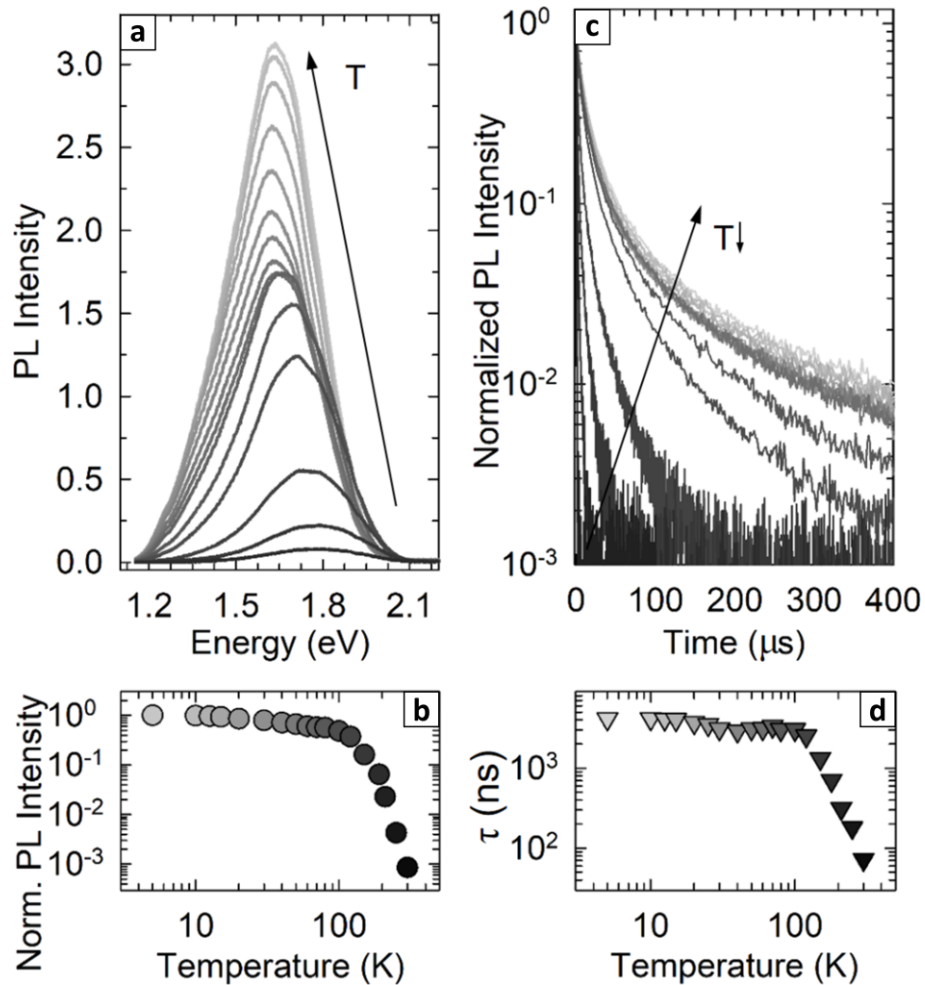
Figure 5.11. Temperature-dependent optical properties of Pb₄S₃Br₂ nanocrystals. a) PL spectra of $Pb_4S_3Br_2$ nanocrystals upon lowering the temperature from T = 300 K to T = 5 K (from black to light grey curves, respectively). b) Integrated PL intensity values as a function of temperature extracted from the PL spectra reported in panel (a= and normalized to the value a T = 5 K. c) Time-resolved PL traces of $Pb_4S_3Br_2$ nanocrystals upon lowering the temperature from T = 300 K to T = 5 K (from black to light grey curves, respectively). d) temperature dependence of the effective PL decay lifetimes (τ, evaluated as the time after which the PL intensity drops by a factor of e) extracted from the PL decay curved reported in panel (c). [Ref. 51]
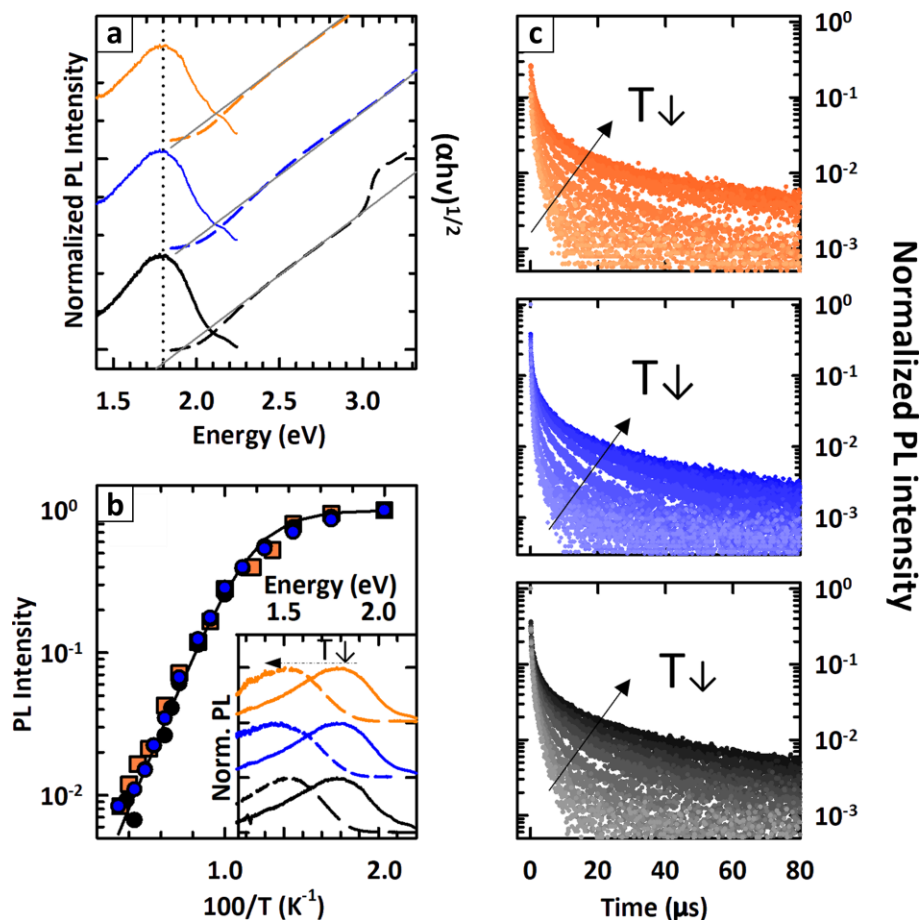
Figure 5.12. Optical properties of lead sulfochloride nanocrystals and Pb₄S₃Br₂/CsPbBr₃ heterostructures. a) Photoluminescence spectra (solid lines) and Tauc plot analysis (dashed lines) of $Pb_3S_2Cl_2$ nanocrystals (blue), $Pb_4S_3Cl_2$ nanocrystals (orange) and $Pb_4S_3Cl_2/CsPbCl_3$ heterostructures (black), superimposed to the corresponding fit lines (grey). b) Temperature dependence of the photoluminescence intensity of $Pb_3S_2Cl_2$ nanocrystals (blue), $Pb_4S_3Cl_2$ nanocrystals (orange) and $Pb_4S_3Cl_2/CsPbCl_3$ heterostructures (black). Inset: temperature-dependent spectral shift of the photoluminescence spectra, measured at 300K (solid lines) and at 77K (dashed lines). c) Time resolved photoluminescence spectra as a function of temperature for the three samples. Darker lines = lower temperatures, lighter lines = higher temperatures. [Ref. 54]
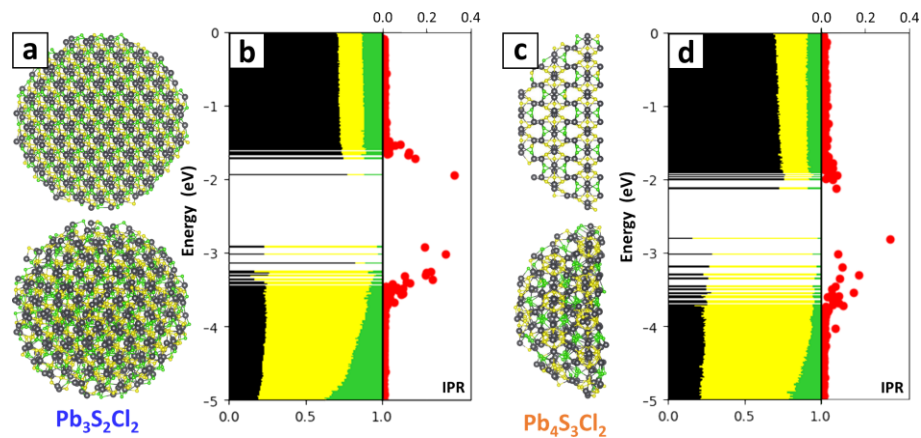
Figure 5.13. DFT calculations on Pb₃S₂Cl₂ and Pb₄S₃Cl₂ nanocrystals. a,c) Models of $Pb_3S_2Cl_2$ (a) and $Pb_4S_3Cl_2$ (c) nanocrystals, before (top) and after (bottom) the structure optimization. The latter model is hemispherical because it was used as a part of the $Pb_4S_3Cl_2/CsPbCl_3$ heterostructure model shown in Figure 5.7f. b,d) Fractional DOS (color-coded by element) and IPR (in red) of models shown in panels (a,c). Atoms color code: Pb = black; S = yellow; Cl = green. [Ref. 54]
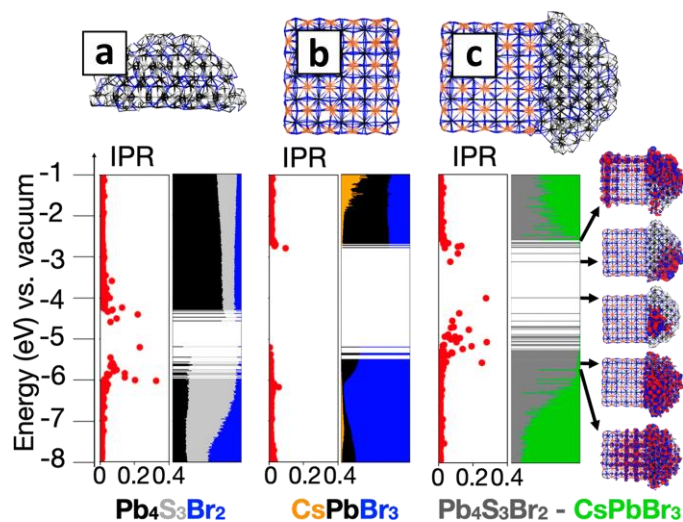
Figure 5.14. Electronic structure and IPR of Pb₄S₃Br₂/CsPbBr₃ heterostructures. a) $Pb_4S_3Br_2$ hemispherical nanocrystal, b) CsPbBr3 cubic nanocrystal, and (c) heterostructure models. Colors indicates the contribution of each nanocrystal element or heterostructure moiety to molecular orbitals. On the right, delocalized and localized molecular orbitals at the band edges. [Ref.51]

CHAPTER 6:

NANOCRYSTAL SOLIDS

6.1 What is a Colloidal Superlattice?

In the previous chapters we explored nanocrystals as individual entities and as domains in heterostructure dimers. The next step in our journey toward increasingly complex nanomaterials is gathering many of them to form ordered nanocrystal solids, which go by the name of colloidal superlattices.

The term *superlattice* is not exclusive to nanochemistry: it derives from thin films made of alternated crystalline materials that were grown by physical methods starting from the 70's.[1–4] There, the name superlattice was chosen because their structure was periodic at two different length scales: at the atomic one, due to the crystallinity of each layer, and at the nanometric one, due to the neat alternation of many layers. Since any periodicity is mathematically described by a lattice, these films were effectively lattices of lattices: hence, superlattice was deemed a fitting name. The colloidal nanocrystals community later borrowed this term for aggregates where particles arrange with a periodic packing geometry, resembling that of atoms in a crystal. Once again, it was the copresence of the nanocrystal atomic lattice and the nanoscale packing that earned them the name of superlattices.

Ordered nanocrystal solids were first reported in 1989 by Bentzon *et al.*, who observed the spontaneous organization of iron oxide spherical nanocrystals upon drop cast on a TEM grid.[5] Since then, the field has grown fast, fueled by the increasing variety of available nanocrystals and by the promises of collective properties deriving from the interaction of particles put in close proximity.[6,7] Indeed, there are reports of collective properties in colloidal superlattices stemming from optical interference,[9,10] and plasmonic,[11,12] electronic,[13,14] vibrational,[15,16] or magnetic coupling.[17,18] More recently, the quest for collective properties led to the observation, still under debate, of an ultrafast photoluminescence burst produced by $CsPbBr_3$ nanocrystal superlattices, one of the systems discussed in this chapter, that was attributed to a collective radiative phenomenon known as superfluorescence.[19–21]

On a structural perspective, the diversity of nanocrystal shapes and sizes results in a variety of packing geometries, formed either by one or many nanocrystal types at the same time. Remarkably, the same geometries are often found in atomic crystals. For example, superlattices containing only one nanocrystal type adopt simple cubic, BCC, FCC, or HCP geometries, all typical of pure elements (Figure 6.1a).[8,22–25] Instead, binary or ternary superlattices, where the interplay of shapes and sizes allows for more complex packing modes, often adopt the same structures as binary and ternary inorganic compounds: NaCl, Cu_3Au, AlB_{13}, $CaTiO_3$, and so on (Figure 6.1b-f).[8,26–29]
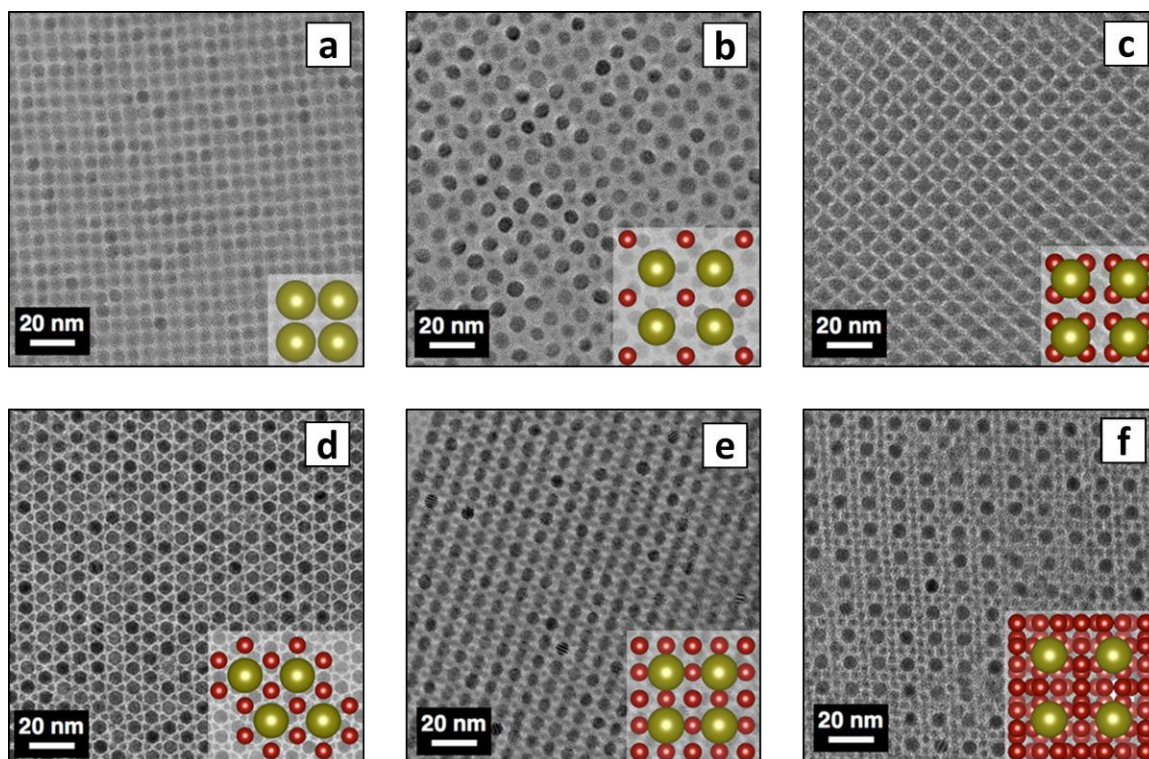
Figure 6.1. Examples of structural diversity in binary superlattices.
a) A superlattice of spherical PbS nanocrystals displays a simple cubic packing. When the same nanocrystals are co-assembled with smaller $Cu_{2-x}S$ nanocrystals in different experimental conditions, the give rise to a variety of different packing modes, that match the symmetry of binary inorganic phases: CuAu (b), AlB_4 (c), AlB_2 (d), Cu_3Au (e), and $AlBi_{13}$ (f). Adapted from Ref. 8.

Given the copresence of atomic and nanometric periodicities, superlattices are ideal samples for diffraction experiments, with Grazing Incidence Small/Wide Angle Scattering (GISAXS/GIWAXS) in the front row.[24,30–34] GISAXS is used to determine the superlattice packing geometry, that can be described by a unit cell and a space group in analogy with atomic crystals. GIWAXS instead is sensitive to the structure and orientation of nanocrystals, that are crucial to describe the interparticle interactions and the superlattice packing. A limit of the GISAXS/GIWAXS combination, however, is that

GIWAXS probes atomic scales, while the GISAXS signal is averaged over the X-ray beam projection on the sample surface, that can encompass thousands of nanocrystals at a time. This leaves a blind spot for the structural characterization at scales comparable with particle-to-particle interactions, that in case of electronic, plasmonic, or magnetic coupling are limited to the close surroundings of a nanocrystal.

In this chapter, I propose a novel approach to the characterization of nanocrystal superlattices, based on a constructive interference effect that is well-known for epitaxial multilayer films,[35] but was not reported before on colloidal systems. This effect, which I refer to as Multilayer Diffraction in analogy, exploits the collective interference of X-rays scattered at wide angles by each individual nanocrystal. Therefore, it is highly sensitive to their local environment, and covers the gap left open by GISAXS and GIWAXS. Such collective interference effect was (re)discovered serendipitously, but once rationalized it proved to be a valuable tool for investigating nanocrystal solids.

6.2 The (Re)discovery of Multilayer Diffraction

The (re)discovery of Multilayer Diffraction was due to chance. In 2019 we were investigating the spectral properties of $CsPbBr_3$ nanocrystal solids grown at a liquid-liquid interface,[36] an approach that, albeit effective, yielded samples submerged in oily liquids and hard to manipulate. Therefore, we started growing superlattices by self-assembling $CsPbBr_3$ nanocrystals (Figures 6.10-11) on silicon substrates, that were more versatile for a variety of experiments. One was X-ray diffraction (Figure 6.2), which we first performed to monitor the sample stability. Based on prior works on nanocrystal assemblies,[37] we

expected to observe few broad reflections selected by the nanocrystals orientation, as only lattice planes parallel to the substrate would produce signals. Indeed, only two of the CsPbBr$_3$ Bragg peaks were visible, but, surprisingly, one was noticeably split in fringes (Figure 6.2a).[38]

If interpreted through the Scherrer equation,[39] the width of such fringes would indicate a ~37 nm crystal size, much larger than the ~10 nm CsPbBr$_3$ nanocubes we self-assembled (Figure 6.10). Moreover, the fringes would shift and change their intensities upon exposing the sample to vacuum (Figure 6.12), but the sample itself did not suffer any other visible alteration. A first hint of their origin came from plotting the pattern in the scattering vector scale $q = 4\pi \sin(\theta)/\lambda_{X-ray}$. This revealed that fringes were regularly spaced in q, compatibly with a real space periodicity of $\Lambda = 2\pi/\Delta q$ = 12.2 nm (Figure 6.2b). Such length matched the nanocrystals center-to-center distance measured by TEM (Figure 6.10), persuading us that the peak split was not due to changes in the nanocrystals structure, but rather to their packing within the superlattice.

Indeed, we soon learned that similar, periodically spaced fringes have been observed in multilayer epitaxial thin films composed of neatly stacked layers of materials with different crystal structures, where they are called satellite peaks. These films have been studied since the 80's, and many theoretical descriptions for their diffraction patterns were developed over the years.[42–49] In what follows, we picked the formalism developed by Schuller and colleagues,[4,35,50,51] whose modular nature makes it easy to tune, and we adapted it to describe superlattices of colloidal nanocrystals. It is fascinating that 40 years after coherent diffraction was first observed on epitaxial thin films[4] the same

effect could be revisited in colloidal superlattices, which are, at first glance, such remarkably different materials.
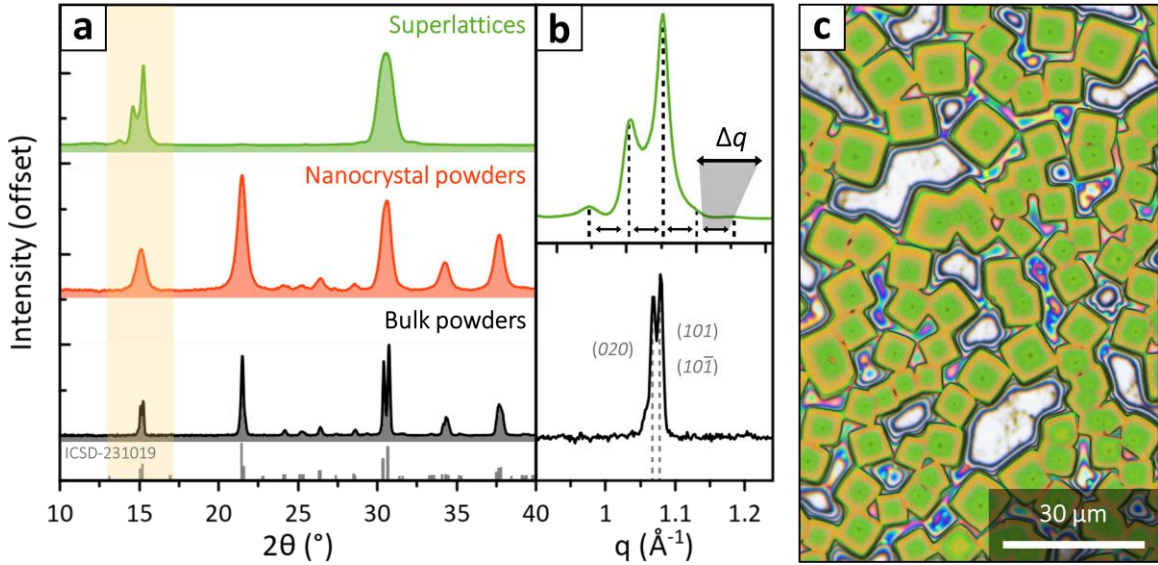
Figure 6.2. XRD patterns of different CsPbBr₃ samples. a) XRD patterns of CsPbBr$_3$ superlattices (green), nanocrystal powders (red), and bulk powders (black, orthorhombic *P*nma reference in grey).[40] Peaks from nanocrystal powders retain the positions and relative intensities of bulk, but are broadened due to the nanometric size. In the superlattices pattern, most peaks are suppressed due to preferred orientation, and the first Bragg peak (yellow) is visibly split. b) Close-up of the first superlattice peak plotted in *q*-scale (top). Superlattice fringes are sometimes confused with the cubic (100) → orthorhombic (020)/(101)/(10$\bar{1}$) peak split, shown on the bulk pattern for comparison (bottom). c) Optical microscopy image of CsPbBr$_3$ nanocube superlattices. Adapted from Ref. 41, data originally from Refs. 22,38.

6.3 Principles of Multilayer Diffraction

Before diving into experimental results we shall provide an overview of the
Multilayer Diffraction theory, here described with the bilayer formalism proposed by
Schuller *et al*.[4,35,50,51] First, we should spend a word on the data collection method. The
ideal experiment for observing Multilayer Diffraction is a symmetric θ:2θ scan, a widely
available diffraction geometry that is often used to characterize powders and thin films.
The main property of such geometry is that the scattering vector q stays always
perpendicular to the sample surface (Figure 6.3a). This condition allows describing the
sample as a vertical stack of planes, disregarding its in-plane structure, and justifies the
analogy between nanocrystals superlattices and thin films. Interference fringes may be
observed in other geometries as well, but the theory discussed here would not enable
their quantitative description.

6.3.1 The bilayer formalism

The diffraction pattern of a multilayer is described by the sum in phase of all the
radiation scattered by each individual layer. This is especially true for the high-angle range
($q > 1$ Å^{-1}), where multiple scattering effects, surface refraction/reflection effects, and the
impact of film roughness are negligible.[35] In principle, the stacking sequence of a
multilayer could be complicated at will. However, a model based on two different
alternating layers, named *A* and *B*, offers enough flexibility to describe most colloidal
superlattices currently within experimental reach (Figure 6.3b). In the model, *A* and *B* are
separated by a non-scattering buffer layer, whose thickness ℓ changes randomly at each

iteration. This dummy layer represents inhomogeneities in the *A-B* interfaces, and is a way of describing the disorder found in real-world samples.
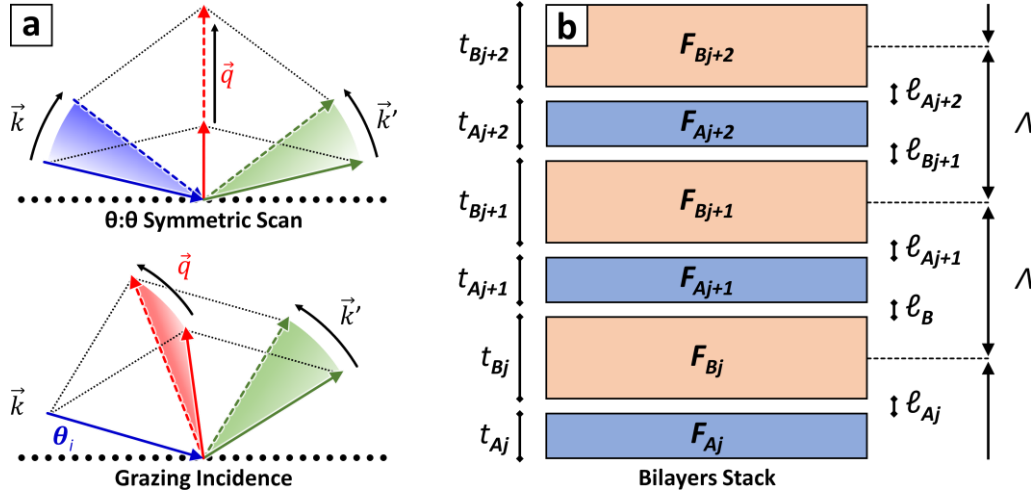
Figure 6.3. Scattering geometries and bilayer formalism. a) Representation of two different scattering geometries: θ:2θ symmetric scan (top) and grazing incidence (bottom). Here, $\vec{k}$ and $\vec{k}'$ are the wave vectors of the incident and scattered radiation, $\vec{q}$ is the scattering vector, and θ$_i$ is the fixed angle of incidence adopted in grazing-incidence geometries (here widened for representation purposes). Both geometries can scan a *q*-range, as suggested by the red arrow changing its length, but only in the first case the scattering vector $\vec{q}$ remains perpendicular to the substrate surface. b) Bilayer representation of a superlattice composed of two materials, *A* and *B*. Adapted from Ref. 41.

Based on these premises, the radiation scattered by a stack of bilayers like that shown in Figure 6.3b can be written as follows (Equation 6.1):

$$F_{ML} = \sum_{j=1}^{M} \left[F_{Aj} + F_{Bj} \cdot e^{iq(t_{Aj}+\ell_j)} \right] e^{iqz_j} \qquad \text{Eq. 6.1a}$$

$$z_j = \sum_{s=1}^{j-1} t_{As} + \ell_{As} + t_{Bs} + \ell_{Bs} \qquad \text{Eq. 6.1b}$$

176

Here, j identifies one of the M bilayers A-B, t_A and t_B are the thicknesses of layers A and B, while ℓ_A and ℓ_B are the thicknesses of buffer layers separating A and B. The term z_j is the height above the substrate where the jth bilayer starts, that is the sum of thicknesses of all bilayers below j.

Finally, F_A and F_B are the scattering factors of the A and B layers. These are of central importance, because they describe the amplitude of the electric field scattered at each q-value by each layer. Ultimately, F_A and F_B combined will define the continuous profile that convolutes the intensity of interference fringes (Figure 6.4). This can be understood intuitively: since interference occurs between radiation scattered by each layer, multilayer fringes can be observed only where layers provide diffracted intensity in first place, and will be more intense where the layers scatter the most (Figure 6.4c,f). For a colloidal superlattice, we need to define two kinds of structure factors: one for the nanocrystals, and one for the layer of organic molecules in between.

6.3.2 Scattering factor of nanocrystals

Nanocrystals are the electron-dense part of a colloidal superlattice, and provide most of the diffracted intensity. For a nanocrystal of generic shape diffracting with its (hkl) planes, $F_{NC}(q)$ is the sum in phase of the radiation scattered by each unit cell plane n (Equation 6.2, see Figure 6.4a-c):

$$F_{NC}(q) = S_{(hkl)} \sum_{n=0}^{N-1} T_{(hkl,n)} e^{-iqn \cdot d_{hkl}}$$

Eq. 6.2

Here, $S_{(hkl)}$ is the structure factor of a unit cell oriented in the [hkl] direction,[52] $d_{(hkl)}$ is the periodicity of (hkl) planes, $T_{(hkl,n)}$ describes the nanocrystal shape through the number of unit cells per plane, and N is the nanocrystal thickness in number of unit cell planes, from which $t = N \cdot d_{(hkl)}$. Depending on circumstances, Equation 6.2 can be simplified: for example, $T_{(hkl,n)}$ is constant for cube-shaped nanocrystals lying flat on the substrate, like in $CsPbBr_3$ superlattices. Moreover, if the analysis is limited to one Bragg peak, the relative intensity of peaks becomes irrelevant, and $S_{(hkl)}$ is considered constant.

6.3.3 The case of thin platelets

The scattering factor of thin platelets is more complex to describe. Due to the sudden crystal truncation and to surface termination effects, nanoplatelets cannot be described by a unit cell and its associates S(*hkl*). Hence, Equation 6.2 is replaced by an atomistic description (Equation 6.3, see Figure 6.4d-f):

$$F_{NPL}(q) = \sum_{j=0}^{J-1} f_j e^{-iqn \cdot z_j} \qquad \text{Eq. 6.3}$$

Here, f_j is the atomic scattering factor of the jth atom, J is the number of atoms in the platelet, and z_j is their vertical coordinate. In principle, J would be a very large number. However, atoms of the same element and belonging to the same plane give identical contributions. Therefore, the summation can be limited to the handful of atoms needed to capture the stoichiometry and vertical alternation of atomic planes in the nanoplatelet (Figure 6.13), greatly simplifying its description. This considered, the nanoplatelet

thickness is simply $t = z_{J-1} - z_0$, where $j = 0$ and $j = J-1$ identify the top and bottom atomic

planes of the platelet. Note that Equation 6.3 could be used to describe nanocrystals as

well, in place of Equation 6.2. This however would be impractical, as the number of atomic

planes increases quickly with the nanocrystal thickness, making the unit-cell based

description handier for thick nanocrystals.

6.3.4 Describing the organic layer

The organic ligands are the electron-sparse component of the superlattice. Their

contribution to the diffracted intensity is often negligible [$F_L(q) \approx 0$], except for samples

with a large organic/inorganic volume ratio, like stacks of thin nanoplatelets. In this case,

$F_L(q)$ can be approximated to the scattering of an amorphous carbon layer (Equation 6.4).

$$F_L(q) = \int_0^{t_L} f_C e^{-iqx} dx \qquad \text{Eq. 6.4}$$

Where f_C is the atomic scattering factor of carbon, and t_L is the organic layer

thickness. Note that Equation 6.4 closely resembles Equation 6.3, except for the nature

of scatterers (atoms *vs* unit cells) and for their continuous *vs* discrete spatial distribution.

The choice of neglecting or considering the scattering of the organic layer opens

two different scenarios. In the first, both *A* and *B* materials in the bilayer are available to

describe nanocrystals, enabling for example the modelling of binary superlattices. In this

case, the non-scattering buffer layers takes the role of describing the ligands, therefore ℓ

$= t_L$. If the scattering of organics is not neglected, instead, one of the two slots in the

bilayer must be spent for that. Since the organic layer thickness should not be counted twice, and is already accounted for by the term $t_A = t_L$, in this case the buffer layer thickness is $\ell = 0$.

6.3.5 A more compact equation for Multilayer Diffraction

Now that all terms have been defined, Equation 6.1 can be used to compute the interference pattern of any bilayer stack. Unfortunately, this equation is cumbersome: it involves six terms (F_A, F_B, t_A, t_B, ℓ_A, ℓ_B) for each of the M bilayers, which in a real-world sample can be up to thousands or more.[22]

Luckily however, Equation 6.1 can be greatly simplified based on some assumptions. First, ℓ_A and ℓ_B are assumed to follow the same Gaussian distribution, with average value $\bar{\ell}$ and standard deviation σ_L (Equation 6.5) Note that $\sigma_L \neq 0$ even when $\bar{\ell} = 0$, as this parameter is still needed to describe fluctuations in the organic layer thickness (see Paragraphs 6.3.4 and 6.3.6).

$$P(\ell) = \frac{1}{\sqrt{2\pi} \cdot \sigma_L} \cdot e^{-\frac{(\ell - \bar{\ell})^2}{2\sigma_L^2}}$$
Eq. 6.5

Second, if layers are statistically independent of each other (*i.e.*, one layer does not influence the structure of surrounding ones), the scattering factors F_A and F_B can be replaced by averages $\bar{F}_A = \langle F_A \rangle$ and $\bar{F}_B = \langle F_B \rangle$. This allows to describe cases where the thickness of the layers A and B is not identical for each layer, but is affected by some uncertainty. Such variability is captured by a distribution $P(t_{Aj})$, which sets the

probability that each *A* layer adopts a specific thickness. Hence, $\bar{F}_A$ (and $\bar{F}_B$ as well) can be written as Equation 6.6:

$$\bar{F}_A = \sum_{j=0}^{\infty} P(t_{Aj}) \cdot F_{Aj}$$

Eq. 6.6

If the thickness distribution of starting nanocrystals is sufficiently narrow, like for ultrathin nanoplatelets samples,[53] this step can be neglected and $\bar{F}_A = F_A$. Otherwise, a simple but effective option is a discrete Gaussian distribution centered around an average thickness $\bar{t}$ (Equation 6.7).[22,35]

$$P(t_j) = \left[\sum_{j=0}^{\infty} e^{\frac{(t_j-\bar{t})^2}{-2\sigma_t^2}} \right]^{-1} \cdot e^{\frac{(t_j-\bar{t})^2}{-2\sigma_t^2}}$$

Eq. 6.7

With these assumptions, Schuller *et al.* developed and reworked Equation 6.1 into a compact expression for calculating the intensity of X-rays diffracted by a stack of bilayers (Equation 6.8):[35]

$$I(q) = M \cdot \left[\langle F_A F_A^* \rangle + \langle F_B F_B^* \rangle + 2\,Re\left(e^{\xi}\phi_A \bar{F}_B\right) \right] +$$

$$+2Re\left[\frac{e^{-\xi}\phi_B \bar{F}_A}{T_A T_B} + \frac{\phi_A \bar{F}_A}{T_A} + \frac{\phi_B \bar{F}_B}{T_B} + e^{\xi}\phi_A \bar{F}_B \right] \cdot \left[\frac{M - (M+1)e^{2\xi}T_A T_B + \left(e^{2\xi}T_A T_B\right)^{M+1}}{(1 - e^{2\xi}T_A T_B)^2} - M \right]$$

Eq. 6.8

Where $\bar{F}_A$ and $\bar{F}_B$ are calculated according to Equation 6.7, and all the other terms are computed as detailed in Equations 6.9a-d below. Equivalent expressions are defined for *B*-related terms.

$$\xi = iq\ell - \frac{q^2\sigma_L^2}{2} \qquad \text{Eq. 6.9a}$$

$$\phi_A = \sum_{j=0}^{\infty} P(t_{Aj}) \cdot F_{Aj}^* \cdot e^{iqt_{Aj}} \qquad \text{Eq. 6.9b}$$

$$T_A = \sum_{j=0}^{\infty} P(t_{Aj}) \cdot e^{iqt_{Aj}} \qquad \text{Eq. 6.9c}$$

$$\langle F_A F_A^* \rangle = \sum_{j=0}^{\infty} P(t_{Aj}) \cdot F_{Aj} \cdot F_{Aj}^* \qquad \text{Eq. 6.9d}$$

Visually, Equation 6.7 does not look any simpler than Equation V1. However, it is much faster to implement in an algorithm compared to Equation 6.1, and it is universal to any bilayer. This enables writing flexible algorithms where the core of interference calculations relies on Equation 6.8, and the simulation is adapted to each sample by simply changing the description of the two bilayers.

6.3.6 Discrete and continuous disorder

One consequence of considering averaged terms in Equation 6.8 is that we can now define an average superlattice periodicity $\Lambda = \bar{t}_A + \bar{t}_B + 2\bar{\ell}$ (see Figure 6.3b). Such periodicity determines the position of interference fringes according to the relation $\Lambda = 2\pi/\Delta q$, where Δq is the distance between two neighboring fringes (Figure 6.4c,f). Deviations from the ideal periodicity Λ represent forms of disorder, and can have a major impact on Multilayer Diffraction. Indeed, each layer can be subject to a misplacement that breaks down into two contributions: a discrete disorder σ_t due to the nanocrystal size distribution (Equation 6.6-7), and a continuous stacking disorder σ_L due to inhomogeneities in the ligands layer thickness (Equation 6.5).
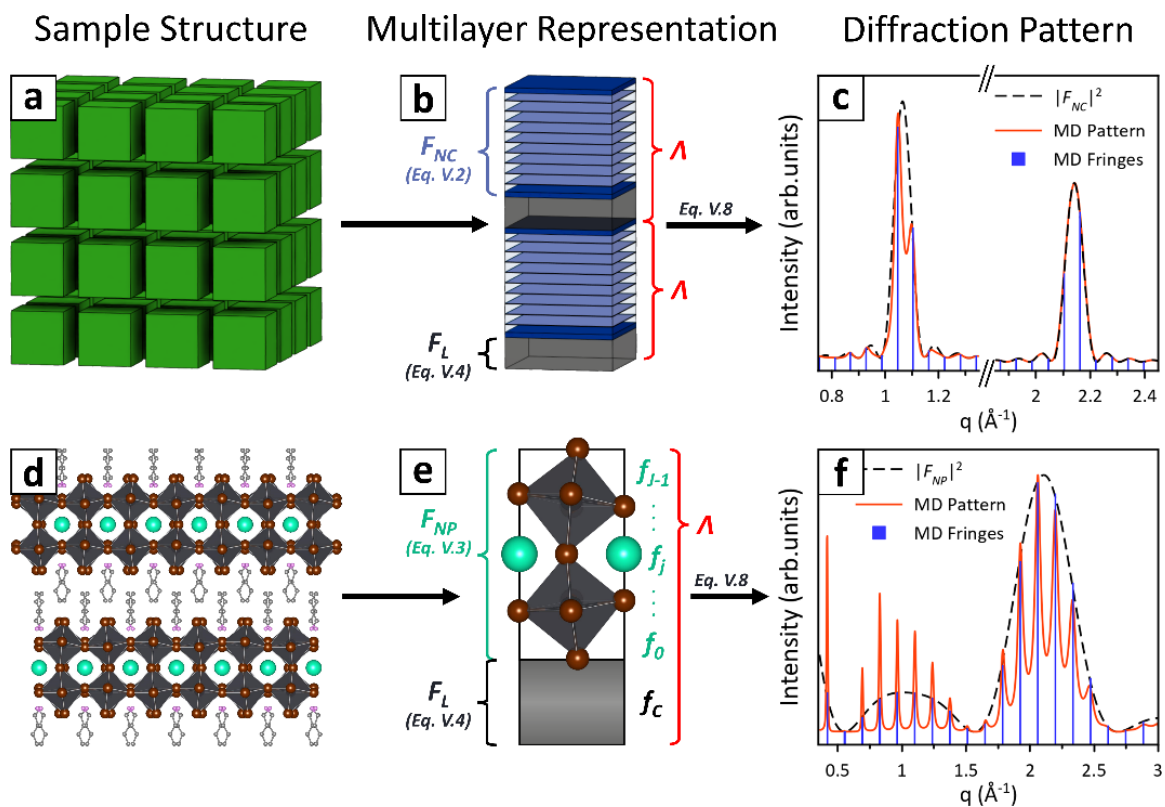
Figure 6.4. Principles of Multilayer Diffraction. A nanocrystal superlattice (a) is composed of (b) alternating inorganic (blue) and organic layers (black), both contributing to the superlattice periodicity Λ (red). Each layer has a scattering factor, F_{NC} for nanocrystals and F_L for organic ligands, computed *via* Equations 1-2, respectively. A Multilayer Diffraction pattern (c, red line) stems from the constructive interference of many of such organic-inorganic bilayers. Fringes are affected by the superlattice periodicity (position, $q_n=2\pi n/\Lambda$), the superlattice disorder σ_L (width), and the scattering factors (intensity). F_{NC} is predominant over F_L due to the high electron density in nanocrystals, resulting in the intensity of fringes being modulated by the nanocrystal Bragg peaks (c, black dashed line). Similarly, a stack of nanoplatelets (d) is a multilayer (e) of alternating inorganic (cyan) and organic layers (black), resulting in the nanoplatelet scattering factor F_{NP} modulating the intensity of the Multilayer Diffraction fringes (f). The only difference between (a-c) and (d-f) panels is that F_{NC} is computed based on unit cells, while for F_{NP} one must consider individually each atomic layer within the platelet ($f_0 \dots f_{J-1}$). Adapted from Refs. 22,41,53.

The disorder associated to the nanocrystal thickness is called "*discrete*" because, being composed by a finite and integer number of unit cells, nanocrystals larger or smaller than the average size will misplace the layers above them by a factor $n \cdot d_{hkl}$, that is a discrete shift. Interestingly, since this shift matches the periodicity of the atomic lattice, it does not disrupt the interference in correspondence of Bragg peaks. Its only effect is a smearing of the interference fringes at the far sides of peaks themselves, that can be neglected if the size distribution of nanocrystals is narrow enough.

Different from discrete disorder, the stacking disorder has a crucial importance in Multilayer Diffraction. In colloidal nanocrystal superlattices, this is caused by random fluctuations in the thickness of the organic layers due to their soft and non-crystalline nature. Crucially, the disorder in superlattices is cumulative, as one misplaced layer will shift all those above (Equation 6.1b). The accumulation of multiple random misplacements results in the broadening of diffraction fringes at higher q-values, and eventually causes them to fade completely.[35,50,51] That is why in CsPbBr$_3$ nanocubes superlattices the peak split is observed only at the first Bragg peak (q ≈ 1 Å^{-1}), and not at the second (q ≈ 2 Å^{-1}, see Figure 6.2).

It follows that a low stacking disorder is mandatory to observe Multilayer Diffraction. As a rule of thumb, $\sigma_L \leq 1$ Å would allow to observe interference up to ∼20° $2\theta_{CuK\alpha}$ (q ≈ 1.5 Å^{-1}). This is both a strength and a weakness of Multilayer Diffraction: on the one hand, it is limited to highly ordered systems. On the other hand, such sensitivity enables high precision in quantifying the disorder. The most remarkable conclusion, however, is that colloidal superlattices can achieve the same structural perfection as

materials grown epitaxially. For example, in CsPbBr$_3$ superlattices $\sigma_L \approx 1$ Å, which is only

~1% of $\Lambda \approx 100$ Å and much shorter than a Pb-Br bond (≈ 3 Å). For comparison, some of

the epitaxial films studied by Schuller *et al.* were even more disordered, with

$\sigma_L = 1.4$ Å.[22,35,50]

6.4 Why Perovskite Nanocrystals?

The literature on metal halide nanocrystals is rich with XRD patterns showing

Bragg peaks split in fringes[21,54–61] or of asymmetric shapes,[62–65] that are typical signatures

of Multilayer Diffraction. However, only few of these studies concern nanocrystal

superlattices (Refs. 21,54,58–60), while most did not target nor mention the formation of

self-assembled structures. On the other hand, Multilayer Diffraction was not reported for

any of the highly ordered superlattices that have been grown for decades from

nanocrystals of other materials. What makes perovskites so suitable for observing this

effect?

Having constructed a picture of Multilayer Diffraction in Paragraph 6.3, we can

now explain the factors contributing to this apparent contradiction. First, the sample

preparation. Nanocrystal samples for XRD are often prepared by drop casting liquid

dispersions on flat substrates. While drying, nanocrystals might self-assemble into

domains that would produce interference fringes even when only few nanocrystals thick,

provided that the inter-nanocrystal distance is consistent across the sample.[22] This

explains why fringes are seen even in samples not recognized as superlattices. One of the

first clues that superlattices have formed upon drop cast is preferred orientation, which is revealed by the suppression or weakening of some diffraction peaks.[66]

Second, the nanocrystal shape and structure. Multilayer Diffraction is primarily challenged by the stacking disorder, which disrupts the fringes starting from higher angles. Here, lead halide perovskite nanocubes have a two-fold advantage. Their first Bragg peak falls at lower angles ($2\theta_{CuK\alpha}\approx15°$) than other popular materials routinely assembled into superlattices like Au ($2\theta_{CuK\alpha}=38°$), PbS ($2\theta_{CuK\alpha}=26°$), or CdSe ($2\theta_{CuK\alpha}=24°$). This relaxes the requirements on the stacking disorder σ_L, making perovskite superlattices more prone to display Multilayer Diffraction. Moreover, the cubic shape of perovskite nanocrystals makes them assemble in the correct orientation for observing such peak. As a counterexample, the lowest-angle peak of PbS is (111), but nanocubes in a simple cubic arrangement would expose the (200) planes instead. Finally, cube-shaped nanocrystals pack with less disorder compared to spheroidal nanocrystals, as the simple-cubic packing is more compact and constrained than the sparser BCC, FCC, and HCP geometries typical of spheres.

Third, nanocrystal superlattices are traditionally studied by Grazing Incidence Small/Wide Angle X-ray Scattering (GISAXS/GIWAXS, see Figure 6.14 for results on $CsPbBr_3$ nanocrystal superlattices). The first operates in the small-angle regime, where diffraction comes from the nanoscale electron density modulation of the entire superlattice. Multilayer Diffraction in the form we are discussing cannot occur there, as it is a secondary interference phenomenon building upon radiation diffracted by nanocrystals at wide angles. GIWAXS instead is a wide-angle technique, so it might in

principle detect such interference. However, current GIWAXS instruments have a worse angular resolution than those operating in a θ:2θ geometry, which could end up hiding interference fringes should they form. Moreover, GIWAXS data are often presented as two-dimensional maps, while Multilayer Diffraction is better seen by integrating data in slices. We therefore suspect that Multilayer Diffraction went unnoticed because θ:2θ scans, which would give the best chances of observing interference fringes, are seldom performed on superlattices in favor of grazing incidence techniques.

Finally, one might wonder why Multilayer Diffraction was first recognized in nanocubes, despite interference fringes being ubiquitous and much stronger in nanoplatelets.[67–73] Indeed, nanoplatelet stacks are typically more ordered thanks to their anisotropic shape and the strong face-to-face interactions. Moreover, due to their extreme thinness nanoplatelets do not produce well-defined Bragg peaks, but rather a broad and continuous diffraction profile (see Figure 6.4c,f), thus allowing to observe Multilayer Diffraction over a much wider angular range. One possible reason is that the XRD patterns of nanoplatelet stacks resemble closely those of layered bulk materials like Ruddlesden-Popper perovskites, and are often rationalized by this analogy. Indeed, most works on perovskite nanoplatelets acknowledge that fringes are due to their stacking, but then assign them Miller indices in analogy with the Bragg peaks of a Ruddlesden-Popper bulk crystal.[67,72,74] This diverts the attention from asking why bulk-like peaks are observed in a colloidal system in first place, and why their intensity appears to be modulated over a broader profile, two key questions that could have led to the identification of a multilayer interference effect.

6.5 What is Multilayer Diffraction good for?

When observable, Multilayer Diffraction is a powerful tool for studying nanocrystal assemblies. On the one hand, it provides insights into their nanoscale periodicity and disorder without the need of specialized grazing-incidence techniques. On the other hand, being a wide-angle technique, it also provides information about the atomic structure of nanocrystals. Below, we present examples illustrating these points.

All case studies come from works investigating superlattices of lead-halide perovskite nanocrystals and nanoplatelets (Refs. 22,38,53,60). Therefore, the sample preparation and characterization steps are largely similar. The same is true for algorithms written to analyze X-ray diffraction data, that witnessed and incremental evolution as our understanding of Multilayer Diffraction improved, but are all based on the bilayer formalism described in Paragraph 6.3. With the intent of providing a comprehensive and clear overview of this journey, I opted for not discussing in detail the samples and methods applied in each paper, and I focused on the general takeaway instead. If interested, I encourage the reader to check the original works, that are all published under Open Access policies. Nevertheless, the most relevant information on the preparation and characterization of samples is provided in the Methods (6.8) and Supplementary Material (6.10) paragraphs of this chapter.

6.5.1 Determination of Λ.

The superlattice periodicity Λ is straightforward to extract: convert the position of fringes from 2θ to q ($q = 4\pi \sin(\theta) / \lambda_{X-ray}$), assign a progressive index to each fringe, and perform a linear regression to extract the slope $\Delta q = 2\pi/\Lambda$. To help resolve closely spaced fringes, the diffraction profile can be decomposed into a sum of gaussians. This is the most accessible application of Multilayer Diffraction, as it does not require modelling the pattern. By this approach we monitored the contraction of $CsPbBr_3$ nanocrystal superlattices under vacuum due to the desorption of residual solvent (Figure 6.15),[38] and tracked the structural changes in mixed-halide $CsPb(Br_xI_{1-x})_3$ nanocrystal superlattices under UV light.[60] In the latter case, the illumination induced the expulsion of iodine, causing a contraction of the nanocrystal unit cell that eventually reduced the superlattice periodicity (Figure 6.5a-c).

Comparing Λ between different samples can be a strategy to study the nanocrystal surface. For example, lead halide nanoplatelets are often synthesized in the co-presence of amines and carboxylic acids as surfactants. To identify which one passivates the surface, we compared Λ of a sample prepared with oleylamine and oleic acid with two other samples: one with a shorter amine (octylamine) and one with a longer carboxylic acid (erucic acid).[53] While the erucic acid left Λ unchanged, the octylamine resulted in its drastic contraction, demonstrating that perovskite nanoplatelets are passivated by amines only (Figure 6.5d-e).
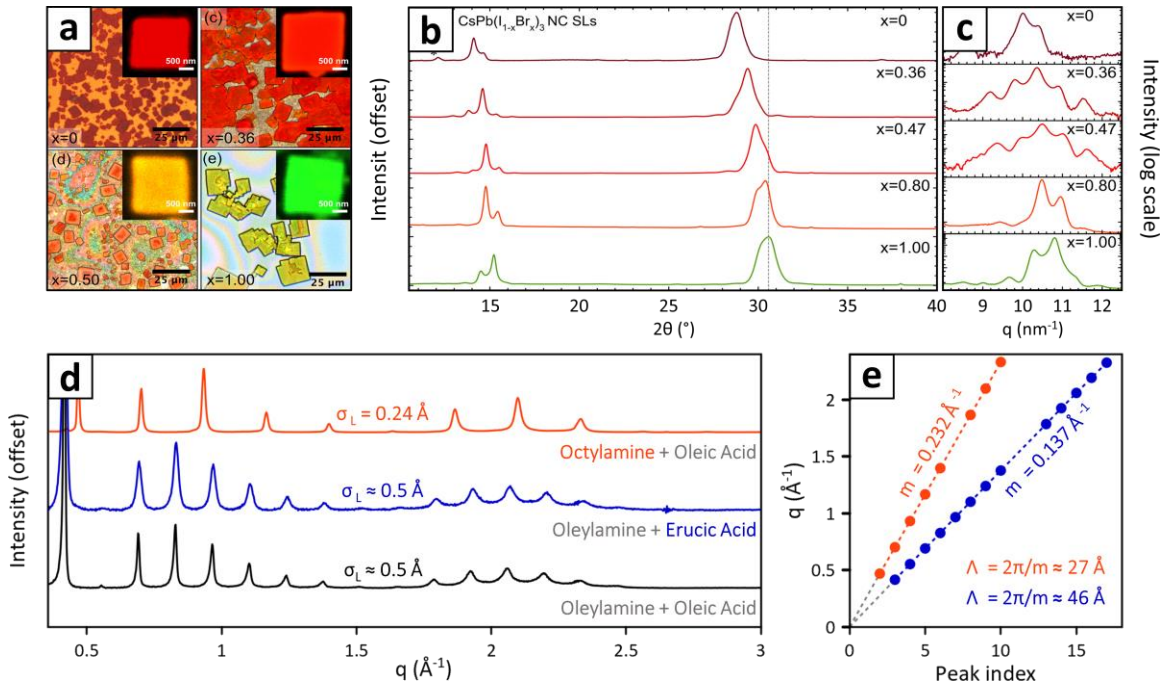
Figure 6.5. Determination of Λ. a) Upon UV-light illumination, $CsPb(Br_xI_{1-x})_3$ nanocrystal superlattices undergo a photoinduced expulsion of iodine that contracts their atomic lattice. b) This is captured both by the Bragg peaks moving toward higher angles and c) by the shift in the Multilayer Diffraction fringes. d) Perovskite nanoplatelet samples prepared with different combinations of ligands. Replacing the carboxylic acid leaves the pattern unchanged, while different ammines result in different stacking periodicities, demonstrating that platelets are passivated by amines only. e) A linear regression allows to extract Δq, and therefore Λ. Adapted from Refs. 41,53,60.

6.5.2 Estimation of stacking disorder

The stacking disorder σ_L is proportional to the width of interference fringes, and can be extracted by fitting the experimental pattern with the open-source Python scripts we developed for nanocrystal superlattices and nanoplatelet stacks.[22,53] Like Λ, σ_L helps comparing samples and treatments. For example, a thermal annealing improves the stacking order in $CsPbBr_3$ nanocube superlattices (Figure 6.6). Instead, disorder in

nanoplatelet stacks benefits from replacing oleylamine with octylamine, highlighting the importance of ligand engineering for optimizing nanocrystal assemblies (Figure 6.5d, see Figures 6.16-17 for a full-profile fit of the patterns).
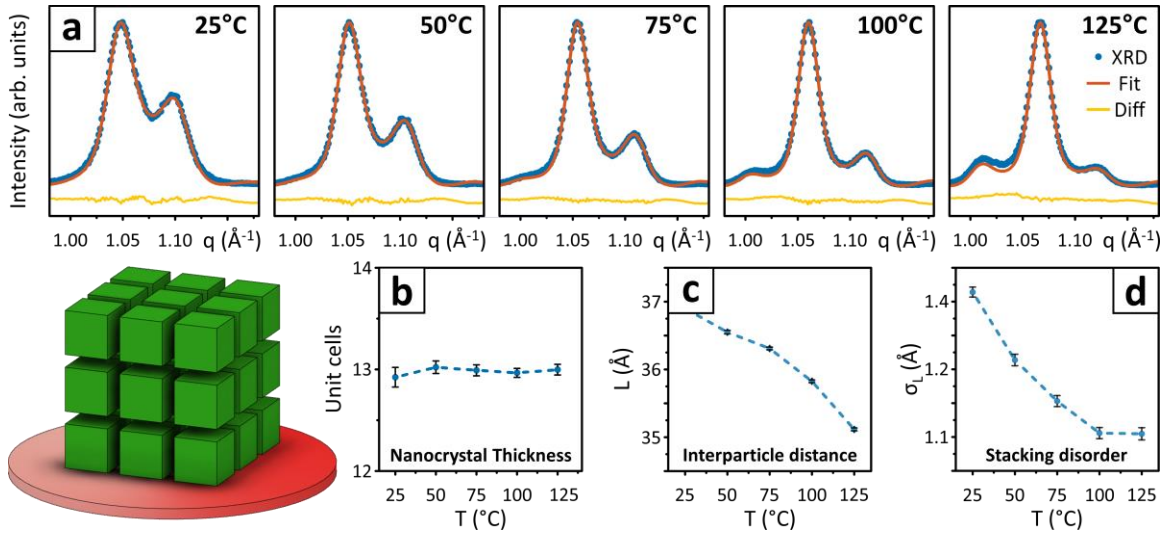
Figure 6.6. Effect of thermal annealing on superlattices. a) Evolution of the first Bragg peak of $CsPbBr_3$ nanocubes superlattices upon thermal annealing. b-d) Evolution of nanocrystal thickness (b), interparticle distance (c), and stacking disorder σ_L (d) tracked by Multilayer Diffraction. Adapted from Refs. 22,41.

The need for a profile fit makes σ_L less accessible than Λ. However, disorder in two different samples can be compared by the width of interference fringes, while a numerical estimate is obtained by observing at which q-value the interference fringes fade out (Equation 6.10).[22]

$$\delta_\Lambda \leq \frac{\pi}{2q_{lim}}$$

<div align="right">Eq. 6.10</div>

Here, q_{lim} is the last q-value at which fringes are observed. Note that δ_Λ is not equivalent to the more rigorously defined σ_L, that should always be preferred when obtainable, but it provides a reasonable estimate. For example, $CsPbBr_3$ nanocubes superlattices show fringes at their first Bragg peak (q≈1 Å^{-1}) but not at the second (q≈2 Å^{-1}), corresponding to 0.7 Å < δ_Λ ≤ 1.6 Å. Indeed, σ_L falls in the range 1-1.5 Å (Figure 6.6d). Instead, for perovskite nanoplatelets fringes can be observed up to q≈2.5 Å^{-1}, corresponding to δ_Λ ≤ 0.4 Å^{-1}: fitting the patterns yielded σ_L values in the range 0.25-0.5 Å^{-1} (Figure 6.7a, see also Figures 6.16-17).

6.5.3 Nanoparticle and organic layer thicknesses

Fitting the XRD pattern allows dividing Λ into nanoparticle and organic layer thicknesses. In fact, the nanoparticle thickness affects its scattering factor according to Equations 6.2-3, and is reflected in the number and intensity of visible fringes. Once both Λ and the nanoparticle thickness are known, the organic layer thickness is determined by difference. For example, on $CsPbBr_3$ superlattices the fit allowed to measure the average nanocrystal size down to the single unit cell (Figure 6.6b), and enabled tracking the contraction of interparticle spacing during a thermal annealing experiment (Figure 6.6c, see also Figure 6.18). For nanoplatelets the sensitivity is even higher, as adding or removing a single atomic plane substantially alters the diffraction profile. For example, for Cs-Pb-Br nanoplatelets we measured a thickness of 11.84 Å and an interplatelet distance of 34.0 Å (Figure 6.7a), in excellent agreement with the reported thickness of pure oleylamine lipid bilayers (3.4 nm).[75]

Here, Multilayer Diffraction provides substantial advantages over other techniques, as it ensures a direct and precise measurement of two independent parameters. Conversely, it is common to measure Λ by diffraction or TEM, and then simply assume an approximate value for the nanocrystal thickness (for perovskites, generally a multiple of 0.6 nm)[74,76] or the interparticle distance (for oleylamine ~2-3 nm)[21,70,77–79] to estimate the counterpart by difference, leading to inaccurate results.

6.5.4 Atomic structure identification and refinement

The structure of nanocrystals has a central role in Multilayer Diffraction, as through Equations 6.2-3 it determines the diffraction profile that convolutes the intensity of interference fringes. This marks the distinction with small-angle techniques like GISAXS, where the diffracted intensity comes from the nanoscale electron density modulation of the superlattice. Due to the θ:2θ data acquisition geometry, Multilayer Diffraction is sensitive only to the vertical position of atoms (see Figure 6.2a), and is therefore unable to determine the atomic coordinates in all the other directions. Hence, powder XRD experiments followed by Rietveld or total scattering analyses are much better suited for refining the structure of nanocrystals.[80–82]

However, Multilayer Diffraction offers a significant advantage for very thin nanoplatelets. Here, the disappearance of Bragg peaks makes Rietveld refinement inapplicable, and total scattering methods might struggle as well, as thin nanoplatelets might bend and curl, causing severe deformations that would be challenging to model. Indeed, the thinnest perovskite nanoplatelets refined by such methods were relatively

193

thick (3.5 nm) and hence much more rigid.[83] Conversely, the neat stacking achieved by nanoplatelet ensures that all particles are optimally aligned and flat. Therefore, a Multilayer Diffraction full-profile fit allows to validate the structure model of nanoplatelets down to the single atomic plane. For example, comparing experimental data with simulated diffraction profiles allowed us to determine unambiguously that Cs-Pb-Br nanoplatelets are passivated by oleylammonium bromide, ruling out competing $PbBr_2$- or CsBr-terminations (Figure 6.7b). Moreover, by leaving the layer occupancies and vertical coordinates as fittable parameters (Figure 6.7a), we could determine the surface coverage (73%), the thickness (11.84 Å) and the degree of octahedra tilting in nanoplatelets. See also Figure 6.19 for an overview of how modifying different aspects of the nanoplatelets structure affects their predicted Multilayer Diffraction pattern.
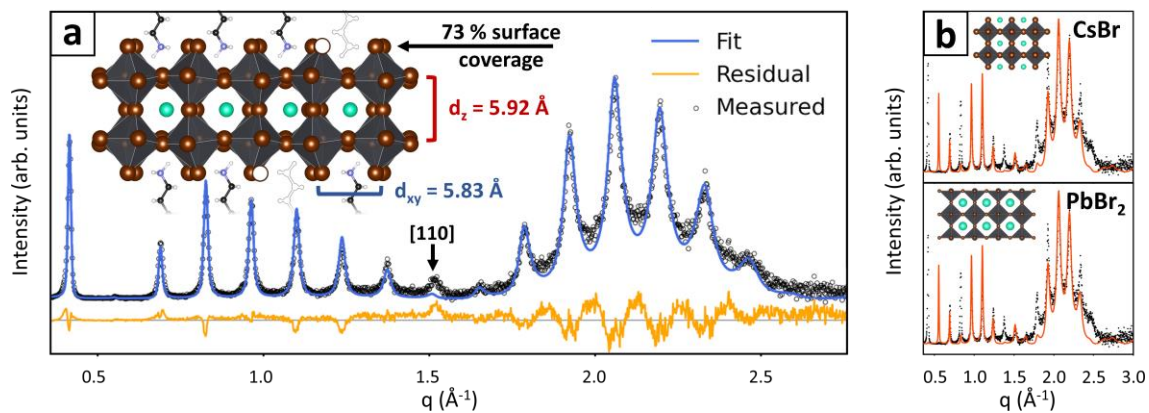
Figure 6.7. Atomic structure identification and refinement. The surface termination of perovskite nanoplatelets is identified by comparing their diffraction pattern with simulations. a) An oleylammonium bromide termination matches the pattern. b) Conversely, CsBr- and $PbBr_2$- terminations are excluded due to mismatching fringes intensities. The quantitative profile fit shown in panel (a) allows refining the vertical atomic coordinates and the surface coverage factor. Adapted from Refs. 41,53.

6.6 Future Applications of Multilayer Diffraction

In addition to what discussed above, here I simulated Multilayer Diffraction patterns for some stimulating case studies, comparing nanocrystals packed in different geometries, nanoplatelets of different thicknesses, and discussing possible results of co-assembling two different materials (Figure 6.8, simulation parameters are summarized in Table 6.1). These simulations aim to capture the general distribution and relative intensities of fringes (*e.g.*, the groups of modulated peaks in Figure 6.8b), but their exact position is dictated by the superlattice periodicity Λ, that could only be estimated. Hence, the fringe positions shall not be used to identify the superlattice, in contrasts with the common practice of recognizing materials by their PXRD peaks positions.

Figure 6.8a compares patterns for spherical Cs_4PbBr_6 nanocrystals packed in different geometries (simple cubic, BCC, FCC, HCP). The nanocrystals size, orientation, and interparticle distance are kept constant for comparison. Each packing geometry results in a different Λ, which is reflected in the fringes periodicity Δq. Note that for FCC, BCC, and HCP packings the measured Λ is half of the superlattice unit cell, because each cell includes two nanocrystal layers.

Figure 6.8b shows instead patterns calculated for cadmium-terminated CdSe nanoplatelets of different thicknesses, increasing from top to bottom, and separated by a constant interparticle distance. As the thickness increases the superlattice periodicity Λ grows larger, resulting in the interference fringes becoming closer to each other. Moreover, the diffracted intensity progressively localizes around 29° 2θ, where the (200) Bragg peak of typical of sphalerite-CdSe would eventually form for thick nanocrystals.

Figure 6.8c addresses the co-assembly of PbS and CsPbBr$_3$ nanocubes into superlattices where the two materials are randomly mixed or alternate in layers. These two cases would be very challenging to tell apart by GISAXS, as the overall superlattice periodicity and geometry is the same. However, Multilayer Diffraction can tell the two cases apart by the periodicity of fringes at the first perovskite Bragg peak (Figure 6.8c, insets). Indeed, alternating the two materials effectively doubles the distance between perovskite nanocrystals, resulting in fringes twice as close to each other. This case is a good demonstration of the sensitivity of Multilayer Diffraction toward the local environment of nanocrystals.

A similar effect is seen in Figure 6.8d, where nanoplatelets of CsPbBr$_3$ and PbS are co-assembled. Again, the effective doubling of the superlattice periodicity results in the appearance of extra fringes in the 0-23° 2θ range (red arrows), which however disappear in the second part of the pattern. This is because CsPbBr$_3$ and PbS have a similar diffraction profile in the 23-37° 2θ range, as seen by the two single-material patterns. Therefore, in that area of the pattern they behave as if they were the same material, thus virtually halving the superlattice periodicity.
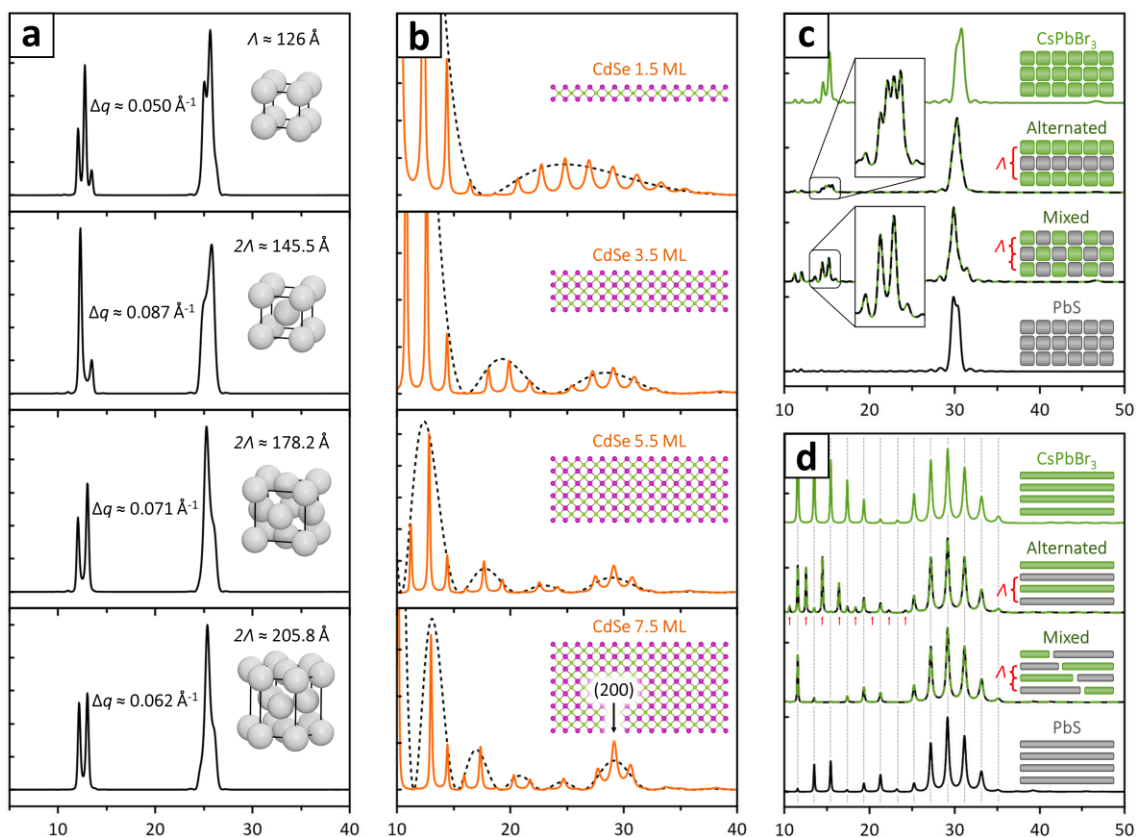
Figure 6.8. Simulated Multilayer Diffraction patterns. a) Cs_4PbBr_6 nanospheres oriented with (012) planes parallel to the substrate and packed in different geometries. From top to bottom: simple cubic, BCC, FCC, HCP. b) Sphalerite CdSe nanoplatelets of different thicknesses. The diffraction profile of a single nanoplatelet ($=|F_{NP}|^2$) is traced by a black dashed curve. c) Simple-cubic superlattices of $CsPbBr_3$ and PbS nanocubes and their mixtures. d) Stacks of $CsPbBr_3$ and PbS nanoplatelets and their mixtures. If two kinds of nanocrystals do not mix and form segregated superlattices, the resulting pattern will simply be the sum of patterns for single-material superlattices. All patterns are plotted in Cu-K$_\alpha$ 2θ scale, and include instrumental intensity corrections (thin-film Lorentz-Polarization, instrumental broadening).[35] Simulation parameters are summarized in Table 6.1. Adapted from Ref. 41.

6.7 Conclusions

To conclude this overview, we encourage the reader to think beyond lead halide

perovskites, because Multilayer Diffraction is by no means a phenomenon exclusive to

them. Indeed, a literature search reveals Multilayer Diffraction effects in a variety of materials (Figure 6.9): apart from halide perovskites,[57,65,67,84] interference fringes are seen for metal oxides and hydroxides,[85–91] for synthetic two-dimensional materials like MXenes, metal dichalcogenides, and intercalated graphite,[92–95] and also for metal-organic salts often used as precursors in the synthesis of nanomaterials.[96–98] In general, any material that is prone to be self-assembled, exfoliated, or stacked, is a suitable building block for constructing ordered multilayer structures. It is in the hands and minds of researchers to recognize Multilayer Diffraction and use it to empower their research.

I want to emphasize that, before being a characterization tool, Multilayer Diffraction is first and foremost an intrinsic behavior of the sample. Therefore, it can be exploited only when naturally present, just like photoluminescence spectroscopies are useful only on intrinsically luminescent samples. When applicable, Multilayer Diffraction analysis is highly complementary to established superlattice characterization techniques. For example, Multilayer Diffraction excels in quantifying the positional disorder of nanocrystals, while GIWAXS is highly sensitive to nanocrystal tilting.

Compared to GISAXS, Multilayer Diffraction enables for a more accurate quantification of Λ, σ_L, and small variations thereof, because information is extracted at higher angles and from multiple fringes. Moreover, Multilayer Diffraction is sensitive to the crystal structure of particles, and because it is based on interference between neighboring nanocrystals, it conveys information about their surroundings. Hence, Multilayer Diffraction is a valid tool for systems composed of two or more mixed nanomaterials, where their relative positioning at the local level would be far from

obvious from small-angle diffraction experiments. Binary and ternary superlattices based on perovskite nanocrystals could be suitable samples to test these predictions.[26,27] On the other hand, Multilayer Diffraction lacks the capability, typical of GISAXS, to unambiguously identify the packing geometry in 3D-superlattices and 2D-monolayer nanocrystal assemblies, although in the first case this can be inferred indirectly from the superlattice periodicity as illustrated in Figure 6.8a.

To conclude, Multilayer Diffraction does not require specialized instrumentation, as it can be measured on any $\theta:2\theta$ lab-grade diffractometer. Moreover, its high information density, stemming from combining atomic- and nanometric-scale information in one single experiment, makes it especially suitable for in-situ and operando experiments, where speed and simplicity become crucial. Nevertheless, there is room for increasing the versatility of Multilayer Diffraction even further. One way would be observing interference patterns in other experimental geometries than $\theta:2\theta$ scans performed on flat macroscopic samples. First steps in this direction have been recently made by recognizing and modelling Multilayer Diffraction in liquid suspensions of $CsPbBr_3$ assemblies investigated by a total scattering approach.[59] Similarly, Multilayer Diffraction might be studied at the single-aggregate level by micro-diffraction experiments, and might provide information on the horizontal structure of superlattices if collected in a transmission geometry. Finally, it will be crucial to develop versatile and user-friendly Multilayer Diffraction software for the routine and high-throughput analysis of nanocrystals and nanoplatelet solids, which would help establishing the method among the colloidal nanocrystal community.
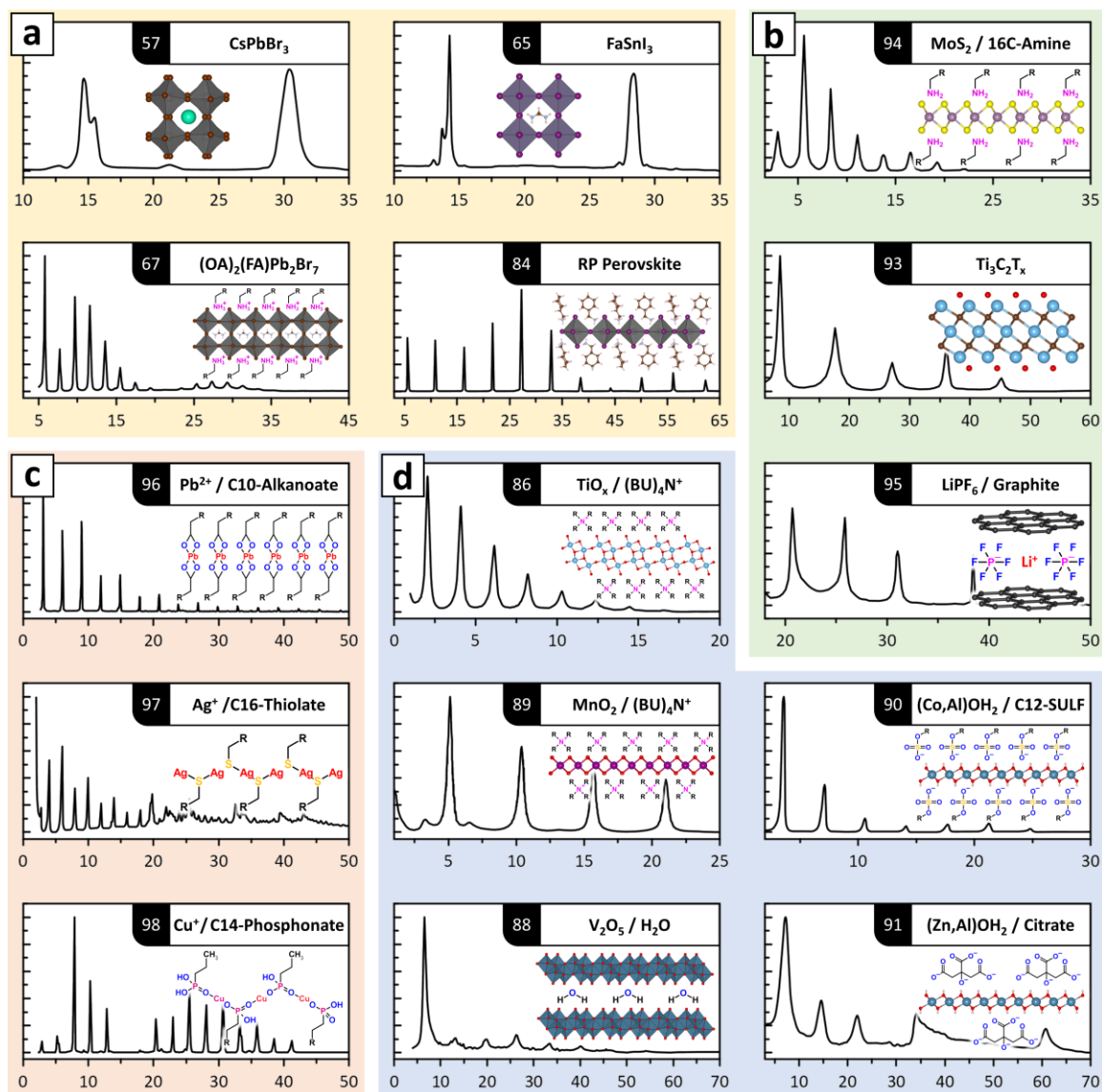
Figure 6.9. Literature patterns showing Multilayer Diffraction. Colors identify classes of materials. a) Yellow: metal-halide perovskites. b) Green: synthetic 2D materials. c) Red: metal-organic precursors for colloidal syntheses. d) Blue: metal oxides and hydroxides. Numbers within black labels indicate the corresponding reference. All patterns were digitized with WebPlotDigitizer[99] from Refs. 57,65,67,84,86,88-91,93-98 and are plotted in the 2θ-Cu$_{Kα}$ scale. Abbreviations: OA = oleylamine; RP = Ruddlesden-Popper; T = (F,OH,O); BU = butyl-; SULF = sulfate. Adapted from Ref. 41.

6.8 Methods

This section summarizes the methods adopted for the experiments and analyses discussed in this chapter. For brevity, only the most relevant information is reported. For additional details, please refer to the original open-access publications [Refs. 22,38,53].

6.8.1 Synthesis methods

Preparation of Cs-Oleate for CsPbBr$_3$ nanocrystals. 400 mg of cesium carbonate were reacted with 1.75 mL of oleic acid (OA) in 15 mL of1-octadecene (ODE) inside a 40 mL glass vial heated to 120°C under N$_2$ until all solid disappeared. The so-prepared precursor becomes cloudy upon cooling.

Synthesis of CsPbBr$_3$ nanocrystal superlattices. CsPbBr$_3$ nanocrystals were prepared as follows. First, 0.2 mmol of PbBr$_2$ were dissolved in 500 μL of oleylamine (OLAM), 50 μL of OA, and 5 mL of ODE at 120° in a 20 mL glass vial under N$_2$ atmosphere. Then, the vial was heated up to 170°C, removed from the hotplate and let cool in air down to 163°C. At that point, 0.5 mL of a previously prepared solution of Cs-oleate were swiftly injected, and the system was cooled to room temperature. CsPbBr$_3$ nanocrystals were recovered by centrifugation at 6000 rpm for 5 minutes. The supernatant was discarded, and the precipitate was centrifuged again without adding solvent. The residual liquid was removed with a paper tissue, the precipitate was redispersed in a small volume of solvent ($\approx$ 200 μL) and centrifuged again at 6000 rpm for 5 minutes to separate aggregates and larger particles. The resulting concentrated CsPbBr$_3$ nanocrystal dispersion was diluted with a solvent until an extrapolated optical density of $\approx$250 at 335 nm and 10 mm

pathlength, to form a stock solution for self-assembly. A small amount of this stock solution, typically 30 μL, was deposited on a 1 x 1 cm polished piece of silicon wafer and placed inside a glass Petri dish to let the solvent evaporate overnight. See Figure 6.10 for TEM images of as-synthesized CsPbBr$_3$ nanocrystals, Figure 6.11 for their optical absorption and photoluminescence spectra, and Figure 6.20 for a High-Resolution SEM image of a superlattice surface.

Preparation of Cs- and Pb-oleate for Cs-Pb-Br nanoplatelets. In separate 4 mL glass vials, dissolve 192 mg of cesium acetate in 1.0 mL of OA (Cs-oleate precursor), and 379 mg of lead acetate trihydrate in 1.0 mL of OA (Pb-oleate precursor) at ≈120°C under continuous stirring under vacuum.

Synthesis of Cs-Pb-Br nanoplatelet stacks. In a 4 mL glass vial equipped with a magnetic stirring bar add 2 mL of decane, 120 μL of OLA, 160 μL of OA, and heat up under mixing to 100°C. Pre-heat the Cs-Oleate and Pb-Oleate precursors, so they become liquid. At that point, add 20 μL of Cs-oleate and 60 μL of Pb-oleate precursors using a micropipette (as warm/hot liquids, to avoid liquid solidification in the pipette plastic tip). After all components are mixed, let the mixture thermalize for a minute, then inject 20 μL of benzoyl bromide (BzBr) using micropipette under stirring. After injecting BzBr, the reaction mixture immediately acquires a clear yellow color. Let the reaction proceed for 60 seconds, then quench the reaction in a room temperature water bath. To recover the so-formed nanoplatelets add ethyl-acetate dropwise, until the solution turns cloudy. Then, centrifuge at 3000 RPM for 2 min, discard the supernatant and repeat the centrifugation without adding any solvent. Remove the accumulated liquid, then dissolve

the remaining solid in 1200 µL of hexane. Centrifuge at 3000 RPM for 2 minutes to remove

aggregates, then transfer the liquid into a clean glass vial. The nanoplatelets stacks are

assembled by diluting the nanoplatelet dispersion with hexane by a factor of 3-to-5 and

depositing 50 µL of it on a 1x1 cm silicon chip, tilted by about ~15°. The assembly is

performed in a closed Petri dish. A successfully assembled film looks iridescent by eye.

See Figure 6.21 for pictures of the nanoplatelets at different stages of the synthesis,

Figure 6.22 for their optical absorption and photoluminescence spectra, and Figure 6.23

for a picture of a successfully self-assembled nanoplatelets film.

6.8.2 XRD data collection methods

θ:2θ diffraction experiments. θ:2θ X-ray diffraction patterns of nanocrystal superlattices

and nanoplatelet stacks were acquired alternatively on two different diffractometers. 1)

Panalytical Empyrean diffractometer, equipped with a 1.8 kW CuKα ceramic X-ray tube

operating at 45 kV, 1 mm wide incident and receiving slits, and 40 mA and a PIXcel3D 2x2

area detector, parallel-beam geometry. 2) Rigaku SmartLab diffractometer, equipped

with a 9kW Cu-K$_\alpha$ rotating anode (40 kV, 150 mA), 1 mm wide incident and receiving slits,

and 0D scintillation counter detector, and operating in a parallel-beam geometry. The

sample was mounted by simply depositing the 1 x 1 cm silicon substrates flat on the

sample holder stage.

Thermal annealing of CsPbBr$_3$ nanocrystal superlattices. A sample of CsPbBr$_3$ nanocrystal

superlattices (1 x 1 cm silicon wafer with superlattices on top) was dried under vacuum

for 2 h. Then, it was mounted in a controlled-atmosphere heating stage filled with N$_2$ and

covered within a Kapton dome. The XRD patterns were acquired every 25°C, starting from room temperature (≈25°C) and up to 300°C. The sample was heated at a speed of 10°C/min with a thermalization time of 10 min before each measurement. The acquisition time at each set point was ~10 minutes.

XRD data reduction procedure. Bidimensional diffraction data collected with the Panalytical Empyrean diffractometer were integrated over a rectangular sector, chosen to exclude or minimize the contribution of other signals than those coming from the multilayers. This step was not needed for data collected with the Rigaku diffractometer, as it already comes in the form of a 1-D pattern. For both instruments, the background was measured on a clean silicon wafer, integrated under the same conditions applied for the sample, and subtracted from the sample diffractogram after being rescaled if needed. The background subtraction was not needed for nanocrystal superlattices because of the much higher signal/background ratio.

If spurious signals not originated by the superlattices were found in a region of the pattern relevant for the fits, they were subtracted by modelling their shape with a sum of gaussians. Finally, the intensity of nanoplatelets patterns was corrected according to the Lorentz-Polarization-Absorption (LPA) factor for thin films (Equation 6.11):[35]

$$I_{LPA} = I_0 \cdot \left[\frac{\left(1-e^{-\frac{2\mu\tau}{sin(\theta)}}\right)\cdot\left(1+cos^2(2\theta_m)\cdot cos^2(2\theta)\right)}{sin(2\theta)} \right] \qquad \text{Eq. 6.11}$$

Where I_0 is the experimental intensity after the background subtraction), μ is the absorption coefficient of the material, τ is the film thickness, and θ_m is the Goebel mirror

Bragg angle of the diffractometer (1° in our case). In the thin-film approximation applied in our works, $\mu\tau \to 0$. The LPA correction is needed to compensate for the geometrical and instrumental contributions to the diffracted intensity, and must be performed whenever a full-profile fit is performed. Since for CsPbBr$_3$ nanocrystals we limited the analysis to the profile of individual Bragg peaks extended over a relatively short q-range, this step could be neglected. Figure 6.24 shows all the steps of the data reduction process as performed on a Cs-Pb-Br nanoplatelet film diffractogram.

Multilayer Diffraction algorithms for superlattice structure refinement. Multilayer Diffraction theory was implemented in least-square fitting algorithms for refining the structure of superlattices starting from experimental data. In short, the structure parameters that we wanted to refine were set as free parameters in a function that, through Equations 6.8-9, computed the superlattice diffraction profile for a given structural input. Such output was then iteratively compared with the experimental diffraction profile (after the data reduction steps) to optimize the match between experimental results and theory prediction. The details of the implementation change from work to work, with the aim of adapting the code to the specific needs of the fit. For details, please refer to the original open-access publications [Refs. 22,53], where the original Python codes are available as Supplementary Information files.

6.9 Source Publications and Contributions

This chapter is based on the following publications:

I. **Toso, S.;** Baranov, D.; Giannini, C.; Marras, S.; Manna, L. *Wide-Angle X-ray Diffraction Evidence of Structural Coherence in CsPbBr3 Nanocrystal Superlattices*. ACS Mater. Lett. 1, 272–276 (2019). [Ref. 38]

II. **Toso, S.;*** Baranov, D.*; Altamura, D.; Scattarella, F.; Dahl, J.; Wang, X.; Marras, S.; Alivisatos, A. P.; Singer, A.; Giannini, C.; Liberato, M.. *Multilayer Diffraction Reveals That Colloidal Superlattices Approach the Structural Perfection of Single Crystals*. *ACS Nano* 15, 6243–6256 (2021). [Ref. 22**]

III. **Toso, S.;** Baranov, D.; Giannini, C.; Manna, L. *Structure and Surface Passivation of Ultrathin Cesium Lead Halide Nanoplatelets Revealed by Multilayer Diffraction*. *ACS Nano* 15, 20341–20352 (2021). [Ref. 53]

IV. **Toso, S.;** Baranov, D.; Filippi, U.; Giannini, C.; Manna, L. *Collective Diffraction Effects in Perovskite Nanocrystal Superlattices*. Submitted to *Accounts of Chemical Research.* [Ref. 41]

*These authors contributed equally

Publication (I) reports the first observations of Multilayer Diffraction in XRD patterns of CsPbBr$_3$ nanocrystal superlattices, provides a qualitative explanation for their formation, and exploits the position of interference fringes to track the evolution of the superlattice periodicity in different experimental conditions. **Publication (II)** describes the implementation of Multilayer Diffraction theory in Python algorithms capable of refining the structure of nanocrystal superlattices and, to some extent, that of thin nanoplatelets. These algorithms were exploited to track the evolution of CsPbBr$_3$ nanocrystal superlattices during a thermal annealing experiment. In the same publication, we reported the GISAXS and GIWAXS characterization of CsPbBr$_3$ nanocrystal superlattices.

Publication (III) focuses on the study of ultrathin nanoplatelets stacks, for which the Python algorithm was extensively revised and optimized. This enabled implementing an atomistic description of the nanoparticle structure, and allowed to model features like the surface termination of nanoplatelets. **Publication (IV)** is a review summarizing all the results obtained in Publications (I-III), and served as a starting point for writing this chapter. It contains simulations performed using the most advanced version of our Multilayer Diffraction scripts, that implement full-profile intensity corrections and shape parameters for nanocrystals superlattices. A literature review of works containing diffractograms that show signature features of Multilayer Diffraction is also included.

The work discussed in this chapter involved many colleagues whom, with their experience and help, were determinant in transforming a serendipitous observation into the full-fledge analytical method that we call Multilayer Diffraction. Hereby, the major contributions are listed. D. Baranov contributed to all aspects of these works, from the design and execution of experiments to the discussion of results and the drafting of manuscripts. C. Giannini contributed to the interpretation of experimental results and the theoretical modelling of Multilayer Diffraction in all published works, thanks to her vast expertise on diffraction techniques applied to nanomaterials and thin films. A. Singer pointed me in the direction of the articles written by Schuller et al. and, during my visit at the Cornell university, helped with the first implementation of Multilayer Diffraction theory in a working algorithm. J. Dahl later turned those preliminary results into the first version of the Python algorithm implementing Multilayer Diffraction. D. Altamura, and F. Cetrella performed the GISAXS and GIWAXS experiments on CsPbBr$_3$ nanocrystal

superlattices and analyzed the results. S. Marras supported the acquisition and interpretation of θ:2θ XRD data. D. Baranov and L. Manna supervised the projects. All other coauthors provided general support to the projects and contributed to edit the manuscripts. To all colleagues goes my deep gratitude for their invaluable help.

6.10 Copyright

Some elements of this chapter were adapted from external sources:

6.11 Bibliography

1.   Esaki, L. & Tsu, R. Superlattice and Negative Differential Conuctivity in Semiconductors. *IBM J. Res. Dev.* **14**, 61–65 (1970).

2.   Tsu, R. & Esaki, L. Nonlinear optical response of conduction electrons in a superlattice. *Appl. Phys. Lett.* **19**, 246–248 (1971).

3.   Chang, L. L., Esaki, L., Howard, W. E. & Ludeke, R. The Growth of a GaAs–GaAlAs Superlattice. *J. Vac. Sci. Technol.* **10**, 11–16 (1973).

4.   Schuller, I. K. New class of layered Materials. *Phys. Rev. Lett.* **44**, 1597–1600 (1980).

5.   Bentzon, M. D., Van Wonterghem, J., Mørup, S., Thölén, A. & Koch, C. J. W. Ordered aggregates of ultrafine iron oxide particles: 'super crystals'. *Philos. Mag. B Phys. Condens. Matter; Stat. Mech. Electron. Opt. Magn. Prop.* **60**, 169–178 (1989).

6.   Boles, M. A., Engel, M. & Talapin, D. V. Self-assembly of colloidal nanocrystals: From intricate structures to functional materials. *Chem. Rev.* **116**, 11220–11289 (2016).

7.   Nie, Z., Petukhova, A. & Kumacheva, E. Properties and emerging applications of self-assembled structures made from inorganic nanoparticles. *Nat. Nanotechnol.* **5**, 15–25 (2010).

8.   Brittman, S. *et al.* Binary Superlattices of Infrared Plasmonic and Excitonic Nanocrystals. *ACS Appl. Mater. Interfaces* **12**, 24271–24280 (2020).

9.   Takeoka, Y. Stimuli-responsive opals: Colloidal crystals and colloidal amorphous arrays for use in functional structurally colored materials. *J. Mater. Chem. C* **1**, 6059–6074 (2013).

10.   Landon, P. B. *et al.* Self-assembly of colloidal silica into opals with large ordered single crystals. *Colloids Surfaces A Physicochem. Eng. Asp.* **259**, 31–33 (2005).

11.   Pinna, N., Maillard, M., Courty, A., Russier, V. & Pileni, M. P. Optical properties of silver nanocrystals self-organized in a two-dimensional superlattice: Substrate effect. *Phys. Rev. B - Condens. Matter Mater. Phys.* **66**, 1–6 (2002).

12.   Tao, A., Sinsermsuksakul, P. & Yang, P. Tunable plasmonic lattices of silver nanocrystals. *Nat. Nanotechnol.* **2**, 435–440 (2007).

13. Kagan, C. R. & Murray, C. B. Charge transport in strongly coupled quantum dot solids. *Nat. Nanotechnol.* **10**, 1013–1026 (2015).

14. Whitham, K. *et al.* Charge transport and localization in atomically coherent quantum dot solids. *Nat. Mater.* **15**, 557–563 (2016).

15. Courty, A., Mermet, A., Albouy, P. A., Duval, E. & Pileni, M. P. Vibrational coherence of self-organized silver nanocrystals in f.c.c. supra-crystals. *Nat. Mater.* **4**, 395–398 (2005).

16. Yazdani, N. *et al.* Nanocrystal superlattices as phonon-engineered solids and acoustic metamaterials. *Nat. Commun.* **10**, 1–6 (2019).

17. Russier, V., Pstit, C. & Pileni, M. P. Hysteresis curve of magnetic nanocrystals monolayers: Influence of the structure. *J. Appl. Phys.* **93**, 10001–10010 (2003).

18. Chen, J. *et al.* Collective dipolar interactions in self-assembled magnetic binary nanocrystal superlattice membranes. *Nano Lett.* **10**, 5103–5108 (2010).

19. Rainò, G. *et al.* Superfluorescence from lead halide perovskite quantum dot superlattices. *Nature* **563**, 671–675 (2018).

20. Krieg, F. *et al.* Monodisperse Long-Chain Sulfobetaine-Capped $CsPbBr_3$ Nanocrystals and Their Superfluorescent Assemblies. *ACS Cent. Sci.* **7**, 135–144 (2021).

21. Baranov, D. *et al.* Aging of Self-Assembled Lead Halide Perovskite Nanocrystal Superlattices: Effects on Photoluminescence and Energy Transfer. *ACS Nano* **15**, 650–664 (2021).

22. Toso, S. *et al.* Multilayer Diffraction Reveals That Colloidal Superlattices Approach the Structural Perfection of Single Crystals. *ACS Nano* **15**, 6243–6256 (2021).

23. Goodfellow, B. W., Yu, Y., Bosoy, C. A., Smilgies, D. M. & Korgel, B. A. The Role of Ligand Packing Frustration in Body-Centered Cubic (bcc) Superlattices of Colloidal Nanocrystals. *J. Phys. Chem. Lett.* **6**, 2406–2412 (2015).

24. Yu, Y., Yu, D., Sadigh, B. & Orme, C. A. Space- and time-resolved small angle X-ray scattering to probe assembly of silver nanocrystal superlattices. *Nat. Commun.* **9**, 1–9 (2018).

25. Mayence, A., Wang, D., Salazar-Alvarez, G., Oleynikov, P. & Bergström, L. Probing planar defects in nanoparticle superlattices by 3D small-angle electron

diffraction tomography and real space imaging. *Nanoscale* **6**, 13803–13808 (2014).

26. Cherniukh, I. *et al.* Perovskite-Type Superlattices from Lead Halide Perovskite Nanocubes. *Nature* **593**, 535–542 (2021).

27. Cherniukh, I. *et al.* Structural Diversity in Multicomponent Nanocrystal Superlattices Comprising Lead Halide Perovskite Nanocubes. *ACS Nano* **13**, 22 (2021).

28. Coropceanu, I., Boles, M. A. & Talapin, D. V. Systematic Mapping of Binary Nanocrystal Superlattices: The Role of Topology in Phase Selection. *J. Am. Chem. Soc.* **141**, 5728–5740 (2019).

29. Ye, X. *et al.* Structural diversity in binary superlattices self-assembled from polymer-grafted nanocrystals. *Nat. Commun.* **6**, 1–10 (2015).

30. Choi, J. J. *et al.* Controlling nanocrystal superlattice symmetry and shape-anisotropic interactions through variable ligand surface coverage. *J. Am. Chem. Soc.* **133**, 3131–3138 (2011).

31. Choi, J. J., Bian, K., Baumgardner, W. J., Smilgies, D. M. & Hanrath, T. Interface-induced nucleation, orientational alignment and symmetry transformations in nanocube superlattices. *Nano Lett.* **12**, 4791–4798 (2012).

32. Hanrath, T., Choi, J. J. & Smilgies, D. M. Structure/processing relationships of highly ordered lead salt nanocrystal superlattices. *ACS Nano* **3**, 2975–2988 (2009).

33. Smilgies, D. M. & Hanrath, T. Superlattice self-assembly: Watching nanocrystals in action. *EPL* **119**, 28003 (2017).

34. Mahmood, A. & Wang, J. L. A Review of Grazing Incidence Small- and Wide-Angle X-Ray Scattering Techniques for Exploring the Film Morphology of Organic Solar Cells. *Sol. RRL* **4**, 2000337 (2020).

35. Fullerton, E. E., Schuller, I. K., Vanderstraeten, H. & Bruynseraede, Y. Structural refinement of superlattices from x-ray diffraction. *Phys. Rev. B* **45**, 9292–9310 (1992).

36. Baranov, D., Toso, S., Imran, M. & Manna, L. Investigation into the Photoluminescence Red Shift in Cesium Lead Bromide Nanocrystal Superlattices. *J. Phys. Chem. Lett.* **10**, 655–660 (2019).

37.   Murray, C. B., Kagan, C. R. & Bawendi, M. G. Self-Organization of CdSe Nanocrystallites into Three-Dimensional Quantum Dot Superlattices. *Science (80-.).* **270**, 1335–1338 (1995).

38.   Toso, S., Baranov, D., Giannini, C., Marras, S. & Manna, L. Wide-Angle X-ray Diffraction Evidence of Structural Coherence in $CsPbBr_3$ Nanocrystal Superlattices. *ACS Mater. Lett.* **1**, 272–276 (2019).

39.   Langford, J. I. & Wilson, A. J. C. Scherrer after sixty years: A survey and some new results in the determination of crystallite size. *J. Appl. Crystallogr.* **11**, 102–113 (1978).

40.   Cottingham, P. & Brutchey, R. L. Depressed Phase Transitions and Thermally Persistent Local Distortions in $CsPbBr_3$ Quantum Dots. *Chem. Mater.* **30**, 6711–6716 (2018).

41.   Toso, S., Baranov, D., Filippi, U., Giannini, C. & Manna, L. Collective Diffraction Effects in Perovskite Nanocrystal Superlattices. *Acc. Chem. Res.* **56**, 66–76 (2022).

42.   Holý, V., Pietsch, U. & Baumbach, T. *High-Resolution X-Ray Scattering from Thin Films and Multilayers*. (Springer Berlin Heidelberg, 1999).

43.   Bowen, D. K. & Tanner, B. K. *High Resolution X-Ray Diffractometry and Topography*. (Taylor & Francis, 1998).

44.   Birkholz, M. *Thin Film Analysis by X-Ray Scattering*. (Wiley, 2005). doi:10.1002/3527607595.

45.   Fewster, P. F. X-ray analysis of thin films and multilayers. *Reports Prog. Phys.* **59**, 1339–1407 (1996).

46.   Prudnikov, I. & Kolparov, A. V. Theory of X-Ray Diffraction in Solid State Superlattices. *Moscow Univ. Phys. Bull.* **4**, 46 (1991).

47.   Tapfer, L. & Ploog, K. Improved assessment of structural properties of $Al_xGa_{1-x}As/GaAs$ heterostructures and superlattices by double-crystal x-ray diffraction. *Phys. Rev. B* **33**, 5565–5574 (1986).

48.   Tapfer, L. High Resolution X-Ray Diffraction in Multilayered Semiconductor Structures and Superlattices. *Phys. Scr.* **T25**, 45–50 (1989).

49.   Holý, V., Kuběna, J., Ohlídal, I. & Ploog, K. The diffuse X-ray scattering in real periodical superlattices. *Superlattices Microstruct.* **12**, 25–35 (1992).

50. Sevenhans, W., Gijs, M., Bruynseraede, Y., Homma, H. & Schuller, I. K. Cumulative disorder and x-ray line broadening in multilayers. *Phys. Rev. B* **34**, 5955–5958 (1986).

51. Locquet, J. P., Neerinck, D., Stockman, L., Bruynseraede, Y. & Schuller, I. K. Discrete and Continuous Disorder in Superlattices. *Phys. Rev. B* **39**, 13338–13342 (1989).

52. Ashcroft, N. & Mermin, N. *Solid State Physics*. (Holt, Rinehart and Winston, 1976).

53. Toso, S., Baranov, D., Giannini, C. & Manna, L. Structure and Surface Passivation of Ultrathin Cesium Lead Halide Nanoplatelets Revealed by Multilayer Diffraction. *ACS Nano* **15**, 20341–20352 (2021).

54. Tong, Y. *et al.* Spontaneous Self-Assembly of Perovskite Nanocrystals into Electronically Coupled Supercrystals: Toward Filling the Green Gap. *Adv. Mater.* **30**, 1801117 (2018).

55. Imran, M. *et al.* Shape Pure, Nearly Monodisperse $CsPbBr_3$ Nanocubes Prepared using Secondary Aliphatic Amines. *Nano Lett.* **18**, 7822–7831 (2018).

56. Brennan, M. C. *et al.* Origin of the Size-Dependent Stokes Shift in CsPbBr3 Perovskite Nanocrystals. *J. Am. Chem. Soc.* **139**, 12201–12208 (2017).

57. Zamani, H., Chiang, T.-H., Klotz, K. R., Hsu, A. J. & Maye, M. M. Tailoring $CsPbBr_3$ Growth Via Non-Polar Solvent Choice and Heating Method. *Langmuir* **38**, 9363–9371 (2022).

58. Ban, J. *et al.* Two-Photon Absorption and Photoluminescence of Individual $CsPbBr_3$ Nanocrystal Superlattices. *J. Phys. Chem. C* **126**, 8400–8407 (2022).

59. Bertolotti, F. *et al.* Size Segregation and Atomic Structural Coherence in Spontaneous Assemblies of Colloidal Cesium Lead Halide Nanocrystals. *Chem. Mater.* **34**, 594–608 (2022).

60. Brennan, M. C. *et al.* Superlattices are Greener on the Other Side: How Light Transforms Self-Assembled Mixed Halide Perovskite Nanocrystals. *ACS Energy Lett.* **5**, 1465–1473 (2020).

61. Bhosale, S. S. *et al.* Functionalized hybrid perovskite nanocrystals with organic ligands showing a stable 3D/2D core/shell structure for display and laser applications. *J. Mater. Chem. C* **9**, 17341–17348 (2021).

62.   Imran, M. *et al.* Benzoyl Halides as Alternative Precursors for the Colloidal Synthesis of Lead-Based Halide Perovskite Nanocrystals. *J. Am. Chem. Soc.* **140**, 2656–2664 (2018).

63.   Almeida, G. *et al.* Role of Acid-Base Equilibria in the Size, Shape, and Phase Control of Cesium Lead Bromide Nanocrystals. *ACS Nano* **12**, 1704–1711 (2018).

64.   Zaccaria, F. *et al.* The Reactivity of CsPbBr3Nanocrystals toward Acid/Base Ligands. *ACS Nano* **16**, 1444–1455 (2022).

65.   Dai, L. *et al.* Slow carrier relaxation in tin-based perovskite nanocrystals. *Nat. Photonics* **15**, 696–702 (2021).

66.   Holder, C. F. & Schaak, R. E. Tutorial on Powder X-ray Diffraction for Characterizing Nanoscale Materials. *ACS Nano* **13**, 7359–7365 (2019).

67.   Peng, S. *et al.* Effective Surface Ligand-Concentration Tuning of Deep-Blue Luminescent $FAPbBr_3$ Nanoplatelets with Enhanced Stability and Charge Transport. *ACS Appl. Mater. Interfaces* **12**, 31863–31874 (2020).

68.   Huang, J., Wu, Y. H., Zhu, Z. G., Shih, W. Y. & Shih, W. H. Control of oleylamine to perovskite ratio in synthesis of $MAPbBr_3$ nanoparticles. *Chem. Phys. Lett.* **702**, 21–25 (2018).

69.   Dahl, J. C., Wang, X., Huang, X., Chan, E. M. & Alivisatos, A. P. Elucidating the Weakly Reversible Cs-Pb-Br Perovskite Nanocrystal Reaction Network with High-Throughput Maps and Transformations. *J. Am. Chem. Soc.* **142**, 11915–11926 (2020).

70.   Guvenc, C. M., Tunc, I. & Balci, S. $L_2[GA_xFA_{1-x}PbI_3]PbI_4$ ($0 \le x \le 1$) Ruddlesden–Popper Perovskite Nanocrystals for Solar Cells and Light-Emitting Diodes. *ACS Appl. Nano Mater.* **5**, 1078–1085 (2022).

71.   Lu, W. G. *et al.* Strong Polarized Photoluminescence from Stretched Perovskite-Nanocrystal-Embedded Polymer Composite Films. *Adv. Opt. Mater.* **5**, 1700594 (2017).

72.   Klein, E. *et al.* Micron-Size Two-Dimensional Methylammonium Lead Halide Perovskites. *ACS Nano* **13**, 6 (2019).

73.   Weidman, M. C., Seitz, M., Stranks, S. D. & Tisdale, W. A. Highly Tunable Colloidal Perovskite Nanoplatelets through Variable Cation, Metal, and Halide Composition. *ACS Nano* **10**, 7830–7839 (2016).

74. Wu, Y. *et al.* In Situ Passivation of $PbBr_6^{4-}$ Octahedra toward Blue Luminescent $CsPbBr_3$ Nanoplatelets with Near 100% Absolute Quantum Yield. *ACS Energy Lett.* **3**, 2030–2037 (2018).

75. Yoshida, T., Mori, T. & Ueda, I. Giant planar lipid bilayer. I. Capacitance and its biphasic response to inhalation anesthetics. *J. Colloid Interface Sci.* **96**, 39–47 (1983).

76. Bekenstein, Y., Koscher, B. A., Eaton, S. W., Yang, P. & Alivisatos, A. P. Highly Luminescent Colloidal Nanoplates of Perovskite Cesium Lead Halide and Their Oriented Assemblies. *J. Am. Chem. Soc.* **137**, 16008–16011 (2015).

77. Borges, J. *et al.* Preparation and characterization of DNA films using oleylamine modified Au surfaces. *J. Colloid Interface Sci.* **358**, 626–634 (2011).

78. Parobek, D., Dong, Y., Qiao, T. & Son, D. H. Direct Hot-Injection Synthesis of Mn-Doped $CsPbBr_3$ Nanocrystals. *Chem. Mater.* **30**, 2939–2944 (2018).

79. Mehetor, S. K., Ghosh, H. & Pradhan, N. Acid-Amine Equilibria for Formation and Long-Range Self-Organization of Ultrathin $CsPbBr_3$ Perovskite Platelets. *J. Phys. Chem. Lett.* **10**, 1300–1305 (2019).

80. Toso, S. *et al.* Nanocrystals of Lead Chalcohalides: A Series of Kinetically Trapped Metastable Nanostructures. *J. Am. Chem. Soc.* **142**, 10198–10211 (2020).

81. Toso, S. *et al.* Halide perovskites as disposable epitaxial templates for the phase-selective synthesis of lead sulfochloride nanocrystals. *Nat. Commun. 2022 131* **13**, 1–10 (2022).

82. Quarta, D. *et al.* Colloidal Bismuth Chalcohalide Nanocrystals. *Angew. Chemie* **61**, e202201747 (2022).

83. Bertolotti, F. *et al.* Crystal Structure, Morphology, and Surface Termination of Cyan-Emissive, Six-Monolayers-Thick $CsPbBr_3$ Nanoplatelets from X-ray Total Scattering. *ACS Nano* **13**, 14294–14307 (2019).

84. Liu, Y. *et al.* Surface-Tension-Controlled Crystallization for High-Quality 2D Perovskite Single Crystals for Ultrahig Photodetection. *Matter* **1**, 465–480 (2019).

85. Wang, L. & Sasaki, T. Titanium Oxide Nanosheets: Graphene Analogues with Versatile Functionalities. *Chem. Rev.* **114**, 9455–9486 (2014).

86. Sasaki, T. & Watanabe, M. Osmotic swelling to exfoliation. Exceptionally high degrees of hydration of a layered titanate. *J. Am. Chem. Soc.* **120**, 4682–4689 (1998).

87. Takimoto, D. *et al.* Synthesis and Oxygen Electrocatalysis of Iridium Oxide Nanosheets. *Electrocatalysis* **8**, 144–150 (2017).

88. Etman, A. S. *et al.* A one-step water based strategy for synthesizing hydrated vanadium pentoxide nanosheets from VO_2(B) as free-standing electrodes for lithium battery applications. *J. Mater. Chem. A* **4**, 17988–18001 (2016).

89. Omomo, Y., Sasaki, T., Wang, L. & Watanabe, M. Redoxable nanosheet crystallites of MnO_2 derived via delamination of a layered manganese oxide. *J. Am. Chem. Soc.* **125**, 3568–3575 (2003).

90. Liu, Z. *et al.* Synthesis, anion exchange, and delamination of Co-Al layered double hydroxide: Assembly of the exfoliated nanosheet/polyanion composite films and magneto-optical studies. *J. Am. Chem. Soc.* **128**, 4872–4880 (2006).

91. Zhang, J., Zhang, F., Ren, L., Evans, D. G. & Duan, X. Synthesis of layered double hydroxide anionic clays intercalated by carboxylate anions. *Mater. Chem. Phys.* **85**, 207–214 (2004).

92. Benchakar, M. *et al.* One MAX phase, different MXenes: A guideline to understand the crucial role of etching conditions on $Ti_3C_2T_x$ surface chemistry. *Appl. Surf. Sci.* **530**, 147209 (2020).

93. Alhabeb, M. *et al.* Guidelines for Synthesis and Processing of Two-Dimensional Titanium Carbide ($Ti_3C_2T_x$ MXene). *Chem. Mater.* **29**, 7633–7644 (2017).

94. Kuo, D.-Y. & Cossairt, B. M. Direct Intercalation of MoS_2 and WS_2 Thin Films by Vacuum Filtration. *Mater. Horizons* **9**, 360–367 (2021).

95. Zhu, D. & Wang, H. Hexafluorophosphate Anion Intercalation into Graphite Electrodes from Propylene Carbonate/Gamma-Butyrolactone Solutions. *Langmuir* **37**, 10797–10805 (2021).

96. Ellis, H. A., White, N. A. S., Taylor, R. A. & Maragh, P. T. Infrared, X-ray and microscopic studies on the room temperature structure of anhydrous lead (II) n-alkanoates. *J. Mol. Struct.* **738**, 205–210 (2005).

97. García-Barrasa, J., López-de-Luzuriaga, J. M., Monge, M., Soulantica, K. & Viau, G. Synthesis of thiolate-protected silver nanocrystal superlattices from an organometallic precursor and formation of molecular di-n-alkyldisulfide lamellar phases. *J. Nanoparticle Res.* **13**, 791–801 (2011).

98.   Pankhurst, J. R. *et al.* Copper Phosphonate Lamella Intermediates Control the Shape of Colloidal Copper Nanocrystals. *J. Am. Chem. Soc.* **144**, 12261–12271 (2022).

99.   Rohatgi, A. WebPlotDigitizer - extract data from plots, images, and maps. *Arohatgi* (2010).

100.   Jiang, Z. GIXSGUI: A MATLAB toolbox for grazing-incidence X-ray scattering data visualization and reduction, and indexing of buried three-dimensional periodic nanostructured films. *J. Appl. Crystallogr.* **48**, 917–926 (2015).
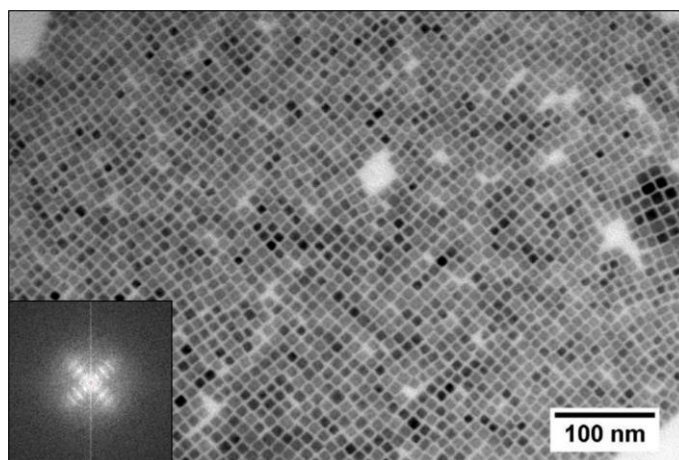
Figure 6.10. CsPbBr₃ cube-shaped nanocrystals. TEM image of a close-packed monolayer of CsPbBr₃ nanocrystals like those used for the preparation of superlattices. The center-center particle distance is ~11.8 nm, as estimated by the FFT (inset). [Ref. 38]
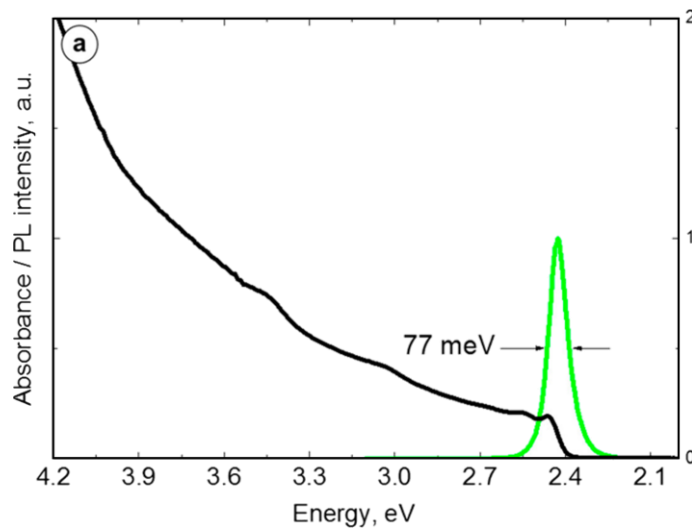
Figure 6.11. Optical absorption and PL spectra of CsPbBr₃ nanocrystals. Steady-state absorption (solid black curve) and PL (solid green curve) of a colloidal dispersion of CsPbBr₃ nanocrystals. Reprinted with permission from J. Phys. Chem. Lett. 2019, 10, 3, 655–660. Copyright 2019, American Chemical Society. https://doi.org/10.1021/acs.jpclett.9b00178. [Ref. 36]
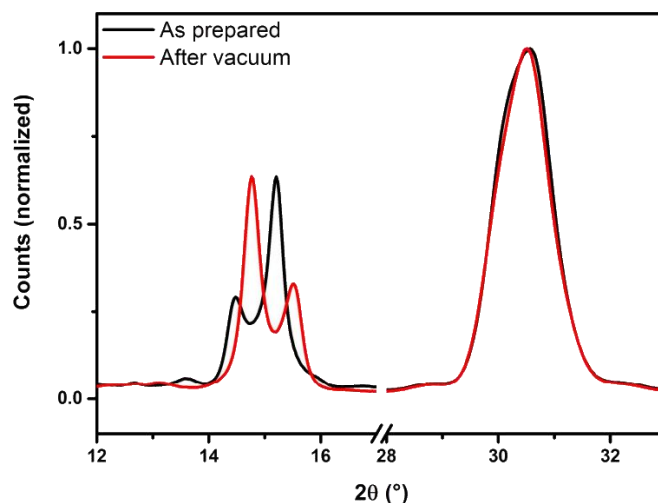
Figure 6.12. Superlattice contraction upon exposure to vacuum. Bragg peaks of a $CsPbBr_3$ nanocrystal superlattice sample before and after the exposure to vacuum. The periodicity Λ contracts from ~12.24 nm to ~12.00 nm, as measured from the position of interference fringes. See also Figure 6.15. [Ref. 38]
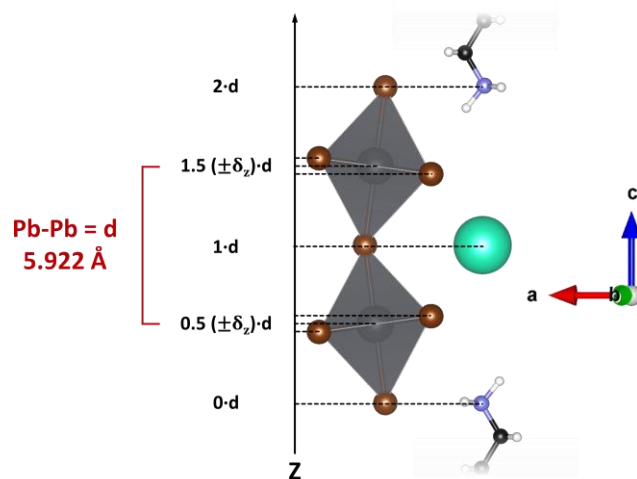
Figure 6.13. Monodimensional representation of a Cs-Pb-Br nanoplatelet. The platelet structure is described by the projection along the *z*-axis of all the atomic planes needed to capture the nanoplatelet stoichiometry. In sequence, from top to bottom: R-$NH_3Br/PbBr_2/CsBr/PbBr_2/NH_3Br$. The tilting of $[PbBr_6]^{4-}$ octahedra is captured by offsetting the vertical coordinates of Br atoms in the $PbBr_2$ planes by a factor δ_z. [Ref. 53]
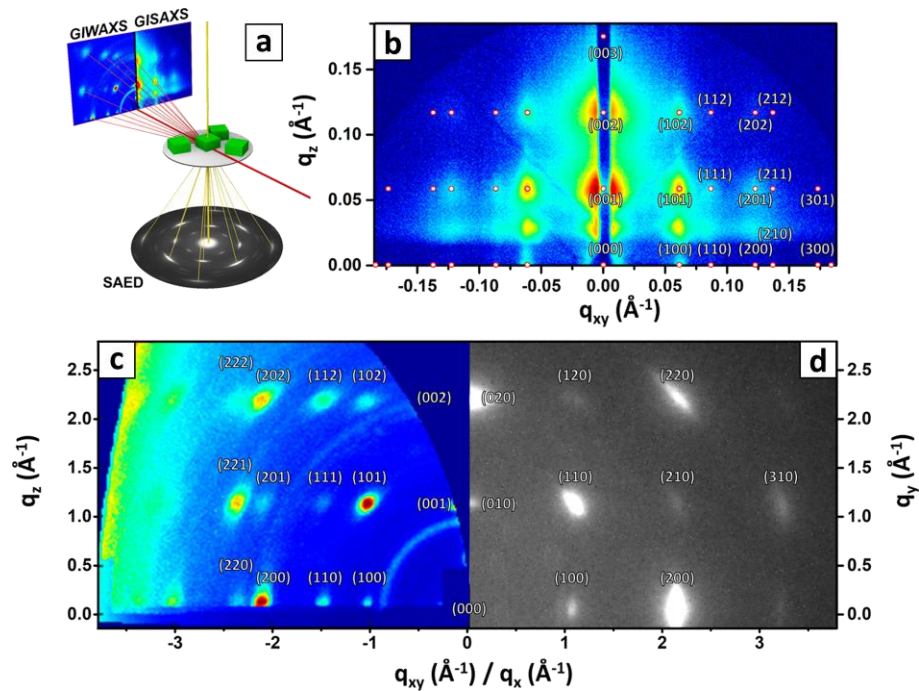
Figure 6.14. GISAXS / GIWAXS / SAED analysis of CsPbBr₃ nanocrystal superlattices. a) Diffraction geometries adopted for experiments in panels(b-d), highlighting the complementarity of grazing incidence techniques and TEM–SAED in terms of spatial directions. b) GISAXS pattern of CsPbBr₃ nanocrystal superlattices indexed according to a simple-cubic symmetry. The diffraction spots are generated by the nanometer-scale periodicity of the superstructure. c) GIWAXS pattern of CsPbBr₃ superlattices. The spots arise from the angstrom-scale periodicity of the CsPbBr₃ nanocrystal atomic lattice. The blue region hiding the (00ℓ) spots is known as the "missing wedge".[100] d) SAED pattern of a single CsPbBr₃ superlattice, featuring slightly elongated spots produced by the atomic lattices of many CsPbBr₃ nanocrystals slightly tilted with respect to each other. Data in panels (c-d) were indexed considering cubic the structure of CsPbBr₃ nanocrystals, for simplicity. [Ref. 22]
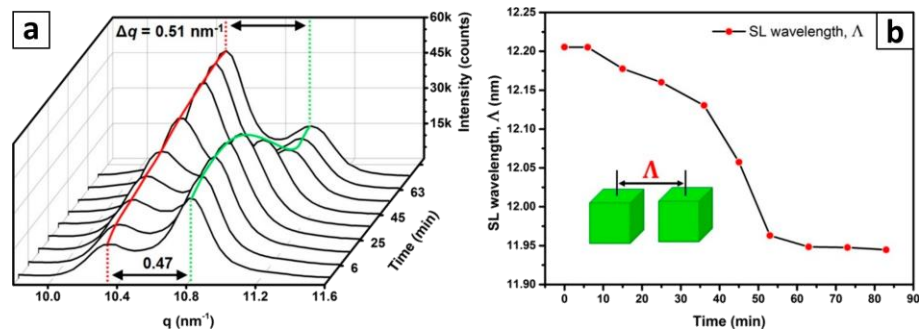
Figure 6.15. Tracking the contraction of CsPbBr₃ nanocrystal superlattices under vacuum. a) Time evolution of the first Bragg peak profile of CsPbBr₃ nanocrystal superlattices under static vacuum. b) Corresponding contraction of the superlattice periodicity Λ as a function of time. [Ref. 38]
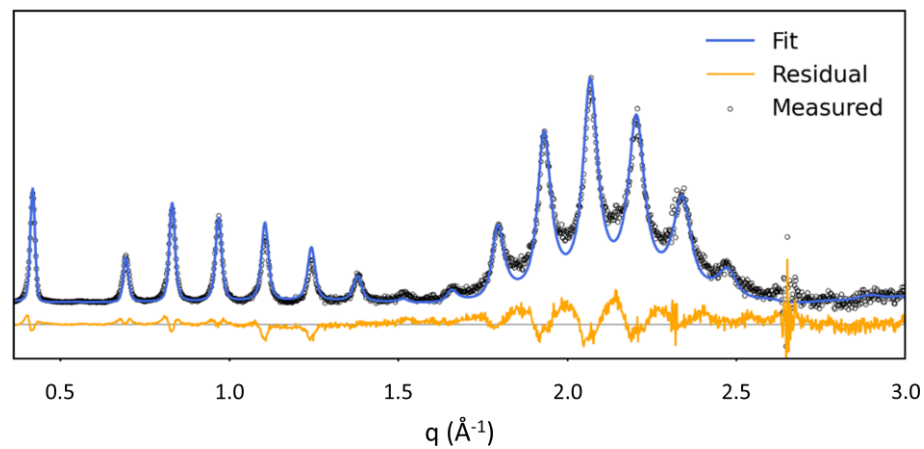
Figure 6.16. Cs-Pb-Br nanoplatelets synthesized with erucic acid. The fit parameters are comparable within error to what measured on samples prepared with oleic acid (see Figure 6.7a): vertical Pb-Pb distance = 5.931 ± 0.006 Å; L = 33.84 ± 0.02 Å; σ_L = 0.491 ± 0.008 Å; surface occupancy = 74 ± 3 %; CsBr layer occupancy = 94 ± 2 %; δ_z = 0.29 ± 0.06 Å. [Ref. 53]
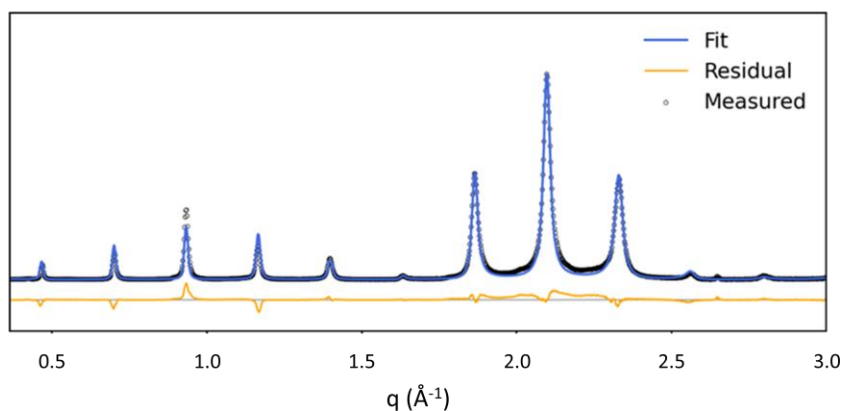
Figure 6.17. Cs-Pb-Br nanoplatelets synthesized with octylamine. The fit captures the shorter interparticle distance and the lowered stacking disorder expected as a consequence of using shorter ligands: Pb-Pb distance = 5.90 ± 0.01 Å; L = 15.16 ± 0.03 Å; σ_L = 0.240 ± 0.006 Å; surface occupancy = 87 ± 4 %; CsBr layer occupancy = 0.96 ± 0.02 %; δ_z = 0.32± 0.05 Å. [Ref. 53]
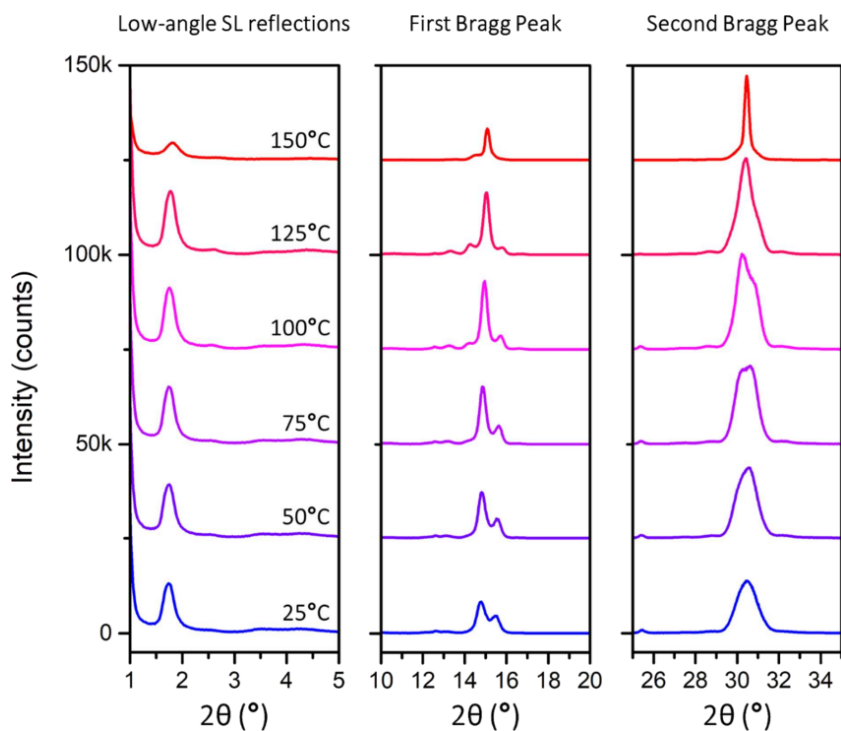
Figure 6.18. Thermal annealing of CsPbBr₃ nanocrystal superlattices. Evolution of all the regions in the CsPbBr₃ nanocrystal superlattices pattern upon thermal annealing. Intensities are not normalized. [Ref. 22]
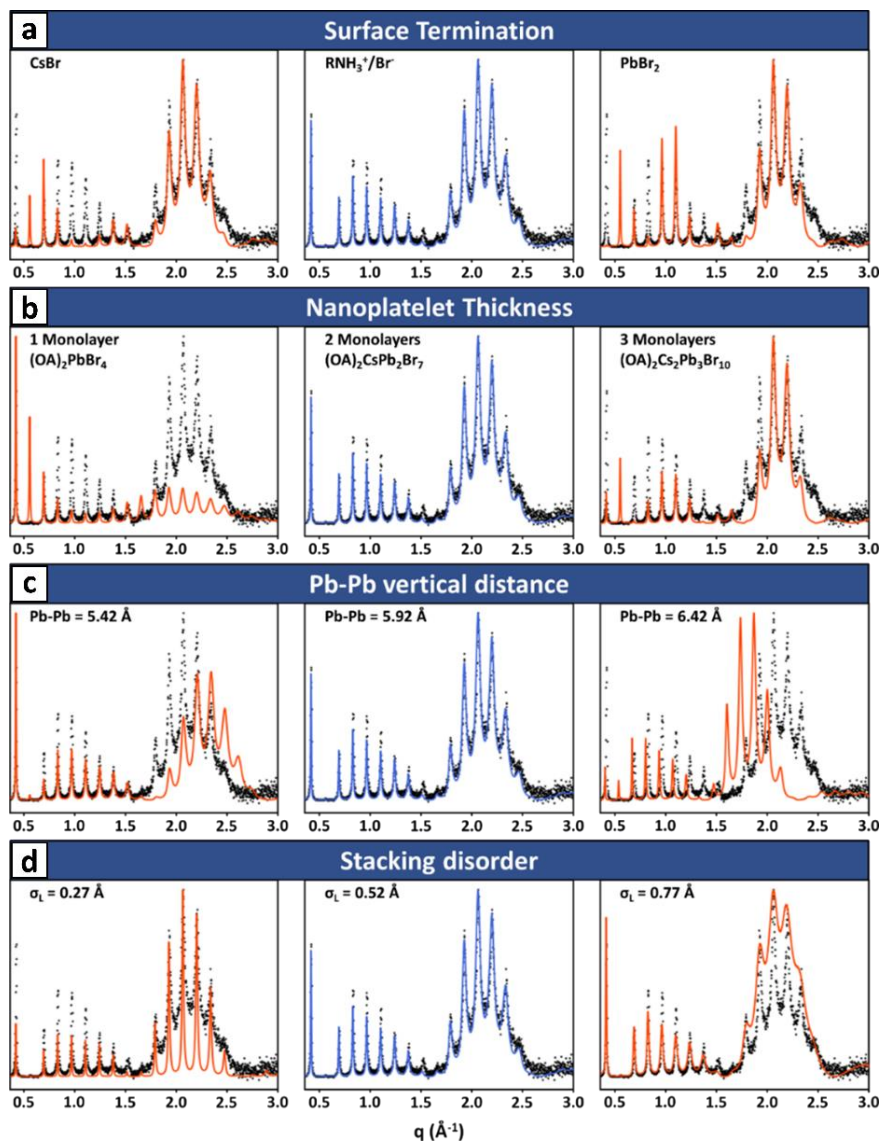
Figure 6.19. Influence of structural parameters on the Multilayer Diffraction pattern of Cs-Pb-Br nanoplatelets. a) Different surface terminations. b) Different nanoplatelet thickness. c) Different Pb-Pb vertical distances, representing the contraction/expansion of the platelet structure along its thinnest direction. d) Stacking disorder. The blue pattern is identical in all the series of simulations, and corresponds to the preliminary best fit (not refining partial occupancies and atomic layer coordinates). The overall multilayer periodicity (*i.e.*, nanoplatelet thickness + interparticle spacing) was kept constant in all the simulations by adjusting the interparticle spacing when needed, to ease comparison. [Ref. 53]

223
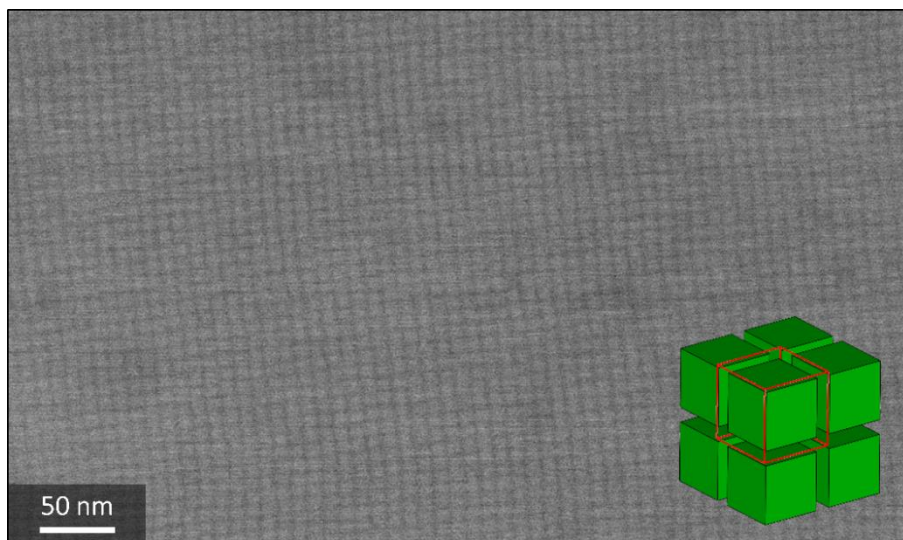
Figure 6.20. High-resolution SEM image of a CsPbBr₃ nanocrystals superlattice. The inset shows a representation of the simple-cubic superlattice structure. The superlattice unit cell is outlined in red. [Ref. 22]
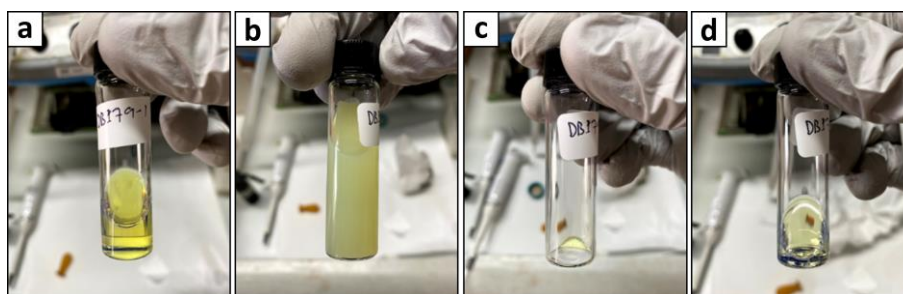
Figure 6.21. Synthesis of Cs-Pb-Br nanoplatelets. Photographs of the various stages of the Cs-Pb-Br nanoplatelet synthesis and purification. a) Reaction mixture after the Bz-Br injection, 1 min growth, and cooling to room temperature in a water bath. b) Cloudy dispersion of flocculated nanoplatelets after the addition of ethyl acetate before the 1st centrifugation. c) Precipitated nanoplatelets after the 2nd centrifugation. d) The isolated solid after being redispersed in 1.2 ml of hexane, yielding a clear light-yellow solution with a faintly visible blue photoluminescence caused by ambient light. [Ref. 53]
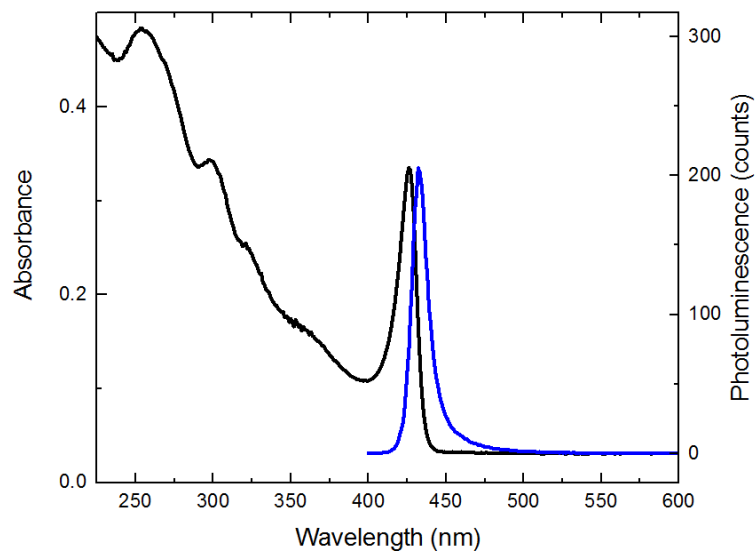
Figure 6.22. Optical absorption and PL spectra of Cs-Pb-Br nanoplatelets. Absorption (solid black curve) and photoluminescence (solid blue curve) of a successfully synthesised nanoplatelet sample diluted in hexane. [Ref. 53]
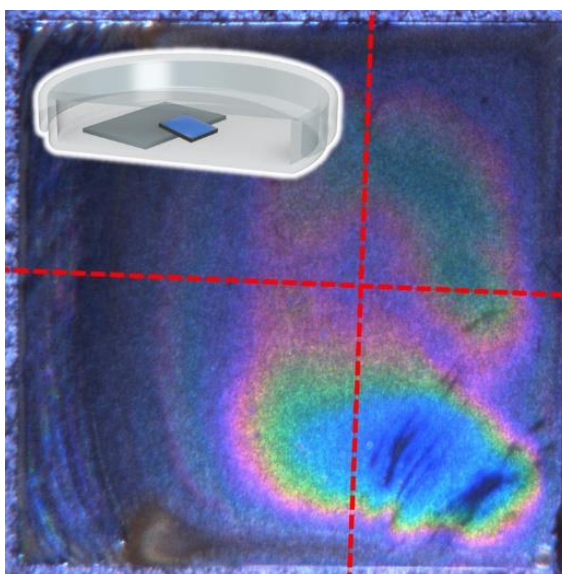
Figure 6.23. Cs-Pb-Br nanoplatelets film. Top view of a sample as seen from the diffractometer alignment system, showing the characteristic iridescence. The red cross indicates the spot chosen for XRD analysis. Inset: graphical representation of the setup used for the self-assembly of thin films. [Ref. 53]
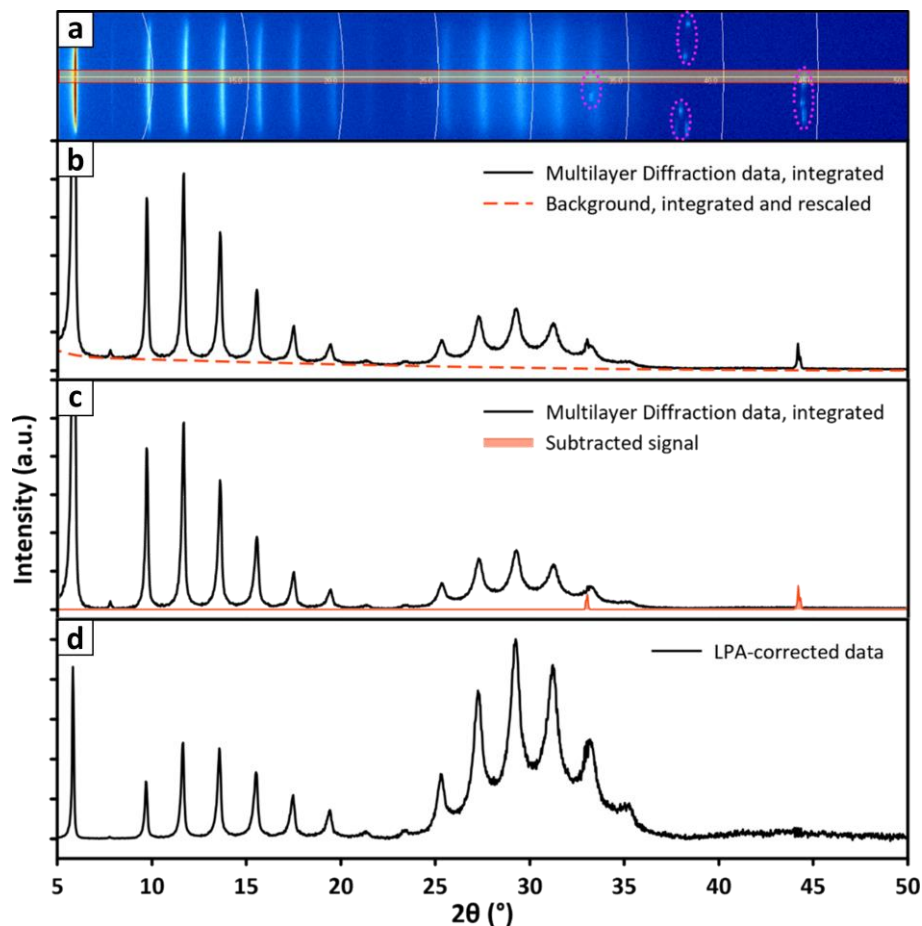
Figure 6.24. Data reduction process for Cs-Pb-Br nanoplatelets.
a) 2D-diffraction pattern from a nanoplatelets film showing the Multilayer Diffraction fringes. Spurious signals coming from the substrate are encircled. The region of interest for the integration is shaded in yellow. b) 1D pattern obtained after integrating the 2D-data region of interest, shaded in yellow in panel (a), shown together with the instrumental background (dashed red line). The instrumental background was measured on a clean silicon wafer, the resulting 2D-diffraction pattern was integrated similarly to the sample, and transformed into a spline for easier data processing. c) Experimental data shown after the subtraction of background and spurious signals (in red). d) Experimental profile after the background subtraction and the application of the Lorentz Polarization Absorption (LPA) correction. [Ref. 53]

226

TABLE 6.1:

SIMULATION PARAMETERS FOR FIGURE 6.8.

Plot	Material	Orientation	Shape	Thickness [nm]	Termination	L [Å]	σ_L [Å]	Packing Geometry	Λ [Å]
a1	Cs_4PbBr_6	(012)	Sphere	9.09	---	34	1.0	S. Cubic	124.9
a2	Cs_4PbBr_6	(012)	Sphere	9.09	---	34	1.0	BCC	2×72.1
a3	Cs_4PbBr_6	(012)	Sphere	9.09	---	34	1.0	FCC	2·88.3
a4	Cs_4PbBr_6	(012)	Sphere	9.09	---	34	1.0	HCP	2×102.0
b1	CdSe	(100)	Platelet	0.43	Cd	40	0.5	Stack	44.3
b2	CdSe	(100)	Platelet	1.29	Cd	40	0.5	Stack	52.9
b3	CdSe	(100)	Platelet	2.15	Cd	40	0.5	Stack	61.5
b4	CdSe	(100)	Platelet	3.01	Cd	40	0.5	Stack	70.1
c1	$CsPbBr_3$	(100)	Cubes	7.59	---	34	1.0	S. Cubic	109.9

TABLE 6.1 (CONTINUED)

c2	CsPbBr$_3$	(100)	Cubes	7.59	---	34	1.0	S. Cubic, alternated	110.5
	PbS	(100)	Cubes	7.71	---				
c3	CsPbBr$_3$	(100)	Cubes	7.59	---	34	1.0	S. Cubic, mixed	2×110.5
	PbS	(100)	Cubes	7.71	---				
c4	PbS	(100)	Cubes	7.71	---	34	1.0	S. Cubic	111.1
d1	CsPbBr$_3$	(100)	Platelet	1.18	R-NH$_3$Br	37	0.5	Stack	48.8
d2	CsPbBr$_3$	(100)	Platelets	1.18	R-NH$_3$Br	36.9	0.5	Stack, alternated	2×48.8
	PbS	(100)	Platelets	1.21	PbS				
d3	CsPbBr$_3$	(100)	Platelets	1.18	R-NH$_3$Br	36.9	0.5	Stack, mixed	48.8
	PbS	(100)	Platelets	1.21	PbS				
d4	PbS	(100)	Platelets	1.21	R-NH$_3$Br	36.8	0.5	Stack	48.8

NOTE: Orientation indicates the planes parallel to the substrate. For CdSe, thickness is indicated in Cd-Se monolayers (ML). Surface terminations are specified only for nanoplatelets, as the unit-cell based description of nanocrystals makes such level of atomistic detail inaccessible. Λ values written as 2×N indicate that the actual superlattice unit cell is double the layer center-to-center distance, that is the distance measured as Λ by Multilayer Diffraction.

CHAPTER 7:

BULK NANOMATERIALS

7.1 The Missing Link between Superlattice and Bulk

In the previous chapters we made our way from individual nanocrystals to highly ordered superlattices, whose structural coherence reaches that of epitaxial films and approaches that of single crystals. Here, we will discuss a class of materials that fills the gap, as they are at the same time fully crystalline bulk solids and nanoplatelets superlattices: the layered metal halides.

We will focus in particular on Ruddlesden-Popper (RP) lead-halides, a class of two-dimensional semiconductors that have recently gained relevance as promising candidates for optoelectronic and photovoltaic applications.[1–6] Described by the formula $L_2A_{n-1}Pb_nX_{3n+1}$,[7] they consist of n bidimensional layers of corner-sharing $[PbX_6]^{4-}$ octahedra (X = Cl, Br, I) held together by isotropic cations (A = Cs^+, methylammonium [MA], formamidinium [FA], …). Individual layers, in turn, are separated by long-chain ammonium cations such as butylammonium (BA) or phenylethyl ammonium (PEA).[3] Such structure confers peculiar properties, as the long-chain cations insulate the semiconducting layers from each other, turning them into quantum wells.[8]

In this respect, RP lead halides are nanomaterials, as their optoelectronic properties are largely comparable with those of lead-halide perovskite nanoplatelets of

the same *n* thickness. To give an example, the optical absorption edge and photoluminescence emission of both mm-size *n = 2* $(BA)_2(MA)Pb_2I_7$ bulk crystals[7] and of *n = 2* $(oleylamine)_2(MA)Pb_2I_7$ colloidal nanoplatelets[9] are found, close to each other, at ~2.1 eV. As *n* increases, the layers become thicker and less confined, eventually yielding conventional 3D perovskites $(APbX_3)$ when $n\to\infty$. Due to these structural similarities, RP layered halides are often called RP perovskites by the community, although the term is technically incorrect for phases with other stoichiometries than ABX_3.[10]

On a structural perspective, RP layered halides are the missing link between nanocrystals assemblies and bulk crystals. When properly oriented, their X-ray diffraction pattern resembles that of nanoplatelets stacks, being characterized by sharp and equally spaced peaks whose intensity is convoluted over the scattering profile of inorganic layers.[5,11] However, the disorder observed in bulk RP crystals is much lower, as expected for a fully crystalline system. This has few important consequences. First, opposite to nanoplatelet stacks, the broadening of diffraction features in patterns of RP layered phases is dominated by instrumental contributions, as the disorder is low enough to produce sharp interference fringes even at high angles ($2\theta_{Cu} > 60$, $\delta_L < 0.4$ Å). This makes the Multilayer Diffraction approach outlined in Chapter 6 non-optimal for their description, as the material contribution to the peak diffraction profile is overshadowed. Second, the organic cations in between the octahedra layers are at least partly crystalline, meaning that a more detailed description of their scattering factor is now required.

However, the most important difference is that RP perovskites, being bulk crystals, do have precise periodicities also in the in-plane directions. This means that it is possible

to associate a 3D lattice to their structure, which is therefore fully described by a unit cell and a space group. As opposed to the nanoplatelets stacks discussed in Chapter 6, where only a vertical periodicity is granted, this allows the application of a traditional Bragg diffraction formalism. In this chapter, we will take full advantage of this possibility to investigate the structure of lead-halide RP phases at the atomic level, with a specific focus on mixed-halide compositions.

7.2 Mixed-Halide Ruddlesden Popper Perovskites

7.2.1 Why mixed-halide compositions?

The many possible combinations of anions and long-chain spacers makes RP phases intrinsically tunable, as they both contribute in determining the optoelectronic properties of such materials.[6,7,12] However, interest has recently extended to mixed bromide-iodide compositions, $L_2A_{n-1}Pb_n(Br_xI_{1-x})_{3n+1}$, where x indicates the bromine fraction. Indeed, alloying halides can offer an additional knob for the fine-tuning of optoelectronic properties,[13] and enables using a wider variety of L cations than single-halide RP phases.[14] Other studies reported the formation of vertical and horizontal heterojunctions, obtained by stacking pre-made RP sheets,[12] or by exploiting halide-diffusion reactions.[15] Moreover, these materials appear promising for integration into 3D-perovskite solar cells, that are typically based on mixed-halide $APb(Br_xI_{1-x})_3$ compositions. Given the tendency of lead-halide compounds to quickly exchange halides, this will probably lead to the in-situ formation of mixed-halide RP layered phases.

Despite progress in the area, applications of 2D mixed-halide perovskites are limited by photoinduced anion segregation. Recent investigations into their photostability highlight a tendency of halide anions to migrate within crystals under illumination,[16–18] similar to what is observed in 3D mixed-halide $APb(Br_xI_{1-x})_3$ perovskites.[16,17] In this regard, photoinduced anion segregation appears to be an intrinsic instability of lead halide perovskites as a whole. As early studies shed light on the behavior of mixed-halide RP perovskites under external stimuli, questions have arisen about their properties when at rest. Indeed, while the structures of 3D mixed-halide perovskites are well described as halide alloys,[19,20] there are reasons to believe that the situation is more complex in 2D mixed-halide RP perovskites.

Compared to 3D-perovskites, RP structures offer a greater diversity of halide crystallographic sites. Of these, some sites are embedded deep within inorganic layers (central sites, Ct), while others protrude directly into the organic cation layers (apical sites, Ap), or alternatively create extended horizontal networks that form the inorganic layers (equatorial sites, Eq). Such diversity may promote the occupation of certain sites by different anions, by virtue of differences in ionic radii or interaction affinities with cations. Recently published theoretical predictions bring arguments to support such preferential positioning of halides in $(PEA)_2Pb(Br_xI_{1-x})_4$.[13] These results are corroborated by single-crystal X-ray diffraction studies on $(ter\text{-}BA)_2Pb(Br_{0.5}I_{0.5})_4$.[14] The same effect has also been reported for other layered metal halides such as $(MA)_2Cu(Cl_xBr_{1-x})_4$.[21–23] This poses a question: are lead-based mixed-halide RP perovskites really mixed alloys?

7.2.2 Sample preparation

Answering this question was the main goal of the research project I developed during the year I spent in the group of Professor Masaru Kuno at the University of Notre Dame, US. All the results discussed in this chapter were obtained in close collaboration with Ms. Irina Gushchina, for the synthesis and characterization of materials, and Dr. Allen G. Oliver for the single-crystal structure determination thereof.

As a case-study material we selected the bilayer $(BA)_2MAPb_2(Br_xI_{1-x})_7$ RP perovskites. The choice of butylammonium as a long-chain ammonium cation was due to its commercial availability, that makes it one of the most used cations for the synthesis of RP perovskites. As for thickness, we have chosen bilayers (n = 2) because they offer a wider variety of halide crystallographic sites compared to n = 1 monolayers, where sites embedded deep in the inorganic layers (Ct) are missing due to insufficient thickness. Samples have been synthesized by adapting published methods.[7,12] Briefly, for each sample a stock solution was prepared by dissolving methylammonium, butylammonium, and lead iodides and bromides in a hot mixture of concentrated HI, HBr and H_3PO_2. Precursor ratios determined the resulting sample stoichiometry. Once solubilized, solutions were cooled to 35-40 °C, causing the precipitation of RP perovskite powders that were used for powder X-ray diffraction (PXRD) analyses. Alternatively, RP crystals were grown on substrates by drop casting the warm solution. This initiated nucleation and growth, which was then halted by drying the substrates with a paper tissue. The procedure yielded platelet-shaped crystals with lateral sizes of ~10-100 mm (Figure 7.1a), which were used for compositional analysis and optical microscopy. Their habit was

remindful of the RP structure,[7] having wide and flat [010] facets, laterally terminated by perpendicular [101] and [10$\bar{1}$] facets.

The composition of all samples was verified using Scanning Electron Microscopy – Energy Dispersive X-ray Spectroscopy (SEM-EDXS). All mixed-halide specimens were found to be significantly richer in iodine than expected from their stock solution feed ratios. This indicates a tendency of RP structures to incorporate iodine over bromine. A calibration curve, relating experimental compositions to those of starting precursor solutions, was therefore constructed (Figure 7.5). Hereafter, samples compositions are labeled using x_{tot} = Br/[Br+I] where Br and I are the measured halide atomic fractions: x_{tot} = 0 stands for pure-iodide samples, while x_{tot} = 1 stands for pure-bromide samples.

7.2.3 Halide-dependent anisotropic cell expansion

All samples were characterized via PXRD (Figure 7.1b). Their diffraction patterns feature a series of intense and periodic (02k0) peaks, typical of RP perovskites (Figure 7.6).[6,7] A Le Bail profile fit was performed on all patterns (Figure 7.1c shows it for x_{tot} = 0, other fits are available in Figure 7.7) to trace how unit cell parameters change with the halide composition. Because RP perovskites are pseudo-tetragonal materials, most reflections that differentiate a and c ($h \neq \ell$) overlap strongly, making their determination unreliable. Instead, a pseudo-tetragonal a^* parameter representing the average of a and c was determined based on the stronger (hkh) reflections.
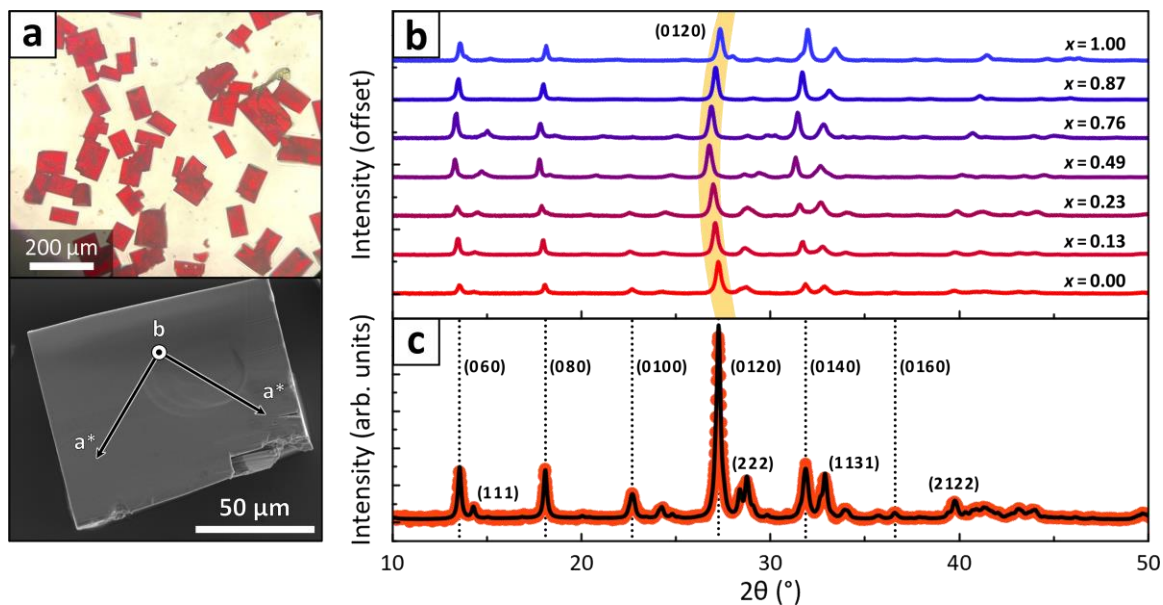
Figure 7.1. PXRD characterization of $(BA)_2MAPb_2(Br_xI_{1-x})_7$. a) Top: optical microscopy image of $(BA)_2MAPb_2(Br_xI_{1-x})_7$ crystals. Bottom: SEM image of a representative crystal, with overlaid lattice vectors. b) PXRD patterns of $(BA)_2MAPb_2(Br_xI_{1-x})_7$ samples. Highlighted are the (0120) peaks, whose shift toward lower angles highlights the anomalous unit cell expansion along the b cell axis for mixed-halide compositions. c) Le Bail profile fit of the $(BA)_2MAPb_2I_7$ PXRD pattern. Vertical grey lines indicate the family of (02k0) peaks typical of RP perovskites. Some (hkh) peaks, which ensured a reliable determination of the a^* parameter, have also been indexed. Adapted from Ref. 24.

As expected, a^* decreases linearly from $a^* = 8.92$ Å for $x_{tot} = 0$ to $a^* = 8.33$ Å for $x_{tot} = 1$ (Figure 7.2a, black asterisks). The b parameter, however, does not change linearly with halide composition (Figure 7.2b, black asterisks). Rather, it first rises and then falls, reaching a maximum at $x_{tot} = 0.5$ ($b = 39.9$ Å). This behavior is foreshadowed in Figure 7.1b by the marked shift of the (02k0) peaks toward lower angles. Together, a^* and b result in a monotonic decrease of the unit cell volume ($V_{cell} = a^{*2}b$) as x_{tot} increases from 0 to 1 (Figure 7.2c, asterisks). The mild positive inflection is due to the nonlinear trend of b.

7.3 A Geometric Model of Mixed-Halide RP Perovskites

Such anomalous dependence of *b* with halide composition suggests that lead-based mixed-halide RP perovskites do not behave as ideal alloys when it comes to placing I⁻ and Br⁻ in the structure. To rationalize this behavior, we therefore constructed a semi-quantitative geometric model (Figure 7.2) relating the RP unit cell parameters to the distribution of halide anions in different crystallographic sites.

The core idea of this model is that the unit cell parameters *a** and *b* are functions of the [Pb-X] bond lengths, of the horizontal and vertical octahedra tilt angles, and of the organic cation layers thickness *L*, as expressed in Equations 7.1-2:

$$a^* = \frac{4 \cdot [\mathrm{Pb} - \mathrm{X}]_{\mathrm{Eq}} \cdot \sin\left(\frac{\beta}{2}\right)}{\sqrt{2}} \qquad \text{Eq. 7.1}$$

$$b = 2L + 4d = 2L + 4 \cdot [\mathrm{Pb} - \mathrm{X}]_{\mathrm{Ct}} \cdot \sin\left(\frac{\alpha}{2}\right) \qquad \text{Eq. 7.2}$$

Where *L* is the Pb-Pb vertical distance between neighboring $[\mathrm{PbX}_6]^{4-}$ octahedra layers, α is the Pb-X-Pb bond angle between vertically stacked $[\mathrm{PbX}_6]^{4-}$ octahedra, and β is the X-Pb-X bond angle between neighboring $[\mathrm{PbX}_6]^{4-}$ octahedra in the equatorial plane (Figure 7.2). Here, subscripts identify each [Pb-X] bond length by the label of the halide forming the bond. All parameters in Equations 7.1-2 depend on the halide occupation of Ap, Eq, and Ct sites, thus making the unit cell parameters dependent on the distribution of halides within the RP structure. To understand how, we need to derive the dependency of each parameter on the composition of halide sites.

7.3.1 Bond lengths

Bilayer RP structures feature a total of 7 halide sites per formula unit, as indicated by the stoichiometry $(BA)_2MAPbX_7$. Of these, 2 are Apical (Ap), 4 are Equatorial (Eq) and 1 is Central (Ct). Equation 7.3 relates the total halide sample composition (x_{tot}), measured by SEM-EDXS, with that of each X site weighted by their multiplicity.

$$x_{tot} = \frac{2}{7}x_{Ap} + \frac{4}{7}x_{Eq} + \frac{1}{7}x_{Ct} \qquad \text{Eq. 7.3}$$

However, since Ct sites closely resemble those found in 3D-APbX$_3$ perovskites, they are more likely to be occupied by both I$^-$ and Br$^-$ with little preference. Therefore, we assumed that $x_{Ct} \approx x_{tot}$. This lowers by one the degrees of freedom in the model, and effectively leaves x$_{Ap}$ (or equivalently x$_{Eq}$) as the sole free parameter of the model (Equation 7.4).

$$x_{Ap} = 3x_{tot} - 2x_{Eq} \qquad \text{Eq. 7.4}$$

The composition of halide sites has a central role in defining the bond lengths within the structure. Indeed, [Pb-X] bond lengths are described as linear combinations of [Pb-Br] and [Pb-I] bond lengths, weighted by the composition of respective halide sites (Equations 7.5). Limiting [Pb-X] bond lengths for $(BA)_2MAPb_2Br_7$ and $(BA)_2MAPb_2I_7$ have been measured by SCXRD and are reported in Table 7.1.

$$[Pb - X]_{Eq} = x_{Eq}[Pb - Br]_{Eq} + (1 - x_{Eq})[Pb - I]_{Eq} \qquad \text{Eq. 7.5a}$$

$$[\text{Pb} - \text{X}]_{\text{Ap}} = x_{\text{Ap}}[\text{Pb} - \text{Br}]_{\text{Ap}} + (1 - x_{\text{Eq}})[\text{Pb} - \text{I}]_{\text{Ap}} \qquad \text{Eq. 7.5b}$$

$$[\text{Pb} - \text{X}]_{\text{Ct}} = x_{\text{Ct}}[\text{Pb} - \text{Br}]_{\text{Ct}} + (1 - x_{\text{Ct}})[\text{Pb} - \text{I}]_{\text{Ct}} \qquad \text{Eq. 7.5c}$$

7.3.2 Bond angles

Differently from bond lengths, the bond angles α and β cannot be related to the stoichiometry of one single halide site, as they depend on how octahedra, that are somewhat rigid three-dimensional bodies comprising multiple halide sides each, tilt within the RP structure. It is important to note here that the two pure-halide compounds, $(\text{BA})_2\text{MAPb}_2\text{Br}_7$ and $(\text{BA})_2\text{MAPb}_2\text{I}_7$, exhibit incompatible octahedra tilting modes.[7,25] It is therefore assumed that a transition structure free of any tilting occurs at $x_{tot} = 0.5$. This assumption was later proven correct by Single-Crystal XRD (SCXRD, see Paragraph 7.4).

To capture variations in octahedra tilting, the angles α and β are assumed to vary linearly within the intervals $0 \leq x_{tot} < 0.5$ and $0.5 \leq x_{tot} \leq 1$, and are therefore expressed as the following weighted sums (Equations 7.6-7):

$$\alpha = \begin{cases} f\alpha_{\text{I}} + (1 - f)\alpha_{x=0.5} & (x < 0.5) \\ (1 - f)\alpha_{x=0.5} + f\alpha_{\text{Br}} & (x \geq 0.5) \end{cases} \qquad \text{Eq. 7.6}$$

$$\beta = \begin{cases} f\beta_{\text{I}} + (1 - f)\beta_{x=0.5} & (x < 0.5) \\ (1 - f)\beta_{x=0.5} + f\beta_{\text{Br}} & (x \geq 0.5) \end{cases} \qquad \text{Eq. 7.7}$$

$$f = \frac{0.5 - x_{\text{tot}}}{0.5} \qquad \text{Eq. 7.8}$$

Where f formulates the Br fraction in the sample in relation with the transition value of $x_{tot} = 0.5$ (Equation 7.8). Figure 7.8 shows resulting α and β values as x_{tot} increases from 0 to 1. Limiting α and β values for $(BA)_2MAPb_2Br_7$ and $(BA)_2MAPb_2I_7$ were determined by SCXRD and are reported in Table 7.1.

7.3.3 Estimation of L as a function of a^* and x_{Ap}

The last parameter left to establish is L, that is the distance between two neighboring $[PbX_6]^{4-}$ bilayers measured at the Pb^{2+} ion plane level. This parameter is the most complex to describe, as it depends on how the long-chain organic cations arrange within the structure. This is in principle affected by a variety of factors, such as the docking geometry of the positively charged NH_3-R^+ ammonium head to the octahedra layer and the interdigitation geometry of the long aliphatic chains.

All these details cannot be implemented easily in a geometric model. However, it is reasonable to assume that the density of atoms in the interlayer space will be constant, as it is dictated by comparable chemical interactions regardless of the sample halide composition. Therefore, we opted for treating the organic cations as an incompressible fluid, and focus on their total occupied volume instead. The volume between octahedra layers is considered occupied by neutral BA-X ligands. To each neutral BA-X unit we can associate a volume V_{L-X} that is defined vertically by the Pb-Pb distance L, and horizontally by the extension of the unit cell along the a^* axes (Equation 7.9).

$$V_{L-X} = \frac{(a^*)^2 L}{4}$$

Eq. 7.9

Here, the ½ factor is due to the presence of two formula units per $(a*)^2$ unit area. Once again, V_{L-x} is assumed to depend on the composition of Ap halide sites through a weighted sum of terminal BA-I and BA-Br volumes, V_{L-Br} and V_{L-I}, that were determined from SCXRD data (Equation 7.10 and Table 7.1).

$$V_{\mathrm{L}} = x_{\mathrm{Ap}}V_{\mathrm{L-Br}} + (1 - x_{\mathrm{Ap}})V_{\mathrm{L-I}}$$ Eq. 7.10

Finally, Equation 7.10 can be inverted to yield L as a function of $a*$, allowing to calculate L for mixed-halide samples (Equation 7.11). Note that L is a function of x_{Ap} through the term V_{L-x}, and a function of x_{Eq} through the term $a*$.

$$L = 4 \cdot \frac{V_{\mathrm{L-X}}}{(a^*)^2}$$ Eq. 7.11

To validate the assumption that $V_{\mathrm{L}} \approx$ constant and V_{L-x} only depends on the composition of the Apical site, we compared the volume variation induced by the Br → I replacement in one unit of BA-X (our samples, Table 7.1) and in one unit of NH_4X (published NH_4X structures, NH_4Br = 66.9 $Å^3$ [ICSD-24916]; NH_4I = 95.7 $Å^3$ [ICSD-22150]). Replacing Br → I in NH_4X results in ΔV = 28.8 $Å^3$, that is very close to $\Delta V = V_{L-I} - V_{L-Br}$ = 27.1 $Å^3$ measured for our samples. This shows that the volume variation comes entirely from the halide replacement, and thus that the volume occupied by ammonium cations remains unchanged.

We also compared the $V_{\text{L-X}}$ values in n = 2 (BA)$_2$MAPb$_2$X$_7$ structures (our samples,

Table 7.1) and in n = 1 (BA)$_2$PbX$_4$ structures (published: COD-1545801; COD-2102938).

These are remarkably close for both bromine-based ($V_{\text{L-Br}}$ = 236.6 Å^3 [n = 1] vs 234.4 Å^3

[n = 2]) and iodine-based compounds ($V_{\text{L-I}}$ = 266.2 Å^3 [n = 1] vs 261.4 Å^3 [n = 2]), even if

the compared structures feature drastically different stoichiometries and adopt different

octahedra tilting modes. Moreover, for n = 1 structures the Br → I replacement results in

ΔV = 29.7 Å^3, again fully compatible with the examples discussed above. This further

demonstrates that considering constant the volume V_{L} occupied by ammonium cations is

a robust and reliable approximation.

7.3.4 Results of the geometric model

Now that all terms in Equations 7.1-2 have been derived, the unit cell parameters

measured experimentally can be related to the halide composition of Apical, Equatorial,

and Central sites respectively. We remind that the sole free variable in the model is x_{Ap},

because Ct sites are assumed to be occupied by both I and Br with no preference (*i.e.*, x_{Ct}

≈ x_{tot}, see also Equation 7.4). To analyze the experimental results based on the developed

model, x_{Ap} values for each sample were optimized so that the predicted *b* axis parameter

matched the experimental values extracted by PXRD (Figure 7.2b, solid orange line). In

return, the model predicted x_{Ct} and x_{Eq} based on Equation 7.4, and estimated the *a** and

V_{cell} parameters based on Equations 7.1-2. The solid-colored lines in Figure 7.2a-c reveal

that the model captures the linear trend of *a**, the peaked behavior of *b*, and the mild

positive inflection of V_{cell} as x_{tot} increases from 0 to 1. These results correspond to a

marked excess of iodine in Ap positions and bromine in Eq positions. The trend is observed over the entire $(BA)_2MAPb_2(Br_xI_{1-x})_7$ composition range (Figure IV.2d). As a point of reference, for $x_{tot} = 0.5$ the halide distribution predicted by the model is: Ap = 23% Br, Eq = 62% Br, and Ct = 50% Br (the latter constrained by assumptions).
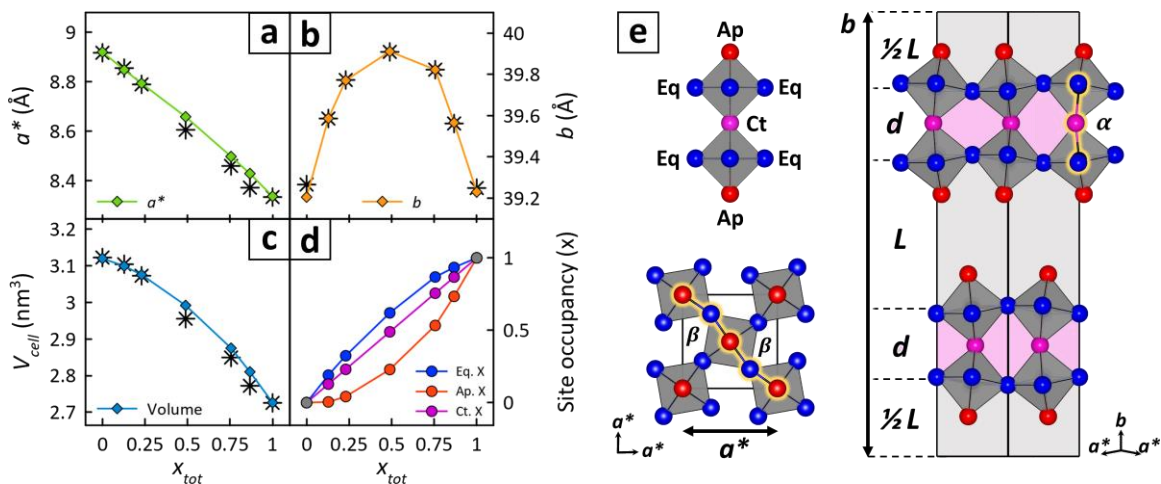
Figure 7.2. Impact of halide distribution on $(BA)_2MAPb_2X_7$ cell parameters. a-c) Experimental RP unit cell parameters (black asterisks) and geometric model predictions (colored lines). d) Halide distribution in apical (Ap), equatorial (Eq), and central (Ct) sites, corresponding to parameters predicted in panels (a-c). e) Visual representation of the model, showing how a^* and b are functions of bond lengths, tilt angles, and of the organic cation spacing L. The inorganic layer thickness, d, is defined in **Equation 7.2**. In panels (d) and (e), red, blue, and purple colors identify Ap, Eq, and Ct sites. Adapted from Ref. 24.

Overall, these results demonstrate that the anisotropic cell expansion observed by XRPD arises from a preferential positioning of halide anions. This behavior is rationalized as the combination of two effects. First, the prevalence of larger I⁻ ions in apical positions results in an elongation of the [Pb-X] bonds parallel to the unit cell b-axis.

Second, the prevalence of smaller Br⁻ ions in equatorial positions shrinks the lattice on the a-c plane. This laterally compresses the BA cations and forces them to expand along the b-axis. What results is an increase of the interlayer distance, L. This conclusion is corroborated by SCXRD-solved structures of $(BA)_2MAPb_2Br_7$ and $(BA)_2MAPb_2I_7$, where L = 13.49 Å in the former and L = 13.15 Å in the latter (see Paragraph 7.4). As both effects are solely dependent on [Pb-X] bond distances, the behavior is expected to be general across RP structures containing different organic cations, and not limited to those based on butylammonium.

Furthermore, the anisotropic expansion along b, that is measured as a bowing in the position of PXRD (02k0) reflections, appears to be a reliable approach for detecting the preferential positioning of halides in mixed-halide RP structures. Indeed, further simulations (Figure 7.9) indicate that the b parameter could grow as much as +4.3% if halides displayed full preferentiality for Apical and Equatorial sites, and would instead decrease by -1.3% if halides were randomly alloyed (with reference value being the average b parameter for pure-halide structures, 39.26 Å).

7.4 Single Crystals and Thin Films

To support and validate our model, single-crystal specimens of $(BA)_2MAPb_2I_7$, $(BA)_2MAPb_2Br_7$, and mixed-halide x_{tot} = 0.5 $(BA)_2MAPb_2(Br_{0.5}I_{0.5})_7$ were grown by slowly cooling precursor solutions and were subsequently analyzed by SCXRD. Data were collected at room temperature to ensure that structure parameters (bond lengths and angles, unit cell parameters) were consistent with those measured in PXRD experiments.

This also prevented any thermal stress from altering the distribution of halide anions in the structure. A detailed description of the SCXRD analysis can be found in the Methods 7.6 paragraph.

SCXRD results on pure-bromide and pure-iodide structures corroborated earlier literature reports,[7,25] confirming that $(BA)_2MAPb_2Br_7$ and $(BA)_2MAPb_2I_7$ crystallize in the $Ccc2$ and $Ccm2_1$ space groups, respectively (Figure 7.3a). $(BA)_2MAPb_2Br_7$ adopts an octahedral tilting mode, denoted $(00\Phi_z)$ in Aleksandrov notation,[26] with pairs of octahedra rotated in antiphase around the b-axis by $\sim10°$. $(BA)_2MAPb_2I_7$ adopts a $(\Phi_1\Phi_10)$ tilting mode, with the two combined tilts resulting in an antiphase rotation of octahedra around the c-axis (8.6°). In contrast, the x_{tot} = 0.5 $(BA)_2MAPb_2(Br_{0.5}I_{0.5})_7$ specimen crystallizes in the higher symmetry space group $Fmmm$ (Figure 7.3, middle). Consistent with assumptions in our geometric model, the transition between these two incompatible tilting modes suppresses any tilt, a condition denoted (000) (Figure 7.3b). This conclusively demonstrates that a coexistence of I^- and Br^- in 2D RP structures can cause major modifications to their crystal symmetry.

Crucially, a bond length analysis of the x_{tot} = 0.5 $(BA)_2MAPb_2(Br_{0.5}I_{0.5})_7$ sample indicates that Ap positions are mostly occupied by iodine (Ap = 29% Br, 71% I). Eq positions are instead richer in bromine (Eq = 74% Br, 26% I) while Ct positions are occupied more homogeneously (Ct = 42% Br, 58% I), corresponding to a crystal composition of x_{tot} = 0.56. Those results are very close to the halide distribution predicted by the geometric model for x_{tot} = 0.5. A complementary analysis of the halide sites occupation via electron densities confirms the same trend, and suggests a more marked preference of Apical and

Central sites for Iodine (Ap = 7% Br, 93% I; Ct = 37% Br, 63% I; Eq = 64% Br, 36% I). The extracted crystal composition is x_{tot} = 0.44, again compatible within error with the target x_{tot} = 0.5 composition.
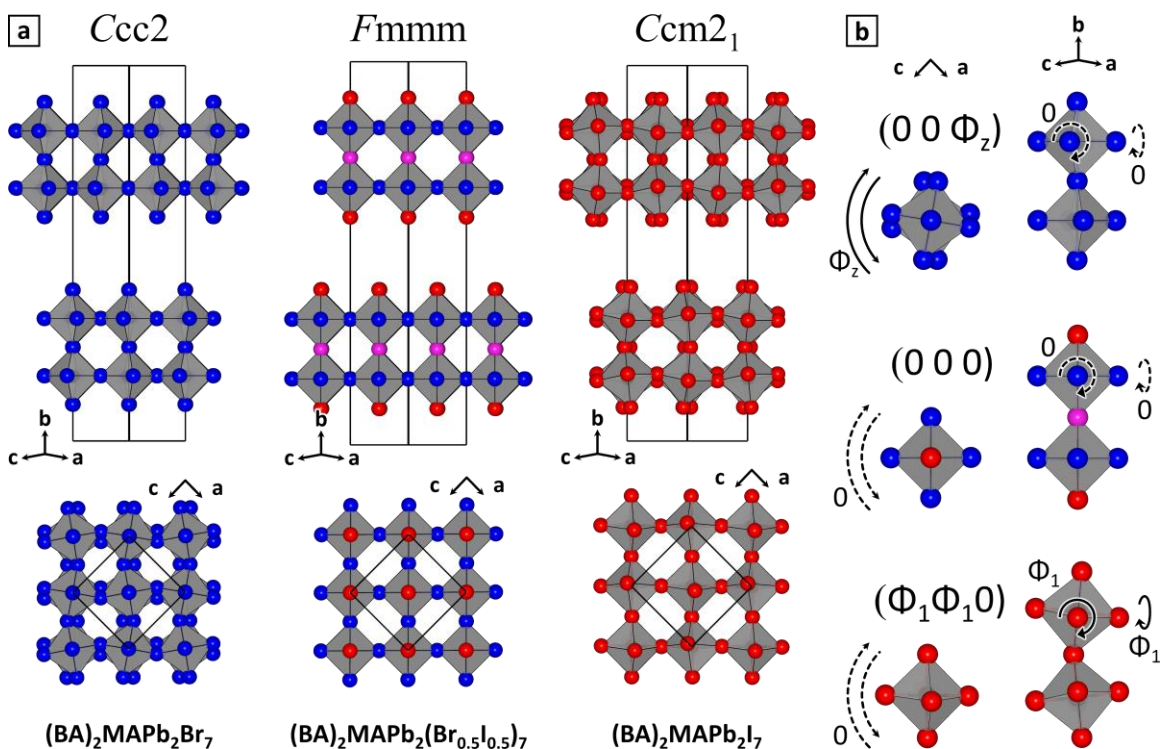
Figure 7.3. Structures of pure- and mixed-halide (BA)$_2$MAPb$_2$X$_7$ samples. a) Crystal structures of (BA)$_2$MAPb$_2$Br$_7$ [left], (BA)$_2$MAPb$_2$(Br$_{0.5}$I$_{0.5}$)$_7$ [middle], and (BA)$_2$MAPb$_2$I$_7$ [right] as solved by SCXRD. Top: (101) projection. Bottom: (010) projection. Halide site color code: blue = Br (exclusive or prevalent); red = I (exclusive or prevalent), purple = comparable Br and I fractions. Organic cations have been omitted for clarity. b) Representation of the octahedra tilting modes in the structures depicted in panel (a), as described by Aleksandrov notation.[26] Adapted from Ref. 24

Overall, both PXRD and SCXRD data point to a preferential positioning of I⁻ and Br⁻

anions in lead-based mixed-halide RP structures. Discrepancies in determined

occupancies likely stem from a combination of model assumptions (e.g., $x_{Ct} \approx x_{tot}$),

approach biases (bond lengths vs electron density), and crystallization speeds. The last

point is especially relevant, given that sample preparation methods might influence the

crystallization dynamics and therefore the distribution of anions within mixed-halide RP

structures. However, both PXRD and SCXRD samples, that crystallized over minutes and

hours, showed clear evidence of preferential halide positioning. Therefore, the question

arises whether faster crystallization conditions might favor a more homogeneous halide

distribution instead.

To address this question, we collected XRD patterns of spin coated $n = 2$

$(BA)_2MAPb_2(Br_xI_{1-x})_7$ and $n = 1$ $(BA)_2Pb_2(Br_xI_{1-x})_4$ RP perovskites thin films (Figures 7.10-11).

The latter $n = 1$ specimens are of particular interest given extensive prior investigations

of these materials.[13,14,16,17] Details of the thin film spin coating synthesis have been

provided in the Methods 7.6 paragraph. For both $n = 1$ and $n = 2$ thin films, Figure 7.4

shows clear non-linear b dependencies with halide composition. This confirms that halide

sites in mixed-halide RP perovskites are preferentially occupied even under the fast

crystallization conditions often adopted for fabricating samples and devices.[1–3,14,16–18,27]

Notably, both $n = 1$ and $n = 2$ samples demonstrate comparable maximum expansion

along b ($n = 1$: +1.58%; $n = 2$: +1.73%).
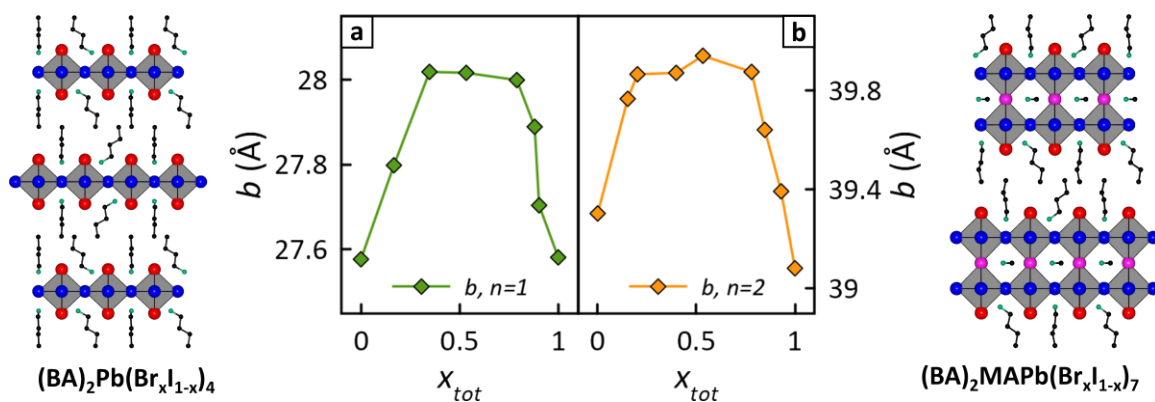
Figure 7.4. Cell parameter *b* in mixed-halide RP perovskite thin films. Experimental *b* parameter measured on *n* = 1 (a) and *n* = 1 (b) thin films prepared by spin coating. The side panels schematize the structures of *n* = 1 (BA)$_2$PbX$_4$ (left) and *n* = 2 (BA)$_2$MAPb$_2$X$_7$ (right) and RP perovskites. Adapted from Ref. 24.

7.5 Conclusions

To conclude, the common assumption that anions in mixed-halide perovskites are homogeneously distributed at the unit cell level, that holds for 3D perovskites because their halide sites share comparable chemical environments,[19,20,28–30] does not apply to RP layered perovskites. In RP perovskites, instead, I⁻ anions preferentially occupy Apical sites that are closest to long chain organic cations, while Br⁻ anions prefer to reside in Equatorial sites, surrounded by lead cations. This preferential positioning occurs regardless of the crystallization speed, and is likely due to the different ionic radii of iodine and bromine. Our conclusions are supported by recent reports on lead-based mixed-halide RP perovskites[14,21,31] and appear to be part of a broader trend that extends beyond the domain of lead-based materials, wherein structural anisotropy emerges to inhibit halide alloying.[21–23,32,33]

Although the impact of such inhomogeneous halide distribution on the optoelectronic properties of mixed-halide RP perovskites has yet to be fully investigated, there are reasons to believe that it might not be negligible. Indeed, we demonstrated that mixed-halide RP samples can adopt altered symmetry and octahedral tilting modes compared to pure-halide RP specimens. This might affect the orbital overlap, and thus the electronic structure of these materials. Moreover, being aware of preferential anion occupation in mixed-halide RP structures might assist in better understanding the recent observations of anion photo-segregation in these materials.

7.6 Methods

This section summarizes the methods adopted for the experiments and analyses discussed in this chapter. For brevity, only the most relevant information is reported. For additional details, please refer to the original open-access publications [Ref. 24].

7.6.1 Synthesis methods

For all RP perovskites samples. MABr, MAI, BABr, BAI, $PbBr_2$ and PbI_2 were weighed inside 8 mL glass vials (MA = methylammonium, BA = butylammonium). To this, known amounts of concentrated, aqueous solutions of HBr, HI and H_2PO_3 were added. Table 7.2 provides the specific amounts of each reagent used. Vials were sealed and heated to 130 °C on a hotplate until their contents became limpid, light-yellow solutions. Gentle shaking was used to speed up this process. Once solutions turned clear, vials were transferred to a thermostatic water bath, maintained at temperatures between 35-40 °C. Crystalline RP precipitates were obtained within a few minutes of immersion.

Crystals on substrates. To synthesize RP crystals on substrates, 50 μL of warm mother liquor solutions were drop cast onto flat glass or silicon substrates. Crystal nucleation was triggered on cooling and was observed through the formation of yellow-to-orange colored films. Crystal growth was halted by pressing paper tissues onto substrates to wick up any excess mother liquor.

Powders for PXRD. To retrieve powders for PXRD analyses, vials were cooled to room temperature and were centrifuged to compact powders onto their bottoms (2500 rpm, 5 minutes). Any supernatant was removed using a pipette. Wet solids were then recovered

249

with a spatula and deposited onto filter paper. Samples were dried through gentle pressing with additional filter paper. Recovered solids were then transferred to a mortar and were gently ground with a pestle to randomize the orientation of RP crystallites. Powders were finally transferred into a cylindric sample holder (~6 mm diameter × 3 mm depth) and were gently pressed to obtain flat pellets for PXRD analysis.

Crystals for SCXRD. Single crystal specimens were prepared in a manner similar to that of powder samples. The main difference was that samples were cooled from 130 °C to room temperature, using a programmable oven with a controlled temperature descent of -2 °C per hour. Additionally, 40 mL vials were used to ease the manipulation of resulting single crystals. Produced specimens contained compact masses of mm-sized crystals, that were highly defective. Consequently, for SCXRD analyses thin shards of approximately 95 mm in lateral size were selected, based on the quality of their polarized light extinction.

Spin-coated films. Pure iodide and bromide precursor solutions were prepared from pure iodide and bromide powder samples, obtained as described above for PXRD specimens. Powders were weighed and dissolved in anhydrous dimethylformamide (DMF), using suitable volumes to produce equimolar solutions of n = 1 $(BA)_2PbBr_4$ and $(BA)_2PbI_4$ and n = 2 $(BA)_2MAPb_2Br_7$ and $(BA)_2MAPbI_7$. To obtain mixed-halide $(BA)_2PbX_4$ and $(BA)_2MAPb_2X_7$ thin film specimens, precursor solutions were pre-mixed in the desired stoichiometric ratio and spin coated onto plasma-treated glass coverslips.

7.6.2 Characterization methods

PXRD and Le Bail analysis. Powder XRD patterns were collected on a Bruker D8 Advance diffractometer, equipped with a Cu-Kα source and a LynxEye pixel detector operating in a Bragg-Brentano geometry in reflection mode. PXRD patterns were analyzed by performing Le Bail fits using the program Profex.[34] Prior to analysis, manual background subtraction was performed to improve fit convergence. The Le Bail analysis does not assume any structural constraints on the intensities of diffraction peaks. Hence, it is ideal for refining unit cell parameters, but does not provide any structural information beyond this.

SCXRD analysis. SCXRD data were collected on a Bruker Apex II single-crystal diffractometer, equipped with a Mo-K$_a$ source and an Apex-II detector. Data were collected at room temperature using Apex-4 software. Subsequent data analysis and structure solution were performed using the software suite Olex2.[35] Data have been recorded at room temperature to allow direct comparisons with room temperature PXRD data. We observed that cooling RP specimens to cryogenic temperatures resulted in lattice deformations, occasionally accompanied by fracturing.

Structures were solved by dual-space methods, and expanded and refined routinely from difference Fourier maps. Due to disorder of alkyl amines in all three structures, organic cations have been modeled using isotropic displacement parameters. In contrast, Pb, I, and Br atoms have all been modeled using anisotropic displacement parameters. Hydrogen atoms could not be located or geometrically placed on disordered MA cations. They have, however, been included in the chemical formula for

completeness. Hydrogen atoms bonded to BA cations have been modeled in an idealized geometry. In all studied cases, BA are found to be disordered in the interlayer space. The proposed models best account for the electron density therein.

The structure of $(BA)_2MAPb_2Br_7$ has been refined with a racemic twin component, yielding a 0.548:0.452 domain ratio. $(BA)_2MAPb_2I_7$ has likewise been modeled with a racemic twin component, yielding a 0.51:0.49 twin ratio. In both cases, the presence of an inversion center was contraindicated by attempts to model the structures in centrosymmetric space groups and by the lack of missed inversion symmetry in the asymmetric unit. Mild restraints were applied to the bond distances, angles, and displacement parameters of BA and MA cations in all structures. For the mixed-halide $(BA)_2MAPb_2(Br_xI_{1-x})_7$, halogen positions have been refined with Br^- and I^- occupying the same site. Standard equivalencies to constrain atom positions and displacement parameters were employed.

7.7 Source Publications and Contributions

This chapter is based on the following publication:

I. **Toso, S.;** Gushchina, I.; Oliver, A. G.; Manna, L.; Kuno, M. <u>Are Mixed-Halide Ruddlesden-Popper Perovskites Really Mixed?</u> Submitted to ACS Energy Letters

The work discussed in this chapter is the result of a collaboration effort. Hereby, the major contributions are listed. Ms. Irina Gushchina helped me with the synthesis of samples and performed the compositional characterization thereof. Dr. Allen Oliver first

trained and then assisted me with the collection of SCXRD data and the structure solution

process. He also contributed to validate the geometric model proposed in this chapter.

Prof. Masaru Kuno took part in developing the geometric mode and in writing the

manuscript. He also provided general supervision and guidance during the process. Prof

Liberato Manna contributed to editing the manuscript.

7.8 Copyright

Some elements of this chapter were reproduced from external sources:

7.9 Bibliography

1.   Li, X., Hoffman, J. M. & Kanatzidis, M. G. The 2D Halide Perovskite Rulebook:
      How the Spacer Influences Everything from the Structure to Optoelectronic
      Device Efficiency. *Chem. Rev.* **121**, 2230–2291 (2021).

2.   Tsai, H. *et al.* High-Efficiency Two-Dimensional Ruddlesden-Popper Perovskite
      Solar Cells. *Nature* **536**, 312–317 (2016).

3.   Smith, I. C., Hoke, E. T., Solis-Ibarra, D., McGehee, M. D. & Karunadasa, H. I. A
      Layered Hybrid Perovskite Solar-Cell Absorber with Enhanced Moisture Stability.
      Angew. Chemie - Int. Ed. **53**, 11232–11235 (2014).

4.   Grancini, G. *et al.* One-Year Stable Perovskite Solar Cells by 2D/3D Interface
      Engineering. *Nat. Commun.* **8**, 1–8 (2017).

5.   Liu, Y. *et al.* Surface-Tension-Controlled Crystallization for High-Quality 2D
      Perovskite Single Crystals for Ultrahigh Photodetection. *Matter* **1**, 465–480
      (2019).

6.   Dhanabalan, B. *et al.* Engineering the Optical Emission and Robustness of Metal-
      Halide Layered Perovskites through Ligand Accommodation. *Adv. Mater.* **33**,
      2008004 (2021).

7.   Stoumpos, C. C. *et al.* Ruddlesden-Popper Hybrid Lead Iodide Perovskite 2D
      Homologous Semiconductors. *Chem. Mater.* **28**, 2852–2867 (2016).

8.   Wang, Q. *et al.* Quantum confinement effect and exciton binding energy of
      layered perovskite nanoplatelets. *AIP Adv.* **8**, 25108 (2018).

9.   Weidman, M. C., Seitz, M., Stranks, S. D. & Tisdale, W. A. Highly Tunable Colloidal
      Perovskite Nanoplatelets through Variable Cation, Metal, and Halide
      Composition. *ACS Nano* **10**, 7830–7839 (2016).

10.   Akkerman, Q. A. & Manna, L. What Defines a Halide Perovskite? *ACS Energy Lett.*
      5, 604–610 (2020).

11.   Mao, L., Stoumpos, C. C. & Kanatzidis, M. G. Two-Dimensional Hybrid Halide
      Perovskites: Principles and Promises. *J. Am. Chem. Soc.* **141**, 1171–1190 (2019).

12.   Pan, D. *et al.* Deterministic Fabrication of Arbitrary Vertical Heterostructures of
      Two-Dimensional Ruddlesden–Popper Halide Perovskites. *Nat. Nanotechnol.* **16**,
   159–165 (2021).

13. Wright, N. E. *et al.* Influence of Annealing and Composition on the Crystal Structure of Mixed-Halide, Ruddlesden-Popper Perovskites. *Chem. Mater.* **34**, 3109–3122 (2022).

14. Ovčar, J. *et al.* Mixed Halide Ordering as a Tool for the Stabilization of Ruddlesden-Popper Structures. *Chem. Mater.* **34**, 4286–4297 (2022).

15. Roy, C. R. *et al.* Anion Exchange of Ruddlesden-Popper Lead Halide Perovskites Produces Stable Lateral Heterostructures. *J. Am. Chem. Soc.* **143**, 5212–5221 (2021).

16. Mathew, P. S., Dubose, J. T., Cho, J. & Kamat, P. V. Spacer Cations Dictate Photoinduced Phase Segregation in 2D Mixed Halide Perovskites. *ACS Energy Lett.* **6**, 2499–2501 (2021).

17. Cho, J., Mathew, P. S., DuBose, J. T. & Kamat, P. V. Photoinduced Halide Segregation in Ruddlesden–Popper 2D Mixed Halide Perovskite Films. *Adv. Mater.* **33**, 2105585 (2021).

18. Liu, Y. *et al.* Photoinduced iodide repulsion and halides-demixing in layered perovskites. *Mater. Today Nano* **18**, 100197 (2022).

19. Brivio, F., Caetano, C. & Walsh, A. Thermodynamic Origin of Photoinstability in the $CH_3NH_3Pb(I_{1-x}Br_x)_3$ Hybrid Halide Perovskite Alloy. *J. Phys. Chem. Lett.* **7**, 1083–1087 (2016).

20. Frost, J. M. *et al.* Atomistic Origins of High-Performance in Hybrid Halide Perovskite Solar Cells. *Nano Lett.* **14**, 2584–2590 (2014).

21. Kubo, H. Distribution of Cl- and Br- Ions in Mixed Crystals $(CH_3NH_3)_2Cu(Cl_{1-x}Br_x)_4$. *J. Phys. Soc. Japan* **52**, 1420–1426 (1983).

22. Martinelli, A., Ray, A., Abdelhady, A. L. & Locardi, F. Structural properties of defective $(CH_3NH_3)_2Cu(Cl_{1-x}Br_x)_4$ compounds. *Acta Crystallogr. B. Struct. Sci. Cryst. Eng. Mater.* **78**, 425–435 (2022).

23. Ray, A. *et al.* Impact of local structure on halogen ion migration in layered methylammonium copper halide memory devices. *J. Mater. Chem. A* **8**, 17516–17526 (2020).

24. Toso, S. *et al.* Are Mixed-Halide Ruddlesden-Popper Perovskites Really Mixed? *ACS Energy Lett.* **17**, 4242–4247 (2022).

25.   Liang, M. *et al.* Free Carriers versus Self-Trapped Excitons at Different Facets of Ruddlesden-Popper Two-Dimensional Lead Halide Perovskite Single Crystals. *J. Phys. Chem. Lett.* **12**, 4965–4971 (2021).

26.   Aleksandrov, K. S. & Bartolome, J. Octahedral tilt phases in perovskite-like crystals with slabs containing an even number of octahedral layers. *J. Phys. Condens. Matter* **6**, 8219–8235 (1994).

27.   Cao, D. H., Stoumpos, C. C., Farha, O. K., Hupp, J. T. & Kanatzidis, M. G. 2D Homologous Perovskites as Light-Absorbing Materials for Solar Cell Applications. *J. Am. Chem. Soc.* **137**, 7843–7850 (2015).

28.   Jong, U. G., Yu, C. J., Ri, J. S., Kim, N. H. & Ri, G. C. Influence of halide composition on the structural, electronic, and optical properties of mixed $CH_3NH_3Pb(I_{1-x}Br_x)_3$ perovskites calculated using the virtual crystal approximation method. *Phys. Rev. B* **94**, 125139 (2016).

29.   Beal, R. E. *et al.* Cesium Lead Halide Perovskites with Improved Stability for Tandem Solar Cells. *J. Phys. Chem. Lett.* **7**, 746–751 (2016).

30.   Lehmann, F. *et al.* The phase diagram of a mixed halide (Br, I) hybrid perovskite obtained by synchrotron X-ray diffraction. *RSC Adv.* **9**, 11151–11159 (2019).

31.   Li, J. *et al.* $Cs_2PbI_2Cl_2$, All-Inorganic Two-Dimensional Ruddlesden-Popper Mixed Halide Perovskite with Optoelectronic Response. *J. Am. Chem. Soc.* **140**, 11085–11090 (2018).

32.   Cortecchia, D. *et al.* Lead-Free $MA_2CuCl_xBr_{4-x}$ Hybrid Perovskites. *Inorg. Chem.* **55**, 1044–1052 (2016).

33.   Chen, H. P. *et al.* Tunable dielectric transitions in layered organic–inorganic hybrid perovskite-type compounds: $[NH_3(CH_2)_2Cl]_2[CdCl_{4-4x}Br_{4x}]$ (x = 0, 1/4, 1). *Dalt. Trans.* **47**, 7005–7012 (2018).

34.   Doebelin, N. & Kleeberg, R. Profex: A graphical user interface for the Rietveld refinement program BGMN. *J. Appl. Crystallogr.* **48**, 1573–1580 (2015).

35.   Dolomanov, O. V., Bourhis, L. J., Gildea, R. J., Howard, J. A. K. & Puschmann, H. OLEX2: A complete structure solution, refinement and analysis program. *J. Appl. Crystallogr.* **42**, 339–341 (2009).
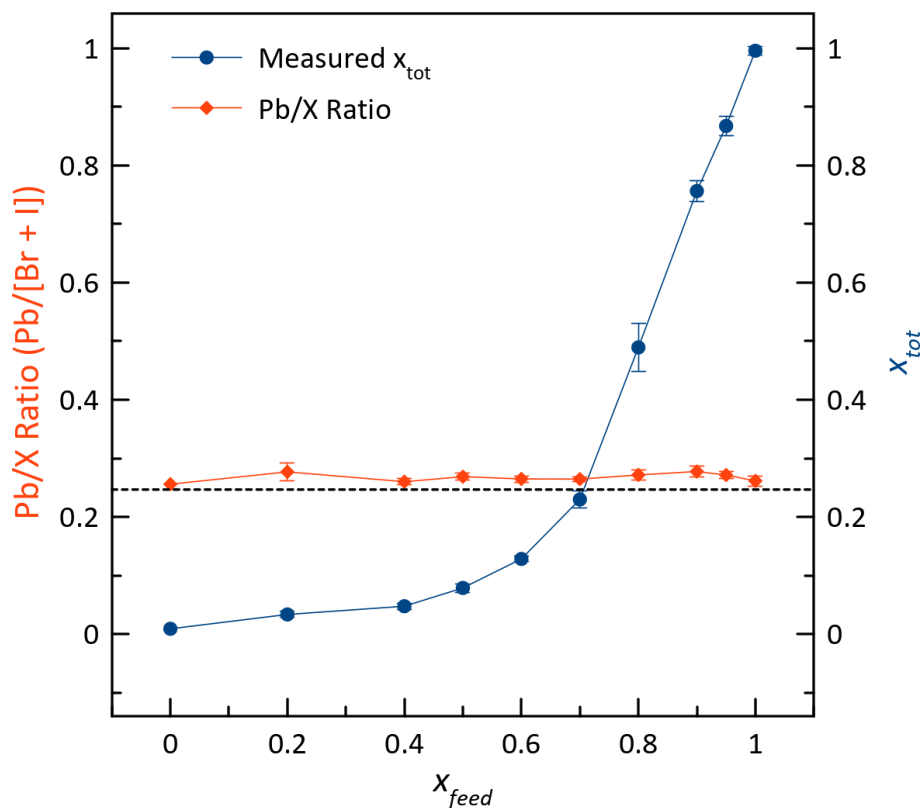
Figure 7.5. Composition calibration curve for (BA)$_2$MAPb(Br$_x$I$_{1-x}$)$_7$ crystals. Blue trace: experimental halide composition plotted versus halide precursor feed ratio. Red trace: experimental Pb/X ratio as measured by SEM-EDXS. In both scales, x = Br/[Br+I] where Br and I are the atomic fractions of bromine and iodine introduced in precursor solutions (feed ratio) and measured experimentally by SEM-EDXS (measured). Solid blue and red lines are guides to the eye. The horizontal black line represents the ideal Pb/X value of 2/7 = 0.286, dictated by the stoichiometry of (BA)$_2$MAPbX$_7$. [Ref. 24]
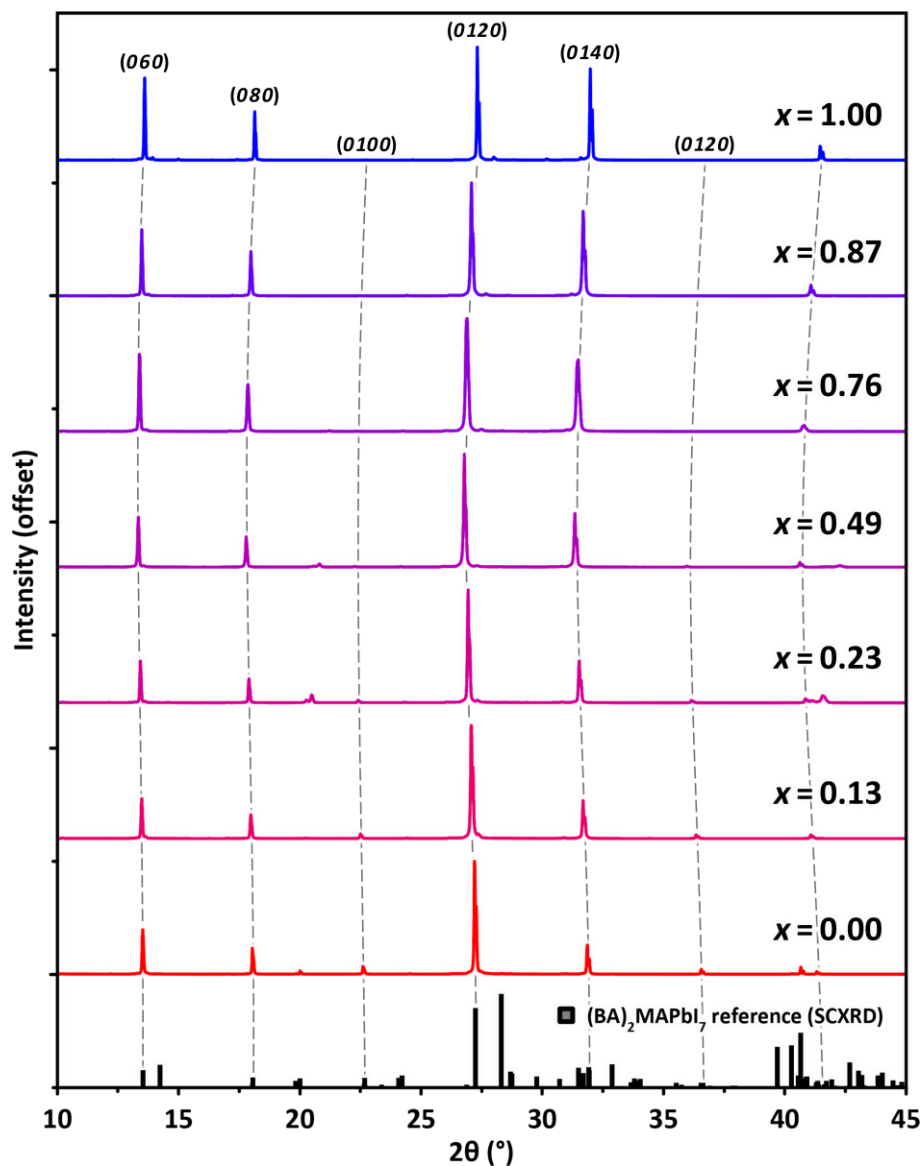
Figure 7.6. XRD of (BA)₂MAPb(Br$_x$I$_{1-x}$)₇ crystals oriented flat on substrates. All patterns show a series of regularly spaced reflections typical of oriented layered crystals. All peaks follow the same periodicity, indicating that n = 2 RP perovskite is the only phase present. The few peaks not belonging to the periodic series come from misoriented crystals of (BA)₂MAPb(Br$_x$I$_{1-x}$)₇, as seen by comparison with the reference pattern (reference structure from this work). [Ref. 24]
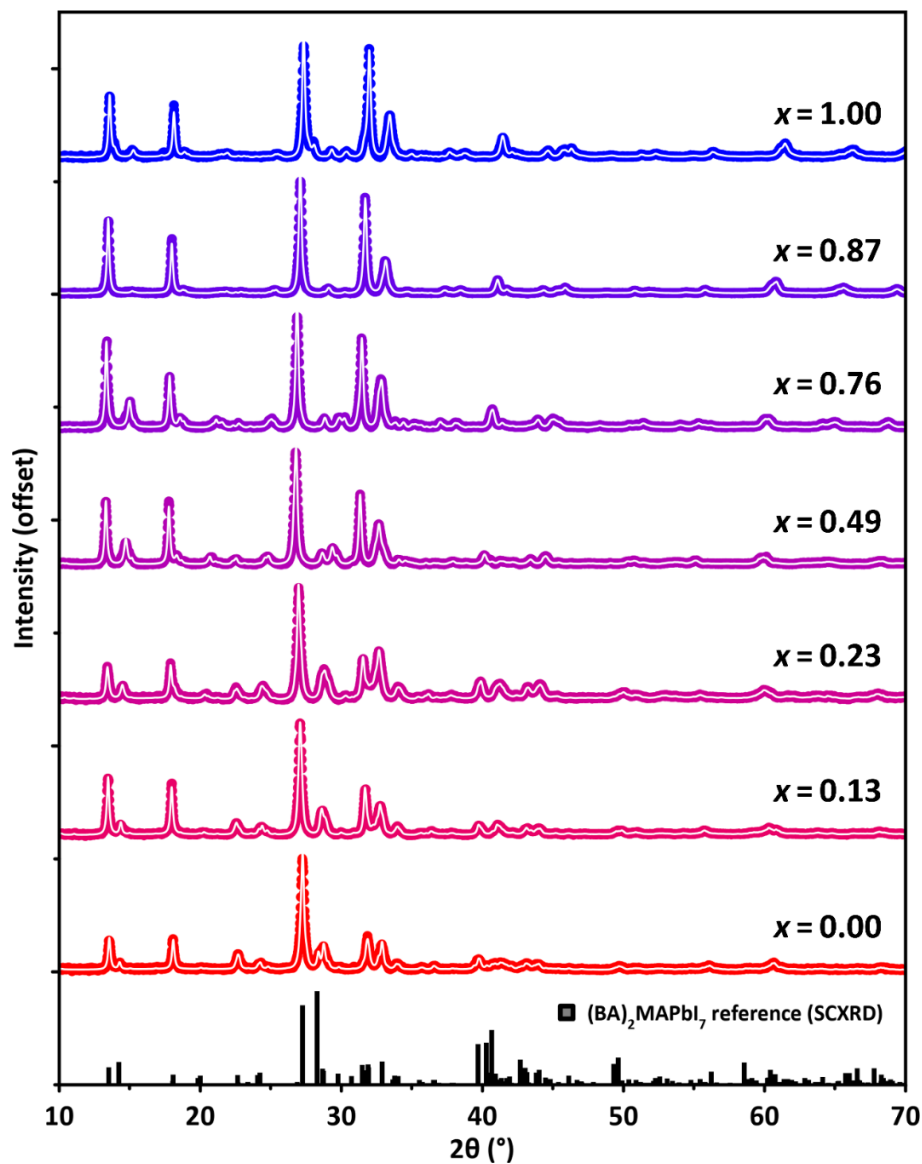
Figure 7.7. Le Bail fits of (BA)₂MAPb(BrₓI₁₋ₓ)₇ PXRD patterns. Experimental PXRD patterns of (BA)₂MAPb(BrₓI₁₋ₓ)₇ samples (colored markers) with Le Bail fit profiles superimposed (solid white lines). All peaks could be indexed based on the expected (BA)₂MAPb(BrₓI₁₋ₓ)₇ structures, indicating that all samples are phase-pure. The reference pattern is calculated based on the (BA)₂MAPbI₇ RP perovskite structure solved in this work by SCXRD. [Ref. 24]
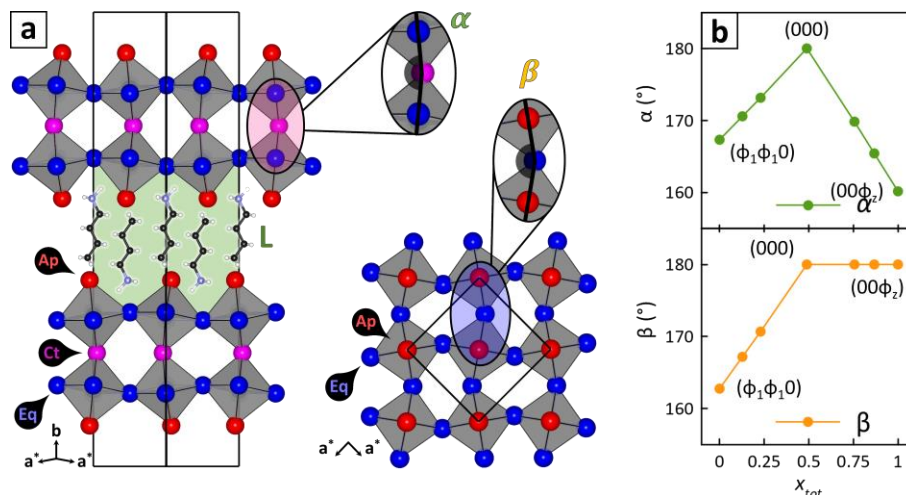
Figure 7.8. RP structure geometric model. a) RP unit cell with labelled Ap, Eq and Ct sites labelled. Insets show the α and β bond angles. b) Modeled dependence of α and β on x_{tot}. Aleksandrov notation shown for the pure-halide limiting structures and for the transition structure at x_{tot} = 0.5. [Ref. 24]
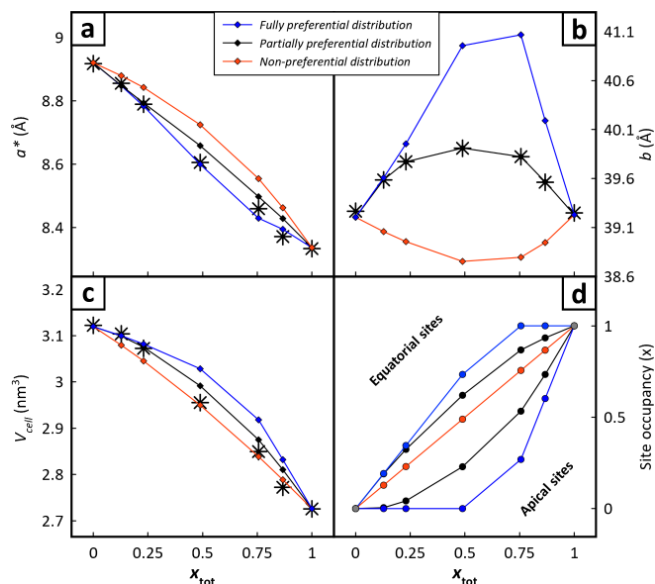
Figure 7.9. Fully preferential and non-preferential halide distribution limits. Simulations performed for two limit cases: fully preferential distribution of halides (blue lines) and non-preferential distribution of halides (red lines). Black lines reproduce the partially preferential distribution of halides shown in Figure 7.2. Black asterisks represent parameters measured experimentally. [Ref. 24]
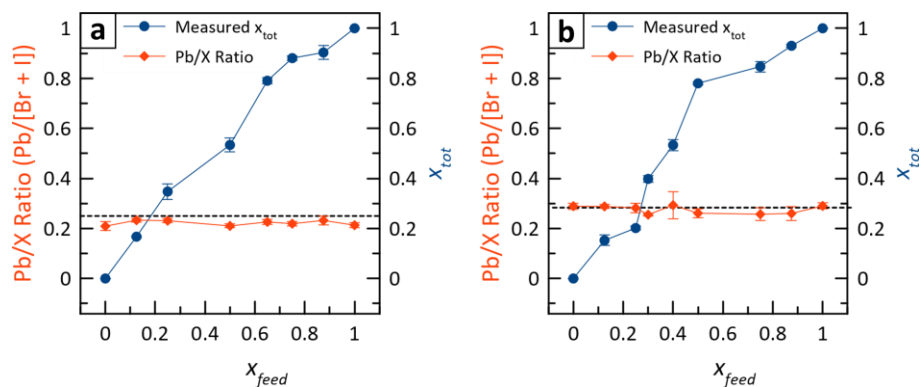
Figure 7.10. Composition calibration curves for spin coated thin films. Calibration curve for (a) $n = 1$ $(BA)_2Pb(Br_xI_{1-x})_4$ and (b) $n = 2$ $(BA)_2MAPb_2(Br_xI_{1-x})_7$. Blue traces: experimental halide compositions plotted versus halide precursor feed ratios. Red traces: experimental Pb/X ratio as measured by SEM-EDXS. The horizontal dashed lines represent the ideal Pb/X values established from the stoichiometry of $(BA)_2MAPbX_7$ and $(BA)_2MAPb_2(Br_xI_{1-x})_7$ respectively. These lines serve as controls to assess the reliability of SEM-EDXS analyses. [Ref. 24]
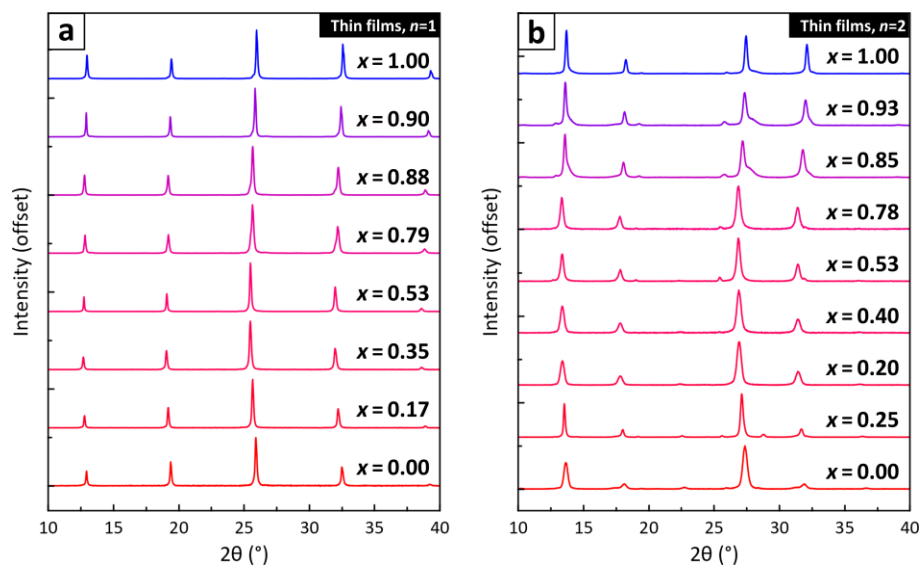
Figure 7.11. XRD patterns of spin coated thin films. XRD patterns collected on (a) $n = 1$ $(BA)_2Pb(Br_xI_{1-x})_4$ and (b) $n = 2$ $(BA)_2MAPb_2(Br_xI_{1-x})_7$ thin films. [Ref. 24]

TABLE 7.1:

STRUCTURE PARAMETERS OF SINGLE HALIDE $(BA)_2MAPBX_7$ FROM SCXRD.

SCXRD Data	$[Pb-X]_{Ap}$	$[Pb-X]_{Eq}$*	$[Pb-X]_{Ct}$	α	β	V_L
$(BA)_2MAPb_2Br_7$	2.914 Å*	2.992 Å	3.064 Å	160.2°	180.0°	468.6 Å^3
$(BA)_2MAPb_2I_7$	3.083 Å	3.173 Å	3.267 Å	167.3°	162.8°	522.9 Å^3

* $[Pb-X]Eq$ values are the average of the four equatorial bond lengths

** $[Pb-Br]Ap$ is calculated between Pb and the average position of two disordered Br sites

TABLE 7.2:

COMPOSITION OF STOCK SOLUTIONS FOR THE SYNTHESIS OF RP PEROVSKITES.

Feed Ratio (x_{feed})	Final Composition (x_{tot})	BABr (g)	BAI (g)	MABr (g)	MAI (g)	PbBr$_2$ (g)	PbI$_2$ (g)	HBr (mL)	HI (mL)	H$_3$PO$_2$ (mL)
0	0	---	0.173	---	0.099	---	0.544	---	1.818	0.182
0.20	0.034	0.026	0.138	0.014	0.079	0.087	0.435	0.321	1.497	0.182
0.40	0.046	0.053	0.104	0.028	0.059	0.173	0.326	0.661	1.157	0.182
0.50	0.079	0.066	0.086	0.035	0.049	0.217	0.272	0.839	0.979	0.182
0.60	0.128	0.079	0.069	0.042	0.039	0.260	0.218	1.023	0.795	0.182
0.70	0.230	0.093	0.052	0.049	0.030	0.303	0.163	1.212	0.606	0.182
0.80	0.489	0.106	0.035	0.056	0.020	0.346	0.109	1.408	0.410	0.182
0.90	0.756	0.119	0.017	0.062	0.010	0.390	0.054	1.610	0.209	0.182
0.95	0.867	0.126	0.009	0.066	0.005	0.411	0.027	1.713	0.105	0.182
1	1	0.132	---	0.069	---	0.433	---	1.818	---	0.182

CHAPTER 8:

CONCLUSIONS

During this journey into the structural characterization of nanomaterials at different complexity and length scales, it has become apparent how even a single class of materials, that of lead halide semiconductors (**Chapter 2**), can offer a huge variety of compositions, structures, morphologies, and interactions. Each of these aspects posed a different challenge, a riddle that had to be solved before the material could be fully understood. For that, my colleagues and I relied on a vast set of approaches and techniques (**Chapter 3**), each time adapted to the specific challenge.

In **Chapter 4**, a combination of X-ray Powder Diffraction, 3D-Electron Diffraction and Electron Microscopy techniques disclosed the structure of novel semiconductor nanocrystals ($Pb_4S_3Br_2$, $Pb_3S_2Cl_2$, and an unknown polymorph of BiSCl). These findings contributed to expand the knowledge on colloidal metal chalcohalide semiconductors, a class of nanomaterials that have been little explored so far, but recently captured the attention of the community as promising candidates for applications in solar cells.

In **Chapter 5**, some of the newly discovered lead chalcohalides demonstrated a remarkable structural and chemical affinity for the $CsPbX_3$ lead halide perovskites, with which they formed epitaxial heterostructures. The nature of their interface could be

rationalized based on prior observations on heterostructures formed by pairs of Cs-Pb-X compounds, which act as intermediates for solid-state reactions occurring in cesium lead halide nanocrystals. This parallel between Cs-Pb-X/Cs-Pb-X and $Pb_4S_3X_2$/CsPbX$_3$ heterostructures inspired the use of CsPbX$_3$ domains as on-demand, phase-selective reaction intermediates for the synthesis of nanocrystals of $Pb_4S_3Cl_2$, a novel lead chalcohalide that could not be obtained by direct synthesis due to the competitive nucleation of $Pb_3S_2Cl_2$. These studies demonstrated that the formation of heterostructures can greatly affect the reactivity of the compounds they are made of, and opened a new route for the design of novel nanomaterials using disposable and phase-selective epitaxial templates.

Chapter 6 explored a different kind of interaction between multiple nanocrystals, that is the formation of colloidal superlattices. Here, the serendipitous observation of an unusual peak profile in the XRD pattern of CsPbBr$_3$ nanocrystal superlattices led to the rediscovery of a coherent interference effect previously reported in epitaxial multilayers grown by physical methods, that we called in analogy the Multilayer Diffraction effect. Once understood, this phenomenon could be exploited to gain insight into superlattices of nanocrystals and nanoplatelets, and proved to be a simple yet effective technique for the characterization of self-assembled nanomaterials, especially in the case of ultrathin nanoplatelets and nanosheets.

Finally, our journey came to a conclusion in **Chapter 7**, where the layered lead halides, a class of hybrid organic-inorganic compounds that serves as a bridge between nanoplatelet superlattices and bulk crystals, brought us back to the characterization of

structures at the atomic scale, closing the loop that started in Chapter 4. There, the presence of an extended lattice periodicity and the large size of samples allowed to exploit a combination of X-Ray Powder Diffraction and Single-Crystal X-Ray Diffraction to determine the distribution of halides at the single unit cell level. By doing so, we demonstrated that mixed-halide layered lead halides are not homogeneous alloys, a fact that might have great impact on their properties and applications in functional devices, where mixed-halide compositions are often used to tune the optoelectronic properties of the material.

All these findings will hopefully contribute to the efforts that the colloidal nanomaterials community devotes to the advancements of fundamental and applied research on lead halide semiconductors, and might provide a basis for further advancements in the field. However, I hope that the legacy of this thesis will not stop there. It is natural to the scientific progress that materials come and go. For example, as we explore the lead halides deeper, we get to know their advantages and weaknesses, and we will eventually drift away towards some other materials that perform better, or promise to do so. What stays, however, are the challenges that the research process poses, and the solutions we adopt for overcoming them. Therefore, I hope that the work presented in this Thesis will serve in the future not only because of the conclusions we reached on the specific materials, but first and foremost to get to those conclusions that we did not reach yet. In the end, it is new materials and properties that motivate research, but it is successful approaches and methods that allow it.

APPENDIX:

PUBLICATIONS

As First Author:

- Quarta, D.; **Toso, S.***; Saleh, G.; Caliandro, R.; Moliterni, A.; Griesi, A.; Divitini, G.; Infante, I.; Gigli, G.; Giannini, C.; et al. *Mixed Valence of Bismuth in Hexagonal Chalcohalide Nanocrystals*. Chem. Mater. 2023, 35, 52.

- **Toso, S.**; Baranov, D.; Filippi, U.; Giannini, C.; Manna, L. *Collective Diffraction Effects in Perovskite Nanocrystal Superlattices*. Acc. Chem. Res. 2023, 56, 1, 66-76.

- **Toso, S.**; Gushchina, I.; Oliver, A. G.; Manna, L.; Kuno, M. *Are Mixed-Halide Ruddlesden–Popper Perovskites Really Mixed?* ACS Energy Lett. 2022, 17, 4242–4247.

- Quarta, D.*; **Toso, S.***; Giannuzzi, R.; Caliandro, R.; Moliterni, A.; Saleh, G.; Capodilupo, A.-L.; Debellis, D.; Prato, M.; Nobile, C.; et al. *Colloidal Bismuth Chalcohalide Nanocrystals*. Angew. Chemie 2022, 61 (22), e202201747.

- **Toso, S.***; Imran, M.*; Mugnaioli, E.; Moliterni, A.; Caliandro, R.; Schrenker, N. J.; Pianetti, A.; Zito, J.; Zaccaria, F.; Wu, Y.; et al. *Halide Perovskites as Disposable Epitaxial Templates for the Phase-Selective Synthesis of Lead Sulfochloride Nanocrystals*. Nat. Commun. 2022 131 2022, 13 (1), 1–10.

- **Toso, S.**; Baranov, D.; Giannini, C.; Manna, L. *Structure and Surface Passivation of Ultrathin Cesium Lead Halide Nanoplatelets Revealed by Multilayer Diffraction*. ACS Nano 2021, 15 (12), 20341–20352.

- **Toso, S.***; Baranov, D.*; Altamura, D.; Scattarella, F.; Dahl, J.; Wang, X.; Marras, S.; Alivisatos, A. P.; Singer, A.; Giannini, C.; et al. *Multilayer Diffraction Reveals That Colloidal Superlattices Approach the Structural Perfection of Single Crystals*. ACS Nano 2021, 15 (4), 6243–6256.

- **Toso, S.**; Baranov, D.; Manna, L. *Metamorphoses of Cesium Lead Halide Nanocrystals*. Acc. Chem. Res. 2021, 54 (3), 498–508.

- **Toso, S.**; Baranov, D.; Manna, L. *Hidden in Plain Sight: The Overlooked Influence of the Cs⁺ Substructure on Transformations in Cesium Lead Halide Nanocrystals*. ACS Energy Lett. 2020, 5 (11), 3409–3414.

- **Toso, S.***; Akkerman, Q. A.*; Martín-García, B.*; Prato, M.; Zito, J.; Infante, I.; Dang, Z.; Moliterni, A.; Giannini, C.; Bladt, E.; et al. *Nanocrystals of Lead Chalcohalides: A Series of Kinetically Trapped Metastable Nanostructures*. J. Am. Chem. Soc. 2020, 142 (22), 10198–10211.

- **Toso, S.**; Baranov, D.; Giannini, C.; Marras, S.; Manna, L. Wide-Angle X-Ray *Diffraction Evidence of Structural Coherence in CsPbBr₃ Nanocrystal Superlattices*. ACS Mater. Lett. 2019, 1 (2), 272–276.

   **These Authors contributed equally*

As Contributor:

- Liu, Y.; Zaffalon, M. L.; Zito, J.; Cova, F.; Moro, F.; Fanciulli, M.; Zhu, D.; **Toso, S.**; Xia, Z.; Infante, I.; et al. *Cu⁺ → Mn²⁺ Energy Transfer in Cu, Mn Coalloyed Cs₃ZnCl₅ Colloidal Nanocrystals*. Chem. Mater. 2022, 2022, 8603–8612.

- Kuno, M.; Gushchina, I.; **Toso, S.**; Trepalin, V. *No One Size Fits All: Semiconductor Nanocrystal Sizing Curves*. J. Phys. Chem. C 2022, 126 (29), 11867–11874.

- Sartori, E.; Campolucci, M.; Baranov, D.; Zeng, M.; **Toso, S.**; Divitini, G.; Ferretti, M.; Hens, Z.; Manna, L.; Locardi, F. *Red-Emissive Nanocrystals of Cs₄MnₓCd₁₋ₓSb₂Cl₁₂ Layered Perovskites*. Nanoscale 2022, 14 (2), 305–311.

- Imran, M.; Peng, L.; Pianetti, A.; Pinchetti, V.; Ramade, J.; Zito, J.; Di Stasio, F.; Buha, J.; **Toso, S.**; Song, J.; et al. *Halide Perovskite-Lead Chalcohalide Nanocrystal Heterostructures*. J. Am. Chem. Soc. 2021, 143 (3), 1435–1446.

- Baranov, D.; Fieramosca, A.; Yang, R. X.; Polimeno, L.; Lerario, G.; **Toso, S.**; Giansante, C.; Giorgi, M. De; Tan, L. Z.; Sanvitto, D.; et al. *Aging of Self-Assembled Lead Halide Perovskite Nanocrystal Superlattices: Effects on Photoluminescence and Energy Transfer*. ACS Nano 2021, 15 (1), 650–664.

- Pavlovetc, I. M.; Brennan, M. C.; Draguta, S.; Ruth, A.; Moot, T.; Christians, J. A.; Aleshire, K.; Harvey, S. P.; **Toso, S.**; Nanayakkara, S. U.; et al. *Suppressing Cation Migration in Triple-Cation Lead Halide Perovskites*. ACS Energy Lett. 2020, 5 (9), 2802–2810.

- Brennan, M. C.; **Toso, S.**; Pavlovetc, I. M.; Zhukovskyi, M.; Marras, S.; Kuno, M.; Manna, L.; Baranov, D. *Superlattices Are Greener on the Other Side: How Light Transforms Self-Assembled Mixed Halide Perovskite Nanocrystals*. ACS Energy Lett. 2020, 5 (5), 1465–1473.

- Brescia, R.; **Toso, S.**; Ramasse, Q.; Manna, L.; Shamsi, J.; Downing, C.; Calzolari, A.; Bertoni, G. *Bandgap Determination from Individual Orthorhombic Thin Cesium Lead Bromide Nanosheets by Electron Energy-Loss Spectroscopy. Nanoscale Horizons*. 2020, 5 (12), 1610–1617.

- Akkerman, Q. A.; García, B. M.; Buha, J.; Almeida, G.; **Toso, S.**; Marras, S.; Bonaccorso, F.; Petralanda, U.; Infante, I.; Manna, L. *Ultrathin Orthorhombic PbS Nanosheets*. Chem. Mater. 2019, 31 (19), 8145–8153.